Doctoral Thesis

Self-Modulation Development of a Proton Bunch in Plasma

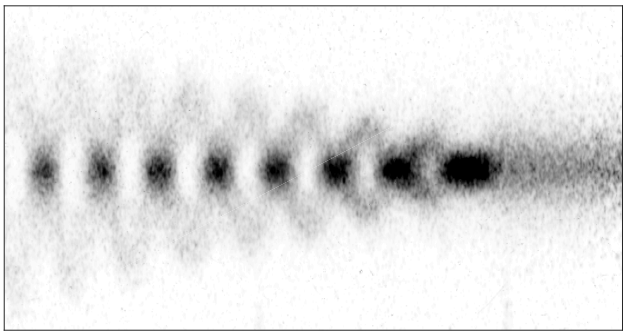

Submitted by

Anna-Maria Bachmann

February, 2021

Department of Physics

Technical University of Munich

Max-Planck Institute for Physics
(Werner-Heisenberg Institute)

CERN

TECHNISCHE UNIVERSITÄT MÜNCHEN
Fakultät für Physik

Max-Planck-Institut für Physik / Werner-Heisenberg-Institut

Self-Modulation Development of a Proton Bunch in Plasma

Anna-Maria Bachmann

Vollständiger Abdruck der von der Fakultät für Physik der Technischen Universität München zur Erlangung des akademischen Grades eines

Doktors der Naturwissenschaften (Dr. rer. nat.)

genehmigten Dissertation.

Vorsitzende:

Prof. Dr. Laura Fabbietti

Prüfer der Dissertation:

1. Hon.-Prof. Dr. Allen C. Caldwell
2. Hon.-Prof. Dr. Frank Jenko

Die Dissertation wurde am 10.02.2021 bei der Technischen Universität München eingereicht und durch die Fakultät für Physik am 13.04.2021 angenommen.

Abstract

Plasma wakefield accelerators (PWFAs) typically use particle bunches with a length shorter than the wakefield period to drive wakefields. The Advanced Wakefield Experiment (AWAKE) takes advantage of the large stored energy in proton bunches from the CERN SPS to drive wakefields. Since these proton bunches are $\sim 8\,\mathrm{cm}$ long, but $\sim$ mm long bunches are necessary to drive $\sim$ GV/m wakefields in plasma with density $\sim 10^{15}\,\mathrm{cm}^{-3}$, AWAKE relies on the self-modulation (SM) of the proton bunch transforming the long bunch into a train of short bunches. SM is seeded with a relativistic ionization front (RIF) co-propagating within the proton bunch. It was shown experimentally that SM occurs, that the modulation frequency is the plasma frequency and that the SM process grows along the plasma.

In this work, I give an introduction to PWFAs and to AWAKE in particular, summarizing some of the previously obtained experimental results of the self-modulated bunch and electrons that are accelerated in the wakefield. Further, I introduce a graphical user interface (GUI), developed for the spatial alignment of the ionizing laser pulse onto the proton bunch trajectory and measure the plasma radius with Schlieren imaging.

The main study of this thesis is the characterization of the self-modulated proton bunch. Using time-resolved images of the modulated bunch obtained in the experiment and from numerical simulations, I study the SM process over the first ten micro-bunches following the seed point, the start of SM. The results presented confirm some of the fundamental characteristics of the SM process. Experimental and simulation results agree well with each other. Simulation results allow for observation of processes along the plasma, something not possible in the experiment. The agreement reinforces the confidence in the experiment and in the simulations and show detailed knowledge and understanding of the SM process. I study the characteristics of both the regions of focused protons along the long bunch, i.e. the micro-bunches, and the regions of defocused protons between the micro-bunches. They yield different and complementary information about the SM process.
From the location of micro-bunches and defocused proton regions along the bunch, I determine the modulation frequency after the second period and the length of the first

modulation period. I show that the first micro-bunch plays an important role in the dephasing of the wakefield along the bunch and plasma. The duration of this micro-bunch is proportional to, but significantly longer than the period of the wakefield, whereas following micro-bunches are shorter than, and separated by the period of the wakefield, calculated from the plasma density. I characterize the width, length and charge of micro-bunches as a result of the focusing wakefield along the plasma with different beam/plasma parameters. I show that the defocused proton distributions are a good diagnostic for the transverse wakefield along the plasma, and measure their growth in transverse width along the bunch. I measure the effect of variations in seed wakefield, wakefield growth and wakefield phase slippage on the defocused proton distributions for different experimental parameters in experiment and simulations. A higher initial bunch density increases the transverse seed wakefield and SM growth. As a result, wider defocused proton distributions are observed. Higher plasma density lowers the amplitude of the transverse seed wakefield, while keeping the growth rate per period constant. Narrower widths of defocused proton distributions are observed with higher plasma density. The phase slippage of the wakefield with respect to protons is counteracted (enhanced) by applying a positive (negative) linear plasma density gradient. The effect of the gradient on the phase slippage can be measured with the defocused proton distributions. The distributions are significantly wider with negative density gradient, as protons initially experience focusing fields over much longer plasma distances and start diverging due to the phase slippage later in the plasma, where the amplitude of the transverse wakefield is higher.

Finally, I study experimentally and in numerical simulations the use of a preceding electron bunch as an alternative SM seeding method to the relativistic ionization front. Experimental results hint at the possibility of seeding, while simulation results show that transverse and longitudinal evolution of the electron bunch along the plasma plays a key role in reaching a sufficient amplitude of the wakefield.

Contents

1 Introduction to Plasma Wakefield Acceleration

We want to accelerate electrons to high energies (GeV-TeV) to be used for high energy physics experiments, as e.g. an electron-proton collider. Beam driven plasma wakefield accelerators are a promising candidate as compact, high gradient future accelerators. With much higher energy gradients than in radio-frequency cavities, they can accelerate particles to higher energies over shorter distances.

1.1 Conventional Accelerators

For the acceleration of charged particles, conventional linear and and circular machines use radio-frequency (RF) cavities, metallic structures with an electromagnetic field applied. The cavities have a maximum acceleration gradient of $\sim 100\,\mathrm{MeV/m}$ due to metallic breakdown, when exceeding this value. Thus, in order to achieve larger energies for the accelerated charged particles, the size of the accelerator needs to be increased (e.g. linear accelerator at SLAC, 3 km for 50 GeV or proposal of CLIC, 20 km for 1.5 TeV as electron-positron collider). Circular machines instead keep the particles on a circle, so the same particle can pass the accelerating fields multiple times (e.g. LHC at CERN, 27 km circumference). The downside of circular machines is the large energy loss E_{loss} due to synchrotron radiation, which is especially high for particles with small rest mass m_0, as $E_{loss} \propto 1/{m_0}^4$ [1]. Thus, circular machines are typically mainly used for heavy particles (protons, ions). As the radiation loss decreases with smaller bending angle, the accelerator size needs to be large enough to let energy gain dominate over the loss, to reach higher energies. Thus, in both cases, for linear and circular machines higher particle energies require an increase in accelerator size.
Due to the demanding financial and technical requirements, research in advanced accelerator techniques, providing an alternative for conventional RF cavities became of importance. Promising candidates are for example THz-accelerators, dielectric accelerators, laser-wakefield accelerators (LWFA) and beam-driven plasma-wakefield accelerators

(PWFA). This thesis focuses on a PWFA driven by a long proton bunch.

1.2 Driving Plasma Wakefields

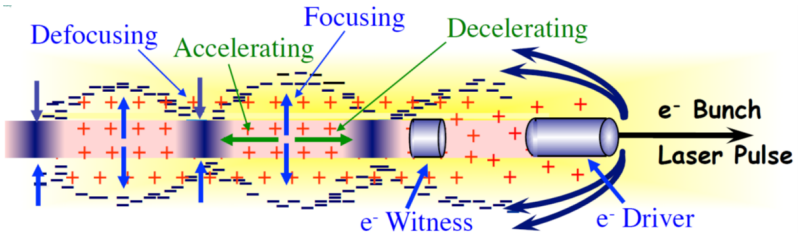

Figure 1.1: Schematic of the principle of plasma wakefield acceleration: A short particle bunch or laser pulse (propagating from left to right) drives a wakefield inside plasma, consisting of focusing/defocusing (blue arrows) and accelerating/decelerating (green arrows) phases. A to be accelerated witness particle (here electron e^-) bunch is injected in the focusing and accelerating phase of the wakefield [2]

A plasma is ionized gas, i.e. it consists of ions and free electrons. When a charged particle bunch (driver) enters the plasma, depending on its charge sign, plasma electrons are either attracted towards or repelled away from the propagation axis of the bunch [3, 4]. The heavy ions can be assumed to remain at rest for short time scales. The light plasma electrons are attracted by the lack of electrons, that arises from being repelled or from overshooting after being attracted, and start to oscillate around the propagation axis. Similarly to a particle bunch, a high-intensity laser pulse can act as a driver, where the ponderomotive force pushes the plasma electrons away from the axis. In this thesis, a proton bunch is used as a driver.

The formed charge distribution of ions and plasma electrons leads to transverse and longitudinal electric and magnetic fields (wakefield) [5–7], as shown in the schematic in Figure 1.1. The transverse wakefield corresponds to focusing and defocusing fields for charged particles, the longitudinal one to accelerating and decelerating fields. A witness bunch is injected in the accelerating and, to maintain a bunch over the plasma, focusing phase of the wakefield. In linear theory, this corresponds to one quarter of the wakefield period. For a relativistic drive and witness bunch, the witness bunch could be accelerated over the entire plasma propagation length. However, if the drive bunch looses enough energy to decrease its velocity dephasing limits the acceleration (length). Unlike with a laser pulse driver, dephasing between two relativistic bunches is usually small over typical accelerator lengths.

The maximum electric fields of RF-cavities is defined by the break-down limit, typically $\sim 100\,\mathrm{MV/m}$. A plasma however can in principle sustain much higher electric fields. The upper limit for electric fields in a plasma is called wave breaking field E_{Wb}. As the limit is defined as all plasma electrons contributing to the plasma oscillation, it scales with the plasma density n_{pe}. The wave breaking field is $E_{Wb} = m_e\, c\, \omega_{pe}\, /e$ [8] with the plasma angular frequency $\omega_{pe} = \sqrt{\frac{n_{pe}\, e^2}{\epsilon_0\, m_e}}$ [9] and the vacuum permittivity ϵ_0, the speed of light in vacuum c, the electron mass m_e and the elementary charge e. Therefore, a plasma density of $n_{pe} = 1 \cdot 10^{15}\,\mathrm{cm^{-3}}$ leads to a wave breaking field of $E_{WB} \approx 3\,\mathrm{GV/m}$.
The drive bunch transfers energy over the wakefield to the witness bunch. Thus the maximum energy that the witness bunch can gain corresponds to a large fraction of the energy of the drive bunch, which makes a proton bunch as a driver particularly interesting.

1.3 Seeded Self-Modulation of a Long Proton Bunch in Plasma

Previous experiments have used either an intense laser pulse or a negatively charged relativistic electron bunch as driver. AWAKE is the first experiment using a proton bunch, the CERN SPS bunch, as a driver [10]. These proton bunches carry a much larger amount of energy than electron bunches or laser pulses, thus more energy can be transferred to the witness bunch. The CERN SPS bunch with $400\,\mathrm{GeV/p^+}$ and $N_{p^+} = 3 \cdot 10^{11}$ protons per bunch carries over 19 kJ.
Proton bunches were not used as a driver in past experiments, as their lengths significantly exceed the length to drive large amplitude wakefields. The bunch length σ_ξ should be on the order of the plasma wavelength λ_{pe} [11], so that $E_{max} = E_{WB} \propto \omega_{pe} \propto 1/\lambda_{pe} \propto 1/\sigma_\xi$. For comparison the CERN SPS proton bunch has a length of $\sigma_\xi \approx 8\,\mathrm{cm}$. AWAKE uses plasma densities of $n_{pe} > 0.9 \cdot 10^{14}\,\mathrm{cm^{-3}}$, i.e. the plasma wavelength is $\lambda_{pe} < 3.5\,\mathrm{mm}$ and therefore $\lambda_{pe} \ll \sigma_\xi$.
However, with the bunch in plasma, the Self-Modulation Instability (SMI) [11] transversely modulates through the transverse wakefield the long ($\sigma_\xi > \lambda_{pe}$) bunch with the plasma periodicity [12–14]. The initially small transverse wakefield at the start of the plasma (seed wakefield) with focusing and defocusing (or less focusing) regions along the long bunch leads to a radial bunch density modulation, i.e. regions with higher and lower bunch density along the bunch. This reinforces the wakefield, and thus the bunch density modulation, leading to a resonant growth of the modulation. If the plasma propagation distance is long enough, the long bunch fully transforms into a train of micro-bunches, with separation equal to the plasma wavelength, as shown by the schematic in Figure 1.2. The micro-bunches then resonantly drive wakefields in the plasma.

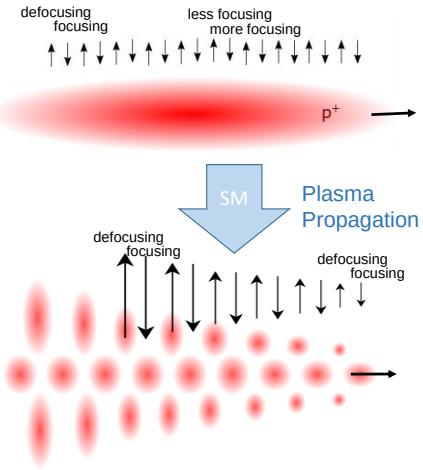

Figure 1.2: Schematic of the self-modulation instability: The transverse wakefield of focusing and defocusing (or less focusing) phase, driven by the initially long charged particle bunch in plasma acts back on the driver, transforming the long bunch into a train of micro-bunches.

The self-modulation (SM) can be seeded by imposing a wakefield larger than noise,

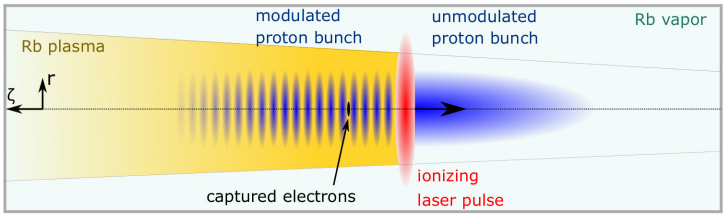

Figure 1.3: Seeding of the proton bunch self-modulation in AWAKE: The ionizing laser pulse co-propagates with the bunch, close to the bunch center, creating the relativistic ionization front at a high incoming bunch density.

initiating the start of the modulation at the seed point, i.e. with a preceding short bunch or intense laser pulse driving a wakefield (see Chapter 7). Alternatively seeding can be provided, by a large initial wakefield (seed wakefield) where the plasma and bunch start to interact, i.e. with an instant high bunch density (cutting the longitudinal distribution of the long drive bunch) or by creating a plasma edge within the bunch (sharp relativistic ionisation front, RIF). In AWAKE the plasma is created by an intense laser pulse ionizing a cylinder of rubidium (Rb) vapor. Here, SM is seeded by co-propagating the RIF within the drive bunch, close to the bunch center [15], as shown by the schematic in Figure 1.3. We expect phase reproducible wakefields and bunch modulation with respect to the RIF, when the SMI is seeded (seeded self-modulation SSM) [16]. Seeding allows choosing and fixing the position of the witness electron bunch, i.e. injecting it into the focusing and accelerating phase of the wakefield, thus providing a stable acceleration and maintaining bunch quality.

1.4 Transverse Wakefield in Linear and SMI Theory

In a plasma, the long particle bunch undergoes self-modulation, dividing the bunch into micro-bunches with a spacing of the plasma period. The resulting plasma wakefield consists of accelerating and decelerating as well as focusing and defocusing phases. In linear PWFA theory, they are shifted by $\pi/2$ with respect to each other along the bunch. Thus one quarter of the period is accelerating and focusing for a given charged particle as e.g. an electron witness bunch. In the following, PWFA linear theory is introduced for the calculation of the seed wakefield driven by the bunch when entering the plasma.

1.4.1 Linear Wakefield Theory

If the plasma density perturbation δn_{pe} is small compared to the plasma density n_{pe} (quasi-neutrality condition $\delta n_{pe} \ll n_{pe}$), we can use linear wakefield theory to calculate the transverse and longitudinal wakefield [17, 18] driven by a particle bunch. Throughout the thesis, the spatial coordinate in the co-moving frame $\xi = ct - z$ is used, see Figure 1.4. The bunch density profile $n_b(r, \xi)$ can be divided in a transverse $f(r)$ and a longitudinal

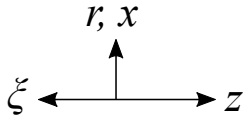

Figure 1.4: Coordinate system used in this thesis.

part $g(\xi)$ with peak bunch density $n_{b,0}$, as

$$n_b(r, \xi) = n_{b,0} \cdot f(r) \cdot g(\xi). \tag{1.1}$$

Then the longitudinal wakefield $W_\parallel$ and transverse wakefield $W_\perp$ can be expressed as [19]

$$W_\parallel(\xi, r) = E_\parallel \cdot R(r) = -\frac{n_{b,0}\, q}{\epsilon_0} \int_{-\infty}^{\xi} g(\xi') \cos\left(k_{pe}(\xi - \xi')\right) d\xi' \cdot R(r) \tag{1.2}$$

and

$$W_\perp(\xi, r) = -\frac{n_{b,0}\, q}{\epsilon_0\, k_{pe}} \int_{-\infty}^{\xi} g(\xi') \sin\left(k_{pe}(\xi - \xi')\right) d\xi' \cdot \frac{dR(r)}{dr} \tag{1.3}$$

with particle charge q of the driver and the radial component $R(r)$

$$R(r) = k_{pe}^2\, K_0(k_{pe}\, r) \int_0^r r'\, f(r')\, I_0(k_{pe}\, r')\, dr' + k_{pe}^2\, I_0(k_{pe}\, r) \int_r^\infty r'\, f(r')\, K_0(k_{pe}\, r')\, dr' \tag{1.4}$$

with k_{pe} the plasma wave number and I_0, K_0 the zeroth order modified Bessel functions of the first and second kind.

For the experiment described in this thesis, the proton bunch to plasma density ratio $n_{b,0}/n_{pe}$ is small, as $n_{pe} \geq 0.9 \cdot 10^{14}\,\mathrm{cm}^{-3}$ and $n_{b,0} \leq 5.6 \cdot 10^{12}\,\mathrm{cm}^{-3}$ (proton bunch peak density with $N_{p^+} = 2.8 \cdot 10^{11}$, $\sigma_\xi = 7.92\,\mathrm{cm}$ and transverse size $\sigma_r = 200\,\mu\mathrm{m}$). We can thus use linear theory to calculate the wakefield driven by the proton bunch with uniform density at the plasma entrance before SM occurs. As mentioned before, we trigger the start of the bunch-plasma interaction by placing the RIF longitudinally within the proton bunch. This is a situation equivalent to that of a bunch with a sharp rise in density, a step or a cut bunch at the location of the RIF, propagating in a preformed plasma.
We can use Equation 1.3 to plot the transverse wakefield $W_\perp$ along the proton bunch at

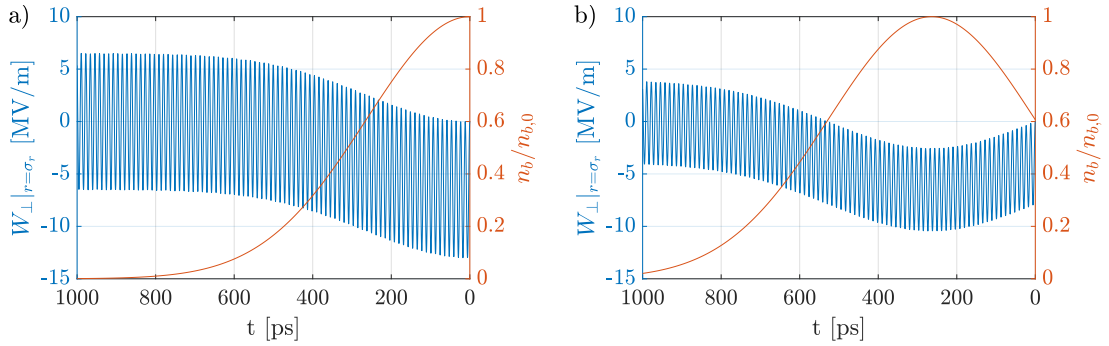

Figure 1.5: Transverse seed wakefield $W_\perp|_{r=\sigma_r}$ (blue line) driven by the proton bunch with Gaussian bunch density profile n_b (normalized to peak density $n_{b,0}$, red line), propagating from left to right, with seeding (bunch cut) a) in the bunch center and b) $1\,\sigma_\xi$ ahead (right figure). Here $N_{p^+} = 2.8 \cdot 10^{11}$, $\sigma_r = 200\,\mu\mathrm{m}$, $\sigma_\xi = 7.92\,\mathrm{cm}$ ($\widehat{=}\ \sigma_t = 264\,\mathrm{ps}$), i.e. $n_{b,0} = 5.6 \cdot 10^{12}\,\mathrm{cm}^{-3}$, and $n_{pe} = 0.92 \cdot 10^{14}\,\mathrm{cm}^{-3}$.

the plasma entrance, i.e. before self-modulation. This gives the focusing and defocusing field acting on the charged particles along the proton drive bunch and a witness particle bunch, if injected. The transverse seed wakefield $W_\perp|_{r=\sigma_r}$ (blue line), periodically focusing and defocusing along the bunch, is plotted for a proton bunch with Gaussian bunch density profile (red line) and bunch cut (seeding position ξ_{Seed}) in the center of the bunch (Figure 1.5 a) and $1\,\sigma_\xi$ ahead of the center (Figure 1.5 b). One can see that seeding at higher initial bunch density n_b ($\xi_{Seed} = 0$, i.e. $n_b = 5.6 \cdot 10^{12}\,\mathrm{cm}^{-3}$, Figure 1.5 a) leads to slightly larger transverse wakefield amplitudes (6.5 MV/m behind the bunch) than seeding at lower initial bunch density ($< 4\,\mathrm{MV/m}$ behind the bunch for $\xi_{Seed} = 1\,\sigma_\xi$, i.e. $n_b = 3.4 \cdot 10^{12}\,\mathrm{cm}^{-3}$, Figure 1.5 b), see Section 1.4.6. A negative (positive) transverse wakefield corresponds to a focusing (defocusing) field for positive charge, as protons. This thesis studies the transverse wakefield acting on protons, therefore negative wakefield amplitudes here are called focusing.

Figure 1.5 visualizes that due to the adiabatic response of the Gaussian drive bunch the transverse seed wakefield is purely focusing, i.e. alternating stronger and weaker (or zero) focusing, at the start of the modulation ($t \approx 0$). For seeding ahead of the bunch center ($\xi_{Seed} > 0$, Figure 1.5 b) focusing fields increase further along the bunch due to the increasing bunch density. They turn defocusing further behind in the bunch when the bunch density decreased more than the local bunch density at the seed position (i.e. $\xi_{Seed} - \xi = 2\,\xi_{Seed}$). For seeding at or behind the bunch center ($\xi_{Seed} \leq 0$, Figure 1.5 a) the transverse wakefield is weakly defocusing from the start due to the decreasing bunch density along the bunch.
This shows that from the linear seed wakefield, when seeding ahead of the bunch center ($\xi_{Seed} > 0$), we expect no defocusing field for protons over the first wakefield periods for the unmodulated bunch. The wakefield and SM must have grown if a defocusing field is observed up to the RIF for frontal seeding. In this thesis, protons are characterized over the first few periods behind the RIF after the plasma, where the bunch is modulated.

1.4.2 Constant Drive Bunch Density Approximation

In the following, a constant bunch density is assumed for ξ close to ξ_{seed}. Equation 1.3 for the transverse wakefield can then be integrated analytically with $g(\xi) \equiv 1$:

$$W_{\perp}(\xi, r) = -\frac{n_{b,0}\, q}{\epsilon_0\, {k_{pe}}^2}\, \frac{dR(r)}{dr}\, \left(1 - \cos\left(k_{pe}\, \xi\right)\right). \tag{1.5}$$

This shows that, due to the adiabatic response (factor 1 in bracket, for constant bunch density), the transverse wakefield has a periodic dependency along the bunch with zero value at $m \cdot \lambda_{pe}$ with $m = 0, 1, 2, ..$ and plasma wavelength λ_{pe} and peak value

$$W_{\perp,max}(r) = -2\frac{n_{b,0}\, q}{\epsilon_0\, {k_{pe}}^2}\, \frac{dR(r)}{dr}, \tag{1.6}$$

i.e. always focusing or zero for protons.
In the experiment, the bunch has a Gaussian longitudinal profile with length $\sigma_\xi \gg \lambda_{pe}$. In this thesis, the first few ($\# \leq 8$) modulation periods are characterized. As the plasma period $\tau_{pe} < 11.6\,\text{ps}$ (for $n_{pe} > 0.92 \cdot 10^{14}\,\text{cm}^{-3}$) and $\sigma_\xi > 250\,\text{ps}$ the change in bunch density over eighth periods is $\frac{n_b(\xi_{seed} - 8\,\tau_{pe}) - n_b(\xi_{seed})}{n_b(\xi_{seed})} \leq 0.4$ for $0 \leq \xi_{Seed} \leq 1.1\,\sigma_\xi$. We expect the effect of initial bunch density $n_b(\xi_{Seed})$ to dominate over the change along the first few periods (Section A.11). For given bunch and plasma parameters one can change the initial transverse wakefield amplitude by varying the location of the RIF.

The amplitude is then simply proportional to the local bunch density $n_b(\xi = \xi_{Seed})$. Experimental results with the seed point symmetrically with respect to the bunch center ($\pm\xi_{Seed}$) show only a small difference and thus a weak dependency on the bunch density slope near ξ_{Seed}, see Section A.11.
Alternatively, one can change the initial wakefield amplitude by changing the initial bunch density via the total bunch population. In practice, when changing the bunch population, additional parameters are changing, such as bunch length, width and emittance and waist position [20]. The influence of emittance on the transverse wakefield and SM evolution is studied in simulations in Section A.8 and in [21].

1.4.3 Micro-Bunch Train in Ramped Bunch Regime

The transverse wakefield, with alternating focusing and defocusing phase along the long proton bunch, radially modulates the bunch. The modulated bunch density increases the amplitudes of the transverse wakefield, self-reinforcing the SM process until the bunch is radially modulated into a train of micro-bunches.
Reference [18] studies the wakefield driven by a train of micro-bunches with micro-bunch

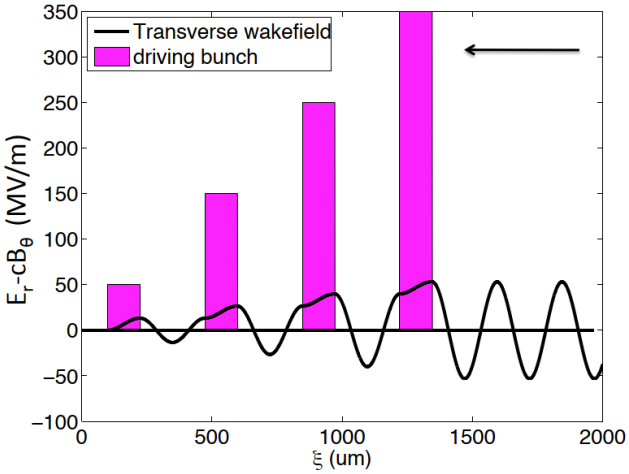

Figure 1.6: Transverse wakefield $W_\perp = E_r - c\,B_\theta$ (black line, from radial electric field E_r and azimuthal magnetic field B_θ), along the train of four square micro-bunches with increasing charge $Q_m = [1, 3, 5, 7]\cdot Q_{m,0}$ (violet bars), from [18].

length L_{bunch} and density $n_b = n_{b,0} \cdot \Theta\,(L_{bunch} - \xi) \cdot \exp\left(-\frac{r^2}{2\,\sigma_{r,0}^2}\right)$ with the Heaviside function $\Theta = 1$ when $0 \leq \xi \leq L_{bunch}$ and 0 otherwise, i.e. longitudinal squared and radial Gaussian bunch density profiles. The micro-bunch lengths are set as $k_{pe}\,L_{bunch} = \pi$ and the relative charge of the m th micro-bunch is increasing along the bunch as $(2\,m-1)\cdot Q_{m,0}$

with $Q_{m,0}$ the charge of the first one and they are placed with distance $1.5\,\lambda_{pe}$ to each other (violet bars in Figure 1.6).
Using Equation 1.3 one obtains the transverse wakefield amplitudes $W_\perp = E_r - c\,B_\theta$ (black line in Figure 1.6) along the train of micro-bunches. They determine the transverse wakefield amplitude of the m th micro-bunch center ξ_{CM} as

$$W_\perp(\xi, r) = -\frac{q\,n_{b,0}}{\epsilon_0\,k_{pe}}\left((m-1)^2 + \sin k_{pe}\,(\xi - \xi_{CM})\right)(1 - \cos k_{pe}\xi)\,\frac{dR(r)}{dr}, \tag{1.7}$$

i.e. increasing wakefield amplitudes along the micro-bunches m. They therefore show the increase of the transverse wakefield along the bunch ($W_\perp \propto (m-1)^2$) from the micro-bunches placed in the right phase, here with increasing charge (density).
The train of micro-bunches as considered here, is a simplified picture of the self-modulated proton bunch in the experiment discussed in this thesis. We thus expect the transverse wakefield to increase along the train of micro-bunches, as shown here, from linear wakefield theory. In this thesis, I demonstrate the increase of the transverse wakefield along the bunch by measuring the increasing width of defocused proton distributions along the bunch (Chapter 6).

1.4.4 Self-Modulation Instability Theory

In the following the growth of the transverse wakefield from the transverse seed wakefield during SM is calculated. The transverse wakefield of the bunch with initial bunch density n_b along propagation distance in plasma $z = c\,t$ can be written as

$$W_\perp(n_b, z) = W_{\perp,0}(n_b)\,e^{\Gamma(n_b,z)\,z} \tag{1.8}$$

with the transverse seed wakefield $W_{\perp,0}(n_b)$ and the growth rate $\Gamma(n_b, z)$. An expression for the growth rate for linear wakefields is derived in [22]

$$\Gamma(n_b, z) = \frac{3\sqrt{3}}{4}\,\omega_{pe}\left(\frac{n_b\,m_e}{2\,n_{pe}\,m_p\,\gamma_b}\,\frac{\xi}{z}\right)^{1/3}. \tag{1.9}$$

Equation 1.9 and Figure 1.7 show that the growth rate Γ decreases with plasma propagation distance z as $\propto z^{-1/3}$ (blue solid line), while the growth $\Gamma\,z$ increases as $\propto z^{2/3}$ (red dashed line). As mentioned earlier, the linear theory approximation holds for small radial modulation of the bunch. We will see later that over a few meters in plasma, for the experimental parameters discussed here, the bunch modulation depth increased significantly and linear theory becomes invalid. Several simulation results show that the

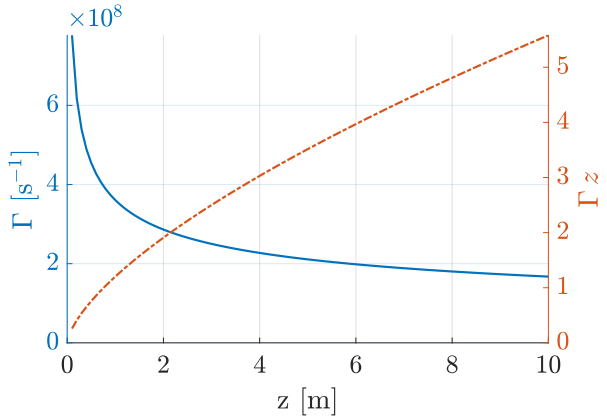

Figure 1.7: Growth rate Γ (blue line) and growth $\Gamma\, z$ (red dashed line) as a function of distance in plasma z at $\xi - \xi_{Seed} = \lambda_{pe}$. Here, $n_b = 5.6 \cdot 10^{12}\,\mathrm{cm}^{-3}$ and $n_{pe} = 0.92 \cdot 10^{14}\,\mathrm{cm}^{-3}$.

wakefield amplitude saturates (or even decreases) after full bunch modulation.

1.4.5 Phase Slippage of Wakefield

It was shown in theory and simulations [22, 23], that during the growth of the self-modulation process the wakefield's phase velocity is slower than that of the relativistic drive bunch. After full modulation is reached, the phase velocity is expected to be essentially equal to the drivers velocity.
I study the effect of the phase slippage onto the bunch modulation, with special focus on the first period. In [24], we showed experimentally that with a plasma density gradient the phase slippage can be partly compensated for. In this thesis, I study the effect of a density gradient on the focused and defocused protons.
Further, theory predicts (for a constant bunch density n_b) that the phase velocity depends (weakly) on the growth rate as [22]

$$\nu_{ph} = \nu_b \left[1 - \frac{1}{2} \left(\frac{\xi}{c\,t} \right)^{1/3} \left(\frac{n_b\, m_e}{2\, n_{pe}\, m_p \gamma_b} \right)^{1/3} \right], \tag{1.10}$$

and thus changes along the bunch and depends on the initial bunch density n_b. A change in the wakefield's phase implies a change in its frequency. Thus, I study the modulation frequency and length of modulation periods for different initial bunch and plasma densities.

1.4.6 Transverse Seed Wakefield and Wakefield Growth for Various Experimental Parameters

I define the transverse seed wakefield amplitude from Equation 1.6 as

$$\begin{aligned} W_{\perp,0} &= W_{\perp}(\xi = \xi_{Seed} + \frac{\lambda_{pe}}{2}, r = \sigma_r) \\ &\approx -2\,\frac{q\,n_{b,0}\,g(\xi = \xi_{Seed})}{\epsilon_0\,{k_{pe}}^2}\,\frac{dR(r=\sigma_r)}{dr}, \end{aligned} \tag{1.11}$$

assuming $g(\xi_{Seed}) \approx g(\xi_{Seed} + \frac{\lambda_{pe}}{2})$. The dependency of the transverse seed wakefield amplitude and growth rate on initial bunch density, plasma density and plasma density gradient is studied in the following.

Effect of Initial Bunch Density on Seed Wakefield and Growth Rate

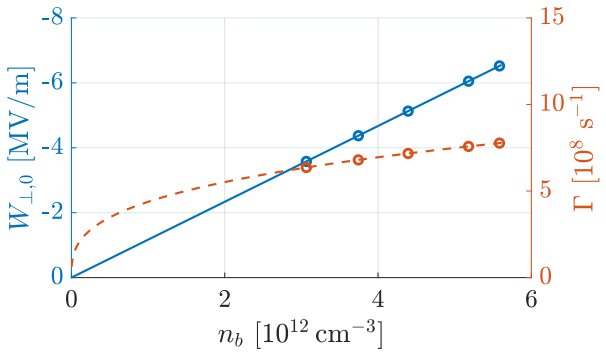

Figure 1.8: Transverse seed wakefield amplitude $W_{\perp,0}$ at $r = \sigma_r$ (Equation 1.11, blue solid line) and growth rate Γ at $z = 0$ and $\xi - \xi_{Seed} = \lambda_{pe}$ (Equation 1.9, red dashed line) as a function of initial bunch density at the seed position. Values for the initial bunch densities used in the experiment later are marked with circles. Here, $n_{pe} = 0.92 \cdot 10^{14}\,\mathrm{cm}^{-3}$.

Equation 1.11 shows that the transverse seed wakefield amplitude $W_{\perp,0}$ is directly proportional to the initial bunch density n_b, i.e.

$$W_{\perp,0} \propto n_b. \tag{1.12}$$

The linear increase of the transverse seed wakefield amplitude with increasing initial bunch density is plotted in Figure 1.8 (blue solid line). Thus, increasing the initial bunch density in the experiment (Section 4.5.1) from $3.1 \cdot 10^{12}\,\mathrm{cm}^{-3}$ to $5.6 \cdot 10^{12}\,\mathrm{cm}^{-3}$ increases also the transverse seed wakefield amplitude from $-3.6\,\mathrm{MV/m}$ to $-6.5\,\mathrm{MV/m}$, i.e. both by a factor

of ~ 1.8.

The corresponding growth rate increases with the initial bunch density as

$$\Gamma \propto n_b^{1/3}, \tag{1.13}$$

and increases along the bunch, see Equation 1.9. The growth rate for the various initial bunch densities, evaluated one plasma period behind the seed position, is plotted in Figure 1.8 (red dashed line).

In Figure 1.8 transverse seed wakefield amplitudes and growth rates are plotted over the range of $0 - 5.6 \cdot 10^{12}\,\mathrm{cm}^{-3}$, covering the initial bunch densities used in the experiment of this thesis (circles), see Section 4.5.1.

Section 2.5.1 shows experimental results that demonstrate the growth of the transverse wakefield along the plasma, as evidenced by the change in radius of the defocused proton distribution [14]. These measurements show larger transverse wakefield amplitudes for higher initial bunch density from higher total bunch population. In this thesis, I study the growth of the transverse wakefield along the bunch. I measure the increasing radius of defocused proton distributions from time-resolved images over the first periods behind the seed position and their dependency on the initial bunch density by varying the seed position along the bunch (Section 6.1). Further, I study the evolution of the transverse wakefield along the plasma from simulations.

Effect of Plasma Density on Seed Wakefield and Growth Rate

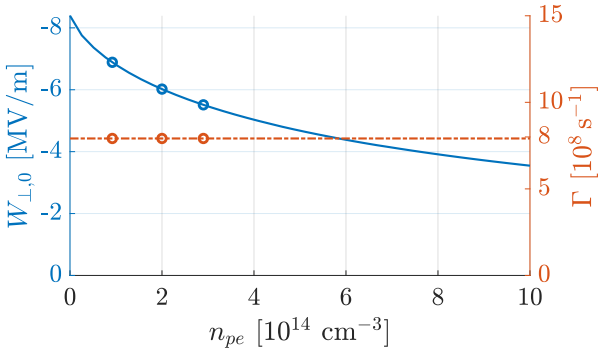

Figure 1.9: Transverse seed wakefield amplitudes $W_{\perp,0}$ at $r = \sigma_r$ (Equation 1.11, blue solid line) and growth rate Γ at $z = 0$ and $\xi - \xi_{Seed} = \lambda_{pe}$ (Equation 1.9, red dashed line) as a function of plasma density. Values for the plasma densities used in the experiment later are marked with circles. Here, $n_b = 5.6 \cdot 10^{12}\,\mathrm{cm}^{-3}$.

The transverse seed wakefield amplitude depends on the plasma density as (Equation 1.6)

$$W_{\perp,0} \propto \frac{1}{k_{pe}^2} \cdot \frac{dR(r, n_{pe})}{dr}. \tag{1.14}$$

Figure 1.9 shows that the transverse seed wakefield amplitude (blue solid line) decreases from $-6.9\,\mathrm{MV/m}$ to $-5.5\,\mathrm{MV/m}$ with increasing plasma density from $0.9 \cdot 10^{14}\mathrm{cm}^{-3}$ to $2.9 \cdot 10^{14}\mathrm{cm}^{-3}$. Thus increasing the plasma density by a factor of ~ 3 leads to a decrease of $\sim 20\,\%$ in the transverse seed wakefield amplitude. This is a weak dependency. Nevertheless wider defocused proton distributions as a result of the higher transverse seed wakefield for the lower plasma density can be measured (Section 6.2).
The growth rate depends on the plasma density as (Equation 1.9)

$$\Gamma \propto n_{pe}^{1/6} \cdot \xi^{1/3}. \tag{1.15}$$

Thus, it increases with increasing plasma density for a fixed ξ. However if we evaluate Γ at a ξ proportional to the given plasma wavelength, as in Figure 1.9 one plasma wavelength behind the seed point, the value is constant (red dashed line).
In Figure 1.9, transverse seed wakefield amplitude and growth rate are plotted over a range of $0 - 10 \cdot 10^{14}\,\mathrm{cm}^{-3}$. The values for $n_{pe} = [0.92, 2.0, 2.9] \cdot 10^{14}\,\mathrm{cm}^{-3}$ (circles), used in the experiment, are highlighted.

Effect of Plasma Density Gradient on Growth Rate

The phase slippage of the wakefield with respect to the relativistic drive bunch during the SM evolution is introduced in Section 1.4.5.
Simulation results show that with a constant plasma density, the wakefield starts from its seed value, grows with bunch propagation and modulation until it reaches saturation and then decreases [11, 22, 25]. In order to achieve very high energies, witness particles generally need to be accelerated over very long distances. Thus, a decrease in the wakefield amplitude after saturation is highly detrimental. Simulation studies suggest that a plasma density step could prevent the wakefield decrease [26].
The wakefield decrease can be explained with the off-resonance evolution due to phase slippage of the wakefield with respect to the drive bunch. With a positive plasma density gradient during the self-modulation phase, the effective wakefield's phase could be manipulated, counteracting the phase slippage between the wakefield and the drive bunch [24, 27, 28]. Plasma gradients were proposed for the same purpose for laser wakefield accelerators [29].

Together with the change in phase slippage, it is expected that the growth of the wakefield is affected by the plasma gradient over the 10 m of plasma. In this thesis, I measure the effect of plasma density gradients on transverse profiles of defocused proton distributions, showing stronger defocusing for negative density gradient, both in experiment and simulation. Simulation results reveal that transverse profiles of defocused proton distributions for varying plasma density gradients are mainly determined by the change in phase slippage between the wakefield and the proton bunch.

2 The AWAKE Experiment

In the following chapter, I introduce the AWAKE experiment, its experimental setup and its implementation in the CERN accelerator complex. I present a laser-beam alignment GUI, developed for the alignment of the ionizing laser beam trajectory onto that of the proton beam and for monitoring the alignment online during the experiment. Further, the plasma radius is studied using Schlieren imaging. I show the first experimental results of the self-modulation of a proton bunch in plasma and acceleration of electrons in its wakefield. Finally, an outline for future measurements at AWAKE is given.

2.1 AWAKE at CERN

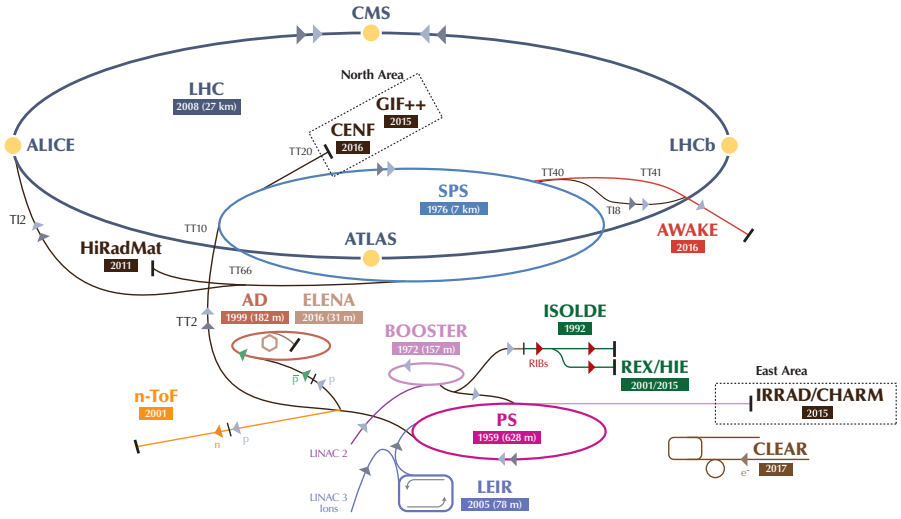

Figure 2.1: Overview of the CERN accelerator complex and the largest experiments [30]. The AWAKE experiment (red line) uses proton bunches, extracted from the SPS ring (bright blue line) with energies of 400 GeV.

The Advanced Wakefield Experiment (AWAKE) is a proof-of principle R&D experiment, located at CERN. AWAKE demonstrated for the first time the self-modulation of a proton bunch in plasma and the acceleration of charged particles (electrons) in the wakefield driven by the modulated bunch, as suggested in [31].

Figure 2.1 shows a schematic of the CERN accelerator complex. Initially, an electric field strips off electrons of hydrogen atoms as a proton source. The protons are first accelerated in a linear accelerator ("LINAC") to 50 MeV, before they are transferred into a chain of circular accelerators. They reach an energy of 1.4 GeV in the Proton Synchrotron Booster ("BOOSTER"), followed by the Proton Synchrotron ("PS", 25 GeV), before they are injected into the Super Proton Synchrotron ("SPS", bright blue circle in Figure 2.1), where they reach energies up to 450 GeV. Protons are extracted from the SPS to the AWAKE experiment (red line) with an energy of 400 GeV. Alternatively, if protons are not extracted from the SPS to one of the experiments, they are injected into one of the two rings of the Large Hadron Collider ("LHC"). Beams of the two rings counter-propagate, enabling beam-beam collision experiments. With its circumference of 27 km, particles can reach energies up to 6.5 TeV. Thus, during a collision, total energies of up to 13 TeV can be reached. Future proposals include using proton bunches of the LHC as a driver of the wakefield in AWAKE and/or possibly a collision experiment of LHC proton bunches with electrons, accelerated in AWAKE.
The overview of the underground AWAKE facility is shown in Figure 2.2. The proton

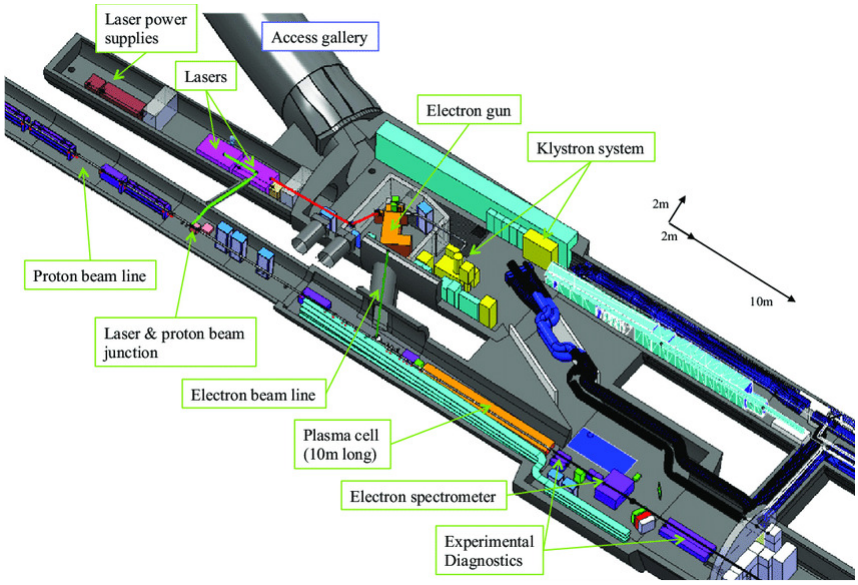

Figure 2.2: Overview of the AWAKE facility [32].

beam line delivers proton bunches, extracted from the SPS, to the experimental area. The area contains a cleanroom for the laser and a radiation shielding room with the electron gun inside. Laser, proton and electron beams are delivered to the main experimental area where the 10 m long vapor source is located. Several proton and electron beam diagnostics are installed after the vapor source, where sensitive equipment, like streak

cameras, are additionally shielded by a wall from radiation in the experimental area, mostly from protons during the experiment.

2.2 Experimental Setup of AWAKE

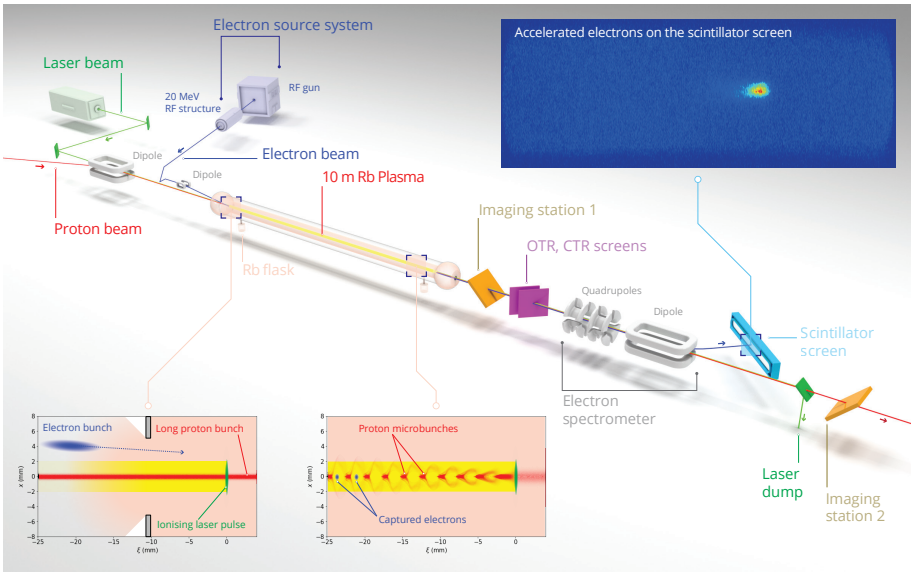

Figure 2.3: Schematic layout of the AWAKE experiment (not to scale): The Rb vapor is ionized by a laser pulse (green line), the proton bunch (red line) self-modulates in the plasma (right inset) and the train of micro-bunches resonantly drive the wakefield. The SM is seeded with the co-moving RIF (left inset). An externally injected electron bunch (blue line) is accelerated in the wakefield. Diagnostics for the self-modulated proton bunch (OTR, CTR screens, imaging stations 1, 2) and for the electron bunch (electron spectrometer) are located after the plasma.

The experimental setup of AWAKE is shown in Figure 2.3. The core of the experiment is the Rb vapor source [33], a 10 m long tube with Rb reservoirs on both ends, as shown in the picture in Figure 2.4. The temperature of the tube is controlled with a fluid heat exchanger to $180\,° - 230\,°$. This enables Rb vapor densities of $(0.5 - 10) \cdot 10^{14}\,\mathrm{cm}^{-3}$ with a very uniform density along the tube. The temperatures of reservoirs on both ends of the vapor source can be controlled individually, enabling the option of a linear vapor density gradient.

The Rb vapor is singly ionized by the 4 TW Ti:sapphire laser pulse (duration 120 fs, maximum energy 450 mJ, spectral bandwidth $\sim$ 20 nm, central wavelength 780 nm) [34], creating a plasma cylinder along the vapor source. The plasma radius is assumed

Figure 2.4: Picture of the 10 m long vapor source in the AWAKE facility [Photo: Maximilien Brice, CERN].

to be larger than 1 mm along the entire 10 m of the source (see Section 2.4). The Rb vapor density is measured at the vapor source entrance and exit with white light interferometry [35].

The CERN SPS provides the drive bunch for the plasma wakefield experiment, a 400 GeV proton bunch with $N_{p^+} = (1-3) \cdot 10^{11}$ particles, a length of $\sigma_\xi = 6 - 12$ cm focused to $\sigma_r = 200\,\mu$m at the entrance of the vapor source. The bunch self-modulates over the plasma and resonantly drives the wakefield. The main diagnostics for the self-modulated proton bunch are fluorescent screens (Imaging Stations 1, 2) for time-integrated transverse profiles, a streak camera acquiring the optical transition radiation (OTR) for time-resolved transverse profiles and heterodyne detectors acquiring the coherent transition radiation (CTR) for determination of the modulation frequency, see Figure 2.3.

An electron bunch is externally injected with an initial energy of 18 MeV into the plasma at the entrance of the vapor source. The electron bunch is created on a photo cathode with the third harmonic of a small fraction of the ionizing laser pulse extracted before amplification. Using the same laser pulse for ionization and seeding as well as for the electron bunch allows precise controlling of the relative timing between the wakefield and the electron bunch. Electrons are accelerated in the wakefield over the 10 m of plasma. After the plasma they are focused and bent onto a scintillator screen by quadrupole and dipole magnets. The light emitted by the scintillating screen is imaged onto a CCD

camera (see Figure 2.3).

2.3 Laser-Proton Bunch Alignment with Laser Alignment GUI

Ideally, the plasma would have an infinite transverse extent. In the experiment however, the plasma radius is $\sim 1 - 2\,\text{mm}$ (Section 2.4), not much larger than the incoming proton bunch rms radius $\sigma_{r,0} = 200\,\mu\text{m}$ or the transverse extent of the wakefield (Figure A.24). In addition, the plasma is 10 m long, i.e. angular variations of the plasma of $\frac{1-2\,\text{mm}}{10\,\text{m}} = 0.1 - 0.2\,\text{mrad}$ are important. If the bunch or the wakefield reach the edge of the plasma with lower or zero density, then the transverse wakefield becomes asymmetric (weaker towards the boundary). This can cause asymmetries (hosing, etc.) to develop, instead of the symmetric SM mode.

The plasma is created by ionization of the Rb vapor with the ionizing laser pulse (Section 2.2). In order to align the laser pulse onto the proton bunch trajectory, I developed a laser alignment GUI in MATLAB. The small exit angular jitter of the laser pulse of $\sim 6\,\mu\text{rad}$ (rms) translates with a distance of $\sim 33\,\text{m}$ from the compressor to the vapor cell entrance into $\sim 0.2\,\text{mm}$ (rms) shot to shot misalignment. The light transport and vibration in mirrors can increase this value. The goal is to achieve on average a spatial overlap between the laser pulse and the proton bunch trajectory. Furthermore, the laser pulse trajectory is monitored with the GUI to manually correct for (e.g. thermal) drifts over time and publishes alignment information into the data acquisition system to correlate observed features of the bunch (SM or hosing instability results) with the alignment of a given event.

Determination of Proton Bunch and Laser Pulse Trajectory

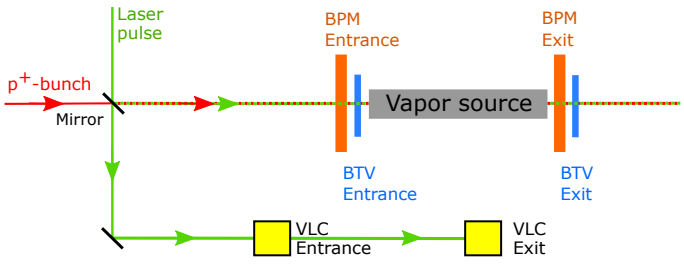

Figure 2.5: Experimental setup with devices used for the alignment of the laser pulse (green line) onto the proton bunch trajectory (red line).

Figure 2.5 shows the devices of the experimental setup used for the laser beam alignment. The laser pulse (green line) is transported in vacuum from the compressor to the vapor source (distance to entrance $\sim 33\,\text{m}$). The light transmission ($\sim 1\,\%$) of a mirror before

the vapor source is sent in air to the virtual line cameras (VLCs). The cameras have an equal propagation distance as from the compressor to the vapor source entrance ("VLC Entrance") and exit ("VLC Exit"). The proton bunch trajectory (red line) is determined with beam position monitors (BPMs) and fluorescent screens (BTVs) surrounding the vapor source.

Before the experiment, first, the proton bunch trajectory is acquired with the BPMs

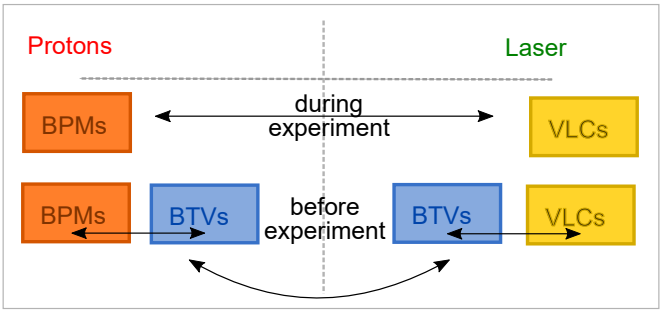

Figure 2.6: Diagnostics for proton bunch trajectory (BPMs and BTVs) and laser pulse trajectory (BTVs and VLCs); Correlation between the trajectories with BTVs.

and BTVs close to the plasma entrance and exit (Figure 2.5). Then, the laser pulse trajectory is acquired with the same BTVs and the VLCs. The common diagnostic, the BTVs, provides the correlation between the trajectories of proton bunch and laser pulse. During the SM experiment, the entrance BTV is removed (for the ionizing laser pulse passage) and the proton bunch trajectory is monitored with the BPMs and the laser pulse trajectory with the VLCs. The diagnostics used before and during the experiment are summarized in Figure 2.6.

The individual functions and the operation of the laser alignment GUI is explained in detail in Section A.1.

Laser Alignment Results

The results of the laser pulse and proton bunch alignment of an experimental run using more than 6000 events are shown as event density plots in Figure 2.7. Here, each point corresponds to the center of gravity (COG) value of the signal on the image. Images (a, c) show the laser pulse alignment from VLCs, images (b, d) the proton bunch alignment from BPMs, both before (a, b) and after (c, d) the plasma. The origin $x = y = 0$ of each figure corresponds to the proton bunch reference trajectory, acquired on a daily basis before the experiment (Section A.1). One can see that both laser pulse and proton bunch are on average well aligned onto the reference trajectory. The larger spread of the laser pulse positions shows the larger spatial pointing variation of the laser pulse than that of the proton bunch. The larger spread in the vertical plane at the plasma entrance originates from a larger uncertainty when determining the COG of the laser

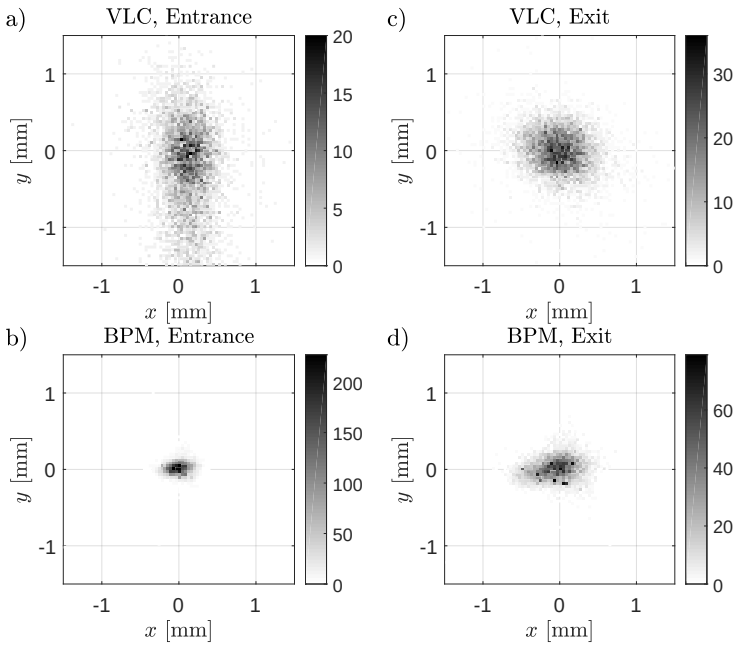

Figure 2.7: Laser alignment results of more than 6000 events. Position of the laser pulse on the VLCs (a, c), position of the proton bunch from BPMs (b, d), before (a, b) and after (c, d) the plasma; counts give number of events. The origin $x = y = 0$ of the figures corresponds to the proton bunch reference trajectory.

pulse assuming radial symmetry (see Figure A.1).

This alignment GUI became an integral part of the experiment and has been used for all measurements of AWAKE and this thesis.

2.4 Schlieren Imaging for Plasma Radius Determination

To ensure a symmetric evolution of the proton bunch SM, the modulated bunch needs to propagate entirely through plasma over the 10 m. Therefore, not only the laser pulse alignment, but also the plasma radius are crucial. We use Schlieren imaging to measure the plasma radius. Schlieren imaging measures the disappearance of Rb vapor with a higher index of refraction than that of plasma. We show experimentally that the plasma radius at the plasma exit is expected to be larger than 1 mm. A larger radius also allows for larger spatial pointing variations of the laser pulse and proton bunch.

Experimental Setup

The detailed experimental setup for the plasma radius measurement using Schlieren imaging can be found in Section A.2. We use a tunable imaging laser with a wavelength close to the Rb D2 transition line at 780 nm. The refractive index of vapor is given by [36]

$$\eta_{vapor} = \sqrt{1 + \frac{N_i\, e^2}{\epsilon_0\, m_e} \sum_{j \neq i} \frac{f_{ij}}{\omega_{ij}^2 - \omega_L^2 + i\gamma_{ij}\omega_L}}, \tag{2.1}$$

with imaging laser frequency ω_L, transition frequency ω_{ij} from lower state i to upper state j, N_i the density of atoms in the lower state i, f_{ij} the oscillator strength of the transition and $\gamma_{ij} = 1/\tau_{ij}$ with τ_{ij} the lifetime of the upper state j. The refractive index of plasma is given by

$$\eta_{plasma} = \sqrt{1 - \omega_{pe}^2/\omega_L^2}. \tag{2.2}$$

Thus, with $N_i = n_{Rb} = 10^{15}\,\mathrm{cm}^{-3}$, tuning the imaging laser to a frequency very close to the transition frequency of the vapor ($\Delta f = \frac{1}{2\,\pi}\,\Delta\omega = 2\,\mathrm{GHz}$, with $\Delta\omega = \omega_{ij} - \omega_L$), the refractive index of the vapor in the ground state ($\eta_{vapor} \approx 1.003$) significantly differs from that of plasma/vacuum ($\eta_{plasma} \approx 1 - 10^{-7} \approx 1$).

The imaging laser beam propagates transversely through the plasma column. The column is imaged with two lenses onto a gated camera. We use a razor blade in the focus of the first lens, to block most of the unbent light (background) and the light that is bent downwards by the plasma. As a result, we obtain images of the transverse profile of the plasma column, where half of the column appears as higher, the other half as lower intensity on the images. An example Schlieren image can be found in the appendix (Figure A.4).

In the following, we define the diameter D of the plasma column as the sum of the full width half maxima (FWHM) of the bright and the dark peak. While this is a consistent way of determining the radial extent during the scans, it remains to determine the ratio of the diameter of this definition with the diameter defined by the edges of the column. The relation is studied numerically in [37] and determined to be essentially linear when diffraction effects on the plasma column edges are small.

Experimental Results

In Figure 2.8, the plasma diameter is measured for various ionizing laser pulse energies with plasma density $n_{pe} = 5 \cdot 10^{14}\,\mathrm{cm}^{-3}$. The signal is acquired 100 ns after the laser pulse passage and with a gate width of 10 ns. We measure at two imaging laser frequencies, one slightly higher (red symbols) and one slightly lower (blue symbols) than the D2 transition frequency. When changing the detuning frequency, we change the index of refraction of the vapor at the imaging laser frequency (Equation 2.1) and thus the strength of

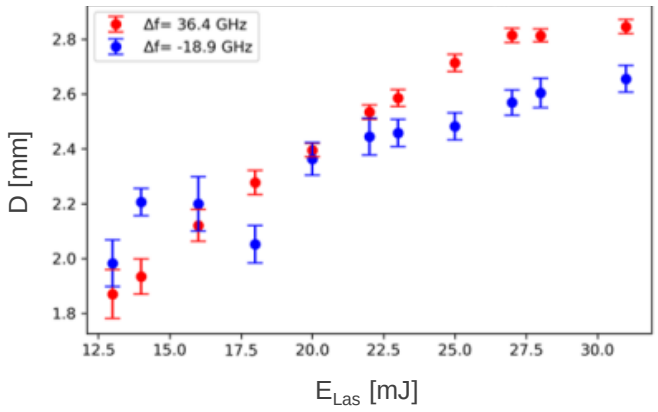

Figure 2.8: Plasma column diameter D versus ionizing laser energy E_{Las} (error bars give the std divided by the square root of number of measurements) with the imaging laser frequency below ($\Delta f = -18.9\,\mathrm{GHz}$, blue symbols) and above ($\Delta f = 36.4\,\mathrm{GHz}$, red symbols) the Rb D2 transition line, from [37].

ray bending and the amount of light being blocked by the razor blade. This changes the Schlieren signal intensity in the images (see Figure A.4). However, the widths of the Schlieren signal, thus the measured plasma diameter, is expected to be independent of the imaging laser frequency. Therefore, measurements with different imaging laser frequencies are used to validate results and their difference gives information about the measurement error.

On Figure 2.8, each data point corresponds to the average of 100 images, the standard deviation divided by the root of number of measurements is given by the error bars. The measurements with both detuning frequencies show a clear increase in plasma diameter with increasing ionizing laser pulse energy from 13 mJ to 31 mJ. The diameter increases from $\sim (1.9 \pm 0.1)\,\mathrm{mm}$ to $\sim (2.8 \pm 0.1)\,\mathrm{mm}$ for the positive and from $\sim (2.0 \pm 0.1)\,\mathrm{mm}$ to $\sim (2.7 \pm 0.1)\,\mathrm{mm}$ for the negative detuning frequency. Thus, an increase of the ionizing laser pulse energy of a factor of ~ 2.4 leads to an increase in the plasma diameter of a factor of ~ 1.4 with both detuning frequencies. Therefore, according to the measurement, the plasma diameter at the plasma exit is not directly proportional to the ionizing laser pulse energy. During SM studies, the ionizing laser pulse energy is typically $\sim 100\,\mathrm{mJ}$. The plasma diameter could not be measured with the high pulse energy, as the diameter is too large to be covered by the imaging laser beam, whose spot size is limited by the view ports of the vapor source. However, from this measurement, we expect the plasma diameter to be larger than 2.5 mm at $n_{pe} = 5 \cdot 10^{14}\mathrm{cm}^{-3}$ during SM experiments, 100 ns after the laser pulse.

In general, the plasma diameter increases with time due to expansion. In Figure 2.9, the

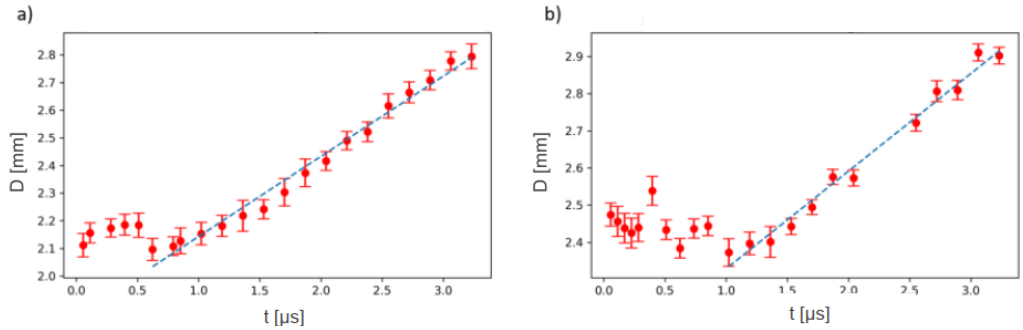

Figure 2.9: Time evolution of the plasma diameter D (error bars give the std divided by the square root of number of measurements) with imaging laser detuning frequencies of a) $\Delta f = -16\,\mathrm{GHz}$ and b) $\Delta f = 8\,\mathrm{GHz}$), from [37].

temporal diameter evolution is measured varying the trigger timing of the gated camera for image acquisition with amplification of the signal over 10 ns. Here, the ionizing laser pulse energy is fixed to $E_{Las} = 6\,\mathrm{mJ}$ and the plasma density is $n_{pe} = 2 \cdot 10^{14}\,\mathrm{cm}^{-3}$. The plasma diameter evolution is shown for two imaging laser frequencies, in Figure 2.9 a) with negative, in Figure 2.9 b) with positive detuning from the Rb D2 transition line. As explained above, the diameter measured should be independent of the imaging laser frequency. Measurements with both imaging laser detuning frequencies lead to similar results with a maximum difference of $\sim 0.3\,\mathrm{mm}$ at early times ($t < 1\,\mu\mathrm{s}$) after plasma creation and decreasing difference for later times. We measure a plasma diameter essentially constant for times $< 1\,\mu\mathrm{s}$. For times $> 1\,\mu\mathrm{s}$ we observe the plasma diameter monotonously increasing from $\sim (2.1 \pm 0.1)\,\mathrm{mm}$ to $(2.8 \pm 0.1)\,\mathrm{mm}$ for the negative and from $\sim (2.4 \pm 0.1)\,\mathrm{mm}$ to $(2.9 \pm 0.1)\,\mathrm{mm}$ for the positive detuning frequency.
Note that if the radius increases, the plasma density must decrease. The change in plasma density changes the refractive index according to Equation 2.1, which is expected to change the intensity of the Schlieren signal, but not the widths and should thus not affect the plasma diameter measurement shown in Figure 2.9.

Conclusion

We used Schlieren imaging with a laser beam that can be tuned to near a resonant transition of Rb from its ground state, to measure the plasma column diameter at the end of the vapor source. This unique tuning feature is possible only with alkali metal vapors, having optical transitions from their ground state in the (near) visible range, allowing this experiment. The Schlieren imaging measurements show a diameter of a few mm, in principle sufficient for SM experiments. The determination of the size evolution

over time is also consistent with plasma density measurements in [38] showing very small changes over the first $\sim 1\,\mu s$, due to recombination and/or plasma radial expansion.

2.5 Experimental Results of AWAKE

AWAKE performed plasma wakefield experiments between 2016 and 2018. First the self-modulation of the long proton bunch was studied, then acceleration of injected electrons was demonstrated.

2.5.1 Seeded Self-Modulation of the Proton Bunch

We measure the time-integrated transverse profile of the self-modulated proton bunch at fluorescent screens, the time-resolved transverse profile from the OTR and the modulation frequency from CTR.

Imaging Stations for Time-Integrated Transverse Bunch Profile

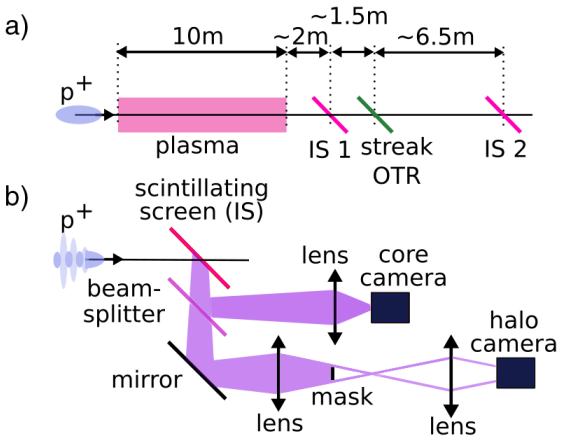

Figure 2.10: Schematic setup of the fluorescent screens for acquisition of the time-integrated transverse proton bunch distribution; a) shows the location of the screens after the plasma, b) the division of the light onto a core camera and a halo camera, where the light of the core is blocked by a mask; from [14].

The self-modulated proton bunch is measured with several diagnostics, located after the plasma exit. It propagates through two fluorescent screens (imaging stations 1 and 2 in Figure 2.3), where the time integrated transverse size of the bunch is measured [14]. The screens are located $\sim 2\,m$ and $\sim 10\,m$ after the plasma, see Figure 2.10 a). Figure 2.10 b) shows that the light is divided onto two cameras, a "core camera" where the entire transverse profile is recorded, and a "halo camera", where the intense light of the core is blocked by a mask to study the wings of the profile, here referred to as halo. By combining the images of the two cameras, a larger dynamic range is achieved. As the self-modulation is a transverse process, defocused protons from between the

micro-bunches appear at larger radii on the screens. The radial distributions of defocused protons reveal information about the growth of the transverse wakefield [14].
Figure 2.11 shows time-integrated images of the bunch from the core camera (a, b) and

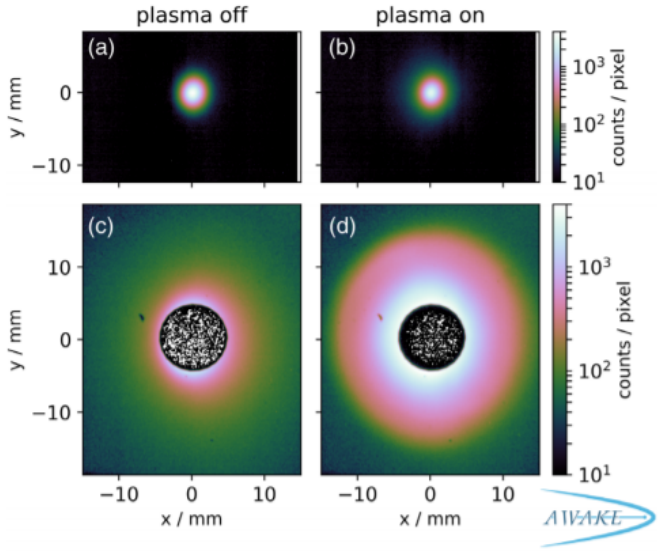

Figure 2.11: Time-integrated transverse proton bunch distribution at imaging station 2, acquired with the core camera (a, b) and with the halo camera (c, d), without plasma (a, c) and with plasma (b, d), from [14].

halo camera (c, d) measured at imaging station 2. Images (a, c) show the bunch after propagating through vacuum, images (b, d) after propagating through 10 m of plasma [14]. One can see clearly the wider transverse proton distribution after propagation through plasma (b, d), i.e. when protons experienced defocusing by the transverse wakefield. These images are similar to the ones acquired at imaging station 1. The effect is larger at imaging station 2, as it is further downstream and protons have diverged more.
We determine the maximum radius of defocused proton distributions from the time-integrated images (Figure 2.11). The average amplitude of the defocusing wakefield protons experienced to reach these radii is calculated. This requires the maximum radius at the imaging station, the distance of interacting with the wakefield and their position where they exit the wakefield. Figure 2.12 shows the minimum average wakefield amplitude $W_{\perp,av,min}$ if protons were interacting over the entire plasma length ($L = 10\,\mathrm{m}$) and exit the wakefield at the plasma exit (black circles). It also shows the average wakefield amplitude using the assumption that protons interact with the wakefield over $L = 1.5\,\mathrm{m}$ and exit the wakefield after 4 m of plasma, as predicted by simulations (blue diamonds). When increasing the proton bunch population, thus initial bunch density, the seed wakefield amplitude increases (Section 1.4.6). The maximum radius of time-integrated transverse profiles for various bunch populations is analyzed. This shows that both the expected average wakefield (blue diamonds) and also the minimum averaged wakefield (black circles) are significantly above the seed wakefield value (red

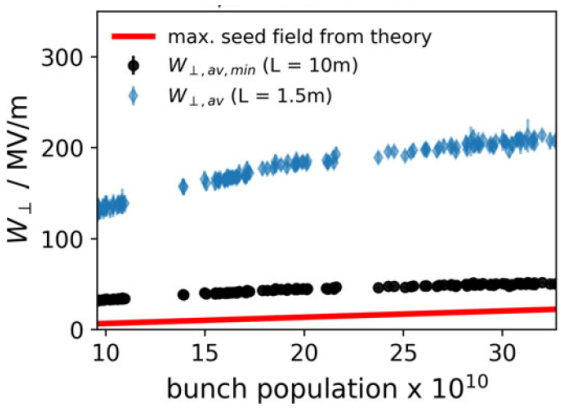

Figure 2.12: Transverse wakefield amplitude as a function of proton bunch population with $n_{pe} = 2.1 \cdot 10^{14}\,\mathrm{cm}^{-3}$. Seed wakefield amplitude (red line), average of the transverse wakefield assuming protons exit the wakefield after $L = 10\,\mathrm{m}$ of plasma ($W_{\perp,av,min}$, black circles) or assuming protons exit the wakefield at 4 m after $L = 1.5\,\mathrm{m}$ distance of interaction with the wakefield ($W_{\perp,av}$, blue diamonds), from [14].

curve). Therefore the growth of the wakefield along the plasma from time-integrated proton bunch distributions is measured.

Measurements of OTR and CTR

To characterize the proton bunch modulation, the bunch propagates through two metal screens (OTR, CTR screens in Figure 2.3) to measure the optical transition radiation (OTR) and coherent transition radiation (CTR) that is hereby emitted.
The prompt OTR light emission retains the time structure of the proton distribution

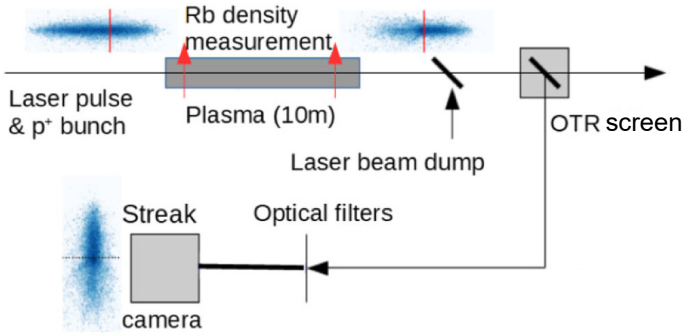

Figure 2.13: Schematic setup of acquisition of time-resolved transverse proton bunch distribution, imaging the OTR screen onto a streak camera, from [13].

and is acquired with a streak camera (Figure 2.13 and Section 3.1). The OTR screen is imaged onto the slit of the streak camera. This leads to a time-resolved image of the transversely modulated proton bunch distribution, as seen in Figure 2.14 a) from [13]. The bunch is moving from bottom to top and the plasma starts at time $\sim -15\,\mathrm{ps}$

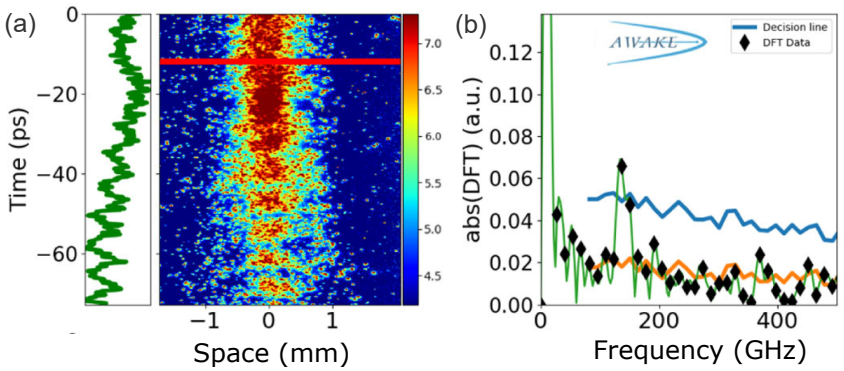

Figure 2.14: a) Streak camera image of the self-modulated proton bunch, propagating from bottom to top, ionizing laser position (red line) and projection of the central density modulation (green curve); b) DFT of the projection and its peaks (black diamonds); dominating frequency that exceeds the noise threshold (blue line) at 137 GHz (here $n_{pe} \approx 2.5 \cdot 10^{14}\,\mathrm{cm}^{-3}$, i.e. $f_{pe} = 142\,\mathrm{GHz}$), from [13].

(timing of the RIF, red horizontal line). Earlier ($> -15\,\mathrm{ps}$, above red line) protons were propagating through vapor, thus the bunch is not modulated, later ($< -15\,\mathrm{ps}$, below red line) protons experienced 10 m of plasma, thus the bunch is modulated. The modulation frequency f_{Mod} can be determined from the discrete Fourier transformation (DFT) of the projection of the central bunch density modulation (green line in Figure 2.14 a) and is plotted in Figure 2.14 b). The DFT's peaks (black diamonds) are determined. Only one peak exceeds the noise threshold ($< 1\%$ probability of a noise peak above this threshold, blue line), the peak at $f_{Mod} = 137\,\mathrm{GHz}$. This shows that the modulation frequency is essentially equal to the plasma frequency (here $f_{pe} = 142\,\mathrm{GHz}$) [13]. This measurement was repeated for various plasma densities (red line in Figure 2.16).
The radiation emitted from the CTR screen is sent to a heterodyne system, where the

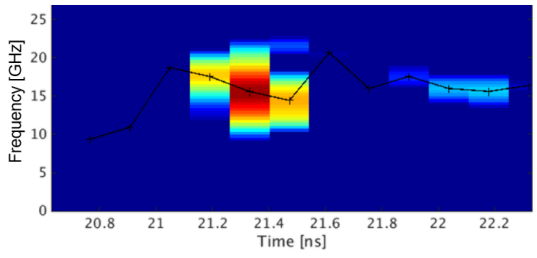

Figure 2.15: Oscilloscope measurement of intermediate beat frequency between CTR signal of the modulated proton bunch and reference signal as a function of time, signal intensity from blue to red, from [39].

signal with the high frequency ($f_{Mod} \sim 100 - 300\,\mathrm{GHz}$) is mixed with a reference signal with similar, slightly detuned frequency, generated by the frequency-multiplication of a tunable local oscillator [40]. The intermediate beat frequency (i.e. frequency difference

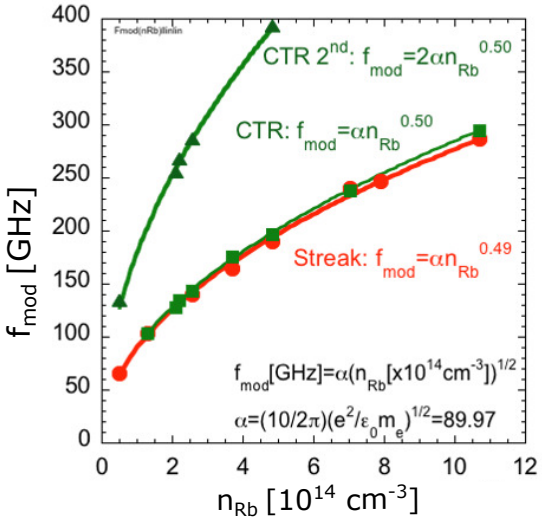

Figure 2.16: Modulation frequency f_{mod} as a function of plasma density n_{Rb}, from the DFT of streak camera images of the OTR (red line) and from the heterodyne systems detecting the CTR (first and second harmonics, green lines), both scaling as the plasma frequency $f_{pe} \propto {n_{pe}}^{-1/2}$, from [39].

between the CTR and the reference signal) of $\sim 5 - 20\,\mathrm{GHz}$ can then be resolved with an oscilloscope. Figure 2.15 shows the time evolution of the measured intermediate beat frequency for a single event of the modulated bunch (signal intensity from blue to red). The modulation frequency is obtained from the reference signal frequency and it is compared to the modulation frequency as determined from the OTR.
Figure 2.16 shows the modulation frequencies from the CTR signal (first and second harmonics, green lines) and from the OTR signal (red line), both for measurements with different vapor densities (and thus plasma density assuming $\sim 100\%$ ionization rate [13]). This shows very good agreement of the two independent measurements and that the modulation frequency can indeed be controlled through the vapor density.

We speak of seeded self-modulation (SSM) when the phase of the modulation is reproducible, i.e. that the modulation starts and that micro-bunches appear at the same position along the bunch from event to event. AWAKE seeds the self-modulation with the co-propagating ionizing laser pulse within the proton bunch. Varying the timing of the laser pulse shows the control of the self-modulation process [16]. With the laser pulse far ahead of the proton bunch center, modulation starts from noise and the phase is not reproducible. With the laser pulse closer to the center, the high bunch density at the RIF seeds the SM process. All events used for this thesis (Chapter 7 excluded) are acquired in this SSM regime. In fact, all data is the result of the combination or "stitching" together of single events with phase reproducible characteristics (see Section 3.2.3). Phase reproducible modulation (i.e. seeding) is important for the injection of a short witness electron bunch into the wakefield at the right phase (focusing and accelerating), so that

its quality can be preserved during acceleration. These measurements are planned for 2027.

Due to the imaging and temporal resolution of the transverse modulation with the streak camera, the images can be used to qualitatively and quantitatively characterize the self-modulation. In this thesis, I determine the lengths and widths of micro-bunches and their relative charge. As a result of lower wakefield amplitudes at the start of the modulation, defocused proton distributions close to the RIF have not diverged far enough to exceed the transverse aperture of the OTR transport line. In this thesis, I use these proton distributions to characterize transverse wakefield amplitudes for different experimental parameters and to confirm fundamental characteristics of the SSM process. In addition, I perform numerical simulations whose results I compare to the experimental ones. Since experimental and simulation results agree well, I use the insight provided by numerical simulations to better explain the evolution of the experimental results along the plasma.

2.5.2 Electron Acceleration

In previous experiments, an electron bunch with a length on the order of the wakefield period was injected into the plasma wakefield. The electrons are injected into the plasma at the entrance of the vapor source with an initial energy of 18 MeV. Some electrons (capture rate up to $\sim$ 10 % in single events, but typically $\sim$ 1 % or lower [41]) are accelerated in the wakefield driven by the proton bunch in the 10 m long plasma [42]. The energy and captured charge of the electrons is measured with the electron spectrometer (see Figure 2.3).
An example of the spectrometer image for an event with accelerated electrons is shown in

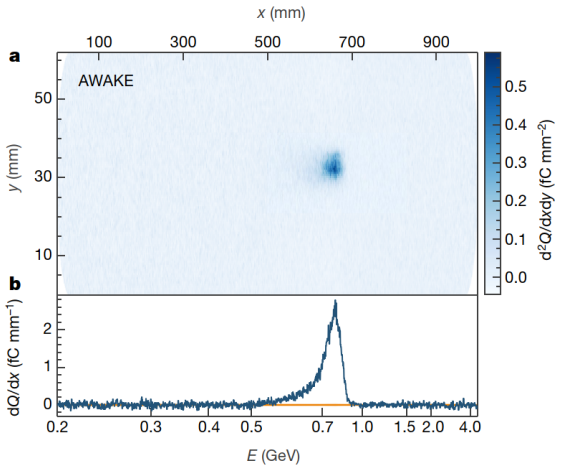

Figure 2.17: Spectrometer image (top figure) of an electron bunch accelerated to $\sim$ 0.7 GeV and the energy projection with background subtraction (bottom figure), from [42].

Figure 2.17, with the energy information on the horizontal axis. Both the spectrometer image (Figure a) and the energy projection (Figure b) show the narrow energy distribution of the accelerated electrons. This event shows electrons accelerated from initially $\sim 18\,\mathrm{MeV}$ to more than $0.7\,\mathrm{GeV}$.
For future applications the reproducibility of events with accelerated electron in charge

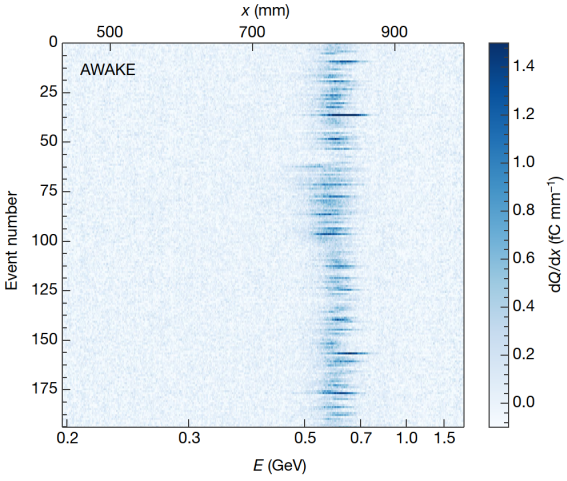

Figure 2.18: Waterfall plot of the electron energy distribution of more than 185 consecutive events, from [42].

(intensity in image) and energy (position in image) is crucial. Figure 2.18 shows the energy projection of more than 185 consecutive events. The peak energy and energy spread are well reproducible. This shows that the electron energy is not strongly fluctuating with experimentally fluctuating parameters such as electron bunch injection angle or position, plasma and drive bunch alignment.
With higher plasma density, a higher amplitude of the longitudinal (thus accelerating)

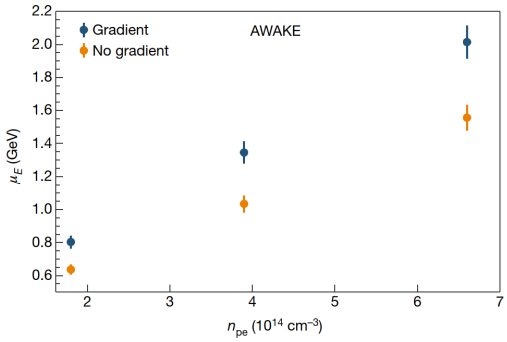

Figure 2.19: Highest peak energy μ_E as a function of plasma density n_{pe} with constant plasma density (orange points) and with optimum linear plasma density gradient (blue points) over the 10 m, from [42].

wakefield is expected from theory [18]. Figure 2.19 shows the increase in energy gain by witness electrons for increasing plasma density. The highest peak energy $\mu_E = (0.8 \pm 0.1)\,\mathrm{GeV}$ for $n_{pe} = 1.8 \cdot 10^{14}\,\mathrm{cm}^{-3}$ increases to $\mu_E = (2.0 \pm 0.1)\,\mathrm{GeV}$ for $n_{pe} = 6.6 \cdot 10^{14}\,\mathrm{cm}^{-3}$ [42]. The measurement suggests that an optimal plasma density gradient ($\Delta n_{pe} = 0.22\,\%/\mathrm{m}$, blue points) generally increases the energy gain compared to

constant density along the 10 m (orange points).

The short summary of experimental results presented here shows that SM of the long ($\sigma_\xi \gg \lambda_{pe}$) proton bunch in the 10 m long plasma occurs. SM is the result of the transverse wakefield growing along the bunch and along the plasma. Externally injected electrons can be accelerated by the longitudinal wakefield, associated with the transverse ones. In this thesis, I characterize the self-modulated proton bunch over the first few periods behind the RIF. I study the micro-bunches as well as defocused proton distributions in between to ultimately conclude on the amplitude of the transverse wakefield, driven by the proton bunch in plasma.

2.6 AWAKE Run 2

In AWAKE Run 1 experiments (2016-2018), we demonstrated the self-modulation of a long proton bunch in plasma and that electrons can be accelerated in the wakefield, driven by the modulated proton bunch. Some of the experimental acceleration results are shown in the previous Section. In AWAKE Run 2 (∼2027), the goal is to preserve the quality of the witness electron bunch during acceleration.
The schematic setup of future AWAKE Run 2 measurements is shown in Figure 2.20.

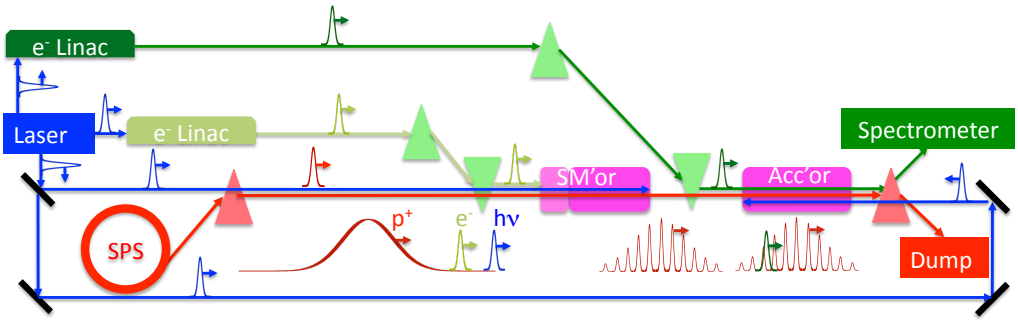

Figure 2.20: Schematic of the AWAKE Run 2 experimental setup from [43]: Plasma is divided into self-modulator ("SM'or") and accelerator ("Acc'or"); In the self-modulator the SM is seeded with a preceding electron bunch in pre-formed plasma.

Unlike previous experiments, the plasma will be divided into two stages, one stage for the self-modulation of the proton bunch (self-modulator), one for the acceleration of an externally injected electron bunch (accelerator). During the self-modulation process of the proton bunch, the phase of the wakefield is slower than the protons (Section 1.4.5). The phase slippage can be partly compensated with a positive linear plasma density gradient [24] or a plasma up-density step $\sim 1-2$ m after the plasma entrance, as it is

planned for the self-modulator plasma [44]. The witness electron bunch (dark green line in Figure) is injected into the accelerator plasma, i.e. into the wakefield, driven by the pre-modulated proton bunch in order to allow electrons to avoid the wakefield phase slippage, that occurs during SM evolution. Therefore, the entire length of the accelerator plasma could be used for acceleration of the electron bunch, placed in the focusing and accelerating phase of the wakefield.
Further, unlike in AWAKE Run 1 measurements, where SM was seeded with the RIF co-propagating close to the proton bunch center, we plan to seed SM with a preceding short electron bunch (bright green line in Figure) [44]. With this method, both bunches, proton and seed electron bunch, propagate in a pre-modulated plasma. The main advantage of this seeding technique is that the entire proton bunch is modulated and that the seed (electron bunch) can be far ahead of the proton bunch center. This is important, once the proton bunch enters the accelerator plasma, to avoid a modulation of the bunch head with non-reproducible phase, that could interfere with the modulated part of the bunch, when seeded with the RIF close to the bunch center. A first experimental study of electron bunch seeding is shown in Chapter 7. This will be one of the core measurements of experiments in 2021-2022.
In previous measurements, the witness electron bunch length was on the order of the plasma period τ_{pe}, to ensure some electrons to cover the accelerating and focusing wakefield phase, without precise timing control. In AWAKE Run 2, a shorter ($\ll \tau_{pe}$) witness electron bunch will be injected. With the accelerator, decoupled from the self-modulator, together with beam loading, the witness bunch matched to the plasma and the short bunch, the goal is to demonstrate the preservation of witness bunch qualities, such as energy spread and emittance, and a high capture rate [44].

3 Optical Transition Radiation Measurements for Self-Modulation Studies

In this thesis, the proton bunch self-modulation is characterized from the time-resolved images. With a streak camera we acquire the optical transition radiation, emitted by the bunch at a screen after the plasma. In the following chapter, the experimental setup of these measurements and the image processing, applied to the streak camera images, are described. Streak camera images require a low intensity input signal for high temporal resolution. We obtain significantly higher signal to noise ratio (SNR) of images from averaging single images. This enables the comparison of characteristics of the self-modulation with different experimental input parameters, using profiles and/or values without large noise contribution from the time-resolved images.

3.1 Experimental Setup for Time-Resolved Streak Camera Images

One of the main diagnostics for the proton bunch self-modulation is the streak camera, see Section 2.5.1. Approximately 3.5 m after the plasma exit, the unmodulated head and the modulated back of the bunch enter an OTR screen (280 µm Silicon wafer coated with 1 µm mirror-finished aluminium) and OTR is emitted [13, 45] (setup in Figure 2.13). The spatio-temporal pattern of the light represents the shape of the bunch at the screen. The light is imaged onto the entrance slit of the streak camera and onto a photo cathode where photons are converted to electrons. Those are accelerated through a streak tube onto a phosphor screen. The transverse bending voltage of the streak tube is time-varying at the ps to ns time scale. Therefore, depending on the time arrival of photons on the photo cathode, emitted electrons are bent weaker or stronger and thus reach the phosphor screen on a different transverse position. Electrons are multiplied by a micro-channel plate (MCP) before the phosphor screen. The light emitted by the screen is imaged onto

a CMOS camera.

We use a streak camera from Hamamatsu (model C10910-05) with a 16-bit, 2048x2048 pixel ORCA-Flash4.0 CMOS sensor, binned to 512x672 pixels for streak operation. The acquisition time window can be varied between 73 ps and 5 ns. In the following, we mainly use the smallest time window, where the streak dynamics limit the temporal resolution to less than 2 ps [45].

The optical magnification of the light transport was measured with a Ronchi grating placed in a conjugated plane to the plane of the OTR screen. The transverse pixel to µm conversion of the streak camera images was hereby determined to 1 px $\widehat{=}$ 22 µm, the demagnification of the light path from the OTR screen onto the camera to ~ 3.7 and the spatial resolution to $\sigma_{res,r} \approx 80\,\mu m$.

The light enters the streak camera through a slit to increase its temporal resolution. In

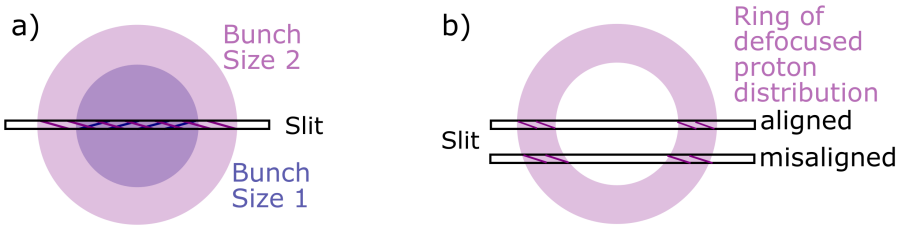

Figure 3.1: Schematic of the light collection through the streak camera slit for a) two different bunch sizes; b) a misaligned bunch

general, the image of the bunch at the screen on the slit has cylindrical symmetry (see Figure 3.1 a). During the following measurements the slit width was kept constant at 20 µm, that corresponds to 74 µm at the OTR screen due to the demagnification by the light transport. In general, the slit width is small when compared to the bunch width (unmodulated bunch width at OTR screen $\sigma_r \approx 570\,\mu m$). Therefore, the light intensity of the images is formed by a transverse slice of the proton bunch, i.e. the intensity is proportional to the bunch charge density. This assumption is confirmed by simulations in Section A.5 comparing the signal from a transverse slice with the one integrated over the slit width.

Generally, spatial misalignment of the proton bunch with respect to the streak camera slit influences the measured intensity profile, as shown by the schematic in Figure 3.1 b). With misalignment of the bunch, the transverse extent of the signal decreases, i.e. charge density is generally measured at slightly smaller radii. However, as studied in Section A.5 using results from simulations, spatial misalignment in the experiment is expected to be small, thus for the wide signals analyzed in this thesis (unmodulated bunch $\sigma_r \approx 570\,\mu m$, defocused proton distributions generally wider than the unmodulated bunch) we expect

misalignment to play a minor role and do not further consider it in this thesis.

All experimental results for the characterization of the self-modulated proton bunch in this thesis are obtained from time-resolved images acquired with the streak camera. The data was taken between September and October 2018. The streak camera was operated with an MCP gain of 40. To decrease temporal smearing due to varying initial electron velocity at the photo-cathode, the broad OTR light passes through a bandpass filter around (450 ± 50) nm.

3.2 Streak Camera Image Processing

In the following, I characterize the streak camera images and describe image processing and analysis procedures used in this thesis for the characterization of focused and defocused proton distributions.

3.2.1 Resolution

I determine qualitatively and quantitatively characteristics of the self-modulated proton bunch using streak camera images. A two dimensional bunch density map (time-resolved images) of the modulated bunch is obtained by imaging the OTR screen onto the streak camera entrance slit. The signal with a transverse size on the order of 1 mm is examined and the spatial resolution of the streak camera images is determined. The characteristic length of the bunch modulation is determined by the plasma period, that is smaller than 11.3 ps for the plasma densities larger than $0.9 \cdot 10^{14}\,\mathrm{cm}^{-3}$ used in this thesis. I therefore determine the temporal streak camera resolution.

Temporal Resolution

In order to determine the micro-bunches length and whether focused and defocused regions are distinguishable and well resolved, the temporal resolution of the streak camera images is determined. The timing reference laser pulse, a mirror bleed-through of the ionizing laser pulse with a duration of ~ 120 fs is sent onto the streak camera. As the laser pulse duration is expected to be shorter than the temporal resolution, its duration on the images is determined. The resolution varies with the operational time window. Images in this thesis are obtained with the 73 ps and 211 ps windows. The temporal resolution decreases with increasing light intensity, thus the streak camera should generally be

operated in the speckle regime for highest temporal resolution.
Figure 3.2 shows streak camera images of the self-modulated proton bunch with the

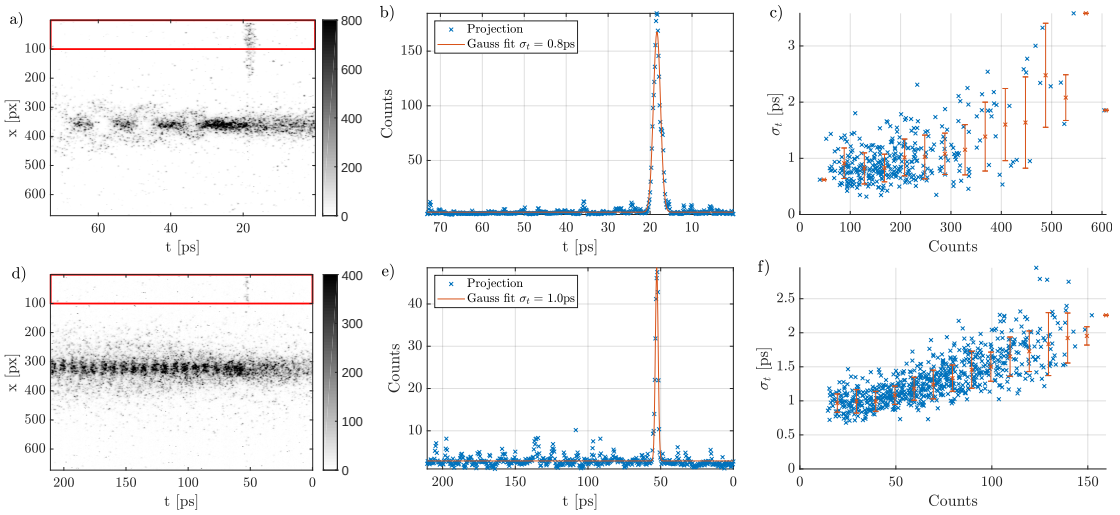

Figure 3.2: Images (a, d) streak camera images with reference laser pulse ($x \leq 100\,\text{px}$, red box). Images (b, e) projection of $x \leq 100\,\text{px}$ of the streak camera images (blue crosses) and Gaussian fit (red line). Images (c, f) width of the fits as a function of fit amplitude (blue crosses) and data binned in amplitude (red crosses with std as error bars). Here, images (a-c) are obtained with the 73 ps and images (d-f) with the 211 ps streak camera time window.

timing reference laser pulse (Figures a, d) and the projection of the reference laser pulse over the region without proton signal $x \leq 100\,\text{px}$ (blue crosses in Figures b, e). The laser signal amplitude is assumed to be essentially constant over the projected transverse range and the mean value of the projection is used for the resolution determination with the peak count value. The projection is fitted with a Gaussian function (red lines in Figures b, e) and the fit's rms width σ_t and amplitude are determined. As the laser pulse duration is significantly shorter than the expected temporal resolution, the width of the measured signal gives the temporal resolution. The fit's width is increasing with the fit's amplitude (Figures c, f). This implies a decrease in temporal resolution with increasing light intensity.
This procedure is used to determine the temporal resolution for the shorter 73 ps (Figures a-c) and the longer 211 ps (Figures d-f) streak camera time windows, as used in this thesis. The resolution with the short window is therefore $(0.9 \pm 0.3)\,\text{ps}$ for a peak amplitude of 90 counts and increases to $(1.4 \pm 0.6)\,\text{ps}$ for a peak amplitude of 370 counts (Figure c). With the longer window it increases from $(1.0 \pm 0.2)\,\text{ps}$ for a signal amplitude of 20 counts to $(1.9 \pm 0.4)\,\text{ps}$ for an amplitude of 140 counts (Figure f).
In order to obtain not only temporal information with highest temporal resolution but

also transverse information of the modulated proton bunch we generally use higher light intensity from protons than for the reference laser pulse. The streak camera images (Figures a, d) show that the signal amplitude of the proton bunch is generally higher (first micro-bunch $\sim$ 800 counts in a; $\sim$ 400 counts in d) than the reference laser pulse signal. Therefore, from extrapolation of the resolution with light intensity (Figures c, f), a lower temporal resolution is expected than determined here with the reference laser pulse signal. For simplicity, in this thesis a temporal resolution of $\sigma_{res,t} = 1.5\,\text{ps}$ is assumed, independent of the signal intensity and for both streak camera time windows.

Spatial Resolution

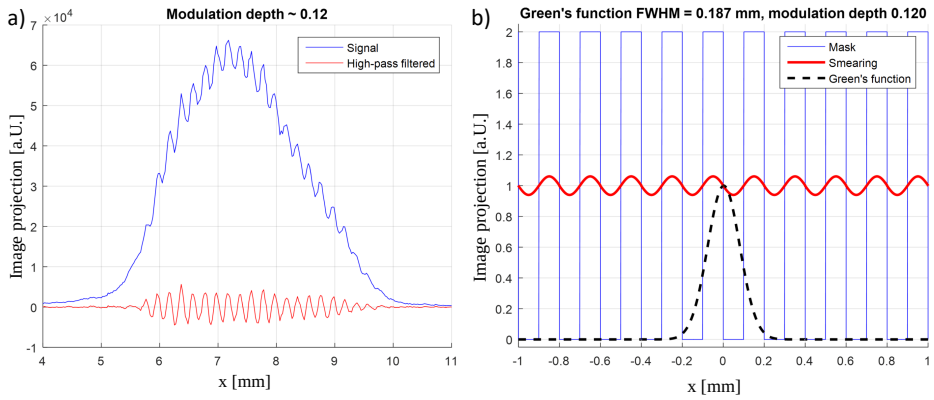

Figure 3.3: a) Projection of the light intensity of a streak camera image with a grid in the object plane without (blue line) and with (red line) high-pass filter to measure the modulation depth of the signal caused by the grid. b) Square shaped grid signal (blue line) convoluted with a Green's function (black dashed line), resulting in a signal with similar modulation depth (red line) as measured for the grid. Both from [46].

The OTR screen, imaged by the streak camera, is located inside vacuum. For technical simplicity, we measure the spatial resolution with a Ronchi grating (line width 100 µm, periodicity 5 lines/mm), placed in a conjugated object plane. Figure 3.3 a) shows the projection of the image of the grid (blue line), the overall bell-shape like light intensity profile superposed with the modulation, that contains the spatial resolution information. When applying a high-pass filter to the signal (red line) we measure a modulation depth of ~ 0.12.

In Figure 3.3 b) the square shaped signal of a grid from 0 to 2 (blue line) is convoluted with the spatial resolution function (Green's function, black dashed line). The width of the resolution function is varied until the convolution (red line) has a similar modulation

depth as in the grid measurement (red line, Figure 3.3 a). The modulation depth of ~ 0.12 is obtained with a resolution width (FWHM) of 0.187 mm, i.e. the spatial resolution is $\sigma_{res,r} \approx 80\,\mu\text{m}$ ($\widehat{=} 4\,\text{px}$) and $1\,\text{px} = 22\,\mu\text{m}$.

3.2.2 Single Image Processing

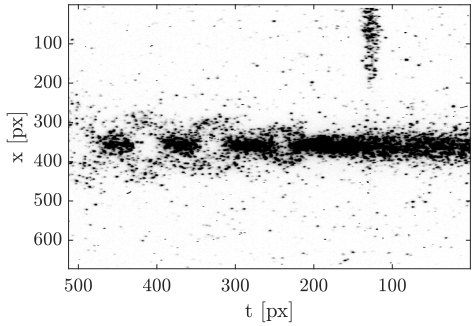

Figure 3.4: Single streak camera image of the modulated proton bunch, propagating from left to right. RIF at $t \approx 120\,\text{px}$ (reference laser pulse $x \leq 200\,\text{px}$).

The following section describes the processing of single streak camera images that contribute to averaged (stitched) images for each data set. Figure 3.4 is an example of a single streak camera image of the modulated proton bunch with the reference laser pulse signal (at $t \approx 120\,\text{px}$ and $x \leq 200\,\text{px}$), here coinciding with the time of the ionizing laser pulse (see Section 3.2.3). The vertical axis corresponds to the transverse component x, the horizontal axis to the temporal position t, i.e. the bunch propagates from left to right. One can see the unmodulated bunch head ($t < 120\,\text{px}$), that propagated through vapor and the modulated bunch ($t > 120\,\text{px}$), that propagated through plasma.

Time Axis Linearization

As explained in Section 3.1, to resolve the light signal in time, the streak camera applies a sweeping voltage bending the electrons from the photo-cathode time-dependent onto the phosphor screen, imaged by the camera. As the sweeping velocity is not constant over one acquisition, the time-axis of the image is slightly non-linear (blue crosses), as given by the streak camera manufacturer, see Figure 3.5. In this thesis all images and their time axis are linearly interpolated (red crosses) as shown for the shorter (a) and longer (b) time window. Note that this procedure conserves the number of counts of the image.

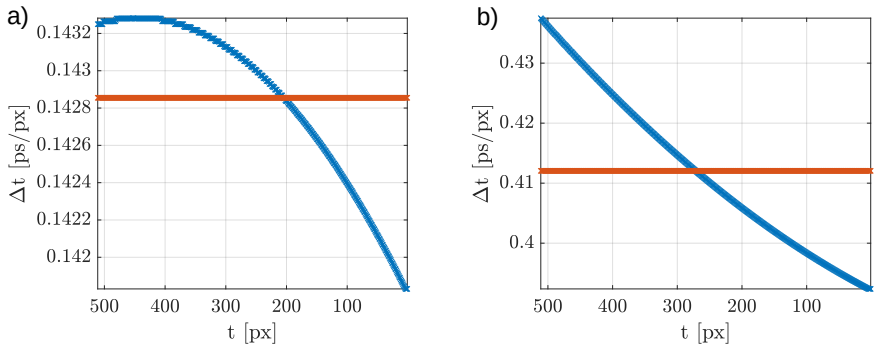

Figure 3.5: Pixel length in time of the original image (blue crosses) and after linearization (red crosses) for the a) 73 ps and b) 211 ps time window.

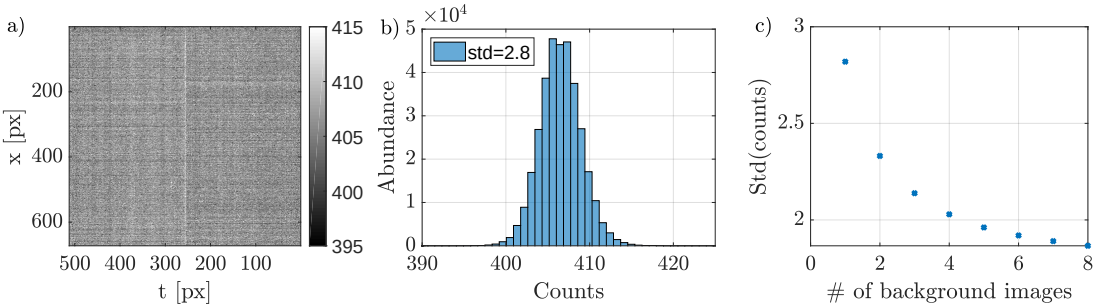

Figure 3.6: a) Streak camera background image (no protons or laser pulse); b) Histogram of counts of a single background image (after applying a hot and dead pixel filter from Section 3.2.4); c) Histogram width (std) as a function of number of averaged background images

Background

The background signal of the streak camera is subtracted from the proton bunch images. Eight images are acquired without proton bunch or laser pulse, using the similar MCP gain (40) and slit with (20 µm) as throughout the experiment. An example of these images is shown in Figure 3.6 a) and the histogram of the counts of the example image in Figure b). The width, the standard deviation (std), of the histogram is determined. This analysis is repeated with averaging multiple background images. The decrease in width as a function of the number of averaged background images is shown in Figure c). The saturation of the width indicates that the average of eight images is sufficient to reduce the statistical noise of the background image, that is subtracted from all proton bunch images in this thesis. Here, hot and dead pixels are filtered from the images before calculating the histograms. The filter is explained in Section 3.2.4.

Bunch Population Normalization

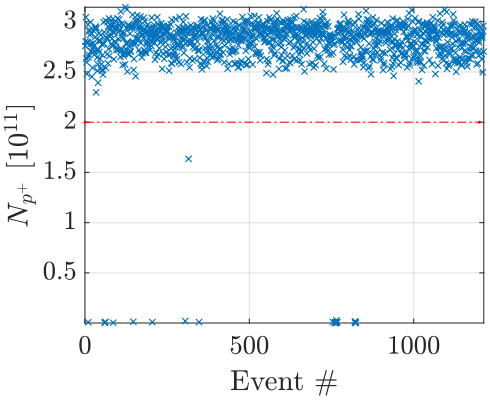

Figure 3.7: Proton bunch population N_{p^+} (blue crosses) of more than 1200 consecutive events, measured by the beam current transformers. Events with a population of $< 2 \cdot 10^{11}$ (red line) are considered failed extractions.

The light intensity emitted by the proton bunch depends on the bunch population, that varies on a small scale for each event, see Figure 3.7. The bunch population, measured by the beam current transformer, is $N_{p^+} = (2.82 \pm 0.14) \cdot 10^{11}$ (std) for more than 1200 subsequent events, excluding failed extractions with populations $< 2 \cdot 10^{11}$. Therefore, rms variations of $\sim 5\,\%$ are expected. For the analysis of this thesis each proton bunch image is normalized to its bunch population and events of failed extraction are excluded.

3.2.3 Stitching of Single Images

Streak cameras are generally used with relatively low light intensity input signals to achieve better temporal resolution (see Section 3.2.1). Assuming a repetitive modulation, averaging multiple events increases the SNR of the noisy images of the bunch (Figure 3.4) significantly. Averaging requires a very small timing variation of the camera trigger, or a reference light signal that is tied to the bunch modulation. The streak camera trigger variation (std) is $\sim 5\,\text{ps}$ [47]. As we analyze a modulated bunch with modulation period similar to the plasma period $\tau_{pe} < 11.6\,\text{ps}$ (see Section 5.2), averaging images of the bunch with this trigger variation would smear out the modulation.
The SM is tied to the RIF, as demonstrated in [16]. Thus the streak camera trigger variation can be overcome by using the reference laser pulse to combine single events. As mentioned earlier (Section 3.2.1), the mirror bleed-through of the ionizing laser pulse is collected and sent through air onto the streak camera entrance slit. Its path length is controlled with a translation stage. The reference laser pulse, that is sent directly onto the streak camera, is temporally aligned with a low energy version of the ionizing laser pulse, acquired by reflection off the OTR screen. With the translation stage we can either overlap in time the arrival of the reference laser pulse with the ionizing laser pulse or let it

arrive with a known time difference behind the ionizing laser pulse. Their relative timing jitter is $< 1\,\mathrm{ps}$ [47]. The reference laser pulse enables to scan with the shortest (73 ps) camera time window, thus highest temporal resolution, along the long ($\sigma_\xi > 250\,\mathrm{ps}$) proton bunch preserving information of the relative position of the micro-bunches along the train. Thus, a specific part of the bunch can be can acquired by shifting the streak camera trigger together with the arrival time of the reference laser pulse.
The reference laser pulse can be seen on a proton bunch image in Figure 3.4 at $x \leq 200\,\mathrm{px}$,

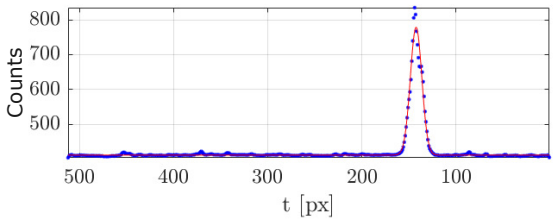

Figure 3.8: Gaussian fit (red line) to the projection of the timing reference laser pulse ($15\,\mathrm{px} \leq x \leq 110\,\mathrm{px}$ of the streak camera image of Figure 3.4) (blue points). The center of the fitted peak is used for temporal alignment of multiple events.

here overlapping with the timing of the RIF. In Figure 3.8, the time of the reference laser pulse is determined as the peak position of a Gaussian fit (red line) to its image projection ($15\,\mathrm{px} \leq x \leq 110\,\mathrm{px}$ on Figure 3.4, blue points). This procedure is repeated for all proton bunch images and the timing of the reference laser pulse is used for temporal alignment for combination (stitching) of the single proton bunch images.
Figure 3.9 shows the temporal alignment of single streak camera images using the timing

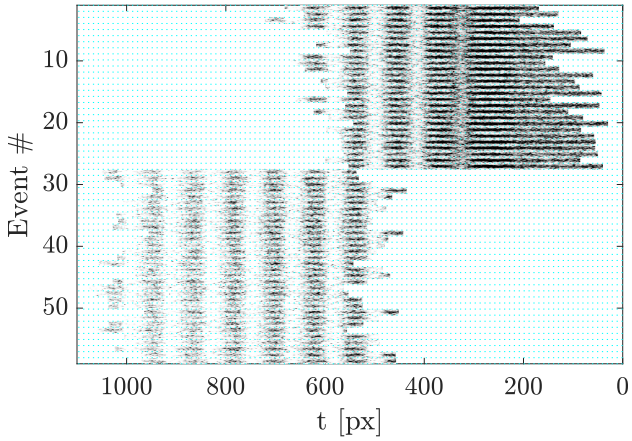

Figure 3.9: Central bunch modulation ($320\,\mathrm{px} < x < 400\,\mathrm{px}$) of 59 proton bunch images. Events $\#1 - 27$ cover the RIF (at $t \approx 200\,\mathrm{px}$), events $\#28 - 59$ are acquired with a 50 ps delay of camera trigger and reference laser pulse.

reference signal locked to the RIF, thus start of the SM. Here, single images are cut transversely for better comparison of the central density modulation and visualization of

the micro-bunches occurrence, temporally locked to the RIF. The figure shows images $\#1 - 27$, covering the RIF (at $t \approx 200\,\text{px}$), and images $\#28 - 59$, where the reference laser pulse and the camera trigger were delayed by $\sim 50\,\text{ps}$ (corresponding to $\sim 350\,\text{pixels}$ for the 73 ps time window used here). The figure demonstrates that micro-bunches are temporally locked to the RIF and thus to the reference laser pulse.
The stitching and averaging of single streak camera images is demonstrated in Figure

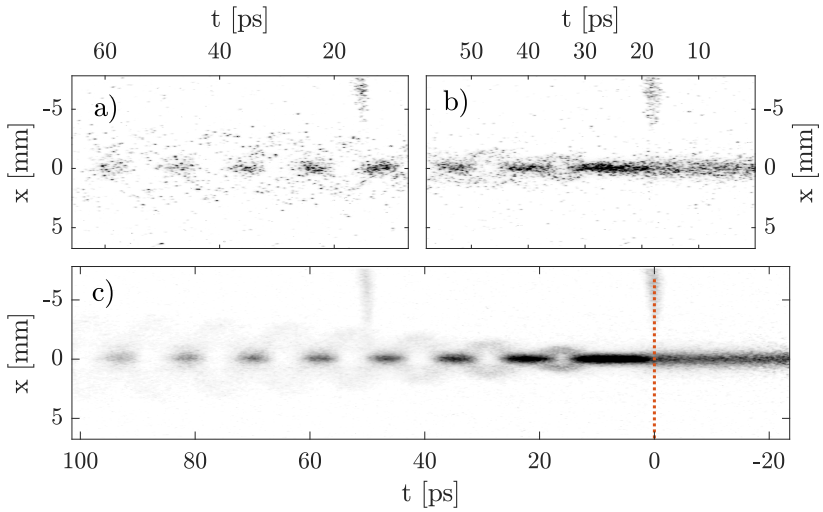

Figure 3.10: a) Single streak camera image with a 50 ps time delay to the start of the SM, b) single streak camera image at the start of the SM and c) sets of the two time delays of 20 streak camera images each stitched together using the timing reference signal [43].

3.10. The images are temporally aligned with the reference laser pulse as shown in Figure 3.9. Figure 3.10 b) shows a single image of the set with the timing of the reference signal overlapping with the RIF (events $\#1 - 27$ in Figure 3.9) and Figure a) a single image with $\sim 50\,\text{ps}$ time delay of the reference laser pulse and the streak camera trigger (events $\#28 - 59$ in Figure 3.9). A set of ~ 20 images is taken for both delays each and they are stitched together (Figure c). The position of the RIF is defined as $t = 0$ throughout this thesis.
The bottom image in Figure 3.10 clearly shows the enhancement of the signal, obtained with the stitching procedure. For the stitched images of the unmodulated bunch, when propagating without plasma, only 2 images are averaged per set, thus a lower signal to noise ratio is obtained.

3.2.4 Stitched Image Processing

In the following, the processing of stitched images is described, including image filtering and the determination of the transverse bunch center, the field of view and the temporal location of focused and defocused proton regions.

Filtering

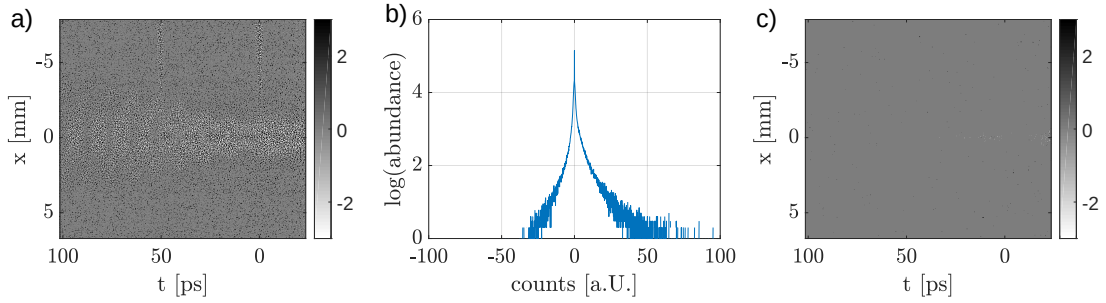

Figure 3.11: a) Difference between original and median filtered image; b) Abundance of the value in count difference from image a); c) Difference between original and filtered image, applying a median filter to selected pixels with abundance ≤ 3 in b).

Hot and dead pixels of the stitched streak camera images are addressed for further analysis. If a 2D median filter (average of five surrounding pixels) is applied onto the entire image, it significantly affects the noisy signal of the modulated proton bunch ($|x| \lesssim 0.5\,\mathrm{mm}$), as shown in Figure 3.11 a), that shows the difference between the original and median filtered image. In Figure 3.11 b), the abundance of a value in count difference between original and the median filtered image (Figure 3.11 a) is plotted. The pixels where the count difference value occurs less than four times (value empirically determined) are selected and the median filter is applied only to those pixels. The difference between the original and the customized filtered image is shown in Figure 3.11 c). The figure shows that the customized filter mainly treats hot and dead pixels, but effectively does not change the signal of the proton bunch around $x = 0$.

Transverse Axis

The transverse center of the proton bunch of the stitched images is determined with the projection of the unmodulated bunch ($-22\,\mathrm{ps} < t < -9\,\mathrm{ps}$, see Figure 3.10 c). In Figure 3.12, the projection (blue dots) is fitted with a Gaussian function (red line) and the center of the bunch is determined as the center of the fit (green dash-dotted line).

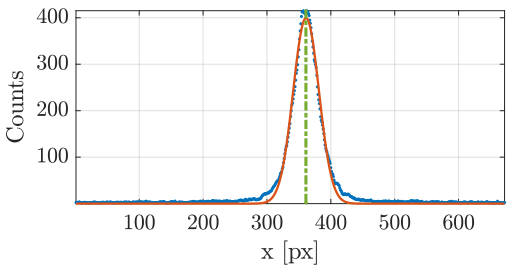

Figure 3.12: Projection of $-22\,\text{ps} < t < -9\,\text{ps}$ of the stitched image (Figure 3.10) (blue dots) fitted with a Gaussian function (red line). The transverse bunch center is determined by the center of the fit peak (green dash-dotted line).

The transverse center is defined as $x = 0$ and the pixel to mm ratio of $1\,\text{px} \mathrel{\widehat{=}} 22\,\mu\text{m}$, as determined in Section 3.2.1, is used for the x scale of the images. This corresponds to the scale at the OTR screen.

Field of View

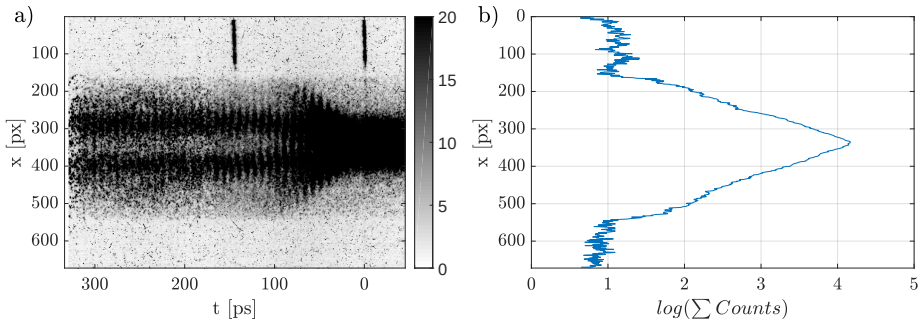

Figure 3.13: a) Stitched proton bunch image and b) its projection on logarithmic scale.

The proton bunch signal on the streak camera images is transversely limited by the light transport aperture and its imaging optics from the OTR screen to the streak camera. The field of view is determined with the stitched image obtained with a negative plasma density gradient, see Figure 3.13 a), as here a large transverse defocusing of protons is observed (Chapter 5 and 6). The image is strongly saturated by manually fixing the color scale to better visualize the field of view. The time-integrated projection of the image is plotted in Figure 3.13 b) on a logarithmic scale. The projection shows that the field of view is limited between $160\,\text{px} < x < 550\,\text{px}$. With the transverse bunch center determining $x = 0$, this corresponds to $-4\,\text{mm} < x < 4.5\,\text{mm}$ for the image shown here. However, as $x = 0$ is determined for each stitched image individually as explained above (Figure 3.12), due to small variations of the proton bunch alignment this varies on a small scale for each stitched image. Hence, in this thesis, the analysis of the proton bunch

signal on stitched images is limited to $|x| \leq 4\,\mathrm{mm}$.

Temporal Location of Micro-Bunches and Defocused Proton Regions

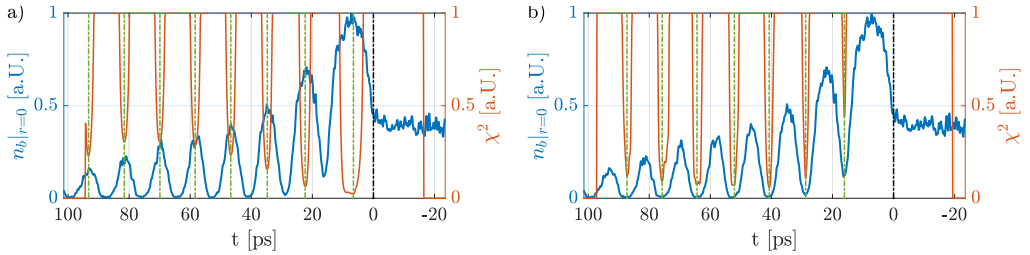

Figure 3.14: Central bunch density modulation ($n_b|_{r=0}$, projection of $|x| \leq 0.11\,\mathrm{mm}$, blue lines), weighted distance squared function χ^2 (cut for high values, red lines) using a parabola as polynomial fit to the data and its minima (green dashed-dotted lines), location of micro-bunches (a) and defocused proton regions (b).

The central bunch charge density modulation ($n_b|_{r=0}$, blue lines in Figure 3.14) of the stitched images is used to determine the temporal center of micro-bunches and defocused proton regions along the bunch. This is obtained by summing counts between $|x| \leq 0.11\,\mathrm{mm}$ to capture only the micro-bunch train and not the defocused charge density. I fit a second order polynomial equation $f(t) = a + b \cdot t + c \cdot t^2$ in order to calculate the weighted distance squared function χ^2 (red lines) between $f(t)$ and the central bunch density modulation curve $n_b|_{r=0}$. The constant c in $f(t)$ determines, whether the parabola is open upwards or downwards, so $c < 0$ is fixed for determining positions of the micro-bunches (Figure a) and $c > 0$ for the defocused proton regions (Figure b). The polynomial function is scanned along the time axis of the image and values of t, where it fits the data the best (minimum value of χ^2), are determined. The range in t covered by the polynomial function is close to the length of a micro-bunch (for $c < 0$) or of a defocused proton region (for $c > 0$).

The weighted distance squared function, that corresponds to the distance between the model expectation and the data, is calculated as

$$\chi^2 = \sum_i \frac{(n_{b,i} - f(t_i|\boldsymbol{\lambda}))^2}{\omega_i^2}, \tag{3.1}$$

with the model $f(t|\boldsymbol{\lambda})$ predicting a value for the data at t, given parameter values $\boldsymbol{\lambda} = \{a, b, c\}$, and $n_{b,i}$ the measured values. Here, the weight $1/\omega_i^2$ is defined as the curvature of the parabola, i.e. $1/\omega_i^2 = 1/c^2$, meaning the stronger the curvature, the

smaller χ^2, the better the fit. The minima of the function correspond to the best guesses and are defined as the center of the micro-bunches or defocused proton regions (green dashed lines in Figure 3.14).
A low streak camera temporal resolution could decrease the central charge density modulation depth. In this case, the minima locations are not affected if the longitudinal charge density profiles of subsequent micro-bunches are similar and symmetric. However, the profiles show that the shape of micro-bunches is similar (Gaussian, most likely due to temporal resolution, see Section 5.3), but the signal amplitude decreases along the bunch. This shifts the location of the defocused proton region slightly towards the subsequent, lower charge density micro-bunch. The shift is the larger, the larger the charge density difference between two micro-bunches.
This analysis to determine the center of micro-bunches ($c < 0$) and defocused proton regions ($c > 0$) is repeated for all streak camera images and for all time-resolved images from simulations. The results can be found in the appendix (Section A.4).

3.2.5 Micro-Bunch Length

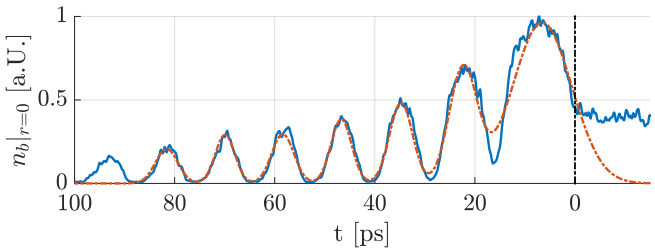

Figure 3.15: Central bunch density modulation $n_b|_{r=0}$ (projection of $|x| \leq 0.11\,\text{mm}$, blue solid line) with its peaks (micro-bunches) fitted with Gaussian functions (sum of the functions, red dash-dotted line) to determine their length.

I determine the length of micro-bunches from the time-resolved images. As for their location determination, in Figure 3.15 the central bunch density modulation (blue solid line) is used and the length of the micro-bunches is determined by fitting Gaussian functions (sum of all Gaussian functions, red dash-dotted line) to the micro-bunches. The range of each function is limited to the location of the surrounding defocused proton regions (and RIF for the first micro-bunch), as determined with the procedure described in Section 3.2.4 (Figure 3.14 b). With the same procedure the position and amplitude of the micro-bunch peak is determined (Figure 3.14 a) and used for the width determination by the fits. The only free parameter of the fit is the width.

Since micro-bunches are close to each other (distance ∼ a few rms widths) the signal of micro-bunches can overlap (e.g. first and second micro-bunch in Figure 3.15). This could be a result of limited temporal resolution with high light intensity and/or the bunch not being fully modulated over these periods. In order to take into account potential overlap of micro-bunches, for each micro-bunch, three subsequent micro-bunches are fitted with three Gaussian functions to determine the width of the central peak. To determine the length of the first (last) micro-bunch, only the subsequent (previous) micro-bunch is included, and thus in this case only two Gaussian functions are fitted.

3.2.6 Bunch Charge

As shown in the schematic in Figure 3.1, the light enters the streak camera through a slit for high temporal resolution. Therefore, when the slit width (20 µm) is much smaller than the bunch diameter ($\sigma_r \approx 150\,\mu\text{m}$ at the slit as the screen to slit demagnification factor is 3.7) the signal recorded by the camera in the t-x-plane corresponds to the bunch charge density $n_b(t,r)$ rather than its charge $Q(t,r)$. Therefore, to obtain the charge as a function of radius, the charge density must be integrated or summed as $Q(t,r) = 2\,\pi\,\int n_b(t,r)\,r\,dr$. Since the streak camera image is a discretized version of the continuous distribution, the charge is $Q(t_i,r_i) = 2\,\pi\,\sum_i n_b(t_i,r_i)\,r_i\,\Delta r_i$.
Figure 3.16 shows the charge density of the bunch measured without plasma (a) and with

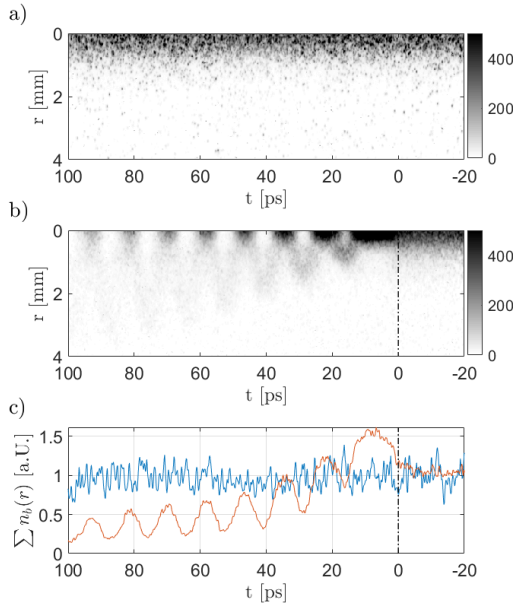

Figure 3.16: Streak camera image (i.e. charge density) of the a) unmodulated and b) modulated bunch; c) charge density integrated over $r \leq 4\,\text{mm}$ of the unmodulated (blue line) and modulated (red line) bunch, both normalized to the mean value of the sum of the incoming bunch charge density over $-15\,\text{ps} \leq t \leq -4\,\text{ps}$. Here, $\xi_{Seed} = -0.1\,\sigma_\xi$.

plasma (b). The focused and defocused regions generated by the SM are clearly visible on Figure b), while the distribution on Figure a) is continuous, all as expected. The

respective slice charge densities along the bunch also show an essentially continuous and constant charge density for the image without plasma (blue line on Figure c) whereas that of the image with plasma (red line) clearly shows modulation. Since Figure b) shows the focusing and the defocusing resulting from SM, the corresponding slice charge density shows the expected variations. These are not present for the case of no plasma as the bunch radius is constant and the charge may vary only because of the underlying Gaussian temporal profile of the incoming proton bunch. In general, the slice charge density of the part of the bunch in the plasma ($t > 0$) is lower than that of the incoming bunch.

Figure 3.17 shows similar results as those of Figure 3.16, except that it displays the charge (as a function of time and radius) instead of the charge density. As expected the plasma off slice charge is essentially constant (blue line on Figure c). However, now the slice charge along the bunch with plasma (red line) is essentially equal to that of the incoming bunch, all along. This shows that in this case the camera image records all the charge of the bunch. It also shows that micro-bunches contain all the charge that was at their corresponding plasma off location along the bunch.

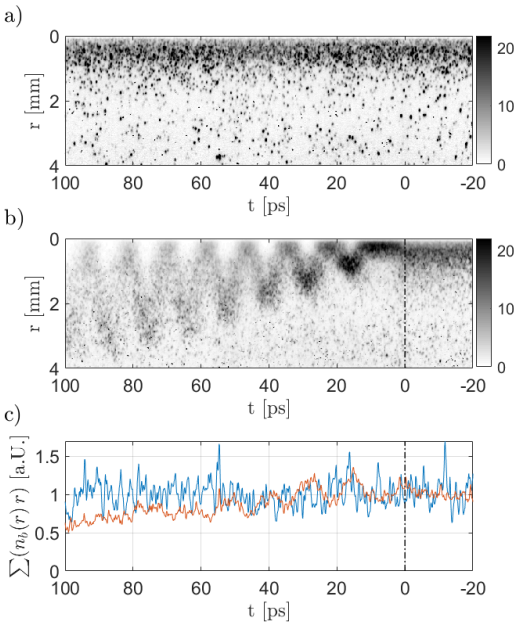

Figure 3.17: Streak camera image multiplied with transverse position (i.e. charge) of the a) unmodulated and b) modulated bunch; c) charge integrated over $r \leq 4\,\mathrm{mm}$ of the unmodulated (blue line) and modulated (red line) bunch, both normalized to the mean value of the sum of the incoming bunch charge over $-15\,\mathrm{ps} \leq t \leq -4\,\mathrm{ps}$. Here, $\xi_{Seed} = -0.1\,\sigma_\xi$ and $\sigma_\xi = 7.92\,\mathrm{cm} \mathrel{\widehat{=}} \sigma_t = 264\,\mathrm{ps}$.

Modulation that remains in the slice charge of the modulated bunch can be explained with the detection threshold of the streak camera. Light that is below the detection threshold for the unmodulated bunch (due to low bunch density) could be detectable in the period of focused protons of the modulated bunch. At the same time, in a period of defocused protons, light could fall below the detection threshold. With larger distance

($t > 80\,\text{ps}$) to the RIF the total charge of the modulated case is not preserved as light from strongly defocused protons is outside the field of view ($x \leq 4\,\text{mm}$, see Section 3.2.4).

3.2.7 Micro-Bunch Charge

The previous section explains that the relative slice charge of the modulated bunch can be obtained from multiplying the streak camera images (intensity proportional to the slice charge density) with the radial position. In Section 5.4, it is shown that for the case discussed here the widths of the micro-bunches (after vacuum propagation to the OTR screen) in the experiment increase along the bunch. Further, in Section 5.3, it is demonstrated that in the experiment the longitudinal shape and length of micro-bunches $\#3 - 7$ are not changing along the bunch. Thus, the relative micro-bunch charge is only determined by the charge, integrated transversely.
The transverse charge density profile is averaged over 1.5 ps (temporal streak camera

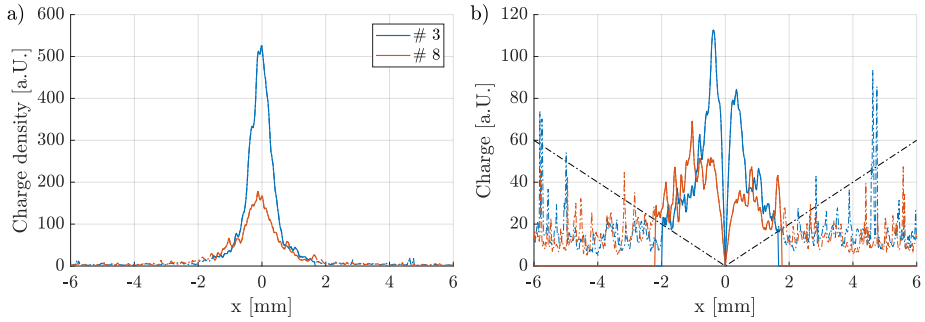

Figure 3.18: Transverse profiles of the charge density (a) and charge (b) of micro-bunch #3 (blue lines) and #8 (red lines) above (solid lines) and below (dashed lines) the noise threshold. Noise threshold for charge density 10 [a.U.], i.e. for charge 10 [a.U.] $\cdot$ $|x[\text{mm}]|$ (black dashed line in b).

resolution), centered around the micro-bunch locations (see Section 3.2.4). In Figure 3.18 a) the relative micro-bunch charge is calculated from the charge density profiles of the third (blue line) and eighth (red line) micro-bunch. The charge density profiles are multiplied with the transverse component $|x| = r$ to obtain the charge profiles, see Figure 3.18 b). In order to suppress the noise contribution when determining the total micro-bunch charge, a noise threshold 10 [a.U.] $\cdot$ $|x[\text{mm}]|$ (black dash-dotted line) is used. To determine the total charge of a micro-bunch, the charge is integrated over the range where it is above the noise threshold (solid lines).
Figure 3.19 shows the integrated charge density (red circles) from Figure 3.18 a) and the integrated charge (blue crosses) from Figure 3.18 b) for all micro-bunches in the image.

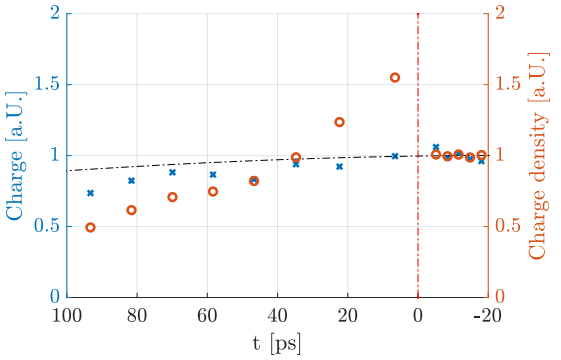

Figure 3.19: Integrated charge density (red circles), integrated charge (blue crosses) and longitudinal incoming bunch charge (density) profile (Gaussian, black dash-dotted line). Here, $\xi_{Seed} = -0.1\,\sigma_\xi$ and $\sigma_\xi = 7.92\,\text{cm} \mathrel{\widehat{=}} \sigma_t = 264\,\text{ps}$.

The results are compared with the incoming bunch charge (density) profile using a Gaussian function with the experimental bunch length and seeding position (black dash-dotted line). All curves are normalized to the value of the average of the five points of the unmodulated bunch head ($t < 0$). The crosses and circles before the plasma ($t < 0$) show the result of the analysis for the unmodulated bunch head. As expected, with constant width, the integration of the charge density and the integration of the charge give the same result to within a constant. Figure 3.19 demonstrates that the charge density of micro-bunches is above that of the incoming bunch charge density for the first two micro-bunches and then decreases rapidly along the bunch. The relative charge per micro-bunch follows well the incoming bunch charge, which means that in this case micro-bunches contain all the charge that was contained in the incoming bunch at their location t along the bunch.

3.2.8 Widths of Defocused Proton Distributions

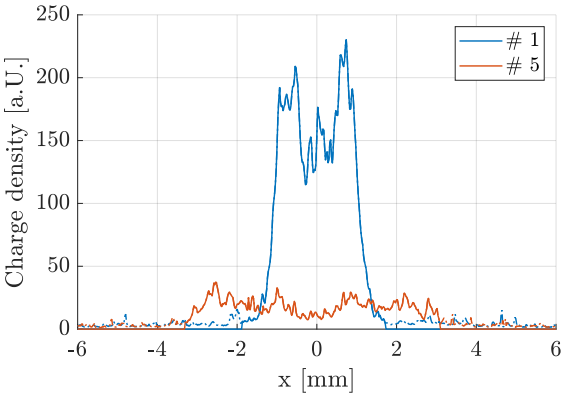

Figure 3.20: Transverse defocused proton distribution of the first (blue line) and fifth (red line) period with the signal above (solid lines) and below (dashed lines) the noise threshold, here 5 [a.U.].

The width of defocused proton distributions are determined from the time-resolved images. As before, the temporal location of defocused proton regions, as determined in Section 3.2.4, are used. The transverse defocused proton distributions are obtained from

the projection over 1.5 ps, centered around the location of defocused proton regions. Figure 3.20 shows that the defocused proton distributions change strongly along the bunch. The charge density of the first period (blue line) is significantly higher than that of the fifth period (red line). Unlike the fifth period, the defocused proton distribution of the first period shows a clear dip in charge density on axis, thus the profile shapes change along the bunch. To avoid taking assumptions on the shape, their width is defined as the rms (root mean square, $\sigma = \sqrt{\frac{1}{n}\sum_i x_i^2}$) of the distribution. For the width determination only the signal above the noise level, here [5 a.U.], is included. The signal above (below) the noise is plotted with solid (dashed) lines.

4 Introduction to Self-Modulation Characterization

The following chapter introduces the physics of SM that are extracted from the time-resolved images of the modulated proton bunch. General parameters of the experiment are summarized. Further, simulation results of the experimental studies are presented and it is shown that they agree well with the measurements. Simulations enable the study of the evolution of the wakefield and bunch modulation along the plasma. Finally, the experimental parameters during the different scans of SM characterization are described.

4.1 Motivation

The self-modulated proton bunch drives a wakefield in plasma, that is used for the acceleration of an injected witness electron bunch. The SM of the proton bunch is the result of the same (transverse) wakefield, experienced by the proton bunch. As we do not have a direct wakefield measurement, instead we analyze the modulated bunch, to understand what transverse wakefield amplitudes the bunch has experienced and thus been driven.

With the streak camera, we acquire time-resolved images of the modulated proton bunch transverse distribution, 3.5 m after the plasma, as shown by the two example stitched images in Figure 4.1. The bunch propagates from left to right, with the bunch interaction with the plasma starting at $t = 0$ (indicated with the red line). One can see that the bunch is indeed unmodulated ahead of the plasma ($t < 0$) and is modulated, i.e. protons are periodically focused and defocused, in the plasma ($t > 0$).

As established in Chapter 3, the proton bunch OTR light enters the streak camera through a slit much narrower than the bunch radius, thus the intensity of images corresponds to the charge density of the proton bunch. I will establish that the decrease in intensity of micro-bunches along the bunch, as particularly visible in image b), comes along with an increase in transverse size of micro-bunches (Section 5.4). These two pieces of information will be used to demonstrate that, while the charge density decreases, the

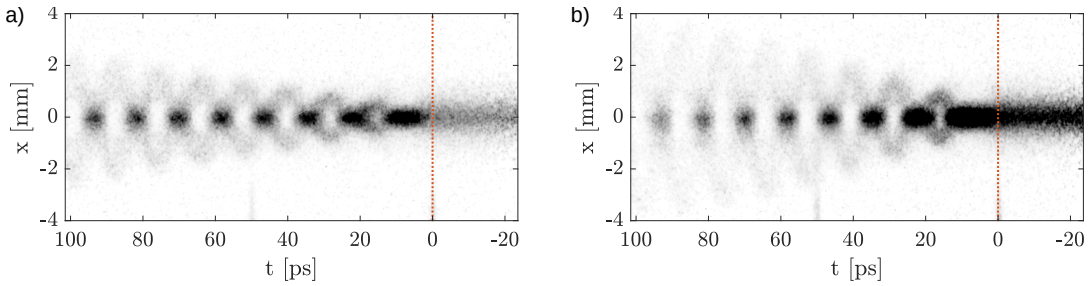

Figure 4.1: Two stitched streak camera images of the modulated proton bunch after plasma. The bunch is propagating from left to right, where the unmodulated head of the bunch propagated through vapor ($t < 0$), the modulated back of the bunch through plasma ($t > 0$). Relativistic ionization front at $t = 0$ (red dotted line). Images are saturated for better visibility of lower charge density defocused proton distributions between micro-bunches. Image a) shows the modulated bunch starting the interaction with plasma at lower ($n_b = 3.1 \cdot 10^{12}\,\mathrm{cm}^{-3}$), image b) with higher ($n_b = 5.6 \cdot 10^{12}\,\mathrm{cm}^{-3}$) initial bunch density. The higher initial bunch density leads to wider defocused proton distributions.

charge per micro-bunch does not necessarily (Section 5.5).

The images show that (excluding the first period behind the RIF, $0 < t < 15\,\mathrm{ps}$) the bunch is modulating with a fixed period. I will demonstrate that the modulation period is determined by the plasma period (Section 5.2). The images also reveal that the first modulation period is always longer than the following ones. I will establish that this is caused by the slippage between the wakefield's phase velocity and the drive bunch velocity (Section 5.1). Quantitative analysis of the images will determine that the micro-bunches further along the bunch are shorter than one quarter of the plasma period (Section 5.3), which is important for an effective driving of the wakefield.

In this thesis, I infer wakefield amplitudes by characterizing the bunch modulation. As in the experiment, images of the modulated bunch are acquired after the plasma, the effect of the integral of the transverse wakefield experienced by the protons over the plasma length is measured. Since focusing fields let particles generally cross the axis, the effect of focusing fields on the protons is not cumulative and only little information can be obtained from transverse profiles of the focused proton distributions (micro-bunches).

I will show that focusing and defocusing wakefields are growing simultaneously along the plasma (Section 4.4). Contrary to focusing fields, the effects of defocusing fields are cumulative. Thus, valuable information about the transverse wakefield can be obtained from characterizing the divergence of protons (Chapter 6): In between the micro-bunches one can see diverging protons that on average experienced defocusing fields along the

plasma. I will show that due to a radially non-linear transverse wakefield, defocused proton distributions diverge in the shape of a ring (in three dimensions). Thus, defocused proton distributions appear hollow near the axis $x = 0$. The radius of the ring increases along the bunch, i.e. defocused protons appear at larger radius further behind in the bunch. This indicates the growth of the transverse wakefield along the bunch.
I will demonstrate that the radius of defocused proton distributions can be controlled with several experimental parameters: Protons are more defocused for larger transverse wakefield amplitudes, as e.g. with lower plasma density or with higher initial bunch density (Sections 6.1 and 6.2). Figure 4.1 demonstrates the effect of an increasing transverse wakefield on the defocused proton distributions. Image a) shows a measurement with low initial bunch density. The smaller transverse wakefield amplitudes lead to smaller radii of defocused proton distributions ($x \approx 2\,\text{mm}$ at $t \approx 100\,\text{ps}$). Image b) shows a measurement with high initial bunch density. The higher transverse wakefield amplitudes lead to larger radii of the distributions ($x \approx 4\,\text{mm}$ at $t \approx 100\,\text{ps}$).
A plasma density gradient has an effect on the defocused proton distributions by decreasing (positive gradient) or increasing (negative gradient) the phase slippage between the transverse wakefield and protons during SM evolution (Section 6.3.1). I will show that the defocused proton distributions can serve as a diagnostic for the wakefield's phase slippage.
I will establish good agreement between simulations and experimental results for all the measurements and then use simulations to study the evolution of focused and defocused protons along the plasma.

4.2 General Experimental Parameters during Self-Modulation Studies

Some general parameters of the experiment are introduced in the following.

Ionization
As explained in Section 2.2, the plasma is created by laser ionization of the Rb vapor. We measure the ionizing laser pulse energy at the last mirror ($\sim 23\,\text{m}$) before the vapor source entrance. A calibrated energy meter measures the light transmission ($\sim 1\,\%$) of a mirror on a single event basis. For all measurements discussed in this thesis, events are only included with a laser pulse energy above 100 mJ, when considered an event with laser pulse, i.e. with plasma.
Simulations predict a plasma radius $> 1.5\,\text{mm}$ for a laser energy $> 70\,\text{mJ}$ over the 10 m

for $n_{pe} = 2.0 \cdot 10^{14}\,\mathrm{cm}^{-3}$ [48], as also suggested by experimental measurements using Schlieren imaging (Section 2.4). Therefore, we consider the plasma radius large enough to assume an infinite plasma for the proton bunch. The effect on the SM evolution of plasma radius variations between $1 - 2\,\mathrm{mm}$ is small, as demonstrated using simulations in the appendix (Section A.10).

Plasma Density

The neutral Rb vapor density is measured with white light interferometry [35] at the vapor source entrance and exit. We assume a $> 99.9\,\%$ ionization fraction of the Rb vapor by the ionizing laser pulse [13] over the entire 10 m, thus it is referred to as plasma density n_{pe} when technically measuring the vapor density throughout this thesis. The density gradient is called positive ($\Delta n_{pe} > 0$), if the density is larger at the plasma exit.
The precise density values for the low ($\sim 0.91 \cdot 10^{14}\,\mathrm{cm}^{-3}$), intermediate ($\sim 2.0 \cdot 10^{14}\,\mathrm{cm}^{-3}$) and high ($\sim 2.9 \cdot 10^{14}\,\mathrm{cm}^{-3}$) plasma density measurements discussed in this thesis are summarized in Table 4.1. It shows the mean values n_{pe} during each measurement, their std variations δn_{pe} and the resulting plasma density gradient Δn_{pe}. The exit density during the scan with higher density was determined only before, not during the measurement. Thus, here the density variations are not determined. During these measurements the density gradient ($\sim 0.1\,\%/\mathrm{m}$) is assumed to be negligible (~ 0) in this thesis. This is justified by the measured effects of a gradient on the SM, throughout gradient measurements discussed in this thesis and in [24].
During gradient measurements, the entrance density is fixed ($\sim 1.8 \cdot 10^{14}\,\mathrm{cm}^{-3}$) and the

Scan	$n_{pe,Entr.}$ [$10^{14}\,\mathrm{cm}^{-3}$]	$\delta n_{pe,Entr.}$ [$10^{14}\,\mathrm{cm}^{-3}$]	$n_{pe,Exit}$ [$10^{14}\,\mathrm{cm}^{-3}$]	$\delta n_{pe,Exit}$ [$10^{14}\,\mathrm{cm}^{-3}$]	Δn_{pe} [%/m]
Low Density	0.912	0.004	0.923	0.005	0.12
Intermediate Density	2.033	0.014	2.043	0.073	0.05
High Density	2.880	0.086	2.912	-	-0.11

Table 4.1: Mean value of the plasma density at the entrance $n_{pe,Entr.}$ and exit $n_{pe,Exit}$, their std variations $\delta n_{pe,Entr.}$ and $\delta n_{pe,Exit}$ and the resulting plasma density gradient Δn_{pe} during the SM studies without deliberately set gradient.

exit density is varied. The mean gradient values Δn_{pe} and the std variations $\delta \Delta n_{pe}$ during these measurements are displayed in Table 4.2.

Δn_{pe} [%/m]	-1.93	-0.94	-0.49	0.01	0.45	0.88	1.29	1.99
$\delta\Delta n_{pe}$ [%/m]	0.03	0.03	0.04	0.03	0.04	0.04	0.04	0.02

Table 4.2: Plasma density gradient mean values Δn_{pe} and std variations $\delta\Delta n_{pe}$ during gradient measurements. Here, the entrance density is fixed to $n_{pe,Entr.} = (1.802 \pm 0.020) \cdot 10^{14}\,\mathrm{cm}^{-3}$.

Incoming Proton Bunch

The incoming population of the proton bunch is measured with a beam current transformer in the extraction line from the SPS ring towards the vapor source for every event. The bunch population for normal operation can be varied between $1 \cdot 10^{11}$ and $3 \cdot 10^{11}$. This thesis shows measurements with a bunch population of $N_{p^+} = (2.82 \pm 0.15) \cdot 10^{11}$ (see Figure 3.7). The effect on the SM from these variations ($\sim 5\,\%$) is expected to be small, as studied with numerical simulations in [49].

The emittance of the bunch is measured with a wire scan in the SPS ring and is expected to decrease when decreasing the bunch population [20]. The effect of a different incoming bunch emittance on the SM is studied in the appendix in Section A.8. Throughout this thesis, we assume the nominal value for the normalized emittance of $\epsilon^* \approx 3.60\,\mu\mathrm{m}$ for $N_{p^+} \approx 3 \cdot 10^{11}$.

The proton bunch is focused onto the entrance of the vapor source. The width is not measured at the waist, thus in this thesis we assume an incoming bunch with Gaussian transverse profile and the nominal value for the width $\sigma_{r,0} \approx 200\,\mu\mathrm{m}$ [50].

The bunch length varies between measurements and is thus determined with the streak camera with the 1 ns time window for each measurement individually. The rms length σ_ξ is 6.6 cm during the plasma density gradient scan. It is 7.9 cm for the low ($0.92 \cdot 10^{14}\,\mathrm{cm}^{-3}$), 9.0 cm for the intermediate ($2.0 \cdot 10^{14}\,\mathrm{cm}^{-3}$) and 7.5 cm for the high ($2.9 \cdot 10^{14}\,\mathrm{cm}^{-3}$) plasma density measurement.

The experimental parameters are summarized in Table 4.3.

4.3 Simulation Setup

Throughout this thesis, the SM results obtained after the plasma from experiments are compared with the ones from simulations. Their good agreement allows the study of the SM evolution along the plasma from simulations.

Parameter	Symbol	Value	Units
Plasma density	n_{pe}	$[0.92\,,\,2.0\,,\,2.9] \cdot 10^{14}$	cm^{-3}
Laser pulse energy	E_γ	> 100	mJ
Plasma radius	r_{pe}	$\gtrsim 1.5$	mm
Bunch population	N_{p^+}	$\sim 2.8 \cdot 10^{11}$	
Normalized bunch emittance	ϵ^*	~ 3.6	µm
Bunch radius	$\sigma_{r,0}$	~ 200	µm
Bunch length	σ_ξ	$6.6\,,\,9.0\,,\,7.9$	cm

Table 4.3: Experimental parameters during SM studies

4.3.1 PIC Codes and QV3D

Numerical codes, simulating plasma-based accelerators, calculate the evolution of beam and plasma particles under the influence of electro-magnetic fields on these particles. Thus, they solve self-consistently the equations of particle motion and Maxwell's equations. In general, there are fluid and Particle-in-cell (PIC) codes. Fluid codes describe the distribution with a single velocity vector (the flow) at every point. They are fast, but only applicable for linear or weakly nonlinear waves.

PIC codes treat the beams and the plasma as a large number of individual macro-particles representing a large number of real particles. Each of these macro-particles has a position and a velocity, allowing the phase-space distribution to be modelled. The particles deposit their charge and current on a grid. Maxwell's equations are integrated to obtain the electro-magnetic fields on the grid, that are interpolated to the particles positions to solve the equations of motions for each particle. While they are computationally expensive, they can be used for highly nonlinear problems. One distinguishes between full PIC codes (e.g. OSIRIS [51] or VLPL [52]) that treat beam and plasma particles equally and quasi-static PIC codes (e.g. QV3D [53]), where the beam evolution is assumed to be slow compared to the plasma oscillations. If the timescale of the beam and plasma evolution ($\propto 1/\omega_\beta$) is slow compared to the characteristic timescale of the modulation ($\propto 1/\omega_{pe}$), the beam and plasma response evolves slowly in the co-moving frame of the beam. They can therefore be treated as equilibrium and the fields are electro-magnetostatic. They are solved as boundary value problem solving backwards from the front of the beam, as opposed to full PIC-codes, solving an initial-value problem, that is subject to the Courant condition, where the maximum time step is linked to the cell size the simulation. This can decrease the computational time of the simulation significantly, especially when simulating relativistic proton beams in a long plasma. The main limitation of the quasi-static approximation is that it does not describe radiation. However, synchrotron radiation

of the heavy proton beam particles can be neglected for our studies.
All simulations in this thesis (Chapter 7 excluded) are performed with the fully three-dimensional quasi-static PIC code QV3D [53], developed on the VLPL platform [52]. They evaluate the current and charge density from beam and plasma distributions. From the current and charge density the fields are calculated. The fields are used to update the beam and the plasma in time steps dt. This code was used to study several related topics of AWAKE [54–56]. The suitability of the quasi-static model for AWAKE was shown, comparing the result from quasi-static PIC codes with the ones from full PIC codes.

4.3.2 Simulation Input Parameters

In the following, the simulation input parameters are introduced and convergence tests of numerical parameters are conducted.

Baseline Parameters for Simulations
We are interested in the bunch density and the wakefield driven by the proton bunch in plasma, obtained from simulations. Similarly to the experiment, the bunch propagates through 10 m of plasma and subsequently 3.5 m of vacuum, the equivalent of the distance between plasma exit and OTR screen in the experiment. Bunch and plasma density distributions and the fields are calculated after every beam time step ($dt = 20\,\mathrm{cm}$).
In the experiment, the longitudinal bunch profile is approximately Gaussian and the plasma-bunch interaction starts within the bunch at the temporal position of the RIF. In the simulations, a uniform plasma is used and instead of simulating the RIF, the proton bunch density profile is cut at a position in time equivalent to that of the RIF in the experiment. Simulation studies have shown that the two methods to trigger the start of the bunch/plasma interactions are equivalent [57]. The initial bunch density profile in the simulations is also Gaussian.
Simulations of the ionization process for the experimental AWAKE setup [48] suggest a plasma radius $r_{pe} > 1.5\,\mathrm{mm}$ and also from experimental measurements using Schlieren imaging (Section 2.4) it is expected that $r_{pe} > 1\,\mathrm{mm}$. In all simulations for the SM characterization, we thus use a plasma radius of $r_{pe} = 1\,\mathrm{mm}$. I show in the appendix (Section A.10) that for an increase of the plasma radius by a factor of two, the results for the transverse wakefield or the divergence of defocused protons over the first five periods as analyzed in this thesis change by $< 10\,\%$, while the longitudinal profile of the bunch is essentially equal.
The baseline parameters of the simulations for the SM analysis in this thesis are summarized in Table 4.4. Here, proton bunch parameters correspond to either the experimentally measured values (bunch population and length, cut position) or the nominal value (bunch

Parameter	Symbol	Value	Value
Plasma density	n_{pe}	$0.92 \cdot 10^{14}\,\mathrm{cm}^{-3}$	
Plasma density gradient	Δn_{pe}	$0\,\%/\mathrm{m}$	
Bunch population	N_{p^+}	$2.8 \cdot 10^{11}$	
Bunch cut	ξ_{Seed}	$-0.1\,\sigma_\xi$	
Initial bunch density	n_b	$5.6 \cdot 10^{12}\,\mathrm{cm}^{-3}$	
Normalized bunch emittance	ϵ^*	$3.6\,\mu\mathrm{m}$	
Plasma radius	r_{pe}	$1\,\mathrm{mm}$	
Bunch radius	σ_r	$200\,\mu\mathrm{m}$	
Bunch length	σ_ξ	$7.92\,\mathrm{cm}$	
Window height	x, y	$\pm 3.9\,\mathrm{mm}$	$\pm 7\,c/w_{pe}$
Window length	z	$3.0\,\mathrm{cm}$	$54\,c/w_{pe}$
Grid size	$\delta x, \delta y$	$10\,\mu\mathrm{m}$	$0.02\,c/w_{pe}$
Grid size	δz	$20\,\mu\mathrm{m}$	$0.04\,c/w_{pe}$
Beam time step	dt	$20\,\mathrm{cm}$	$360\,c/w_{pe}$
Plasma time step		$10\,\mu\mathrm{m}$	$0.02\,c/w_{pe}$
Particles per cell, plasma electrons		4	
Particles per cell, proton bunch on axis		32	

Table 4.4: Baseline input parameters of simulations for SM studies

emittance and radius). The effect of a lower incoming bunch emittance is studied in the appendix (Section A.8). Throughout the thesis, a Gaussian transverse profile of the incoming bunch with a fixed width and waist position at the plasma entrance is assumed. A possible effect of a change in transverse profile, width or waist position on the SM is not presented in this work. The assumption of values for the incoming emittance [58], transverse size or profile and waist position, is expected to be a possible source for deviation of results obtained from simulations and experiment. However, we keep their values unchanged, so that the change in SM or wakefield amplitudes when studying the variation of given experimental parameters is expected to show the desired trends.

Throughout the studies, we vary the plasma density n_{pe}, the density gradient Δn_{pe} or the seed position ξ_{Seed} (position of bunch cut), which changes the initial bunch density n_b, while keeping the remaining parameters constant.

Convergence Tests

In all QV3D simulations presented in this thesis, the numbers of particles per cell, transverse and longitudinal resolution and time step are kept constant to ensure that simulation

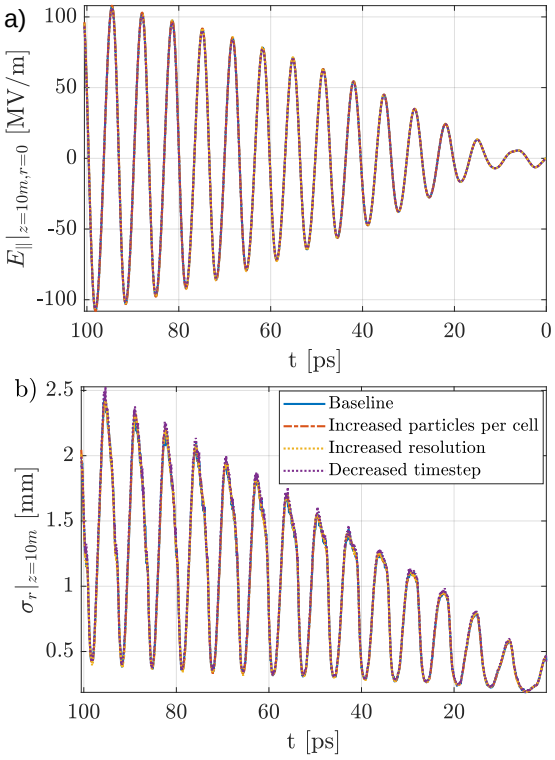

Figure 4.2: a) On-axis ($r = 0$) longitudinal electric field $E_{||}$; b) rms bunch width distribution, both as a function of time t along the bunch (bunch cut at $t = 0$) and at the plasma exit ($z = 10\,\mathrm{m}$). Baseline simulation (blue lines) with particles per cell 4 (plasma electrons) and 32 (on-axis, proton bunch), grid size $\delta x, \delta y = 10\,\mu\mathrm{m}$, $\delta z = 20\,\mu\mathrm{m}$ and time step $dt = 20\,\mathrm{cm}$. Simulation results for particles per cell 16 (plasma electrons) and 128 (on-axis, proton bunch) (red dash-dotted lines), for grid size $\delta x, \delta y = 5\,\mu\mathrm{m}$, $\delta z = 10\,\mu\mathrm{m}$ (yellow dotted line) and for time step $dt = 10\,\mathrm{cm}$ (violet dotted line). Here, $n_{pe} = 2.9 \cdot 10^{14}\,\mathrm{cm}^{-3}$ and bunch parameters from Table 4.4.

results are independent of numerical parameters. In Figure 4.2 it is shown that these numerical parameters are sufficient to describe the physics at hand. I study the longitudinal on-axis field $E_{\|,r=0}$ (Figure a) and the rms bunch width (Figure b), both along the bunch and at the plasma exit $z = 10\,\mathrm{m}$. As higher plasma density, i.e. smaller skin depth, generally requires higher resolution and higher number of particles per cell, the convergence is shown for the highest plasma density discussed in this thesis ($n_{pe} = 2.9 \cdot 10^{14}\,\mathrm{cm}^{-3}$), to ensure the simulation results of all plasma densities use sufficiently high numerical parameters. The other simulation input parameters can be found in Table 4.4.
Here, the baseline simulation (blue lines) corresponds to the simulation with 4 particles per cell for plasma electrons, 32 particles per cell on-axis for the proton bunch (bunch initiated with equal weight of macro-particles, thus decreasing number of macro-particles in x, y) and the values for the resolution and time step from Table 4.4. Figure 4.2 shows that the simulation results do not change when increasing the particles per cell for plasma electrons and protons, both by a factor of four (red dash-dotted lines). Results are also similar when increasing the resolution by decreasing the grid size $\delta x, \delta y, \delta z$, all by a factor of two (yellow dotted lines). Lastly, also when reducing the time step dt by a factor of two (violet dotted lines), the results do not change.

Thus, all four simulations show very good agreement, both in the longitudinal on-axis wakefield and bunch width, both along the bunch, evaluated after the plasma. Therefore, it is concluded that the numerical parameters, such as particles per cell, resolution and time step, as used for the simulations in this thesis, are sufficient for studying the physics of interest.

4.3.3 Convolution of Simulation Results with Experimental Resolution

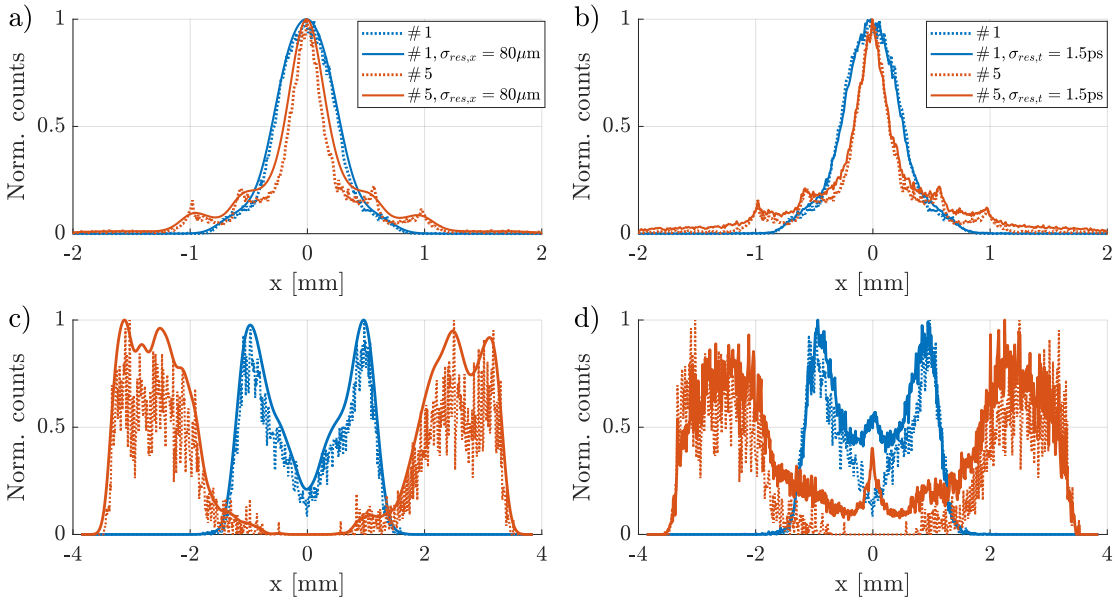

Figure 4.3: Transverse profiles of focused (a, b) and defocused (c, d) proton distributions of the first (blue lines) and fifth (red lines) period of time-resolved images after the plasma in simulations with parameters of Table 4.4. Figures a, c) show the results without (dotted lines) and with (solid lines) spatial $\sigma_{res,x} = 80\,\mu$m Gaussian convolution; Figures b, d) without (dotted lines) and with (solid lines) longitudinal $\sigma_{res,t} = 1.5\,$ps Gaussian convolution. All curves normalized to 1.

The resolution limits of the streak camera images are determined in Section 3.2.1. The resolution impacts the light intensity distribution on the images of the modulated proton bunch. In the following, I study from simulations how the resolution of the experiment is expected to affect the charge density profiles of focused and defocused proton distributions. Therefore, the time-resolved image of the modulated proton bunch at the position of the OTR screen, obtained from simulations (parameters in Table 4.4), is convoluted with the streak camera resolution.

Figure 4.3 shows that transverse profiles of focused (Figure a) and defocused (Figure

c) proton distributions are very similar before (dotted lines) and after (solid lines) convolution with the spatial streak camera resolution. Transverse features analyzed in this thesis (e.g. width of the distribution) are on a larger scale than the spatial resolution. The profiles suggest that the experimentally measured shape and maximum radius of focused and defocused proton distributions for both periods (#1 blue lines, #5 red lines) are essentially not affected by the spatial resolution. Thus, in this thesis the time-resolved images obtained from simulations are generally not convoluted with the spatial resolution. Figure b) compares the focused proton distributions before (dashed lines) and after (solid lines) convoluting the image with the temporal streak camera resolution. It shows that the distributions of focused protons, i.e. micro-bunches, are essentially not affected by the temporal resolution of the experiment. This comes from the significantly lower charge densities of regions temporally surrounding the micro-bunches (defocused proton regions). However, the temporal resolution is crucial for the defocused proton distributions (Figure d), as defocused proton regions are temporally surrounded by regions with much higher on-axis charge density (micro-bunches). As $\sigma_{res,t} \approx 1.5\,\text{ps}$ is on the order of the plasma periods discussed in this thesis ($\tau_{pe} = 6.5 - 11.6\,\text{ps}$), the profiles of defocused proton regions overlap with the ones from micro-bunches, increasing the on-axis charge density significantly, as visible by the on-axis peaks arising after temporal resolution convolution (solid lines in Figure d). This simulation is performed with the lowest plasma density of this thesis (i.e. longest plasma period $\tau_{pe} = 11.6\,\text{ps}$). The impact of temporal resolution is larger than demonstrated here, for measurements with higher plasma density. Unlike the on-axis charge density of defocused proton distributions, the maximum radius is not affected by the temporal resolution, as micro-bunches are significantly narrower and their high charge-density is transversely constrained to a region close to the axis (Figures a, b). In this thesis, I generally compare the experimental results with both the profiles from simulations without and with temporal resolution convolution of the time-resolved images. While the convoluted profiles serve to demonstrate the agreement between experiment and simulations, the original profiles are studied to decouple physics from diagnostic effects.

4.3.4 Comparison Experimental and Simulation Results

Throughout this thesis, I compare experimental results of the SM with results obtained with simulations. This section shows the agreement between experiment and simulations at the position of the OTR screen, 3.5 m after the 10 m of plasma. From their agreement, I conclude that simulations can be used to study the evolution of focused and defocused protons along the plasma/vacuum propagation in order to explain the results measured

at the OTR screen.

Time-resolved images from simulations have a much smaller temporal resolution of approximately the grid size ($\delta z = 20\,\mu m$, i.e. $\delta t = 0.06\,ps$). The simulation results are thus convoluted longitudinally with a Gaussian function with $\sigma_t = 1.5\,ps$, the experimental temporal resolution (Section 3.2.1). As in the previous sections, it is shown that even though the experimental temporal resolution is smaller than the typical modulation period ($\tau = 11.6\,ps$), convoluting the time-resolved images from simulations leads to better agreement between experiment and simulations. Parameters of the simulations can be found in Table 4.4.

Figure 4.4 shows that simulation and experimental time-resolved images contain the same

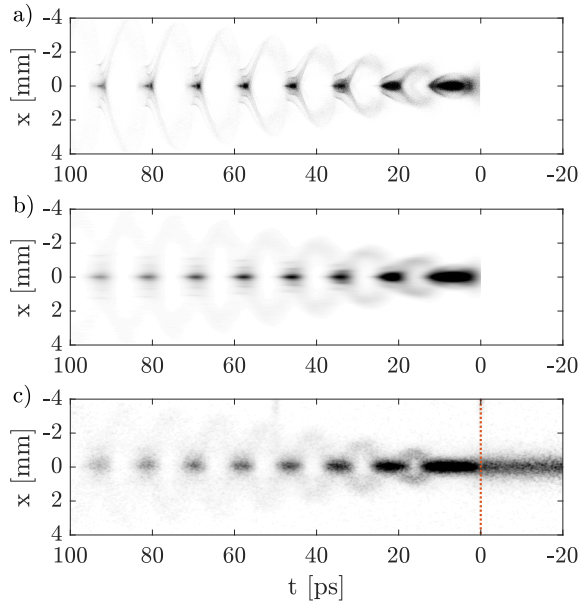

Figure 4.4: Time-resolved images from the simulation (parameters in Table 4.4) without (a) and with (b) Gaussian $\sigma_t = 1.5\,ps$ resolution convolution and from experiment (c). Color scale saturated to 50 % of the maximum value for better visibility of defocused proton distributions.

essential features (micro-bunches, defocused protons regions, etc). One can see that the simulation image convoluted with the streak camera temporal resolution (Figure b) is much more similar to the experimental one (Figure c) than the original one (Figure a). This suggests that finite temporal resolution significantly affects the experimental images. The on-axis bunch charge density of time-resolved images from the simulation is compared with the one from the experiment in Figure 4.5. The bunch density profile from the simulation (light blue line) is much more peaked than that from the experimental image (red line). However, the profile from the simulation image convoluted with the temporal resolution (dark blue line) is very similar to the experimental one. The profiles are used throughout this thesis to determine SM characteristics, as e.g. modulation period, micro-bunch length and more.

In Chapter 6, I analyze the growth of the transverse wakefield along the bunch from the

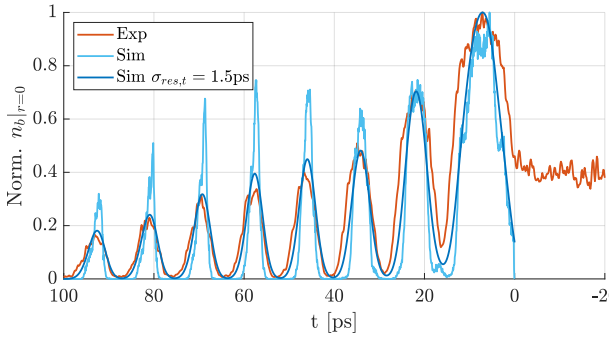

Figure 4.5: Normalized on-axis bunch charge density (projection of $|r| \leq 0.1\,\text{mm}$) of the simulation before (bright blue curve) and after $\sigma_{res,t} = 1.5\,\text{ps}$ Gaussian resolution convolution (dark blue curve) and of the experiment (red curve).

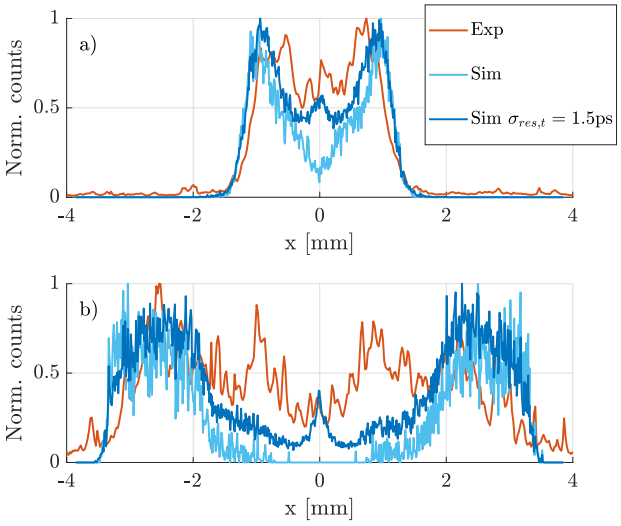

Figure 4.6: Transverse profile of defocused proton distributions of the first (a) and fifth (b) modulation period of the simulation without (bright blue curves), with (dark blue curves) $\sigma_{res,t} = 1.5\,\text{ps}$ Gaussian temporal resolution convolution and from the experiment (red curves). Projection with $\Delta t = 1.5\,\text{ps}$ centered at the location of defocused proton regions determined in Section A.4

transverse profiles of the defocused proton distributions. Thus, in Figure 4.6 the profiles from the simulation are compared with the ones from experiment for the first (Figure a) and fifth (Figure b) modulation period. The profiles from the simulation (bright blue curve without, dark blue curve with temporal resolution convolution) and from experiment (red curve) show a good agreement in terms of maximum radius of defocused proton distributions.

As previously established for the longitudinal charge density profiles (Figure 4.5) the temporal convolution also improves the agreement between simulations and experiment for the transverse profiles of the defocused proton distributions. The overall profiles agree well for the first period (Figure 4.6 a), while there is a higher charge density close to the bunch axis measured in the experiment compared to the simulation further along the

bunch (Figure b).
When using the temporal resolution convoluted image, a narrow peak close to the bunch axis arises (blue line in Figure b). However, the bunch density from simulations corresponds to a transverse narrow bunch slice of the grid size ($\delta x, \delta y = 10\,\mu\text{m}$) at the center of the transverse bunch. For a small spatial misalignment of the bunch signal on the streak camera slit, the on-axis peak is expected to disappear from the profiles, as demonstrated from simulations in the appendix in Section A.5. Further, misalignment of the OTR light with respect to the streak camera slit could increase the charge density close the axis: if the ring of defocused protons is not centered around the slit, it would decrease the measured radius of defocused protons and increase the charge density close the axis. The effect of misalignment is further studied in the appendix (Section A.5). As spatial misalignment is not taken into account in the profiles from simulations in this thesis, it is a possible explanation for small deviations between simulations and experiment.

Overall we see good agreement between simulation and experimental results. I showed that longitudinally and transversely the agreement is improved by convoluting the simulation results with the temporal resolution, as it is measured in the experiment.

4.3.5 Motivation for Experiment/Simulation Comparison

I determine experimentally characteristics of the self-modulation, the focused and defocused protons. The measurements cannot be compared directly to theory, as linear SM only holds for small radial modulation. The experiment was designed to reach full modulation of the proton bunch, i.e. saturation of the SM process, over $\leq 10\,\text{m}$ of plasma. Thus, instead of comparing measurements with linear theory, I compare them with the results from simulations, which also describe the saturation after exponential growth of wakefields.
Good agreement between simulations and experimental results was established in the previous section. Simulations allow the study of the evolution of the SM proton bunch and the wakefield along the plasma and the subsequent propagation in vacuum.
The evolution of time-resolved transverse bunch density profiles along plasma/vacuum propagation is shown in Figure 4.7 with the simulation parameters of Table 4.4. The bunch density is essentially uniform at the beginning of the plasma (incoming bunch, here $z = 0.2\,\text{m}$, closest dump to $z = 0$, Figure a). The bunch is clearly modulated after 5 m (Figure b), with the formation of micro-bunches, high charge density on-axis, and defocused protons in between, starting to diverge from the bunch axis. Defocused protons form rings, corresponding to two peaks in the cylindrical symmetric image. As defocusing fields

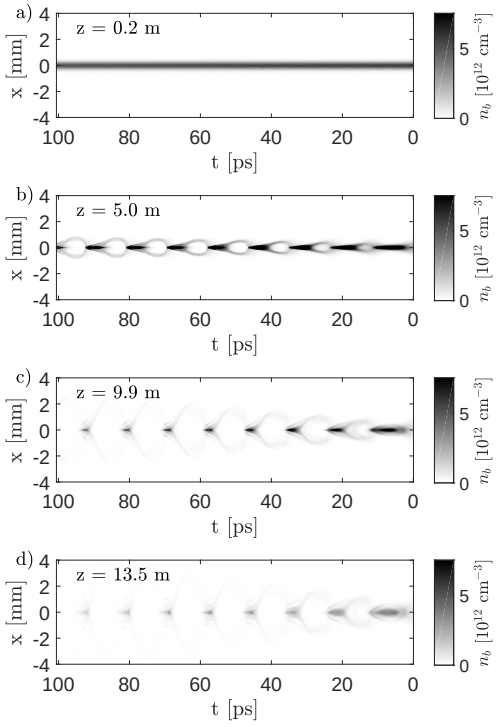

Figure 4.7: Time-resolved images of the proton bunch after 0.2 m, 5.0 m, 9.9 m of plasma (a-c) and subsequent 3.5 m of vacuum propagation after the 10 m of plasma (d) from simulation with parameters in Table 4.4.

are maximum between the micro-bunches (the result of focusing fields), with decreasing defocusing amplitudes closer to the micro-bunches also the radius of the defocused protons ring is maximum between the micro-bunches and decreasing close to the micro-bunches. With further propagation until the plasma exit (10 m, closest simulation dump at 9.9 m, Figure c), defocused protons diverge to larger radii and some radially leave the simulation box further along the bunch. In this thesis, I only analyze defocused proton distributions close to the bunch cut, where protons have not left radially the simulation box. Natural divergence in the subsequent vacuum propagation between $z = 10 - 13.5$ m decreases the overall bunch density, i.e. of focused and defocused proton distributions (Figure d).
The bunch density evolution along the plasma allows the study of the formation of micro-bunches, the divergence of defocused proton distributions and also the evolution of the increasing length of the first modulation period during SM, that lets micro-bunches appear further behind in the bunch along the plasma during SM evolution.

4.4 Transverse Wakefield Evolution

The transverse wakefield $W_\perp$ at the incoming proton bunch radius $r = \sigma_{r,0}$ along the plasma z for the simulation with parameters of Table 4.4 is plotted in Figure 4.8. The curves correspond to the maximum defocusing field ($W_\perp > 0$, solid lines) and maximum

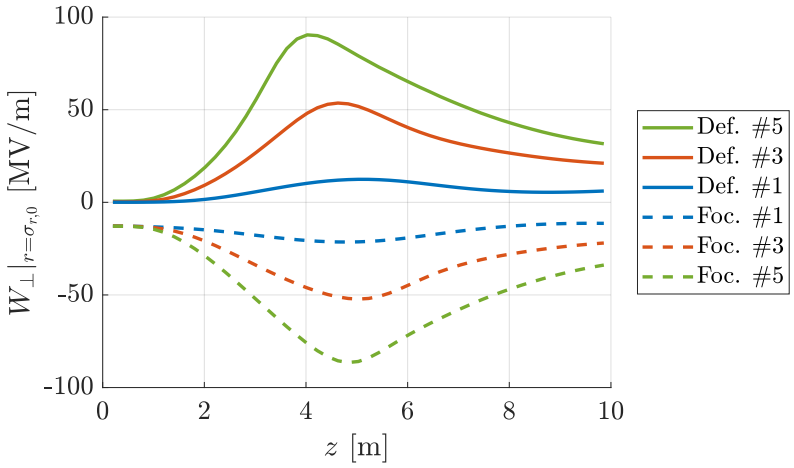

Figure 4.8: Transverse wakefield $W_\perp$ at the incoming proton bunch radius $r = \sigma_{r,0}$ as a function of distance in plasma z. Maximum defocusing fields (solid lines) and maximum focusing fields (dashed lines) over the first (blue lines), third (red lines) and fifth (green lines) modulation period.

focusing field ($W_\perp < 0$, dashed lines) over the first (blue lines), third (red lines) and fifth (green lines) period behind the SM start (bunch cut). The bunch cut here is $\xi_{Seed} = -0.1\sigma_\xi$ behind the bunch center, which leads to the small defocusing field from the start of the plasma ($z = 0$), see Section 1.4. In general, one can see an essentially similar evolution of focusing and defocusing fields in terms of growth ($< 4\,\mathrm{m}$), maximum amplitudes ($\sim 4{-}5\,\mathrm{m}$) and decrease ($> 5\,\mathrm{m}$). Therefore, we can look at either the focusing or the defocusing wakefield to determine the evolution of the transverse wakefield.

4.5 Parameter Scans Performed in Experiment and Simulation

In this thesis, I study the effect on SM such as modulation frequency, micro-bunch size and width of defocused proton distributions, varying experimental parameters that change the wakefield by changing its seed value, growth rate or phase slippage with respect to the driver.

4.5.1 Initial Bunch Density

Throughout this thesis the local on-axis charge density of the bunch at the longitudinal position of the start of the SM (RIF in experiment, bunch cut in simulations) is called "initial bunch density". The initial bunch density can be changed either by varying bunch parameters (population or size), or, a more convenient and consistent way, by moving

the seed position longitudinally along the proton bunch with approximately Gaussian longitudinal charge density profile. A change in initial bunch density changes seed values and growth rate of the wakefield (Section 1.4.6). In experiment, we change the seed position by moving the timing of the ionizing laser pulse, i.e. RIF, with respect to the timing of the proton bunch. In simulations, we cut the proton bunch at a position along the bunch, similar to the laser pulse in experiment. Throughout the thesis, $\xi_{Seed} = 0$ is referred to as the bunch center, positive seed positions ($\xi_{Seed} > 0$) as ahead and negative seed positions ($\xi_{Seed} < 0$) as behind the bunch center. It is shown in the appendix (Section A.11) that for the parameters used in the experiment, SM over the first few modulation periods is essentially independent of the slope of the bunch density. This implies that a seeding ahead or behind with the same distance to the bunch center leads to similar results.

The SM is studied with different initial bunch densities at multiple plasma densities, $n_{pe} = [0.92, 2.0, 2.9] \cdot 10^{14}\,\mathrm{cm}^{-3}$. Due to the longer plasma period (thus as shown later also modulation period), we can benefit from a better relative temporal resolution obtained with low plasma density in the experiment. Therefore, in the following I study the dependency on SM of initial bunch density using the measurement with the lowest plasma density. The parameters of the experiment and the simulations are summarized in Table 4.5.

The time-resolved images of the bunch after the plasma are shown in Figure 4.9, starting

Parameter	Symbol	Units	Experiment	Simulation
Plasma density	n_{pe}	cm^{-3}	$0.92 \cdot 10^{14}$	$0.92 \cdot 10^{14}$
Plasma dens. gradient	Δn_{pe}	%/m	~ 0	0
Bunch population	N_{p^+}		$(2.8 \pm 0.1) \cdot 10^{11}$	$2.8 \cdot 10^{11}$
Bunch length	σ_ξ	cm	7.9	7.9
Seed position	ξ_{Seed}	σ_ξ	$-0.1, 0.4, 0.6, 0.9, 1.1$	$-0.1, 0.4, 0.6, 0.9, 1.1$
Initial bunch density	n_b	cm^{-3}	$[5.6, 5.2, 4.7, 3.7, 3.1] \cdot 10^{12}$	$[5.6, 5.2, 4.7, 3.7, 3.1] \cdot 10^{12}$

Table 4.5: Experimental parameters during SM studies with different initial bunch densities

the SM process at high initial bunch density (Figures a-c) and at low initial bunch density (Figures d-f). Here, Figures (a, d) show the simulation result, Figures (b, e) the temporal resolution convoluted simulation and Figures (c, f) the experimental images.

There is no clear dependency of the modulation frequency or micro-bunch length on initial bunch density visible from the images. They show a decrease in charge density

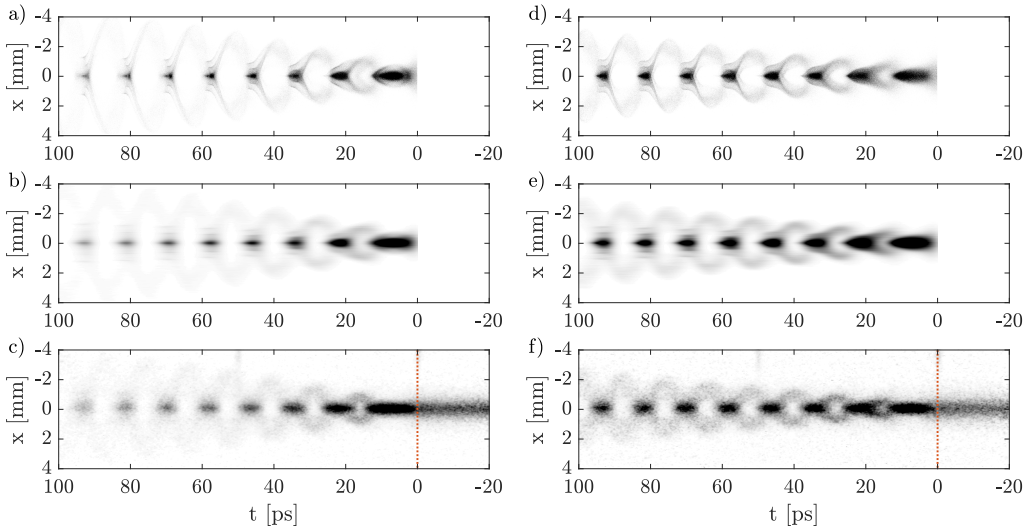

Figure 4.9: Time-resolved images of the bunch after the plasma with initial bunch density $n_b = 5.6 \cdot 10^{12}\,\mathrm{cm}^{-3}$ (a-c) and $n_b = 3.1 \cdot 10^{12}\,\mathrm{cm}^{-3}$ (d-f). Images (a, d) are simulation results without, (b, e) with $\sigma_{res,t} = 1.5\,\mathrm{ps}$ temporal resolution convolution and (c, f) the corresponding experimental images. Color scale saturated to 50 % of the maximum value. Here, $n_{pe} = 0.92 \cdot 10^{14}\,\mathrm{cm}^{-3}$ and $\Delta n_{pe} = 0$.

of micro-bunches along the bunch, more pronounced when seeding at high initial bunch density (Fig a-c). It will be shown later that this comes along with an increase in transverse size and that for both initial bunch densities the charge per micro-bunch is following the longitudinal incoming bunch charge profile (Section 5.5). This means that the charge density decreases proportionally with the transverse size. The images clearly show that defocused proton distributions reach larger distances to the bunch axis, earlier along the SM, for a higher initial bunch density. This is expected from the higher (transverse) wakefield amplitudes for higher initial bunch density and is analyzed in Section 6.1.

4.5.2 Plasma Density

According to Section 1.4.6, for a higher plasma density a lower transverse seed wakefield is expected, but similar growth when evaluated at the respective period behind the seed point. Measurements are performed at different plasma densities. The parameters are summarized in Table 4.6. The table shows that the proton bunch during the experimental measurement with intermediate plasma density is significantly longer (8.9 cm) than for the low (7.5 cm) and high (7.9 cm) plasma densities, while the bunch population is similar. As

we used a similar seed position, relative to the given bunch length, for the measurements at different plasma densities, this results in a lower initial bunch density at the RIF. Thus, the experimental data point with intermediate plasma density is not included for SM analysis that depends on the initial bunch density when analyzing the dependency on plasma density. The initial bunch density at both the low and high plasma density from both experiment and simulations is approximated to $n_b = 5.6 \cdot 10^{14}\,\mathrm{cm}^{-3}$ throughout this thesis for comparison of the effect of the plasma density.
The time-resolved images from simulations and experiment for different plasma densities

Parameter	Symbol	Units	Experiment	Simulation
Plasma density	n_{pe}	cm^{-3}	$[0.92, 2.0, 2.9] \cdot 10^{14}$	$[0.92, 2.0, 2.9] \cdot 10^{14}$
Plasma density gradient	Δn_{pe}	%/m	–	–
Bunch population	N_{p^+}		$[(2.8 \pm 0.1), (2.8 \pm 0.2), (2.8 \pm 0.1)] \cdot 10^{11}$	$2.8 \cdot 10^{11}$
Bunch length	σ_ξ	cm	$7.9, 8.9, 7.5$	$7.9, 9.0, 7.9$
Seed position	ξ_{Seed}	σ_ξ	-0.1	-0.1
Initial bunch density	n_b	cm^{-3}	$[5.6, 5.0, 5.9] \cdot 10^{12}$	$[5.6, 4.9, 5.5] \cdot 10^{12}$

Table 4.6: Experimental parameters during SM studies with different plasma densities.

are shown in Figure 4.10. Generally, the characteristic length of SM is $c/\omega_{pe} \propto n_{pe}^{-1/2}$. In Section 5.2 it is demonstrated that the modulation period (from the third period on) is equal to the plasma period $\tau_{mod} \equiv \tau_{pe} \propto n_{pe}^{-1/2}$. Thus, the images with high plasma density (Figures 4.10 d-f) show a similar number of modulation periods (~ 8) over a shorter ($< 60\,\mathrm{ps}$) time axis as the images with low density over a longer (100 ps) time axis (Figures 4.10 a-c), for both simulations (Figures a, b, d, e) and experiment (Figures c, f). When increasing the plasma density, we expect a decrease in the transverse seed wakefield amplitude (for the density and bunch parameters here from $-6.5\,\mathrm{MV/m}$ to $-5.5\,\mathrm{MV/m}$), as explained in Section 1.4.6. In agreement with this, the time-resolved images show sightly narrower defocused proton distributions for the higher (Figures d-f) than for the lower (Figures a-c) plasma density. The dependency of focused and defocused proton distributions on the plasma density is studied in more detail in Chapters 5 and 6.

4.5.3 Plasma Density Gradient

During the growth of the SM, the wakefield's phase velocity is slower than the velocity of the drive bunch. This can be partly compensated by a slightly increasing plasma

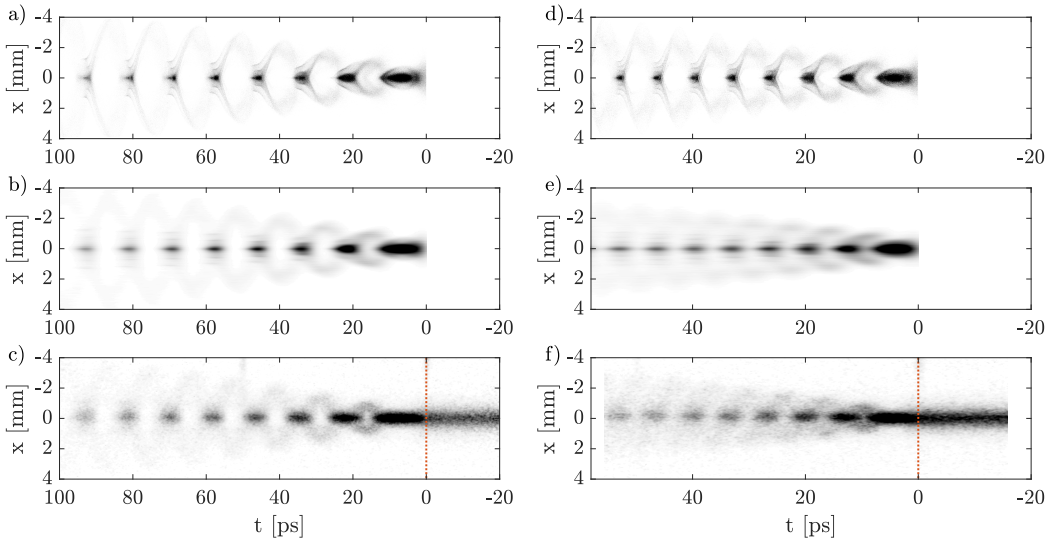

Figure 4.10: Time-resolved images of the bunch after the plasma with plasma density $n_{pe} = 0.92 \cdot 10^{14}\,\mathrm{cm}^{-3}$ (a-c) and $n_{pe} = 2.9 \cdot 10^{14}\,\mathrm{cm}^{-3}$ (d-f). Images (a, d) are simulation results without, (b, e) with $\sigma_{res,t} = 1.5\,\mathrm{ps}$ temporal resolution convolution and (c, f) the corresponding experimental images. Color scale saturated to 50 % of the maximum value. Here, $n_b = 5.6 \cdot 10^{12}\,\mathrm{cm}^{-3}$ and $\Delta n_{pe} = 0$.

density (positive gradient), where the decrease in the local plasma period counteracts the increased period of the driven wakefield. A decreasing plasma density (negative gradient) on the other hand would increase the phase slippage between the wakefield and the proton bunch. The wakefield's phase slippage is expected to influence the radial bunch modulation due to (possibly multiple) passing of focusing and defocusing fields at any position along the bunch. Thus, a plasma density gradient scan is performed to study the effect of the phase slippage on the SM [24].

During the measurements, the plasma entrance density is fixed to $n_{pe,Entr.} = (1.804 \pm 0.004) \cdot 10^{14}\,\mathrm{cm}^{-3}$ and the plasma density at the exit is varied, to obtain a linear gradient along the plasma. The gradient is varied between $-1.9\,\%/\mathrm{m}$ and $+2.0\,\%/\mathrm{m}$, which corresponds to a relative change in density of $-19\,\%$ and $20\,\%$ over the 10 m of plasma. The parameters of the scan used in the experiment and simulations are summarized in Table 4.7. The initial bunch density from both experiment and simulations is approximated to $n_b = 5.6 \cdot 10^{14}\,\mathrm{cm}^{-3}$ throughout this thesis for comparison of the effect of the plasma density gradient. This approximation is justified as the difference in initial bunch here has only a small effect on the SM, as studied in [49] (for bunch parameter variations of $\pm 5\,\%$) and with the initial bunch density scans in Chapters 5 and 6. During the gradient scan the 211 ps streak camera time scale window is used, thus the images

possibly have a slightly lower temporal resolution, here also assumed to be $\sigma_{res,t} = 1.5\,\mathrm{ps}$ for temporal convolution with simulation results.
The time-resolved images of the bunch in Figure 4.11 show clearly the decrease/increase

Parameter	Symbol	Units	Experiment	Simulation
Plasma density entrance	$n_{pe,Entr.}$	cm^{-3}	$1.8 \cdot 10^{14}$	$1.8 \cdot 10^{14}$
Plasma density exit	$n_{pe,Exit}$	cm^{-3}	$[1.5, ..., 1.8, ..., 2.2] \cdot 10^{14}$	$[1.5, 1.8, 2.2] \cdot 10^{14}$
Plasma density gradient	Δn_{pe}	%/m	$-1.9, ..., 0, ..., 2.0$	$-1.9, 0, 2.0$
Bunch population	N_{p^+}		$(3.0 \pm 0.2) \cdot 10^{11}$	$2.8 \cdot 10^{11}$
Bunch length	σ_ξ	cm	6.9	6.9
Seed position	ξ_{Seed}	σ_ξ	0.6	0.6
Initial bunch density	n_b	cm^{-3}	$5.8 \cdot 10^{12}$	$5.4 \cdot 10^{12}$

Table 4.7: Experimental parameters during SM studies with different plasma density gradients

of protons, remaining on-axis for negative (a-c)/positive (d-f) plasma density gradient. This was also reported in [24]. The micro-bunch size and charge is quantified in Sections 5.4 and 5.5. The figures also show that defocused proton distributions reach significantly larger radii with the negative gradient (a-c), as studied in Section 6.3.

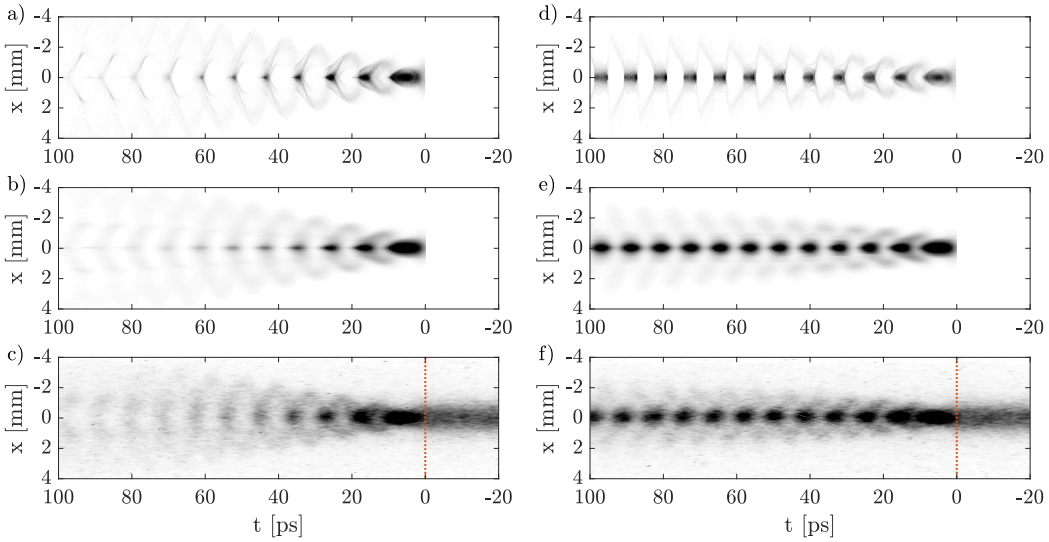

Figure 4.11: Time-resolved images of the bunch after the plasma with plasma density gradient $\Delta n_{pe} = -1.9\,\%/\mathrm{m}$ (a-c) and $\Delta n_{pe} = 2.0\,\%/\mathrm{m}$ (d-f). Images (a, d) are simulation results without, (b, e) with $\sigma_{res,t} = 1.5\,\mathrm{ps}$ temporal resolution convolution and (c, f) the corresponding experimental images. Color scale saturated to 50 % of the maximum value. Here, the plasma entrance density is fixed to $n_{pe,Entr.} = 1.8 \cdot 10^{14}\,\mathrm{cm}^{-3}$ and $n_b = 5.6 \cdot 10^{12}\,\mathrm{cm}^{-3}$.

5 Characterization of the Self-Modulated Proton Bunch Train

As the proton bunch experiences its own wakefield, we can study the SM of the proton bunch to characterize the wakefield it is driving. In the following, I study the modulation frequency along the bunch and establish the dependency on plasma density and/or initial bunch density. I analyze the first modulation period, which is longer than the SM period, to conclude on a slippage between the wakefield's phase and the driver's velocity. I characterize the size and charge of micro-bunches to establish their dependency on wakefield amplitudes and phase evolution. In all studies, the initial bunch density, the plasma density and the plasma density gradient are varied. Throughout the studies the locations of micro-bunches and defocused proton regions are used, as described in Section 3.2.4. The locations for the different scans are summarized in the appendix (Section A.4).

5.1 Length of the First Modulation Period

All time-resolved images presented here, as well as time profiles of the bunch distribution, show that the first micro-bunch, appearing immediately after the seed position (RIF in experiment and bunch cut in simulations), is longer than others, see e.g. Figure 4.1. The evolution of its length along the plasma is studied from simulations.
At the plasma entrance the wakefield driven by the proton bunch over the first few periods is mainly (purely if seeding ahead of the bunch center) focusing, due to the adiabatic response of the plasma to the long bunch, as established from linear wakefield theory in Section 1.4.1. The evolution of the first micro-bunch is shown in Figure 5.1. The on-axis bunch density $n_b|_{r=0}$ (blue lines) is constant when entering the plasma ($z = 0.2\,\mathrm{m}$, closest simulation dump to the start of the plasma (Figure a). Over the first period, the transverse wakefield $W_\perp|_{r=\sigma_r}$ (red lines) is either ~ 0 ($t = \alpha \cdot \tau_{pe}$, $\alpha = 0, 1$) or focusing. The maximum focusing field is half a period behind $t = 0$, the seed position (bunch cut). The focusing field leads to an increase in bunch density at this position along the bunch, as plotted at $z = 2.0\,\mathrm{m}$ (Figure b). The wakefield at higher bunch density leads to a

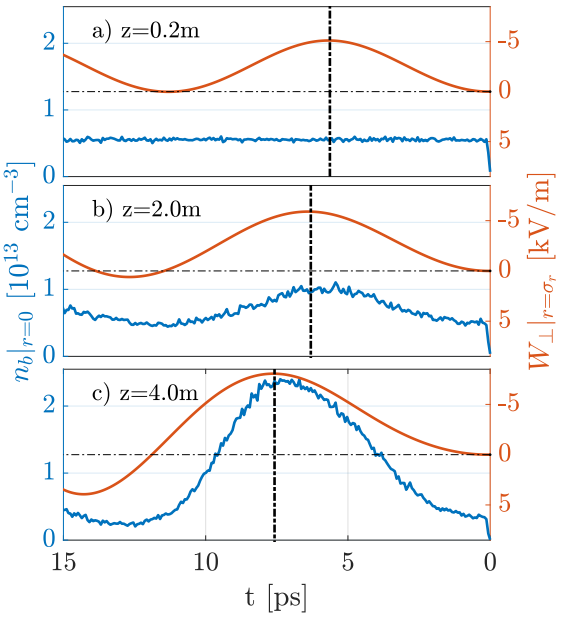

Figure 5.1: On-axis bunch density $n_b|_{r=0}$ (blue lines) and transverse wakefield $W_\perp|_{r=\sigma_r}$ (red lines) over the first modulation/wakefield period after a distance of 0.2 m (a), 2.0 m (b) and 4.0 m (c) in plasma, obtained from the simulation with parameters of Table 4.4, i.e. $\tau_{pe} = 11.6$ ps.

higher contribution of the phase of the wakefield further along the bunch. As the bunch density peak is shifted with respect to the seed position, the phase of the wakefield is shifted as well. The maximum focusing wakefield of the first period (black dash-dotted vertical lines) shifts along the bunch during SM evolution (from Figure a to c). This process reinforces itself until the bunch is fully modulated. This explains the general backward shift of the first focusing wakefield period, together with the peak density of the first micro-bunch along the bunch during SM evolution (see Section 1.4.5).

I study the evolution of the length of modulation periods along the plasma. Here, the minima of the on-axis charge density distribution, i.e. the location of defocused proton regions, are used. The length of the first modulation period is defined as the time distance between the seed position and the first charge density minimum. The lengths of the following modulation periods are defined as the time distance between two minima.

The length evolution along the plasma of the first (res crosses) and fourth (blue squares) modulation period are plotted in Figure 5.2. It shows that the fourth modulation period is constant along the plasma ($\tau_4 = (11.1 \pm 0.2)$ ps) and equal to the plasma period ($\tau_{pe} = 11.1$ ps for $n_{pe} = 1 \cdot 10^{14}$ cm^{-3}, black line). The length of the first modulation period starts with the value of the plasma period ($z \leq 2$ m) and increases significantly during SM. It saturates after 8 m at $\gtrsim 15$ ps. Note that due to the growth of the wakefield along the bunch, the corresponding bunch modulation saturates earlier along the plasma, later in the bunch (see Figure 4.8). The saturation all the way to the first modulation period, verifies that when measuring the time-resolved bunch density after the plasma in experiment and simulations, we study the modulated bunch after saturation.

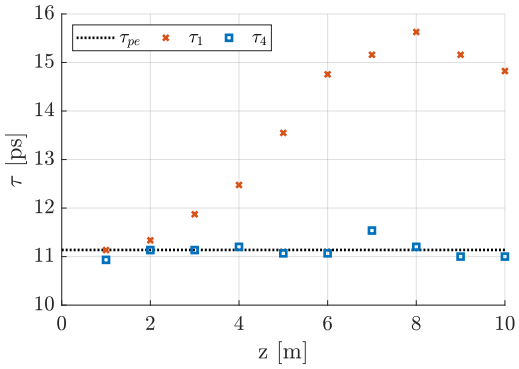

Figure 5.2: Length τ of the first (red crosses) and fourth (blue squares) modulation period as a function of distance in the plasma z, as obtained from simulations (Table 4.4 except $n_{pe} = 1 \cdot 10^{14}\,\mathrm{cm}^{-3}$), compared to the plasma period ($\tau_{pe} = 11.1\,\mathrm{ps}$, black dotted line).

In the following, I determine the lengths of the first modulation periods, as measured after the plasma, i.e. after saturation, and their dependency on initial bunch density, plasma density and plasma density gradient.

Effect of Initial Bunch Density

Theory [22] suggests that the phase of the SM depends on the growth rate of the SM process. As according to linear theory (Section 1.4.6), the growth rate increases with increasing initial bunch density, the first modulation period is analyzed when varying the initial bunch density at the seed position.

Figure 5.3 shows the modulation periods τ from experiments (Figure a) and from simu-

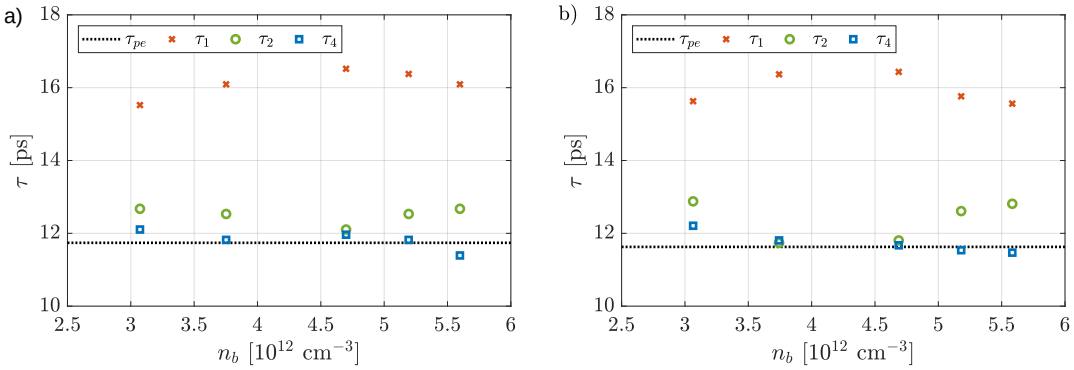

Figure 5.3: Length τ of the first (red crosses), second (green circles) and fourth (blue squares) modulation period as a function of initial bunch density, obtained from experiment (a) and simulations (b, parameters in Table 4.4). The black dotted line shows the plasma period ($\tau_{pe} = 11.6\,\mathrm{ps}$, as $n_{pe} = 0.92 \cdot 10^{14}\,\mathrm{cm}^{-3}$).

lations (Figure b) as a function of initial bunch density n_b. Simulations and experiment agree well in numbers, as also summarized in Table 5.1.

Both experiment and simulation results show that the first modulation period τ_1 (red

Modulation Period	τ_1 [ps]	τ_2 [ps]	τ_4 [ps]
Experiment	16.1 ± 0.4	12.5 ± 0.2	11.8 ± 0.3
Simulation	16.0 ± 0.4	12.4 ± 0.6	11.7 ± 0.3

Table 5.1: Length of the modulation periods $\tau_{1,2,4}$ from experiment and simulations; errors show the rms variation from different initial bunch densities n_b. Here, $\tau_{pe} = 11.6\,\text{ps}$.

crosses) is significantly longer than the following modulation periods, and significantly longer than the plasma period ($\tau_{pe} = 11.6\,\text{ps}$, black dotted line). Also the length of the second modulation period is slightly above the plasma period. Thus, the first and second modulation periods are excluded from modulation period considerations later.
The measured length of the fourth modulation period τ_4 (blue squares) is equal to the value of the plasma period within the determined uncertainty of the experiment and simulations, further studied in Section 5.2. Therefore, the spread observed in the fourth modulation period ($\pm 0.3\,\text{ps}$ in experiment and simulations) is considered as the error in following measurements.
With this method, there is no dependency on the (first) modulation period of the initial bunch density measured, neither in experiments, nor in simulations. Possibly, the effect is too small to be measured with the method of determining defocused proton locations (estimated precision $\pm 0.5\,\text{ps}$) and/or the diagnostic noise/resolution limits. In fact, using Equation 1.10, theory predicts an increase in the phase shift of $< 0.1\,\text{ps}$ for the increasing bunch density, i.e. indeed smaller than the precision of the method. Thus, while the shift of the wakefield with respect to the seed position (RIF or bunch cut) is clearly measurable in experiment and simulations, its dependency on the initial bunch density must be smaller than the variations observed. Further, according to Figure 5.2, the modulation period here is measured after saturation of SM. Thus, a difference in length of the first modulation period during SM growth, as described in theory [22], is possibly not expected after saturation.

Effect of Plasma Density

In the previous section, it was shown that the first modulation period is significantly longer ($\tau_1 = (16.1 \pm 0.4)\,\text{ps}$ in experiment, $\tau_1 = (16.0 \pm 0.4)\,\text{ps}$ in simulations) than the plasma period ($\tau_{pe} = 11.6\,\text{ps}$), as a result of the wakefield's phase shifting from the seed position. It was established from theory (Section 1.4.6) that the growth rate at a given plasma period after the seed position is independent of the plasma density. Thus, phase

dependency from a change in growth rate, as it is described in [22], is not expected. However, as the characteristic length of the modulation and the wakefield is the plasma period, we expect the wakefield's shift, and thus the length of the first modulation period, to be proportional to the plasma period.
The lengths of the first modulation periods as a function of plasma density are shown in

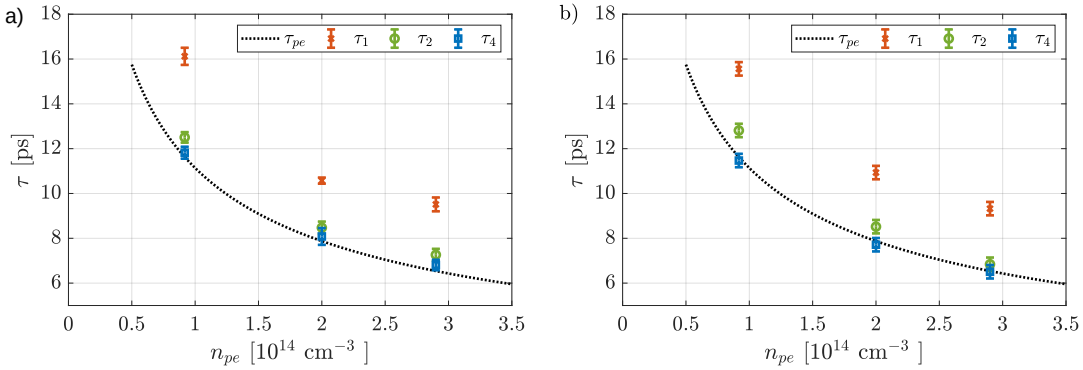

Figure 5.4: Length τ of the first (red crosses), second (green circles) and fourth (blue squares) modulation period as a function of plasma density, obtained from experiment (a) and simulations (b, parameters in Table 4.4). The black dotted line shows the plasma period ($\tau_{pe} = [11.6, 7.9, 6.5]$ ps for $n_{pe} = [0.92, 2.0, 2.9] \cdot 10^{14}\,\mathrm{cm}^{-3}$). The error bars show the rms variation from different initial bunch density measurements in Figure 5.3.

Figure 5.4 from experiment (Figure a) and simulations (Figure b). It was shown in the previous section that the length of modulation periods after the plasma is independent of initial bunch density within the accuracy of the method presented here. Thus, the variations observed in the previous measurement with various initial bunch densities are used as an indication of the errors that can be expected here and they are plotted as uncertainty. For the results from simulations, the absolute uncertainty of the fourth modulation period from the different initial bunch densities at the low plasma density ($n_{pe} = 0.92 \cdot 10^{14}\,\mathrm{cm}^{-3}$), previously determined to ± 0.3 ps, is used. As the temporal resolution in simulations is much smaller than the plasma periods the uncertainty is not expected to change significantly for different plasma densities.
Table 5.2 summarizes the plasma periods τ_{pe} (black dotted line in Figure 5.4) and measured modulation periods for the different plasma densities. This shows that in experiment and simulations, for all plasma densities, the first modulation period τ_1 (red crosses in Figure 5.4) is significantly longer than the plasma period. In the experiment, τ_1 is $\sim [39, 34, 46]$ % and in the simulations τ_1 is $\sim [34, 38, 43]$ % longer than the respective plasma period τ_{pe} for the densities $[0.92, 2.0, 2.9] \cdot 10^{14}\,\mathrm{cm}^{-3}$. Thus for both experiment and simulations, the first micro-bunch is more than one third longer than the plasma

Plasma density	n_{pe} [cm^{-3}]	$0.92 \cdot 10^{14}$	$2.0 \cdot 10^{14}$	$2.9 \cdot 10^{14}$
Plasma period	τ_{pe} [ps]	11.6	7.9	6.5
Mod. period #4 Exp	τ_4 [ps]	11.8 ± 0.3	8.1 ± 0.4	6.8 ± 0.2
Mod. period #4 Sim	τ_4 [ps]	11.5 ± 0.3	7.7 ± 0.3	6.5 ± 0.3
Mod. period #1 Exp	τ_1 [ps]	16.1 ± 0.4	10.6 ± 0.1	9.5 ± 0.3
Mod. period #1 Sim	τ_1 [ps]	15.6 ± 0.3	10.9 ± 0.3	9.3 ± 0.3

Table 5.2: Length of the modulation periods $\tau_{1,4}$ from experiment and simulations and plasma period τ_{pe} for different plasma densities n_{pe}; errors show the rms variation from different initial bunch densities n_b.

period.

This shows that, as expected, the increasing length of the first modulation period scales proportionally with the plasma period. Variations in the proportionality are expected from the accuracy of the procedure.

The lengths of the modulation periods further behind in the bunch correspond to the plasma period at the given plasma density, as shown with the overlap of the fourth modulation period τ_4 (blue squares in Figure 5.4, values in Table 5.2) with the plasma period. This is further studied later, when determining the modulation frequency.

Effect of Plasma Density Gradient

I have established that the length of the first modulation period scales with the plasma density. During the plasma density gradient scan, we change the density over $\pm 20\,\%$ over the 10 m. This corresponds to a change in plasma period of $\pm 10\,\%$. Since SM occurs at least over the saturation length of the process and since the plasma density changes along that process, one may expect that the period of the modulation also changes.

The plasma density gradient leads to a plasma period change from $\tau_{pe,Entr.} = 8.3\,\text{ps}$ to $\tau_{pe,Exit} = 9.2\,\text{ps}\,(7.6\,\text{ps})$ for $\Delta n_{pe} = -1.9\,\%/\text{m}\,(+2.0\,\%/\text{m})$, i.e. $\Delta\tau_{pe} = +0.9\,\text{ps}\,(-0.7\,\text{ps})$. This is very close to the accuracy of the procedure to determine the length of the first modulation period ($\pm 0.3\,\text{ps}$ in experiment for the 73 ps window and $\pm 0.3\,\text{ps}$ in simulations, as established from the initial bunch density scan). During the gradient scan, we use the 211 ps streak camera window. Here, the range in plasma period change $\Delta\tau_{pe}$ at the exit for the two largest gradients of 1.6 ps corresponds to less than four pixels, possibly too small to be measured.

Figure 5.5 shows the length of the first modulation period for different plasma density gradients in experiment (a) and simulations (b). The plasma density is varied at the exit ($\tau_{pe,exit}$, blue dotted line), keeping the density at the entrance constant ($\tau_{pe,Entr.}$, black

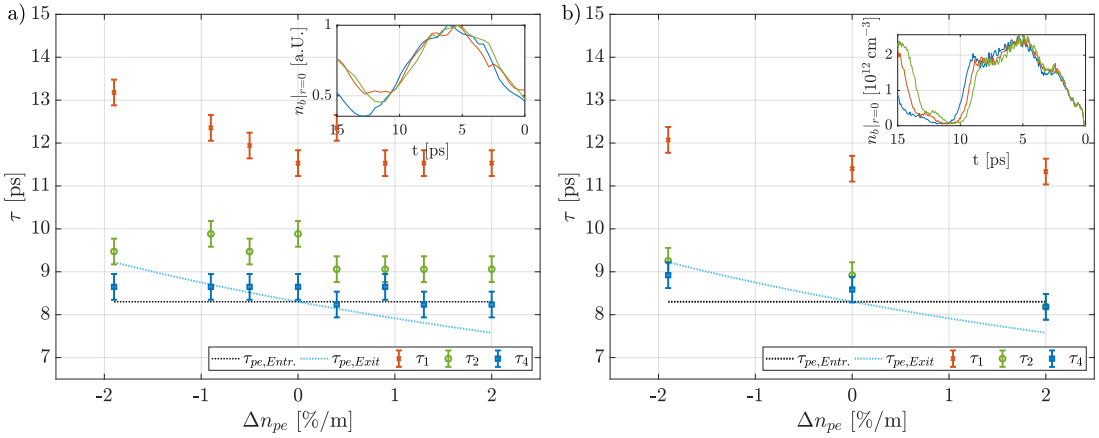

Figure 5.5: Length τ of the first (red crosses), second (green circles) and fourth (blue squares) modulation period as a function of plasma density gradient Δn_{pe}, obtained from experiment (a) and simulations (b, parameters in Table 4.4). The black dotted line shows the plasma period at the entrance ($\tau_{pe,Entr.} = 8.3\,\mathrm{ps}$ for $n_{pe,Entr.} = 1.8 \cdot 10^{14}\,\mathrm{cm}^{-3}$), the blue dotted line at the exit ($\tau_{pe,Exit} = (9.2 - 7.6)\,\mathrm{ps}$ for $n_{pe,Exit} = (1.46 - 2.16) \cdot 10^{14}\,\mathrm{cm}^{-3}$). The error bars show the rms variation from different initial bunch density measurements. Insets: Normalized on-axis charge density of the first modulation period for $\Delta n_{pe} = -1.9\,\%/\mathrm{m}$ (blue lines), $\Delta n_{pe} = 0$ (red lines) and $\Delta n_{pe} = 2.0\,\%/\mathrm{m}$ (green lines).

dotted line).

The values for the plasma period and the measured first and fourth modulation periods are summarized in Table 5.3. Together with Figure 5.5, it demonstrates, as also previously established without gradient, that the first modulation period (red crosses) is consistently longer than the plasma period after the plasma, for all gradients.

The modulation periods also indicate a trend towards shorter lengths with more positive density gradient, in experiment and simulations, see Table 5.3. However, due to the accuracy of the method, the result is not sufficient to prove the trend. The error bars in Figure 5.5 show that the accuracy of the method is on the order of the expected change in modulation length from the change in plasma period.

The small difference in length of the first modulation periods is determined with a procedure (determination of the defocused proton regions) with a precision ($\sim \pm 0.5\,\mathrm{ps}$) expected to be close to the value to be measured. The insets therefore show the normalized on-axis bunch density over the first modulation period. It indeed shows a decrease in length from negative gradient (blue curve) over constant density (red curve) to positive gradient (green curve).

The fourth modulation period (blue squares), with the same absolute error as the first

Plasma density gradient	Δn_{pe} [%/m]	-1.9	0	2.0
Plasma period exit	$\tau_{pe,Exit}$ [ps]	9.2	8.3	7.6
Mod. period #4 Exp	τ_4 [ps]	8.6 ± 0.3	8.6 ± 0.3	8.2 ± 0.3
Mod. period #4 Sim	τ_4 [ps]	8.9 ± 0.3	8.6 ± 0.3	8.2 ± 0.3
Mod. period #1 Exp	τ_1 [ps]	13.2 ± 0.3	11.5 ± 0.3	11.5 ± 0.3
Mod. period #1 Sim	τ_1 [ps]	12.1 ± 0.3	11.4 ± 0.3	11.3 ± 0.3

Table 5.3: Length of the modulation periods $\tau_{1,4}$ from experiment and simulations and plasma period at the plasma exit $\tau_{pe,Exit}$ for different plasma density gradients Δn_{pe}; errors show the rms variation from different initial bunch density measurements in Figure 5.3.

modulation period, does not show a clear trend in decreasing length with increasing plasma density gradient, in experiment or simulations. A frequency change with plasma density gradient along the bunch is further studied later (Section 5.2), taking advantage of the accumulative effect of a frequency change along the bunch.
Overall, the decrease in length of the first modulation period is in agreement with the general increase in modulation frequency when increasing the plasma period. This is further studied in the following section.

5.2 Modulation Frequency

The radial modulation of the bunch is the result of the transverse wakefield that is focusing and defocusing along the long bunch. As the wakefield frequency is expected to be the plasma frequency ($f_{pe} \propto {n_{pe}}^{1/2}$), we also expect the modulation frequency to be equal to the plasma frequency ($f_{Mod} = f_{pe}$), i.e. determined by the plasma density. This was experimentally shown in [13] when changing the plasma density over a wide range (factor ~ 10). In the following, the modulation frequency is determined from the micro-bunch positions in time, as opposed to from the DFT of the bunch train profile, as used in [13]. When comparing the positions of early with late micro-bunches, the effect of small phase shifts adds up with every period and can thus be detected with this method regardless the temporal resolution of the streak camera being close to the plasma period. The measured modulation frequency is compared with the plasma frequency for various plasma densities.
According to theory [22], the wakefield's phase velocity is changing along the modulated bunch due to the increasing wakefield growth. Wakefield amplitudes are higher for higher initial bunch density due to larger seed values and larger growth rate (Section 1.4.6).

With the SM as a result of the transverse wakefield, this implies that theory suggests a correlation of the modulation frequency with the initial bunch density, but possibly on a scale smaller than the method's precision, thus not measurable.
With a plasma density gradient, the plasma frequency is changing along the plasma z (i.e. $f_{pe}(z) \propto n_{pe}(z)^{1/2}$). From the DFT of the signal the modulation frequency was determined as a value between the plasma frequencies at the entrance and the exit of the plasma [24]. In the following, the modulation frequency is also determined with density gradient, using the method of this work.
The method's uncertainty for the modulation frequency determination comes from the determination of micro-bunch locations, here estimated from the profiles in the appendix (Section A.4) as $\sigma = 0.5\,\text{ps}$ (std). As it was established that the first two modulation periods are longer than the ones further along the bunch (Section 5.1), the first two micro-bunches are excluded from the modulation frequency determination.

Effect of Plasma Density

Figure 5.6 shows the determination of the modulation frequency from experiment (Figures a-c) and from simulations (Figures d-f). The micro-bunch location t is plotted versus micro-bunch number for low (blue crosses), intermediate (red circles) and high (green squares) plasma density for the data from experiment (Figure a) and simulations (Figure d). To determine the modulation frequency, a linear fit is applied to the data of micro-bunch #3 to #7-8, shown with the dash-dotted lines of the respective colors. The micro-bunch locations along the bunch (symbols in a, d) follow well the linear fit (dash-dotted lines in a, d). This demonstrates that the modulation frequency is constant along the part of the bunch from micro-bunch #3 to #7-8.
The fits' slopes give the modulation frequency. In Figures (b) and (e) the modulation frequencies (blue crosses) are compared to the plasma frequencies (red curve). Their overlap confirms that the modulation frequency matches the plasma frequency, as also shown in [13]. The difference between the modulation and plasma frequency is plotted in Figures (c) and (f). The deviation between modulation and plasma frequency, for all plasma densities measured, is less than 1 GHz in experiment (c) and less than 2 GHz in simulations (f). Interestingly, it is observed in both experiment and simulations, that the modulation frequency is slightly below the plasma frequency. However, the plasma frequency f_{pe} is within the error bars (from a micro-bunch location std uncertainty of 0.5 ps) of f_{Mod} in experiment and simulations. These results are in agreement with those from single period length measurements (fourth modulation period in

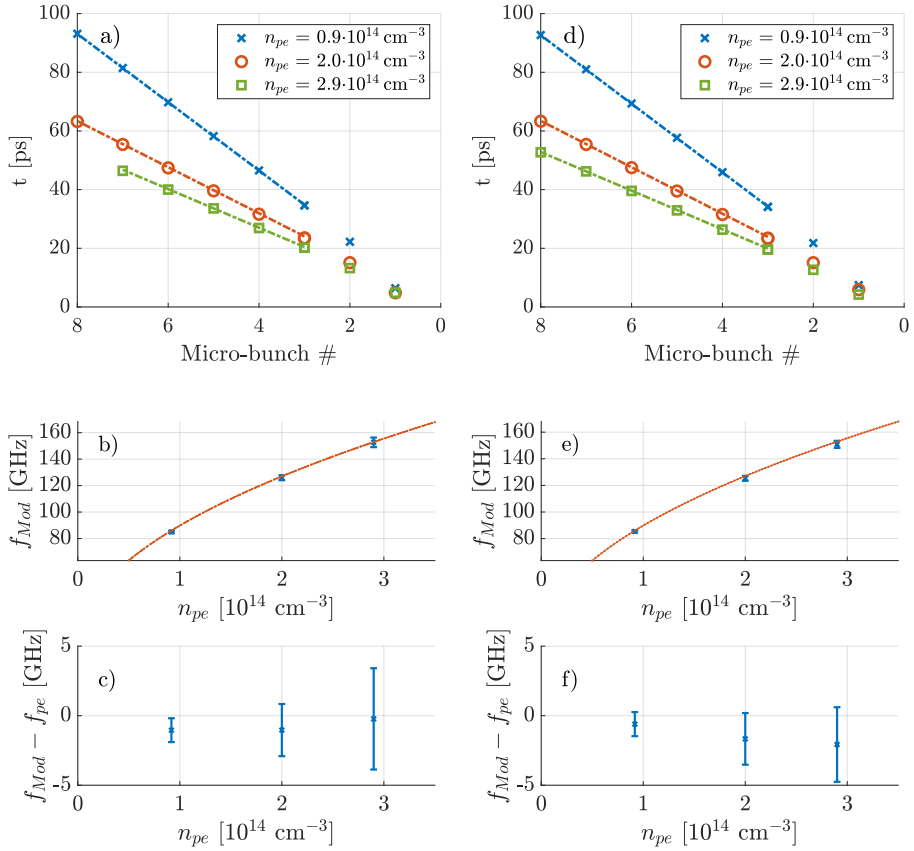

Figure 5.6: Modulation frequency determination from experiment (a-c) and simulations (d-f). Images (a, d) micro-bunch locations (see appendix, Section A.4) for plasma densities $n_{pe} = [0.9, 2.0, 2.9] \cdot 10^{14}\,\mathrm{cm}^{-3}$ (blue crosses, red circles, green squares) and their linear fit (dashed lines). Images (b, e) modulation frequency f_{Mod} from the slope of the fit (blue crosses, error bar for a micro-bunch location std uncertainty of 0.5 ps) versus plasma density and the corresponding plasma frequency (red line). Image (c, f) difference between modulation and plasma frequency for the various plasma density measurements.

Figure 5.4). The modulation frequency is consistently slightly below the plasma frequency.

Effect of Initial Bunch Density

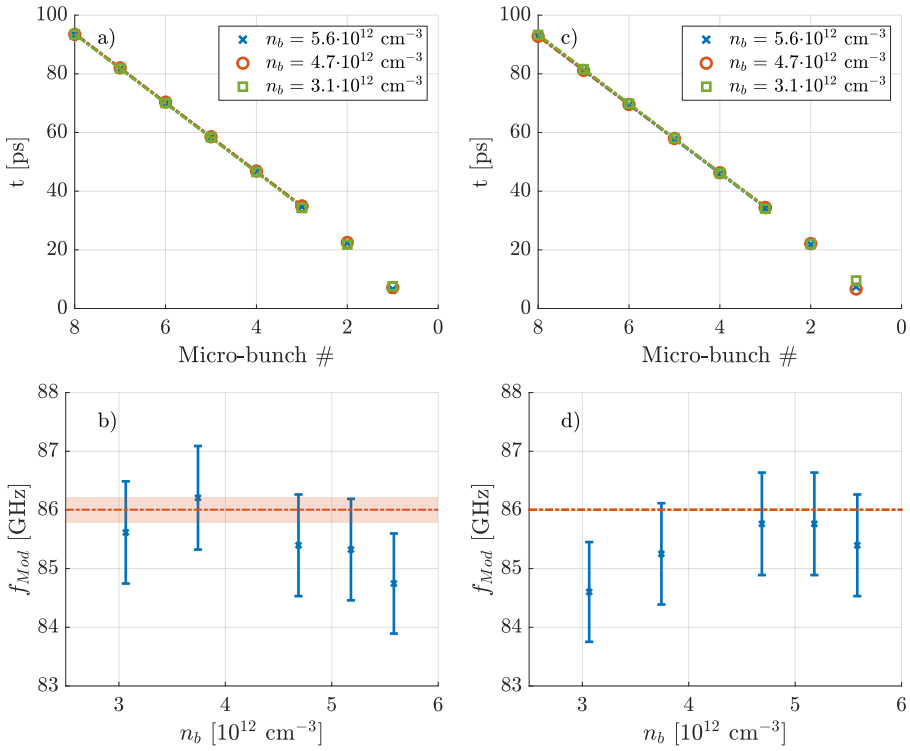

Figure 5.7: Modulation frequency determination from experiment (a, b) and simulations (c, d). Images (a, c) micro-bunch locations (see appendix, Section A.4) for initial bunch densities $n_b = [5.6, 4.7, 3.1] \cdot 10^{12}\,\mathrm{cm}^{-3}$ (blue crosses, red circles, green squares) and their linear fits (dashed lines). Images (b, d) modulation frequency f_{Mod} from the slopes of the fits (blue crosses, error bar for a micro-bunch location std uncertainty of 0.5 ps) versus initial bunch density and plasma frequency $f_{pe} = 86.0\,\mathrm{GHz}$ for $n_{pe} = 0.9175 \cdot 10^{14}\,\mathrm{cm}^{-3}$ (red line). The error of the plasma frequency in experiment (b) results from the Rb density measurement precision of $< 0.5\,\%$.

In Figure 5.7, the modulation frequency of the bunch, measured in the experiment (Figures a, b) and in simulations (Figures c, d), is determined for different initial bunch densities by varying the seed position. The micro-bunch locations appear to overlap for the different initial bunch densities both in experiment and simulations. As in the case of different plasma densities, there is no deviation from the linear fit visible, thus there is no frequency change along the bunch larger than the precision of the measurement between micro-bunch

#3 and #8.
The modulation frequency f_{Mod} from the fits' slopes is plotted in the bottom images (blue crosses). It is compared to the plasma frequency ($f_{pe} = 86.0\,\text{GHz}$, red line, shaded area gives the uncertainty from the Rb density measurement precision $< 0.5\,\%$ [59]). The modulation frequency is close to the plasma frequency ($f_{pe} - f_{Mod} \approx 1\,\text{GHz}$, i.e. $\sim 1\,\%$ of f_{pe}) in both experiments and simulations. Except for one data point, the modulation frequency is slightly below the plasma frequency for all initial bunch densities, in experiment and simulations. This is in agreement with the results presented in Figure 5.6.
The data from experiment and simulations show no trend for the increasing initial bunch

Initial bunch density	n_b [cm^{-3}]	$3.1 \cdot 10^{12}$	$5.6 \cdot 10^{12}$
Modulation frequency Exp	f_{Mod} [GHz]	85.6 ± 0.9	84.7 ± 0.9
Modulation frequency Sim	f_{Mod} [GHz]	84.6 ± 0.9	85.4 ± 0.9

Table 5.4: Modulation frequency f_{Mod} for different initial bunch densities, from experiment and simulations; errors from the 0.5 ps std uncertainty for micro-bunch locations. Here, $f_{pe} = 86.0\,\text{GHz}$ ($\pm 0.2\,\text{GHz}$ in experiment).

density within the measurement's precision, as summarized in Table 5.4.
Therefore, we conclude that if the modulation frequency changes along the bunch or with initial bunch density, variations are smaller than the method's precision ($\sim 1\,\text{GHz}$, i.e. $\sim 1\,\%$ of f_{pe}). In fact, Equation 1.10 from theory [22] predicts a decrease in frequency of $\Delta f = 1.2\,\text{GHz}$ for the increasing initial bunch density, thus a change very close to the method's determined uncertainty.
Further, the modulation (i.e. wakefield) frequency being independent of the initial bunch density analyzed here demonstrates that the restoring force on displaced, oscillating plasma electrons is dominated by the decrease in on-axis plasma electrons, as opposed to the positive charge of the drive bunch. This is expected to be a result of the proton bunch density being significantly smaller than the plasma density.

Effect of Plasma Density Gradient

When changing the plasma density gradient by $\sim \pm 2\,\%/\text{m}$, the plasma frequency ($\propto {n_{pe}}^{1/2}$) changes over the 10 m by $\sim \pm 10\,\%$, larger than the precision of the measurement, previously determined. Thus, in the following, the bunch modulation frequency is determined with plasma density gradient in experiment and simulations.
The top images in Figure 5.8 show the distance in time from the seed position of the first eighth micro-bunches from experiment (a) and simulations (c) for various plasma density gradient values. In total eighth density gradient values are measured in experiment,

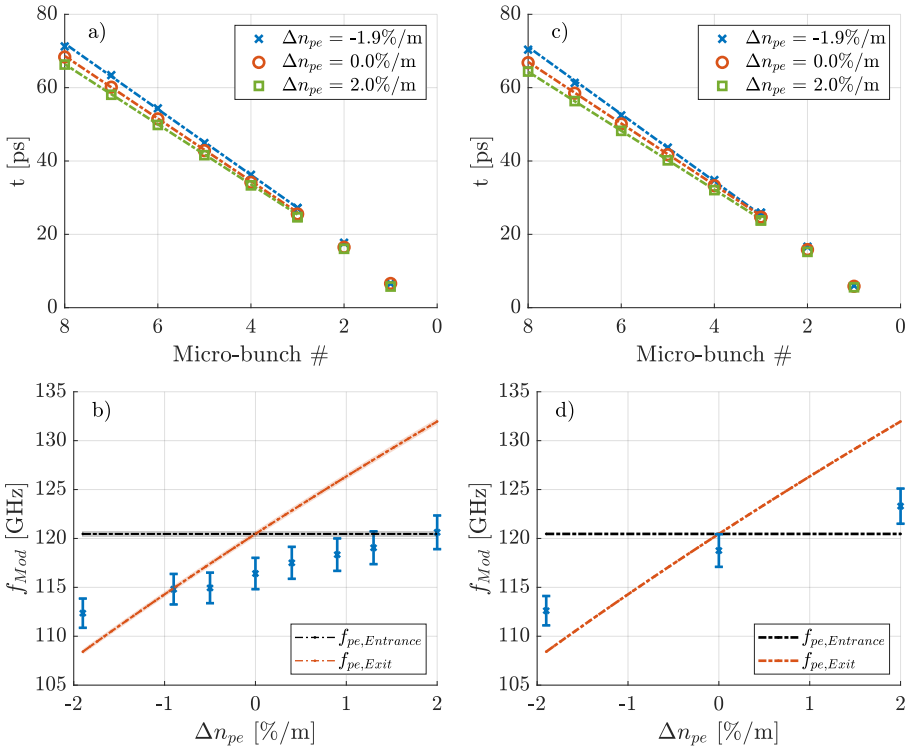

Figure 5.8: Modulation frequency determination from experiment (a, b) and simulations (c, d). Images (a, c) micro-bunch locations (see appendix, Section A.4) for plasma density gradients $[-1.9, 0, 2.0]$ %/m (blue crosses, red circles, green squares) and their linear fit (dashed lines). Images (b, d) modulation frequency f_{Mod} from the slope of the fit (blue crosses, error bar for a micro-bunch location std uncertainty of 0.5 ps) versus density gradient $[-1.9, (-0.9), (-0.5), 0, (0.4), (0.9), (1.3), 2.0]$ %/m (values in brackets only in experiment) and plasma frequency at the entrance $f_{pe,Entr.} = 120.5$ GHz for $n_{pe} = 1.8 \cdot 10^{14}\,\mathrm{cm}^{-3}$ (black line) and exit $f_{pe,Exit} = 108.4 - 132.0$ GHz for $n_{pe} = 1.46 - 2.16 \cdot 10^{14}\,\mathrm{cm}^{-3}$ (red line).

while (a) displays the measurements with most negative (blue crosses), most positive (green squares) and without (red circles) density gradient. The micro-bunch positions are linearly fitted (dashed lines) and their frequencies are determined from the fit's slope. As with changing initial bunch density or changing plasma density, the data overlaps well with the fit over the micro-bunches $\#3 - 8$, i.e. there is no change in frequency along the bunch measured with the precision of this procedure. However, the positions of the micro-bunches consistently shift backwards (larger t) with the more negative gradient, as shown by the data points and their fits not overlapping for the different gradient values. Therefore, the modulation frequency is determined as a function of the gradient value

Plasma density gradient	Δn_{pe} [%/m]	-1.9	0	2.0
Modulation frequency Exp	f_{Mod} [GHz]	112.4 ± 1.5	116.4 ± 1.6	120.6 ± 1.7
Modulation frequency Sim	f_{Mod} [GHz]	112.6 ± 1.5	118.8 ± 1.6	123.3 ± 1.8

Table 5.5: Modulation frequency f_{Mod} for different plasma density gradients, from experiment and simulations; errors from the 0.5 ps std uncertainty for micro-bunch locations. Here, $f_{pe,Entr.} = 120.5\,\text{GHz}$ and $f_{pe,Exit} = [108.4, 132.0]\,\text{GHz}$ for $\Delta n_{pe} = [-1.9, 2.0]\,\%/\text{m}$.

from experiment (b) and simulations (d). On the same figures, the constant plasma entrance frequency (black line) and the plasma exit frequency (red line) are plotted. The modulation frequency is in-/decreasing with in-/decreasing density gradient from the no gradient case in experiment and simulations, see also Table 5.5. The change in frequency from the entrance plasma frequency (120.5 GHz) is larger for negative gradients than for positive gradients. This general behavior is in agreement with results presented in [24], where it is explained that a stronger dephasing is expected for a bunch train with more on-axis charge (positive gradient).
Experimental results (Figure 5.8 b) indicate that the modulation frequency saturates for large plasma density gradients, where modulation and local plasma frequency become non-resonant.

5.3 Micro-Bunch Length

Considering linear theory with a drive bunch or train with square longitudinal density profile, the strongest wakefield would be driven by micro-bunches filling one quarter of the period, the focusing and decelerating phase. Micro-bunches produced by SM are not expected to be square and appear with Gaussian longitudinal profiles in the experiment. Thus, the optimum length is not well defined. In general, the more charge in the focusing

and decelerating field and the less in the focusing but accelerating phase, the better for driving the wakefield: Focusing to avoid divergence and keeping a high charge density; decelerating to give the energy to the wakefield without transferring energy back to the protons in the accelerating phase.
Figure 5.9 shows a simplified schematic of a train of Gaussian micro-bunches (red line)

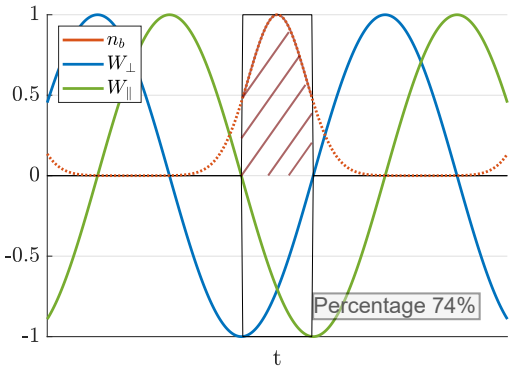

Figure 5.9: Schematic of a train of Gaussian micro-bunches (n_b red line) in a linear wakefield approximated with cosine functions ($W_\perp$ blue line, negative for focusing, $W_\parallel$ green line, negative for decelerating) with wakefield period τ_{cos}. A micro-bunch length of $\sigma_t = 0.1\,\tau_{cos}$ results in 74 % of the charge in one quarter of the wakefield period τ_{cos}.

in a linear transverse ($W_\perp$ blue line) and longitudinal ($W_\parallel$ green line) wakefield, both approximated with a cosine function with wakefield period τ_{cos}, all normalized to 1. Here, the micro-bunch length is $\sigma_t = 0.1\,\tau_{cos}$. As a result, 74 % of the micro-bunch charge resides in one quarter of the wakefield period, the focusing ($W_\perp < 0$) and decelerating ($W_\parallel < 0$) phase. Note that here the micro-bunch phase was set to be in the center of the desired phase. This simplified calculation should give an idea of the percentage of micro-bunch charge, that contributes to driving the wakefield effectively, for a micro-bunch of a given length with optimized phase.

In the following, I determine the length of the Gaussian micro-bunches in the experiment and compare it with that of the micro-bunches from simulations. I quantify the percentage of charge effectively driving the wakefield, if in the right phase, from their length. I analyze the dependency of micro-bunch length on experimental parameters and whether their length is constant along the bunch. The length is expected to be proportional to the plasma period, thus changing with varying plasma density (gradient), since, as I showed before, the modulation period changes with plasma density (gradient). If the modulation is fully saturated, as it can be expected after 10 m of plasma (see e.g. Figure 5.2), we expect it to be independent of the strength of driving the wakefield, thus of the initial bunch density.
For this analysis, the on-axis micro-bunch profiles $n_b|_{r=0}$ are generated by averaging the

time-resolved bunch density images from experiment and simulations over a range of ± 0.1 mm around the bunch axis. Then, Gaussian functions are fitted to each micro-bunch (further explained in Section 3.2.5). For the fitting, the peak position of the micro-bunch fits are fixed to the micro-bunch locations (summarized in the appendix, Section A.4) and their amplitudes are fixed by the micro-bunch charge density value at their positions. Thus, the only free parameter is their width, in order to determine the micro-bunch length. Data (Figures 5.10, 5.12 and 5.14) shows that this fit choice describes the profiles well. As previously, the analysis focuses on the results from the third micro-bunch on, as the lengths of the first two modulation periods are longer than the plasma period. To ensure a large enough on-axis density further along the bunch together with a similar number of analyzed micro-bunches from measurements with different experimental parameters for better comparability, the length is determined up to the seventh micro-bunch.

Effect of Initial Bunch Density

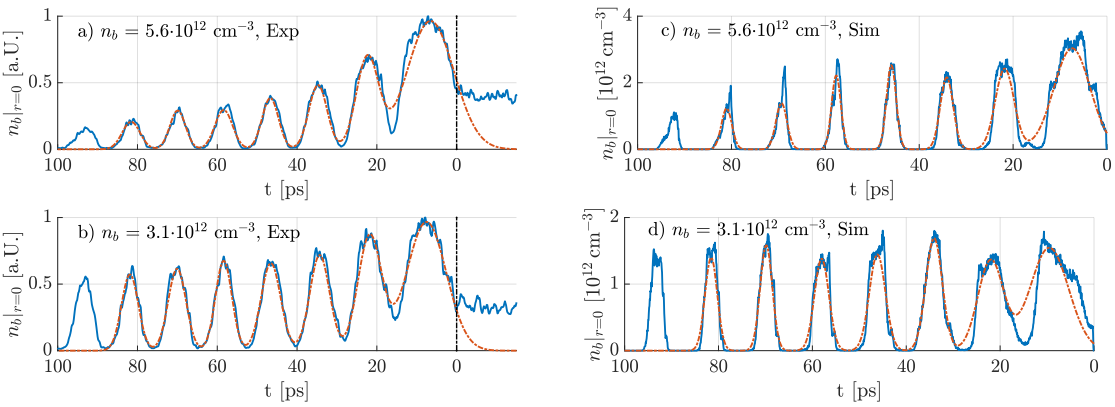

Figure 5.10: On-axis charge density (blue curves) with Gaussian fits to each micro-bunch (red curves) for initial bunch density $n_b = 5.6 \cdot 10^{12}\,\mathrm{cm}^{-3}$ (a, c) and $n_b = 3.1 \cdot 10^{12}\,\mathrm{cm}^{-3}$ (b, d), experimentally (a, c) and from simulations (b, d). Here, $n_{pe} = 0.9 \cdot 10^{14}\,\mathrm{cm}^{-3}$ and $\Delta n_{pe} = 0$.

Figure 5.10 shows that the Gaussian fits (red curves) describe well the on-axis charge density profiles (blue curves) for the high (a, c) and low (b, d) initial bunch density over the periods $\#3 - 7$, in the experiment (a, b) and in simulations (c, d). Figure 5.10 also shows that the micro-bunch amplitude decreases faster along the bunch in the high (a, c) than in the low initial bunch density (b, d) case.

The rms length of each micro-bunch from the fits for three initial bunch densities, for experiment (Figure a) and simulation (Figure c) profiles, is plotted in Figure 5.11. In both cases, the first and second micro-bunch length duration is longer that that of the

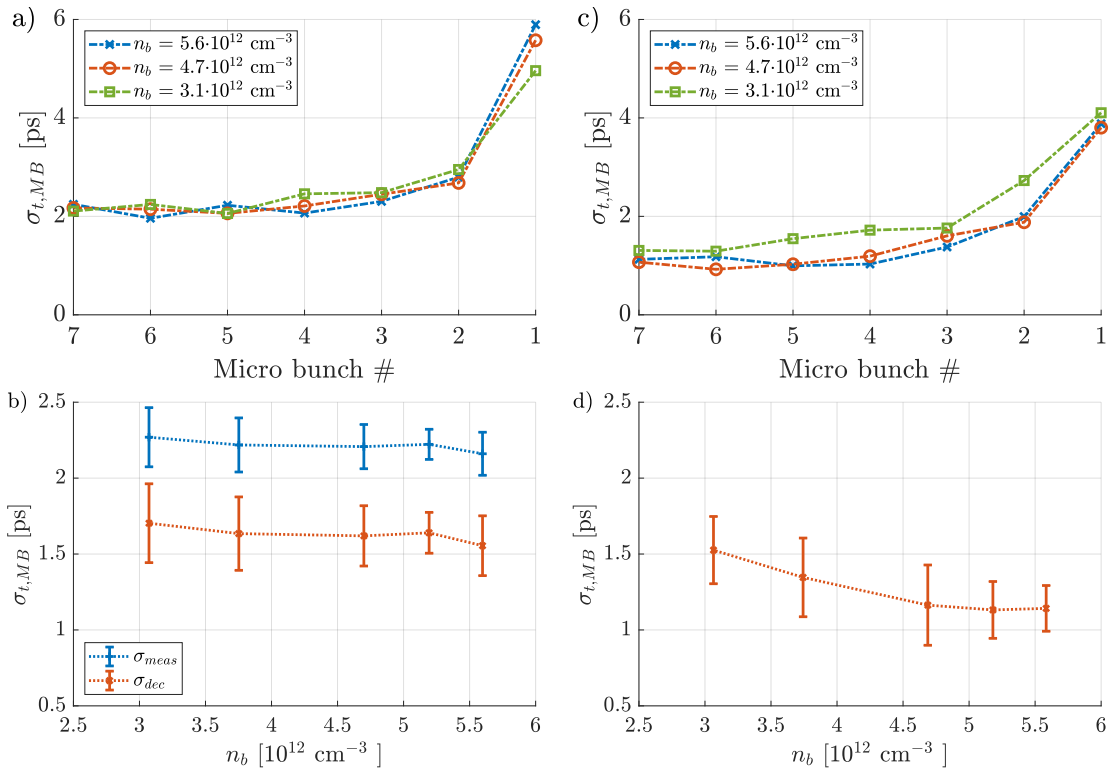

Figure 5.11: Length $\sigma_{t,MB}$ of the fits of the individual micro-bunches for the data with various initial bunch densities $n_b = [5.6, 4.7, 3.1] \cdot 10^{12}\,\mathrm{cm}^{-3}$ (blue crosses, red circles, green squares) from experiment (a) and simulations (c). Averaged length over micro-bunch $\#3 - 7$ as a function of initial bunch density from experiment (b) and simulations (d). The error bars give the std variations between micro-bunch #3 and #7. The experimental data (b) contains the directly measured length (blue symbols) and the length deconvolved with $\sigma_{res,t} = 1.5\,\mathrm{ps}$ (red symbols). Here, $n_{pe} = 0.9 \cdot 10^{14}\,\mathrm{cm}^{-3}$ and $\Delta n_{pe} = 0$.

following ones ($\#3 - 7$), whose duration is essentially constant, both in experiment and simulations. The mean value of the micro-bunches $\#3 - 7$ and standard deviation (error bars) are plotted as a function of initial bunch density for the experimental (blue symbols, Figure b) and simulation (Figure d) data. The values demonstrate that the micro-bunch length does not change with initial bunch density in the experiment on a measurable scale with the presented method. Simulations suggest a slight decrease in length with increasing initial bunch density, however differences are within the variations of the individual micro-bunches.

The measured micro-bunch duration is longer in the experimental results ($\sim 2 - 2.5\,\mathrm{ps}$) than in the simulation results ($\sim 1 - 2\,\mathrm{ps}$). However, the value of the micro-bunch length

is close to the temporal resolution of the streak camera ($\sigma_{res,t} = 1.5\,\text{ps}$, determined in Section 3.2.1). Therefore, the plots distinguish between the directly measured micro-bunch length (σ_{meas} blue symbols) and the length when deconvolving with the diagnostics temporal resolution ($\sigma_{dec} = \sqrt{{\sigma_{meas}}^2 - {\sigma_{res,t}}^2}$, red symbols) in the experiment. The lengths after deconvolution ($\sim 1.5 - 2\,\text{ps}$) are closer to the ones from simulations.
This analysis shows that the experiment and simulation results do not show a clear dependency of micro-bunch duration on the initial bunch density within the measurement limits. This implies that the efficiency of driving the wakefield, contributed to the charge distribution over the wakefield period, is independent of the strength of driving the wakefield.

Effect of Plasma Density

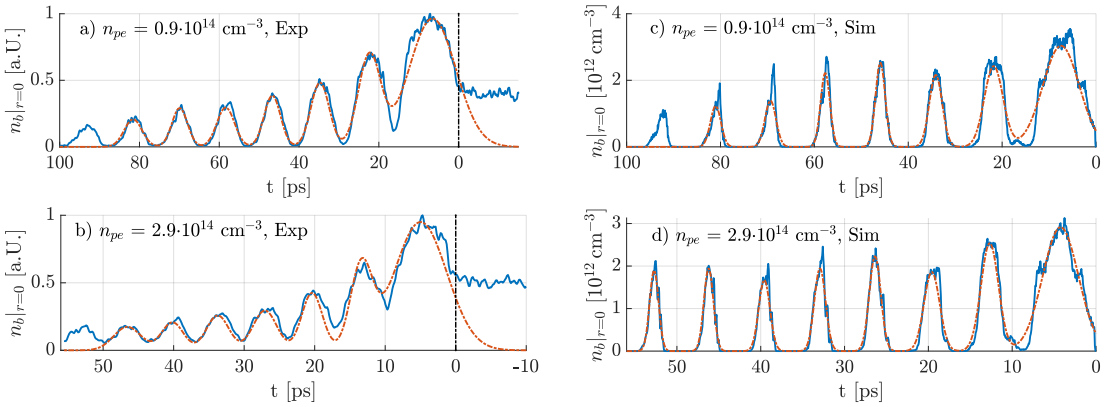

Figure 5.12: On-axis charge density (blue curves) with Gaussian fits to each micro-bunch (red curves) for plasma density $n_{pe} = 0.92 \cdot 10^{14}\,\text{cm}^{-3}$ (a, c) and $n_{pe} = 2.9 \cdot 10^{14}\,\text{cm}^{-3}$ (b, d), experimentally (a, b) and from simulations (c, d). Here, $n_b = 5.6 \cdot 10^{12}\,\text{cm}^{-3}$ and $\Delta n_{pe} = 0$.

The above analysis is repeated, this time changing the plasma density, see Figure 5.12. Once again, one can see that the Gaussian fits (red curves) agree well with the longitudinal profile (blue curves) for micro-bunch $\#3 - 7$ in both experiment (a, b) and simulations (c, d) for the low (a, c) and high (b, d) plasma densities. In general, the micro-bunch amplitude decreases faster along the bunch in the experimental profiles (a, b) than in the simulation ones (c, d).
It has been established in Figure 5.11 that the micro-bunch length is independent of the initial bunch density. Thus, the procedure is repeated at each plasma density with various initial bunch densities and the mean and rms value of the micro-bunch length (including micro-bunch $\#3 - 7$) are determined. The micro-bunch lengths, resulting from the Gaussian fits, as a function of plasma density are shown in Figure 5.13 from experiment (a)

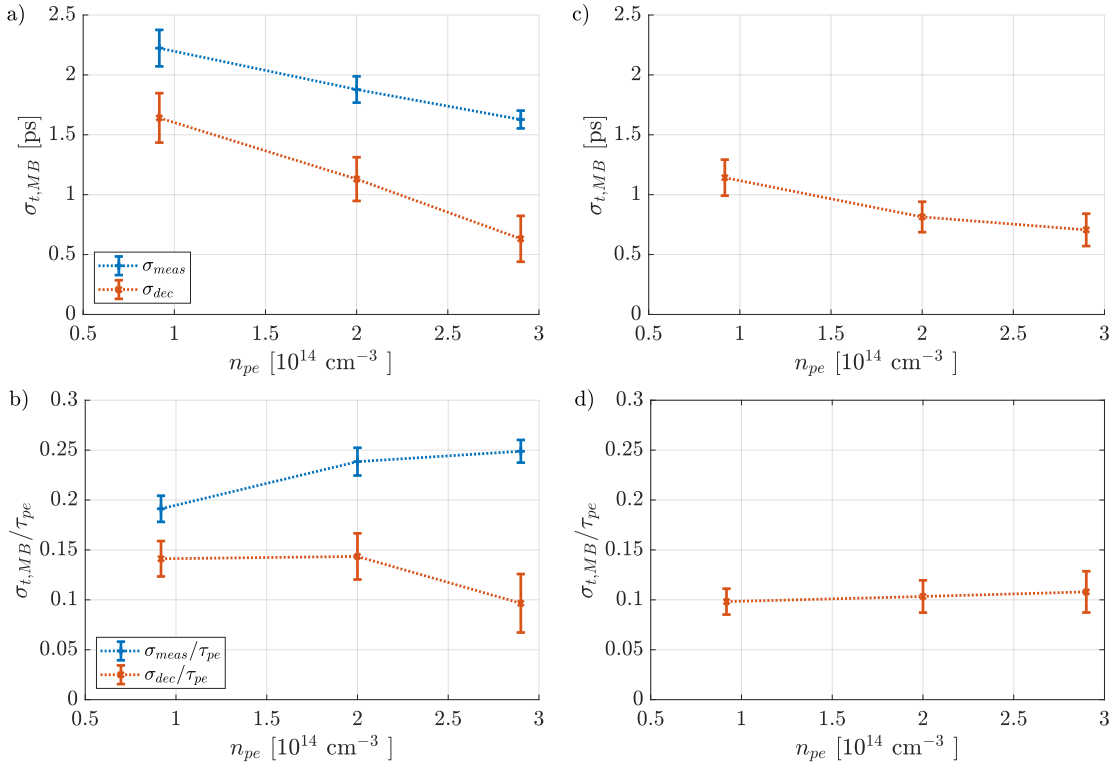

Figure 5.13: Micro-bunch length determined from Gaussian fits as a function of plasma density in experiment (a, b) and simulations (c, d). Images (a, c) show the absolute micro-bunch length, images (b, d) the length normalized to the corresponding plasma period. The error bars give the rms variations from different initial bunch density measurements and from micro-bunch $\#3-7$. The experimental data contains the directly measured length (blue symbols) and the length deconvolved with $\sigma_{res,t} = 1.5\,\mathrm{ps}$ (red symbols). Here, $n_b = 5.6 \cdot 10^{12}\,\mathrm{cm}^{-3}$ and $\Delta n_{pe} = 0$.

and simulations (c). The error bars are the rms variations from the measurements with different initial bunch densities for micro-bunch $\#3-7$. As previously, when determining the length for different initial bunch densities, the length obtained from the experiment (blue symbols) is deconvoluted with the streak camera temporal resolution $\sigma_{res,t} = 1.5\,\mathrm{ps}$ (red symbols).

The micro-bunches are formed by the transverse wakefield with the wakefield period essentially equal to the plasma period. Thus, we expect the micro-bunch length to decrease with increasing plasma density. Both in experiment (a) and simulations (c), the micro-bunch length $\sigma_{t,MB}$ decreases with increasing plasma densities, see also Table 5.6. It also shows that also after deconvolution, the micro-bunches in experiments are slightly longer than in simulations. This could come from either longer micro-bunches in experiment or

Plasma density	n_{pe} [cm^{-3}]	$0.92 \cdot 10^{14}$	$2.0 \cdot 10^{14}$	$2.9 \cdot 10^{14}$
Micro-bunch length Exp deconv.	$\sigma_{t,\mathrm{MB}}$ [ps]	1.6 ± 0.2	1.1 ± 0.2	0.6 ± 0.2
Micro-bunch length Sim	$\sigma_{t,\mathrm{MB}}$ [ps]	1.1 ± 0.2	0.8 ± 0.1	0.7 ± 0.1

Table 5.6: Micro-bunch length for different plasma densities.

be an effect of the fixed temporal resolution, that is assumed here, but in reality depends on the intensity of the signal on the streak camera, i.e. possibly varying from image to image and from micro-bunch to micro-bunch (see Figure 3.2).
To determine the micro-bunch length proportionality to the plasma period, the micro-bunch length is plotted normalized to the plasma period in Figures 5.13 (b) and (d). The mean micro-bunch length in experiment (b) is between 10 % and 15 % of the plasma period. The variations with varying plasma density are essentially within the rms variation. The micro-bunch length in simulations (d) is essentially a constant fraction of the plasma period for various plasma densities, $\sim 10\,\%$ of τ_{pe}. The error bars determine the precision of the procedure for the micro-bunch length as a fraction of the plasma period. The precision in the experiment is $< 22\,\%$, in the simulations it is $< 20\,\%$.
This shows that indeed the micro-bunch length is proportional to the plasma period $\sigma_{t,MB} \approx 0.1 - 0.15\,\tau_{pe}$ in experiment and $\sigma_{t,MB} \approx 0.1\,\tau_{pe}$ in simulations. As established earlier, the length of micro-bunch $\#3 - 7$ does not change on a measurable scale with the diagnostic and method (Figure 5.11). Hence, in the following, the micro-bunch length is considered constant along the bunch with a fixed fraction of the plasma period.
As shown by the schematic in Figure 5.9, a micro-bunch length of $0.1\,\tau_{pe}$ can principally lead to $\sim 3/4\,\mathrm{th}$ of the micro-bunch charge in one quarter of the wakefield period. However, this analysis does not specify the position with respect to the decelerating and focusing phase of the wakefield, which is desirable for driving wakefields effectively.

Effect of Plasma Density Gradient

It was established previously that the micro-bunch length is proportional to the plasma period. With a plasma density gradient, the plasma period changes along the plasma and thus the micro-bunch duration is expected to change as well. However, since density variations along the plasma ($\pm 20\,\%$) are much smaller than the plasma density variations of the previous section, the effect can be expected to be smaller. In the following, I determine the effect of a gradient on the micro-bunch length, measured in experiment and simulations.
The same procedure as used in the previous sections is applied. Figure 5.14 demonstrates that the Gaussian fits (red curves) describe the on-axis charge density profiles (blue

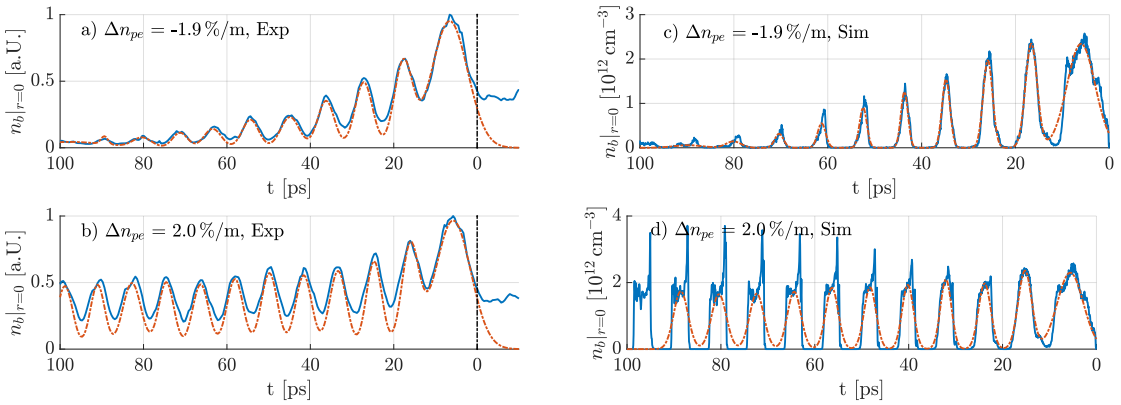

Figure 5.14: On-axis charge density (blue curves) with Gaussian fits to each micro-bunch (red curves) for plasma density gradient $\Delta n_{pe} = -1.9\%/\mathrm{m}$ (a, c) and $\Delta n_{pe} = 2.0\%/\mathrm{m}$ (b, d), experimentally (a, b) and from simulations (c, d). Here, $n_{pe,Entr.} = 1.8 \cdot 10^{14}\,\mathrm{cm}^{-3}$ and $n_b = 5.6 \cdot 10^{12}\,\mathrm{cm}^{-3}$.

curves) well with negative plasma density gradient in the experiment (a) and the simulation (c). The on-axis charge density decreases faster along the bunch with a negative (Figures 5.14 a, c) than without (see Figure 5.12) or with positive density gradient (Figures 5.14 b, d) both in experiment and simulations. This is a feature, also highlighted in [24], and is further analyzed in Section 5.5. A signal close to the noise, decreases the fit quality of micro-bunches further behind the seed position.

The bottom images (b, d) show that with a positive density gradient the train of micro-bunches cannot be described well with a train of Gaussian functions, neither in experiment (b), nor in simulations (d). The Gaussian fits from experiment underestimate the micro-bunch length and show a deeper modulation of the charge density. Simulations suggest a significantly different shape of micro-bunches with positive density gradient, compared to the data without or with negative gradient. Instead of longitudinally Gaussian shaped micro-bunch profiles, they appear as squared profiles with high frequency features. With a non-Gaussian micro-bunch profile, the width $\sigma_{t,MB}$ of the Gaussian fits does not describe well their length.

Nevertheless, in Figure 5.15, the micro-bunch length is plotted versus plasma density gradient from experiment (a), directly measured (blue symbols) and temporal resolution deconvolved (red symbols) and from simulations (b). Here, the error bars correspond to the rms variation from micro-bunch $\#3 - 7$, for only one initial bunch density measurement.

The micro-bunch lengths for the various plasma density gradients are also summarized in Table 5.7. The analysis shows that experimentally, the micro-bunch length is essentially constant and the variations with density gradient are within the micro-bunch length

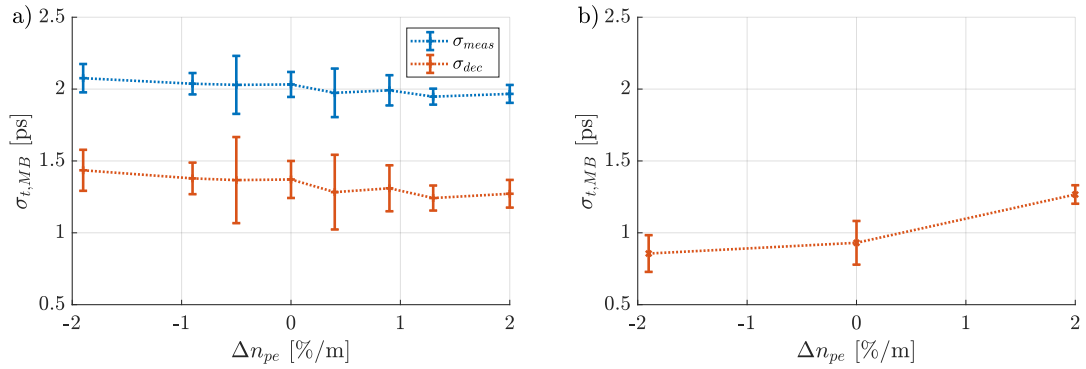

Figure 5.15: Micro-bunch length determined from Gaussian fits as a function of plasma density gradient in experiment (a) and simulations (b). The error bars give the rms variations from micro-bunch #3 − 7. The experimental data contains the directly measured length (blue symbols) and the length deconvolved with $\sigma_{res,t} = 1.5\,\text{ps}$ (red symbols). Here, $n_{pe,Entr.} = 1.8 \cdot 10^{14}\,\text{cm}^{-3}$ and $n_b = 5.6 \cdot 10^{12}\,\text{cm}^{-3}$.

Plasma density gradient	Δn_{pe} [%/m]	−1.9	0	2.0
Micro-bunch length Exp deconv.	$\sigma_{t,\text{MB}}$ [ps]	1.4 ± 0.1	1.4 ± 0.1	1.3 ± 0.1
Micro-bunch length Sim	$\sigma_{t,\text{MB}}$ [ps]	0.9 ± 0.1	0.9 ± 0.1	1.3 ± 0.1

Table 5.7: Micro-bunch length for different plasma density gradients.

variations along the bunch.

The lengths are approximately $15 - 17\,\%$ of the plasma period at the exit $\tau_{pe,Exit} = 9.2 - 7.6\,\text{ps}$ (from most negative to most positive gradient). This is slightly above the value determined for different plasma densities as $10 - 15\,\%$. This could be a result from the temporal resolution deconvolution. During the plasma density scan, we measured with the shortest streak camera time window (73 ps), during the gradient scan with a longer window (211 ps). Potentially, the temporal resolution value is slightly larger than assumed here ($\sigma_{t,res} = 1.5\,\text{ps}$).

The micro-bunch length determined from the simulations is shown in Figure 5.15 b) and values can also be found in Table 5.7. The length increases slightly from a negative to a positive density gradient. While the micro-bunch length with negative or without gradient is in agreement with the previously determined fraction of $\sim 10\,\%$ of the plasma period, the micro-bunch length with positive gradient is slightly above ($\sim 17\,\%$). This can be assigned to the change in micro-bunch profile to more square bunches, not well represented by the Gaussian fits (Figure 5.14 d). Also in simulations, the effect on the micro-bunch lengths on the small change in plasma period ($\pm 10\,\%$ at the exit), is smaller

than the rms variations of micro-bunches along the bunch.
Thus, with this procedure the effect of the plasma density gradient on the micro-bunch length cannot be measured. The change in plasma period $\pm 10\,\%$ is smaller than the error of the measurement, also as determined in Section 5.3 as $\sim 22\,\%$ in experiment and $\sim 20\,\%$ in simulations.

5.4 Transverse Profiles of Micro-Bunches

It was established from theory (Section 1.4.6) that an increase in initial bunch density increases the wakefield's seed value and growth rate. When increasing the plasma density, the seed wakefield amplitudes decrease, while the growth rate is the same at the same period. This change in the transverse wakefield, thus change in focusing, affects the transverse profiles of micro-bunches as analyzed in the following.
It was established in theory (Section 1.4.5), simulations [22] and in experiment [24] that during SM development the phase velocity of the wakefield is slower than the proton bunch velocity. That means that protons can experience alternating focusing and defocusing fields along their propagation in the plasma. Protons in the focusing phase can oscillate around the propagation axis (betatron oscillations). When changing from focusing to defocusing, or vice versa, protons can either exit the wakefield, or be recaptured. The distributions observed after the plasma are therefore the result of the integrated history of the protons in the transverse wakefield. This history is most visible in the case of negative density gradient in which case the difference between phase and proton bunch velocity is the largest, which leads to radial layers of defocusing/focusing proton charge density, see Figure 4.11 c).
The transverse profiles shown in this section are obtained from time-resolved images at the OTR screen position (3.5 m after the 10 m plasma exit). The transverse profiles correspond to the average around the micro-bunch center (summarized in the appendix, Section A.4) over 1.5 ps, the temporal resolution of the streak camera in the 73 ps window (Section 3.2.1). They are normalized to their peak value for better comparison of their width. To establish the change of transverse micro-bunch profiles along the bunch, the profiles of micro-bunch #1 and #5 are studied.

Effect of Initial Bunch Density

The transverse profiles of micro-bunches are shown in Figure 5.16 with high (a, b) and low (c, d) initial bunch density, for the first (a, c) and fifth (b, d) micro-bunch. The

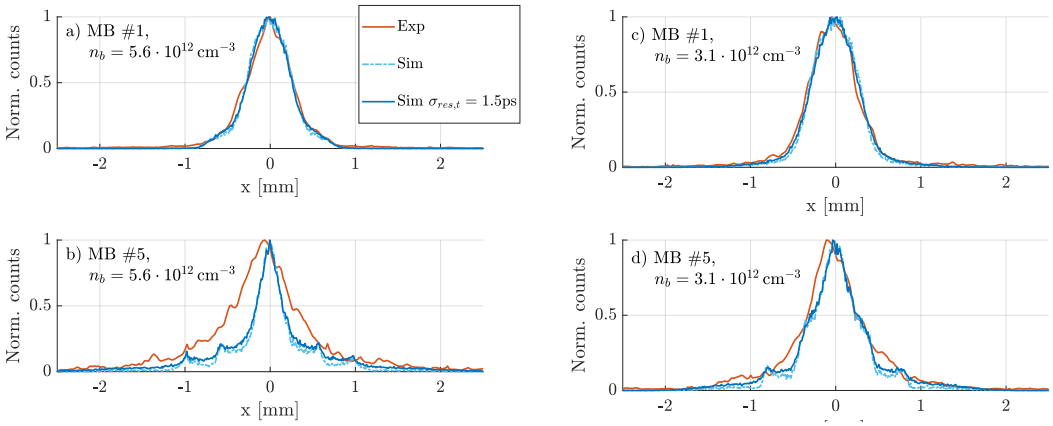

Figure 5.16: Normalized transverse charge density profiles with initial bunch density $n_b = 5.6 \cdot 10^{12}\,\mathrm{cm}^{-3}$ (a, b) and $n_b = 3.1 \cdot 10^{12}\,\mathrm{cm}^{-3}$ (c, d) for the first (a, c) and fifth (b, d) micro-bunch. Profiles from simulations (bright blue dashed lines), their convolution with temporal resolution $\sigma_{res,t} = 1.5\,\mathrm{ps}$ (dark blue solid lines) and the experimental profiles (red solid lines). Here, $n_{pe} = 0.92 \cdot 10^{14}\,\mathrm{cm}^{-3}$ and $\Delta n_{pe} = 0$.

figure compares the profiles from the simulations (bright blue dashed lines), the temporal resolution convoluted profiles (dark blue solid lines) and the ones from experiment (red solid lines).

The spatial resolution in experiment is determined as $\sigma_{res,x} = 80\,\mu\mathrm{m}$, i.e. $\mathrm{FWHM}_{res,x} \approx$

Initial bunch density	n_b [cm^{-3}]	$5.6 \cdot 10^{12}$	$3.1 \cdot 10^{12}$
Micro-bunch width #1	$\mathrm{FWHM}_{x,\mathrm{MB},1}$ [mm]	0.5 ± 0.2	0.6 ± 0.2
Micro-bunch width #5	$\mathrm{FWHM}_{x,\mathrm{MB},5}$ [mm]	0.7 ± 0.2	0.5 ± 0.2

Table 5.8: Micro-bunch FWHM width for different initial bunch densities in experiment. The uncertainty corresponds to the spatial resolution (Section 3.2.1).

0.2 mm (Section 3.2.1) and used here as uncertainty for experimental measurements. The micro-bunch FWHM widths of the two periods for the different initial bunch densities in experiment from Figure 5.16 are summarized in Table 5.8. It shows that the variations between micro-bunch profiles are smaller or equal to the spatial resolution. Therefore, experimental results suggest similar micro-bunch widths within the resolution limits, potentially with an increase in width along the bunch for the high initial bunch density case.

The spatial resolution in simulations is approximately the grid size $\delta x = 10\,\mu\mathrm{m}$ (Table 4.4), thus has essentially no effect on the in comparison wide transverse profiles. Simulation results show narrower width for the fifth than for the first micro-bunch and narrower

width for higher initial bunch density. This could be a result of increasing focusing field along the bunch and higher wakefield amplitudes for higher initial bunch density.
Experimental and simulation results are in relatively good agreement in three of the profiles (a, c, d), but are different for the fifth micro-bunch with high initial bunch density (b). In general, wider micro-bunches measured 3.5 m after the plasma could come from a stronger divergence during vacuum propagation of actually narrower micro-bunches at the plasma exit and/or an increase in emittance either along the bunch or with increasing wakefield. The difference between experiment and simulations could thus come from a different divergence due to a larger emittance in experiment after evolution along the plasma and/or along the bunch.

Effect of Plasma Density

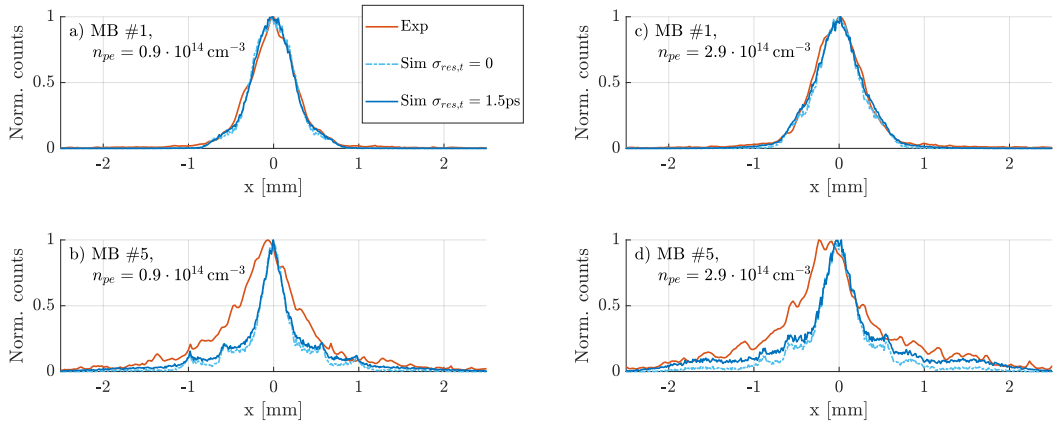

Figure 5.17: Normalized transverse charge density profiles with plasma density $n_{pe} = 0.92 \cdot 10^{14}\,\mathrm{cm}^{-3}$ (a, b) and $n_{pe} = 2.9 \cdot 10^{14}\,\mathrm{cm}^{-3}$ (c, d) for the first (a, c) and fifth (b, d) micro-bunch. Profiles from the simulation (bright blue dashed lines), their convolution with temporal resolution $\sigma_{res,t} = 1.5\,\mathrm{ps}$ (dark blue solid lines) and the experimental profiles (red solid lines). Here, $n_b = 5.6 \cdot 10^{12}\,\mathrm{cm}^{-3}$ and $\Delta n_{pe} = 0$.

Figure 5.17 shows the transverse micro-bunch profiles from experiment (red solid lines) and simulations (bright blue dashed lines without, dark blue solid lines with temporal resolution convolution) for low plasma density ($n_{pe} = 0.92 \cdot 10^{14}\,\mathrm{cm}^{-3}$, Figures a, b) and high plasma density ($n_{pe} = 2.9 \cdot 10^{14}\,\mathrm{cm}^{-3}$, Figures c, d).
Therefore, simulations suggest also for the higher plasma density that the micro-bunch #5 (d) is narrower than micro-bunch #1 (c). This is in agreement with the expectation of the (transverse) wakefield growing along the bunch, i.e. stronger focusing later along

the bunch (Section 1.4.3). Further, in simulations, micro-bunch #5 is slightly wider for higher (FWHM $\sim 0.4\,\mathrm{mm}$, Figure d) than for lower plasma density (FWHM $\sim 0.3\,\mathrm{mm}$, Figure b). This is in agreement with a slightly lower transverse seed wakefield, i.e. weaker focusing, and equal growth rate for a given wakefield period behind the seed position (Section 1.4.6) when increasing the plasma density.
The micro-bunch FWHM widths of the two periods, measured in experiment, with different plasma densities are summarized in Table 5.9. The values suggest that micro-bunches are getting slightly wider from the first to the fifth micro-bunch and slightly wider from lower to higher plasma density. As mentioned before, the changes are within the uncertainty of the measurement, and might also be the result of a stronger divergence due to narrower micro-bunches at the plasma exit and/or increasing emittance along the bunch.

Plasma density	n_{pe} [cm^{-3}]	$0.92 \cdot 10^{14}$	$2.9 \cdot 10^{14}$
Micro-bunch width #1	FWHM$_{x,\mathrm{MB},1}$ [mm]	0.5 ± 0.2	0.6 ± 0.2
Micro-bunch width #5	FWHM$_{x,\mathrm{MB},5}$ [mm]	0.7 ± 0.2	0.9 ± 0.2

Table 5.9: Micro-bunch FWHM width for different plasma densities in experiment. The uncertainty corresponds to the spatial resolution (Section 3.2.1).

Effect of Plasma Density Gradient

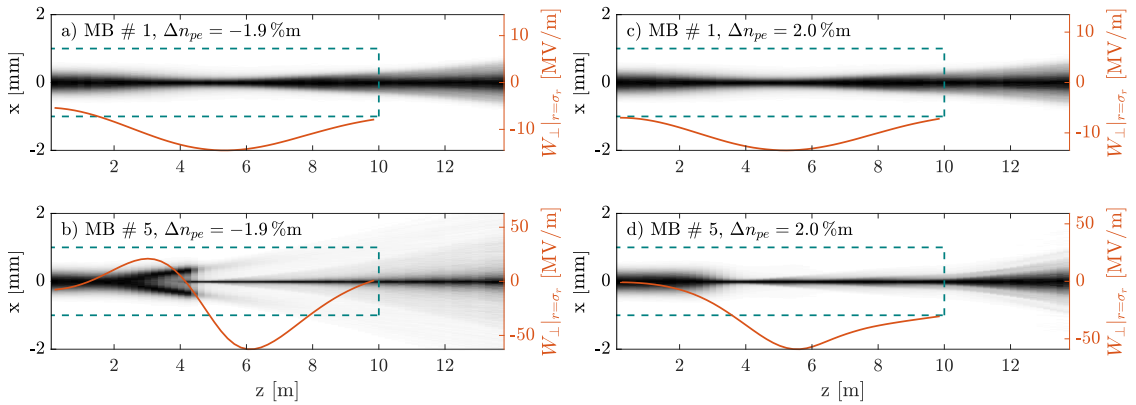

Figure 5.18: Micro-bunch evolution for a plasma density gradient of $\Delta n_{pe} = -1.9\,\%/\mathrm{m}$ (a, b) and $\Delta n_{pe} = 2.0\,\%/\mathrm{m}$ (c, d), for the first (a, c) and fifth (b, d) micro-bunch (location ξ determined in Section A.4). The 2D plots show the transverse profile of the charge density, normalized to 1 for each position z. The red curves show the transverse wakefield at $r = \sigma_{r,0} = 200\,\mu\mathrm{m}$ along z. The plasma edge is marked with the blue dashed lines.

Since a plasma density gradient influences the phase velocity of the wakefield, both along the plasma and along the bunch, on Figure 5.18, the bunch density and the amplitude of the transverse wakefield $W_\perp$ at the initial bunch radius $\sigma_{r,0}$ and the ξ locations along the bunch of the first (a, c) and fifth (b, d) micro-bunch are plotted from simulations. The fixed micro-bunch location ξ is determined after the plasma (summarized in the appendix, Section A.4). The bunch density and the transverse wakefield are plotted for the two extreme gradient values $\Delta n_{pe} = -1.9\,\%/\mathrm{m}$ (a, b) and $\Delta n_{pe} = 2.0\,\%/\mathrm{m}$ (c, d). In all cases, at the plasma entrance, the transverse wakefield (red curve) is focusing (or zero), as the seeding position is $\xi_{Seed} = 0.6\,\sigma_\xi$ ahead of the bunch (see Section 1.4.1). At the location of the first micro-bunch (a, c) the transverse wakefield remains focusing all along the plasma, since neither the natural evolution of the wakefield (see Sections 1.4.5 and 5.1), nor the addition of a (small) density gradient lead to any significant shift or dephasing of the wakefield. As the wakefield here remains focusing over the entire 10 m but the protons have a minimum transverse size around $z \approx 5\,\mathrm{m}$, this shows that protons in these regions undergo a sort of betatron oscillation.
In contrast, for micro-bunch #5 and $\Delta n_{pe} = -1.9\,\%/\mathrm{m}$ (Figure 5.18 b), the wakefield

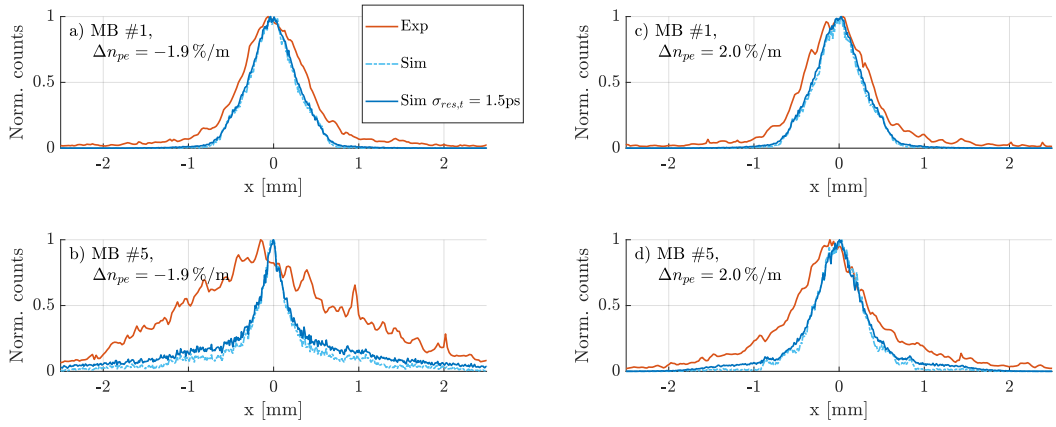

Figure 5.19: Normalized transverse charge density profiles for a plasma density gradient $\Delta n_{pe} = -1.9\,\%/\mathrm{m}$ (a, b) and $\Delta n_{pe} = 2.0\,\%/\mathrm{m}$ (c, d) for the first (a, c) and fifth (b, d) micro-bunch. Profiles from the simulation (bright blue dashed lines), their convolution with temporal resolution $\sigma_{res,t} = 1.5\,\mathrm{ps}$ (dark blue solid lines) and the experimental profiles (red solid lines). Here, $n_{pe,Entr.} = 1.8 \cdot 10^{14}\,\mathrm{cm}^{-3}$ and $n_b = 5.6 \cdot 10^{12}\,\mathrm{cm}^{-3}$.

switches from initially focusing ($z < 0.5\,\mathrm{m}$) to defocusing and back again to focusing ($z > 4.5\,\mathrm{m}$). Some protons are sufficiently defocused in $0.5\,\mathrm{m} < z < 4.5\,\mathrm{m}$ to leave the wakefield transversely and drift to the screen. They form the wide wings (up to $|x| \approx 2\,\mathrm{mm}$) in the charge distribution observed on Figure 5.19 (b).

The case of the addition of a positive phase velocity by the positive density gradient prevents the switch from focusing to defocusing (Figure 5.18 d). In all three cases of focusing only, the wakefield at the micro-bunch locations (Figures 5.18 a, c, d) leads to relatively narrow, bell shaped micro-bunches (Figures 5.19 a, c, d) in simulations and experiment. The wakefield switching between focusing and defocusing (Figure 5.18 b) leads to a narrow profile ($|x| < 0.5\,\mathrm{mm}$) on top of the broad population in the micro-bunch profile in the result from simulations (blue lines in Figure 5.19 b). These multiple features in transverse profiles are typical of the transverse wakefields switching. Also in experiment, the profile of the fifth micro-bunch with the most negative density gradient is significantly wider (red line in Figure 5.19 b) than the one with most positive gradient (red line in Figure 5.19 d). The fact that the narrow feature of the fifth micro-bunch profile with negative gradient in the simulation results (blue lines in Figure 5.19 b) is not visible in the experiment (red lines) can be explained with small spatial misalignment of the OTR light from the protons with respect to the streak camera slit. With a small misalignment, possibly only the broad wing of protons, without the narrow on-axis peak, is acquired in experiment. This is further analyzed in the appendix (Section A.5, Figure A.23).
The FWHM widths of the experimental profiles are summarized in Table 5.10. The first

Plasma density gradient	Δn_{pe} [%/m]	−1.9	2.0
Micro-bunch width #1	$\mathrm{FWHM}_{x,\mathrm{MB},1}$ [mm]	0.8 ± 0.2	0.8 ± 0.2
Micro-bunch width #5	$\mathrm{FWHM}_{x,\mathrm{MB},5}$ [mm]	2.1 ± 0.2	0.9 ± 0.2

Table 5.10: Micro-bunch FWHM width for different plasma density gradients in experiment. The uncertainty corresponds to the spatial resolution (Section 3.2.1).

micro-bunch is not affected by the gradient on a measurable scale. The wider micro-bunch #5 for negative gradient is in agreement with the wing of defocused protons seen in simulations.

5.5 Experimental Determination of the Relative Micro-Bunch Charge

Streak camera images show the charge density of the proton bunch $n_b(\xi) \propto \frac{Q(\xi)}{\sigma_r(\xi)}$ in a slice $\sim 74\,\mu\mathrm{m}$-wide along the transverse x-axis of the proton bunch, whose transverse rms size without plasma is $\sim 580\,\mu\mathrm{m}$ [60], see Sections 3.2.6 and 3.2.7. These images show that the charge density generally decreases along the bunch. The determination of micro-bunch

distributions at the measurement location (OTR screen) is important to also understand the micro-bunch evolution along the plasma. The decrease in charge density along the bunch is often misunderstood as the fact that the charge decreases along the bunch train. The same streak camera images also show that the width of the micro-bunch profiles may be increasing along the bunch train (Figures 5.16, 5.17 and 5.19). In this section, I analyze the charge along the train of micro-bunches from the charge density distribution. I determine a relative charge per micro-bunch along the bunch for experimental data. Here, measurements with different plasma density gradients are used as here the effect is the largest, due to the strong change in transverse profiles of micro-bunches along the bunch and with gradient, as shown in the previous section. With this procedure the charge can be recovered in all cases.
It is established in Section 5.3 that the variation in length of micro-bunch $\#3-7$ along the bunch or with plasma density gradient is smaller than the measurement's precision. Thus, in the following, I determine the relative charge per micro-bunch from their transverse profiles, integrated over 1.5 ps around the micro-bunch temporal center (summarized in Section A.4). Details of the method applied here and transverse micro-bunch charge profiles can be found in Section 3.2.7.

Figure 5.19 demonstrates that the charge density profiles of micro-bunches from experiment are significantly wider with negative density gradient and wider further along the bunch. It was also shown that micro-bunch shapes are changing along the bunch and with gradient. Therefore, for a fixed ξ position along the bunch, instead of calculating the charge Q as $Q = n_b\,\sigma_r$ with a value for the width and the density, it is used $Q = \sum n_{b,i}\,r_i$. Thus, the charge density of the transverse micro-bunch profile (i.e. the number of counts of a pixel $n_{b,i}$) is multiplied with the distance to the bunch axis x_i (or r_i) to obtain the charge. The charge profiles are cut at a bunch axis distance (radius), where it reaches the noise level (see Section 3.2.7).
The analysis can also be applied to regions of the bunch ($t < 0$) that have not been affected by the plasma and have an essentially Gaussian profile. Assuming a Gaussian longitudinal profile for the bunch, knowing the bunch length and seed position, the expected incoming charge profile can be calculated. The calculated charge profile of the bunch train can then be compared with that of the incoming bunch for both $t > 0$ and $t < 0$.
Figure 5.20 shows that for $t < 0$ (no SM) the integrated charge density ($\sum n_{b,i}$, red circles) and the integrated charge ($\sum n_{b,i}\,x_i$, blue crosses) both follow the trend of the incoming bunch (black dash-dotted line), increasing with time, as $t = 0$ at $\xi_{Seed} = 0.6\,\sigma_\xi$ ahead of the bunch center. All curves here are normalized to their mean value of the five

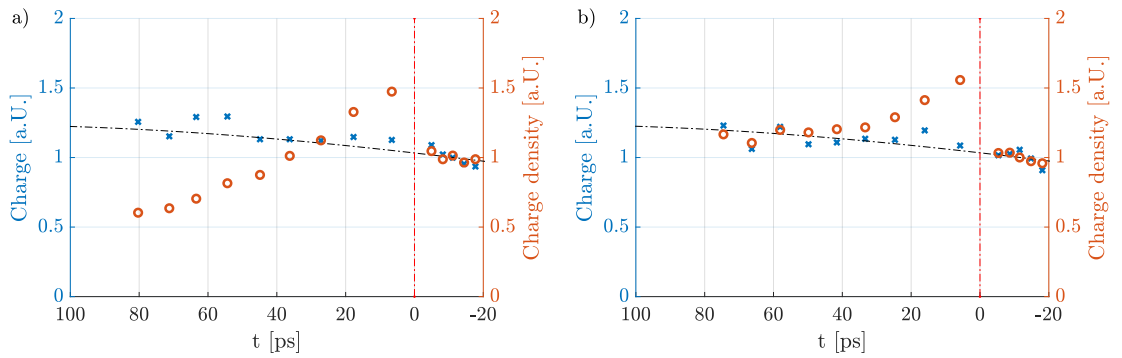

Figure 5.20: Integrated charge density ($\sum n_{b,i}$, red circles), integrated charge ($\sum n_{b,i}\, x_i$, blue crosses) and longitudinal incoming bunch charge (density) profile (Gaussian, black dash-dotted line) with plasma density gradient $\Delta n_{pe} = -1.9\%/\mathrm{m}$ (a) and $\Delta n_{pe} = 2.0\%/\mathrm{m}$ (b). Here, $n_{pe,Entr.} = 1.8 \cdot 10^{14}\,\mathrm{cm}^{-3}$, $n_b = 5.6 \cdot 10^{12}\,\mathrm{cm}^{-3}$, $\sigma_\xi = 6.6\,\mathrm{cm}$, i.e. $\sigma_t = 230\,\mathrm{ps}$ and $\xi_{Seed} = 0.6\,\sigma_\xi$.

points of the unmodulated bunch at $t < 0$.

In both plasma density gradient cases, the most negative ($\Delta n_{pe} = -1.9\,\%/\mathrm{m}$, Figure a) and the most positive ($\Delta n_{pe} = 2.0\,\%/\mathrm{m}$, Figure b), the integrated charge density of micro-bunch #1 and #2 is significantly larger ($\sim 120 - 150\,\%$) than that of the incoming bunch. While with positive gradient (b) micro-bunches $\#3 - 9$ follow the incoming bunch, they are significantly lower ($\sim 50\%$) and reveal a different trend with negative gradient (a). However, in both cases the charge calculation produces values that are very close to that of the incoming bunch (deviations $\sim \pm 20\%$) and that follow the incoming bunch profile. This shows that the SM process focuses all the incoming bunch charge in the first eight micro-bunches to a transverse size smaller than the field of view ($\pm 4\,\mathrm{mm}$, aperture of the OTR transport line, Section 3.2.4).

Further, it shows that the first two micro-bunches are focused to a smaller size than the incoming bunch. This lets the first micro-bunches appear more intense than the incoming bunch in the time-resolved images. This can be seen in all time-resolved images presented and is true for the different initial bunch densities, plasma densities and plasma density gradients analyzed in this thesis (see e.g. Figures 4.1, 4.9, 4.10, 4.11).

Fluctuations of the integrated charge (blue crosses in Figure 5.20) and values above the incoming charge indicate the precision of the method ($\sim 20\,\%$). The precision decreases along the bunch and with more negative density gradient due to the low charge density, i.e. a signal close to noise, visible e.g. from the on-axis profiles in Figure 5.14.

This analysis shows that the decrease in on-axis charge density, visible on streak camera images (see Figure 4.9) comes from wider micro-bunches along the bunch. Note that here

micro-bunches are defined without restraining their shape (e.g. a bunch instead of a ring) or limiting the transverse size (charge close to the axis/inside the plasma), while generally it is expected that the transverse profiles of micro-bunches affect the driving of wakefield.

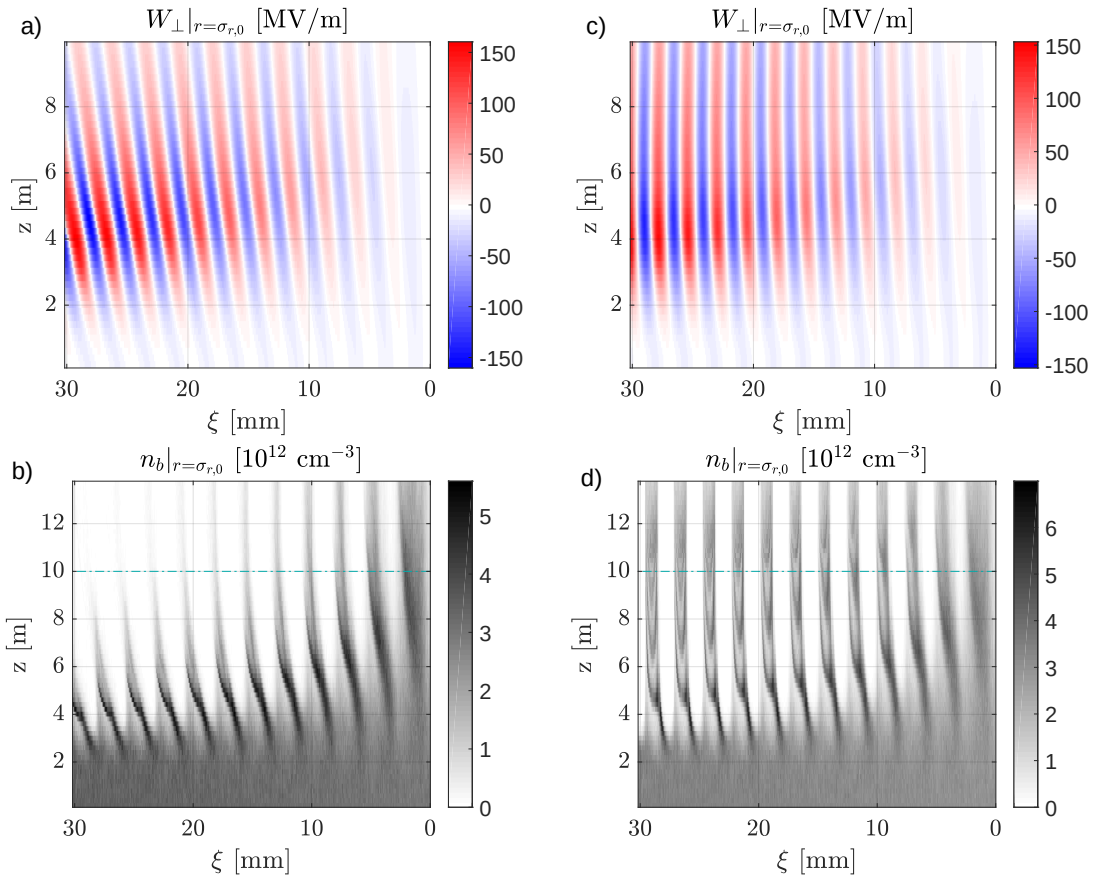

Figure 5.21: Transverse wakefield (a, c) and bunch density (b, d) at $r = \sigma_{r,0} = 200\,\mu\text{m}$ along the bunch ξ and along the plasma z with plasma density gradient $\Delta n_{pe} = -1.9\,\%/\text{m}$ (a, b) and $\Delta n_{pe} = 2.0\,\%/\text{m}$ (c, d). Images are saturated to also show small wakefield amplitudes and densities. Plasma ends at $z = 10\,\text{m}$ (cyan dash-dotted line in b, d). Here, $n_b = 5.6 \cdot 10^{12}\,\text{cm}^{-3}$ and $n_{pe,Entr.} = 1.8 \cdot 10^{14}\,\text{cm}^{-3}$.

In general, a larger size after vacuum propagation can originate from either a larger distribution (transverse displacement) or a larger transverse velocity distribution (stronger divergence) at the plasma exit. The latter can arise from either a larger emittance or a smaller size. However, simulations show that with negative density gradient protons are transversely displaced within the plasma, as demonstrated in Figure 5.18.

The phase slippage of the transverse wakefield with density gradients and its effect on

the on-axis charge density in simulations is studied in Figure 5.21. The images show the transverse wakefield (a, c) and the charge density (b, d), both along the plasma z and along the bunch ξ at a fixed radius, the incoming proton bunch radius $\sigma_{r,0}$.
It is expected that a negative (positive) density gradient increases (decreases) the difference in velocity between the wakefield's phase and the drive bunch during SM, by increasing (decreasing) the local plasma period with the density gradient. Transverse wakefields in simulations confirm this expectations. The wakefield's phase is shifting backwards over the entire 10 m of plasma with negative density gradient (a), while it stops evolving after ~ 2 m with positive density gradient (c).
As also shown for a fixed micro-bunch position ξ in Figure 5.18, the phase shift of Figure 5.21 a) leads to protons experiencing both focusing and defocusing fields along the plasma. As a result the charge density close to the bunch axis decreases significantly. This is visible on Figure 5.21 b) that shows the proton bunch charge density in the same domain as that of the wakefield of Figure 5.21 a). On the contrary, with a positive density gradient the compensation of the phase slippage (Figure 5.21 c) results in a better conservation of the charge (density) along the bunch and along the plasma (Figure 5.21 d).
The modulated bunch charge density at the plasma exit (cyan lines in Figures 5.21 b, d) can be compared with the one after further vacuum propagation. The bunch density with negative gradient is already much lower at $z = 10$ m and not only decreasing during vacuum propagation between $z = 10 - 13.5$ m. Thus, the bunch density evolution confirms that the low charge density with negative gradient is not dominated by a larger divergence (e.g. due to an increase of emittance or decrease of the transverse size along the bunch), but it is dominated by transverse displacement along the plasma. Simulations suggest that the lower charge density observed in the experiment with $\Delta n_{pe} = -1.9\,\%/\mathrm{m}$ (red circles, Figure 5.20 a) indicates that the micro-bunch charge density (micro-bunch $\# > 2$) is not only lower at the screen ($z = 13.5$ m), but also along the plasma, after saturation of the SM process ($z > 5$ m). Ultimately, the increased (counteracting) phase shift of the wakefield with respect to the driver with negative (positive) density gradient is measured in the experiment by the strong decrease of charge (density) close to the bunch axis.

5.6 Conclusion

In both experiment and simulations the first modulation period is always longer than the plasma period. This is a result of the wakefield's phase being slower than the driver velocity during SM: Right after the seed position the wakefield is focusing. With the

wakefield shifting backwards along the bunch during SM, the length of the modulation period increases. While the length of the first modulation period scales with the plasma period, when increasing the plasma density by a factor of 3, a dependency on plasma density gradient with density gradients $\pm 20\,\%$ over the 10 m is not measured, possibly as the effect is smaller than the method's accuracy. With the accuracy of the measurement, there is also no measurable dependency on the wakefield amplitudes (initial bunch density).

The SM frequency is, to zeroth order, determined by the plasma frequency. The modulation frequency is indeed measured to be equal to the plasma frequency, in simulations and experiment. It is demonstrated that the modulation frequency changes with plasma density gradient. This analysis benefits from the effect of a modulation frequency/phase change adding up from period to period along the bunch, by comparing the time (location) of early (#3) with late (#7) micro-bunches. The initial bunch density, and thus the wakefield amplitude, is expected to have a higher order effect on the SM frequency. Therefore, there is no dependency on initial bunch density measured with the accuracy of the method described here.

The micro-bunch length was measured as constant along the bunch within micro-bunch $\#3-7$ with a measurement precision of $\sim 20\,\%$. The micro-bunch length is determined as a fraction of the plasma period (rms length $\sim 0.1-0.15\,\tau_{pe}$ in experiment, $\sim 0.1\,\tau_{pe}$ in simulations), and independent of the strength of the wakefield (initial bunch density). The effect of a plasma density gradient of $\pm 20\,\%$ over 10 m in density is too small to be measured with the method's precision.

Transverse profiles of micro-bunches are analyzed to study focusing wakefield amplitudes and the wakefield's phase slippage. In simulations, micro-bunches are observed as slightly more focused for higher transverse wakefield amplitudes (higher initial bunch density, lower plasma density or further along the bunch). For these parameters, in the experiment the change of transverse micro-bunch profiles is dominated by the spatial resolution. Plasma density gradients are studied to in- or decrease the phase slippage between the wakefield and drive bunch. Significantly wider transverse micro-bunch charge density distributions are measured with negative density gradient as a result of micro-bunches experiencing defocusing fields due to the phase slippage in both experiment and simulations.

All streak camera images show that the charge density of micro-bunches decreases along the bunch. At the same time the transverse extent of the micro-bunch charge distribution increases. The charge in each micro-bunch can be recovered for the first eighth micro-bunches over the transverse size of the images. This is demonstrated for the two extreme cases, the most negative (positive) density gradient, leading to the strongest

(weakest) decrease in on-axis charge density along the bunch.

Micro-bunches are the result of the focusing transverse wakefield. The effect of the focusing field experienced by the protons is not cumulative, as protons remaining in the focusing phase of the wakefield can cross the bunch axis multiple times. This complicates the extraction of information on transverse wakefield amplitudes from analyzing micro-bunches at a distance of 3.5 m after the plasma exit and with fixed plasma length. However, it was established in Section 4.4 that focusing and defocusing wakefields evolve similarly along the plasma. Thus, instead of analyzing the effect of the focusing field on micro-bunches, in the following chapter I analyze the effect of the defocusing transverse wakefield on diverging protons.

6 Characterization of Defocused Proton Distributions during Self-Modulation

It was established (Section 5.4, Figure 5.18 a, c) that the focusing field leads to protons periodically crossing the axis during plasma propagation. Thus, the effect of the focusing field on protons is not cumulative. Therefore, transverse distributions of focused protons are not conclusive for the determination of the transverse wakefield. Figure 4.8 shows that the amplitude of the focusing and defocusing wakefields evolve similarly along the plasma. Hence, in the following, I study the effect of the defocusing wakefield on the proton distribution. The outwards momentum gain is cumulative and therefore more information about the transverse wakefield can be extracted.
The dependency of wakefield amplitudes (seed wakefield and wakefield growth) on initial bunch density, plasma density and plasma density gradient is described in Section 1.4.6 using linear wakefield and linear SMI theory. These theories are only valid for small radial perturbation, i.e. for short (with parameters used in the experiments described here $\lesssim 4\,\mathrm{m}$) propagation distance in plasma. The setup of the experiment is designed to ensure saturation of SM with the experimental parameters discussed in thesis. After 10 m of plasma, the proton bunch is fully modulated up to the seed position (see Section 5.1). Therefore, the amplitude of the wakefields after long propagation distances in plasma cannot be derived from linear theory and the results from the experiment, measured after the plasma, cannot directly be compared with theory. Thus, in this chapter, I analyze simulations that predict the wakefield and SM behaviour beyond the point of linear wakefield theory. Using the time-resolved images, obtained after the plasma, I compare the defocused proton distributions from simulations and experiment. As there is a good agreement between the two, I study the wakefield and bunch modulation evolution along the plasma in simulations.
Due to the adiabatic response, with a seed position ahead of the proton bunch center, the seed wakefield along the bunch is periodically stronger and weaker focusing over the first few wakefield periods, i.e. initially not defocusing (Section 1.4.1). With propagation in plasma, the bunch self-modulates and the transverse wakefield evolves to be periodically focusing and defocusing. As in the experiment the plasma length is fixed to 10 m, I

study in simulations from which distance in plasma protons start to diverge due to the defocusing field and how their trajectories evolve along the bunch and along the plasma.

The transverse wakefield grows along the micro-bunch train, as shown from linear theory in Section 1.4.3. The increasing radius of defocused proton distributions along the bunch, as measured with the time-resolved images, is the result of the transverse wakefield growing along the bunch. The systematic change in radius of defocused proton distributions, when changing initial bunch density, plasma density or plasma density gradient, shows the change in wakefield amplitude (seed wakefield and/or growth) or phase slippage between the wakefield and protons.

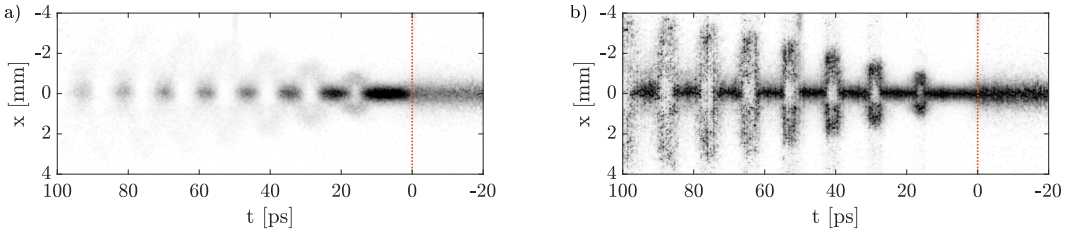

Figure 6.1: Time-resolved images of the modulated bunch; a) original image b) transverse profiles normalized to 1 for each pixel along t. Here, $n_{pe} = 0.92 \cdot 10^{14}\,\mathrm{cm}^{-3}$, $\Delta n_{pe} = 0$ and $n_b = 5.6 \cdot 10^{12}\,\mathrm{cm}^{-3}$.

In this chapter, time-resolved images are shown from simulations and experiment obtained at a location 3.5 m after 10 m of plasma with normalization of transverse profiles for each position t along the bunch. The streak camera images in Figure 6.1 show that, as focused and defocused protons appear periodically in time along the bunch, the normalization (Figure 6.1 b) makes defocused proton distributions with lower charge density appear more visible than in the original image (Figure 6.1 a). From the time-resolved images, I analyze the transverse defocused proton distributions, averaged over the streak camera temporal resolution of 1.5 ps (see Sections 3.2.1 and 4.3.4), centered around the location of defocused proton regions (summarized in the appendix in Section A.4). The rms width $\left(\sigma = \sqrt{\frac{1}{n}\sum_i^n x_i^2}\right)$ of defocused proton distributions is calculated from time-resolved images from simulations and experiment. Here, the signal is used over the transverse range where it dominates over the noise for streak camera images, as explained in Section 3.2.8.

6.1 Effect of Initial Bunch Density

The initial bunch density at the seed position is increased by moving the RIF (experiment) or bunch cut (simulations) closer to the bunch center. A higher initial bunch density leads to larger transverse seed wakefield amplitudes and larger wakefield growth (see Section 1.4.6). The larger wakefield amplitudes with higher initial bunch density are studied by analyzing the increasing width of defocused proton distributions. In the appendix (Section A.11), it is shown that over the first five periods, for the evolution of proton defocusing and transverse wakefield, the effect of the initial bunch charge density at the seed position dominates over the effect of the slope of the incoming bunch charge density profile. Therefore, the initial bunch density n_b is increased from $3.1 \cdot 10^{12}\,\mathrm{cm}^{-3}$ up to $5.6 \cdot 10^{12}\,\mathrm{cm}^{-3}$ by moving the seed position ξ_{Seed} from $1.1\,\sigma_\xi$ to $-0.1\,\sigma_\xi$. A detailed description of the experimental parameters of this study can be found in Section 4.5.1.
All time-resolved images from both simulations (Figures 6.2 a, b, d, e) and experiment

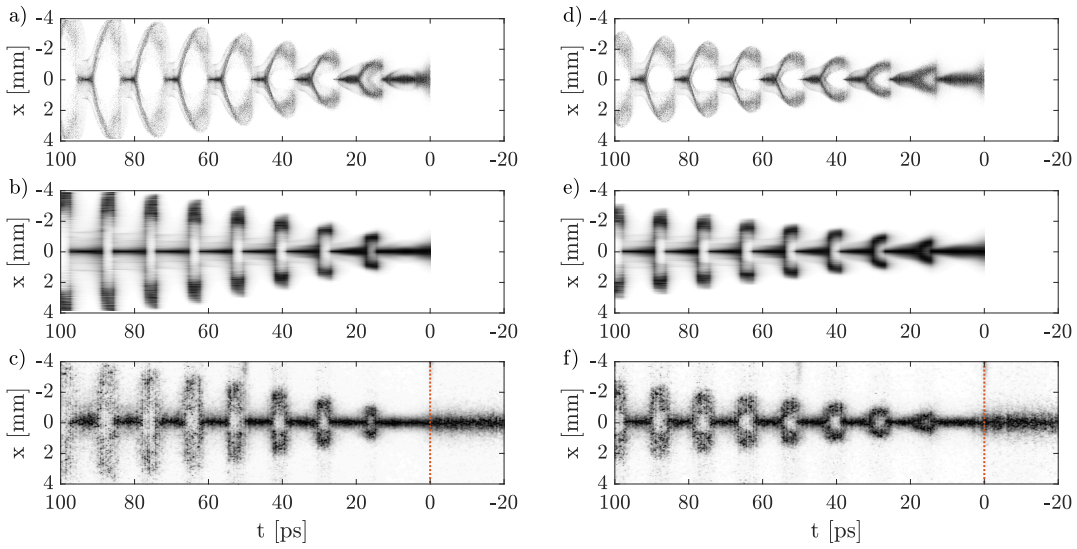

Figure 6.2: Normalized time-resolved images of the modulated bunch with seed position $n_b = 5.6 \cdot 10^{12}\,\mathrm{cm}^{-3}$ (a-c) and $n_b = 3.1 \cdot 10^{12}\,\mathrm{cm}^{-3}$ (d-f). Images (a, b) show the simulation results without, (b, e) with $\sigma_{res,t} = 1.5\,\mathrm{ps}$ Gaussian temporal resolution convolution and (c, f) the streak camera images. Here, $n_{pe} = 0.92 \cdot 10^{14}\,\mathrm{cm}^{-3}$ and $\Delta n_{pe} = 0$.

(Figures 6.2 c, f), show clearly the increase in transverse width of the defocused proton distributions along the bunch. The defocused protons have reached larger radii with higher (a-c) than with lower (d-f) initial bunch density in each and every defocused region. This is in agreement with the expectation that protons experience larger defocusing wakefield amplitudes due to the higher seed wakefield amplitudes and larger growth

rate for higher initial bunch density, i.e. higher for Figures (a-c) than for (d-f). In the following, the defocusing and divergence along the bunch for the first five periods is quantified for the different initial bunch densities.

6.1.1 Transverse Profiles of Defocused Proton Distributions

Transverse profiles of defocused proton distributions are analyzed from experiment and simulations. Their shape, width and maximum radius are compared to eventually conclude on protons experiencing a higher defocusing wakefield with higher initial bunch density.

Defocused Proton Distributions in Experiment

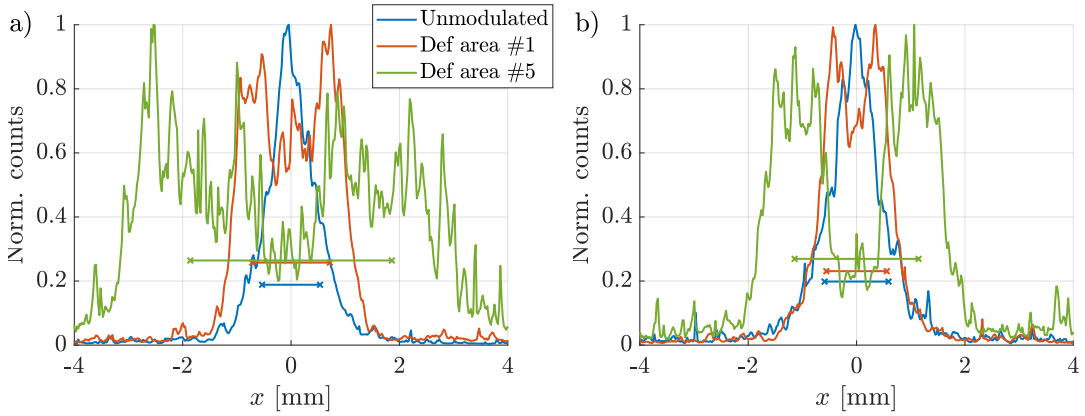

Figure 6.3: Normalized transverse defocused proton distributions from experiment with initial bunch density $n_b = 5.6 \cdot 10^{12}\,\mathrm{cm}^{-3}$ (a) and $n_b = 3.1 \cdot 10^{12}\,\mathrm{cm}^{-3}$ (b). Transverse profiles of the unmodulated head (blue lines), the first (red lines) and the fifth (green lines) period. The horizontal lines show the rms width of the given distribution with the respective colors. Here, $n_{pe} = 0.92 \cdot 10^{14}\,\mathrm{cm}^{-3}$ and $\Delta n_{pe} = 0$.

Figure 6.3 shows that the defocused proton distributions evolve as a ring (three dimensional), i.e. double peaks with minimum on-axis charge density for the (one dimensional) transverse profiles. With a radially linear defocusing field a Gaussian distribution, as that of the incoming bunch, would result in a wider Gaussian distribution. Therefore, the ring of defocused proton distributions indicates a radially non-linear defocusing field.
The radius of the ring increases along the bunch from the first (red lines) to fifth (green lines) period, and so is the rms width of the distributions (horizontal lines). This shows that protons of defocusing regions further along the bunch experience more defocusing fields, as expected from theory (Section 1.4.3). The defocused proton distributions are

wider than the freely (13.5 m of vacuum) propagated head of the bunch (blue lines).
The distributions of defocused protons from both periods are significantly wider for higher (Figure 6.3 a) than for lower (Figure 6.3 b) initial bunch density. The phase slippage between the wakefield and proton bunch over the first few periods is essentially independent of the here considered initial bunch densities, as established in Chapter 5 and in the appendix, Section A.7. Therefore, it is concluded that the stronger divergence of defocused proton distributions is indeed the result of larger wakefield amplitudes with higher initial bunch density due to higher seed wakefield amplitudes and a larger wakefield growth (Section 1.4.6).
The on-axis charge density does not reach zero for the profiles shown here. Potentially, this results from spatial and temporal resolution limits in the experiment, as analyzed by convoluting the simulation results later on.
Figure 6.4 shows that for all initial bunch densities the rms width σ_r of defocused proton

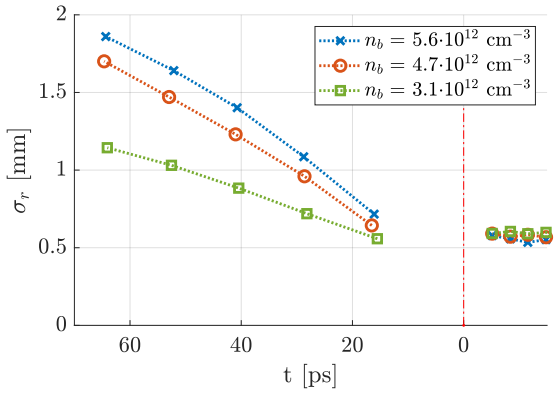

Figure 6.4: The rms width of defocused proton distributions along the bunch in experiment with initial bunch density $n_b = 5.6 \cdot 10^{12}\,\mathrm{cm}^{-3}$ (blue crosses), $n_b = 4.7 \cdot 10^{12}\,\mathrm{cm}^{-3}$ (red circles) and $n_b = 3.1 \cdot 10^{12}\,\mathrm{cm}^{-3}$ (green squares). RIF at $t = 0$; points at $t < 0$ correspond to rms bunch size from the unmodulated bunch head. Here, $n_{pe} = 0.92 \cdot 10^{14}\,\mathrm{cm}^{-3}$ and $\Delta n_{pe} = 0$.

distributions (horizontal lines on Figures 6.3) increases over period $\#1 - 5$ along the bunch. The widths over the first five periods are the larger, the higher the initial bunch density.
In the next section, I study from simulations whether this is the result of increasing wakefield amplitudes and/or increasing divergence distance due to earlier defocusing.

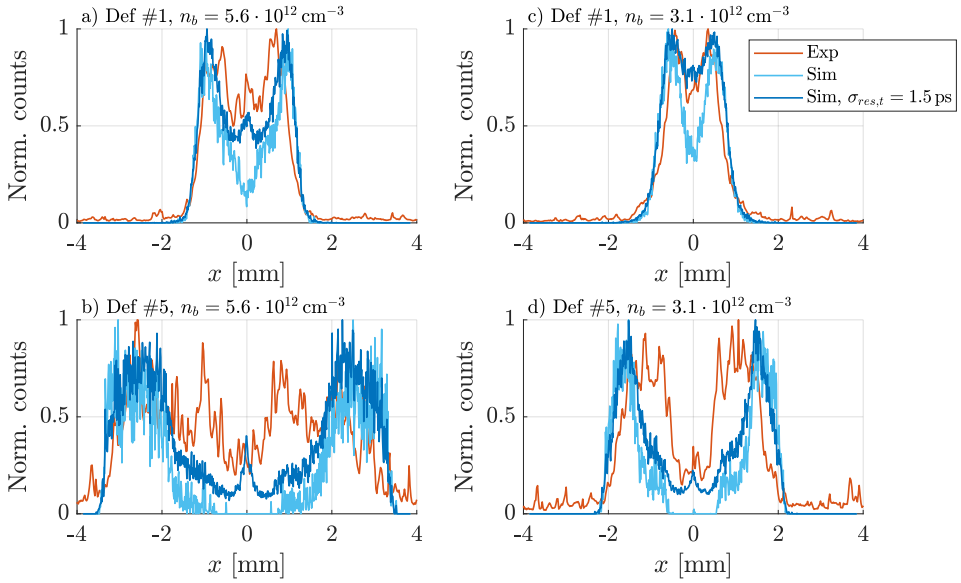

Figure 6.5: Transverse profiles of defocused proton distributions from experiment (red lines) and simulations without (bright blue lines) and with (dark blue lines) $\sigma_{res,t} = 1.5\,\mathrm{ps}$ Gaussian temporal resolution convolution, with initial bunch density $n_b = 5.6 \cdot 10^{12}\,\mathrm{cm}^{-3}$ (a, b) and $n_b = 3.1 \cdot 10^{12}\,\mathrm{cm}^{-3}$ (c, d), of the first period (a, c) and fifth period (b, d). Here, $n_{pe} = 0.92 \cdot 10^{14}\,\mathrm{cm}^{-3}$ and $\Delta n_{pe} = 0$.

Comparison Experiment - Simulations

Figure 6.5 shows that defocused proton distributions from experiment (red lines) and simulations (blue lines) have a very similar maximum radius, for both the first (a, c) and fifth period (b, d) and with both high (a, b) and low (c, d) initial bunch density. All profiles show that more charge remains on-axis ($x \approx 0$) in experiment than in the simulations. Temporal resolution convolution (dark blue lines) of the results from simulations (bright blue lines) better fits the experimental on-axis charge density and leads to a good agreement with experimental results. This suggests that focused proton regions (micro-bunches), longitudinally surrounding the defocused proton regions, increase the on-axis charge density of defocused proton distributions, due to the limited temporal resolution in experiment. The narrow on-axis peak in profiles from simulations, arising with convolution from charge of surrounding micro-bunches, is expected to smear out by spatial resolution in the experiment ($\sigma_{res,x} \approx 80\,\mu\mathrm{m}$, Section 3.2.1). Further, it is shown in the appendix (Section A.5) that a small spatial misalignment of the proton bunch OTR light onto the streak camera slit could lead to the disappearance of the on-axis peak in the profiles from simulations and could be a reason for the charge density of defocused

proton distributions to appear at slightly smaller radius in the experiment.

Width of Defocused Proton Distributions

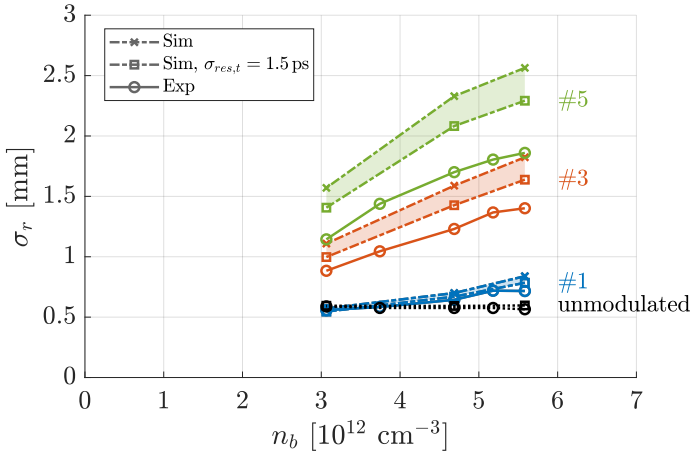

Figure 6.6: The rms width of defocused proton distributions from experiment (circles) and simulations without (crosses) and with (squares) $\sigma_{res,t} = 1.5\,\mathrm{ps}$ resolution convolution as a function of initial bunch density n_b of the first (blue symbols), third (red symbols) and fifth (green lines) period and rms width of unmodulated bunch (black symbols). Here, $n_{pe} = 0.92 \cdot 10^{14}\,\mathrm{cm}^{-3}$ and $\Delta n_{pe} = 0$.

The difference between the rms width of the defocused proton distributions and the unmodulated bunch is studied in Figure 6.6. The bunch head (black circles) is used for results from the experiment[1] and a bunch propagating 13.5 m in vacuum (black squares) for results from simulations. The rms widths of the defocused proton distributions are plotted for the first (blue symbols), third (red symbols) and fifth (green symbols) periods for various initial bunch densities. Convoluting the results from simulations (crosses) with the streak camera temporal resolution decreases the rms width (squares) due to the higher on-axis charge density from light of surrounding focused proton regions and leads to better agreement with the rms width measured in the experiment (circles). However, there is a higher on-axis charge density in the distributions from experiments than the convoluted simulations results (see Figure 6.5). Thus, the widths in the experiment are consistently smaller than that from simulations with convolution. The difference is increasing with increasing period and $\lesssim 22\,\%$ in period #5.

[1] The width of defocused proton distributions can be compared to either the unmodulated bunch head or to the bunch width from stitched images without plasma. As the latter consists of only two instead of 20 events (Section 3.2.3) it has a lower SNR and the width of the bunch head is used instead.

As earlier (Figures 6.2-6.5), Figure 6.6 shows the increasing width of defocused proton distributions along the bunch, which is consistent with the increasing transverse (defocusing) wakefield along the bunch. It also shows the general increase in width of defocused proton distributions with increasing initial bunch density, which is consistent with larger transverse wakefield amplitudes due to higher seed values and larger growth (Section 1.4.6).

The analysis shows that profiles and rms widths of the transverse distributions of defocused protons after the plasma from experiment and simulations are similar, over the first five periods and for various initial bunch densities. While the rms width from experiment is slightly smaller than that from simulations due to higher on-axis charge density, the maximum radius of defocused proton regions agree well. Thus, defocused protons must have accumulated a similar transverse (defocusing) wakefield in experiment and simulations. Therefore, the evolution of the transverse wakefield and bunch density modulation along the plasma is studied from simulations in the following.

6.1.2 Transverse Wakefield and Divergence in Simulations

The increase in transverse seed wakefield amplitudes and wakefield growth when increasing the initial bunch density is explained in Section 1.4.6 using linear theory, valid over a distance much shorter (a few meters) than the propagation distance of protons in the experiment. I therefore use numerical simulations, with similar parameters as the ones from the experiment, to study the evolution of the transverse wakefield all along the plasma.

Transverse Wakefield Evolution along the Plasma

Figure 6.7 shows the transverse wakefield $W_\perp$ at the initial bunch radius $\sigma_{r,0}$ of defocused proton distributions along plasma propagation z. Here, the higher initial bunch density corresponds to a seed position essentially central of the bunch ($\xi_{Seed} = -0.1\,\sigma_\xi$), whereas the lower one corresponds to $1.1\,\sigma_\xi$ ahead of the bunch center, see Table 4.5. Due to the adiabatic response (Section 1.4), initially, i.e. at $z = 0$, the transverse wakefield is only (mainly) focusing over the first five periods for the seeding ahead of (at) the bunch center.[2] Due to the phase slippage of the wakefield with respect to protons during SM (Sections 1.4.5 and A.7) the protons experience a focusing field over the first few meters of plasma. The transverse wakefield turns defocusing between $\sim 3 - 4\,\mathrm{m}$. The defocused

[2] As here the wakefield amplitude is evaluated at a fixed ξ, the initial amplitude is not necessarily stronger focusing for the seeding further ahead of the bunch center.

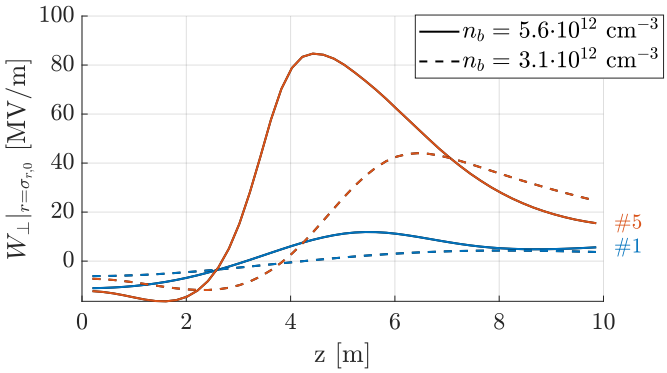

Figure 6.7: Transverse wakefield $W_\perp$ at $r = \sigma_{r,0}$ of defocused proton distributions of the first (blue lines) and fifth (red lines) period as a function of distance in plasma z with $n_b = 5.6 \cdot 10^{12}\,\mathrm{cm}^{-3}$ (solid lines) and $n_b = 3.1 \cdot 10^{12}\,\mathrm{cm}^{-3}$ (dashed lines). Here, $n_{pe} = 0.92 \cdot 10^{14}\,\mathrm{cm}^{-3}$ and $\Delta n_{pe} = 0$.

proton distributions of the fifth period (red lines) for both and of the first period for high initial bunch density (blue solid line) reach a maximum (between $\sim 4 - 6\,\mathrm{m}$) and decrease with further plasma propagation. The transverse wakefield experienced by the protons of the first period with low initial bunch density (blue dashed line) is small and has not reached its maximum over the 10 m of plasma, i.e. SM still evolves. Generally, the maximum defocusing field is reached earlier along the plasma for higher than for lower initial bunch density and the defocusing field increases along the bunch, as amplitudes increase from the first to the fifth period.

This analysis shows that the wakefield grows stronger for higher initial bunch density, as predicted from linear SMI theory. The wakefield's phase slippage is similar for the different initial bunch densities (see also Section A.7 in the appendix). The transverse wakefield turns defocusing at $z = 2.7 - 3.1\,\mathrm{m}$ with the higher and at $z = 3.8 - 4.2\,\mathrm{m}$ with the lower initial bunch density for the two periods shown in Figure 6.7. Thus, the main contribution to wider defocusing proton distributions is expected to come from larger wakefield amplitudes as opposed to different defocusing lengths. From the larger wakefield, defocused protons acquire larger transverse momentum and therefore a larger radius of defocused proton distributions with higher initial bunch density, as shown next.

Defocusing Evolution

The rms width of defocused proton distributions (at fixed ξ position, determined after the plasma) along propagation (10 m of plasma and subsequent 3.5 m of vacuum) is shown in Figure 6.8.

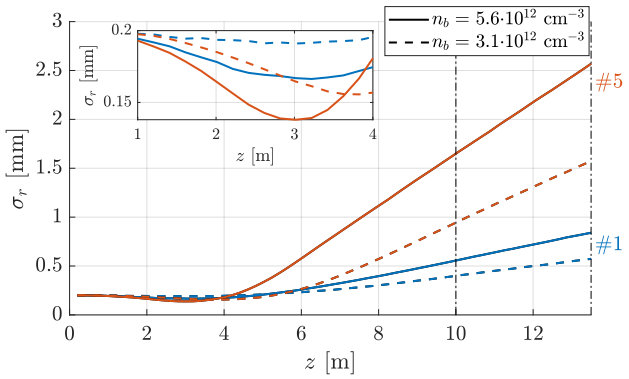

Figure 6.8: The rms width of defocused proton distributions σ_r as a function of propagation distance z (plasma $z = 1 - 10\,\mathrm{m}$, vacuum $z = 10 - 13.5\,\mathrm{m}$) with seed position $n_b = 5.6 \cdot 10^{12}\,\mathrm{cm}^{-3}$ (solid lines) and $n_b = 3.1 \cdot 10^{12}\,\mathrm{cm}^{-3}$ (dashed lines) at a fixed ξ of the first (blue lines) and fifth (red lines) period. Inset zooms in at $z = 1 - 4\,\mathrm{m}$. Here, $n_{pe} = 0.92 \cdot 10^{14}\,\mathrm{cm}^{-3}$ and $\Delta n_{pe} = 0$.

Due to the adiabatic response, the transverse wakefield is initially (mainly) focusing, thus protons are converging over the first few meters in plasma. Additionally, as a result of the phase slippage between wakefield and proton bunch during SM, protons at a fixed position along the bunch experience initially an increasing focusing wakefield before they are defocused by the transverse wakefield (see Figure 6.7). This leads to a minimum transverse width of defocused proton distributions over the first few meters, as shown in the inset of Figure 6.8.

With higher initial bunch density (solid lines) the transverse (focusing and defocusing) wakefield is stronger than with lower density (dashed lines), see Figure 6.7. This leads to slightly smaller transverse widths for the higher than for the lower initial bunch density, as shown in the inset of Figure 6.8. They are $\sim 170\,\mu\mathrm{m}$ (first period, blue solid line) and $\sim 140\,\mu\mathrm{m}$ (fifth period, red solid lines) for the high, and $\sim 190\,\mu\mathrm{m}$ (first period, blue dashed line) and $\sim 160\,\mu\mathrm{m}$ (fifth period, red dashed lines) for the low initial bunch density, i.e. they are less than 13 % smaller with the higher density. The minimum width is reached at similar plasma distances with the high ($z = 3.1 - 3.2\,\mathrm{m}$) as with the low density ($z = 3.0 - 3.8\,\mathrm{m}$).

Figure 6.8 shows that once diverging ($z > 6\,\mathrm{m}$), defocused proton distributions are much wider for higher than for lower initial bunch density. As the initially focusing field leads to similar minimum widths at similar positions in z for the different initial bunch densities, the dominant cause for the wider defocused proton distributions during divergence are the higher defocusing wakefield amplitudes.

Transverse Wakefield Experienced by Defocused Proton Distributions

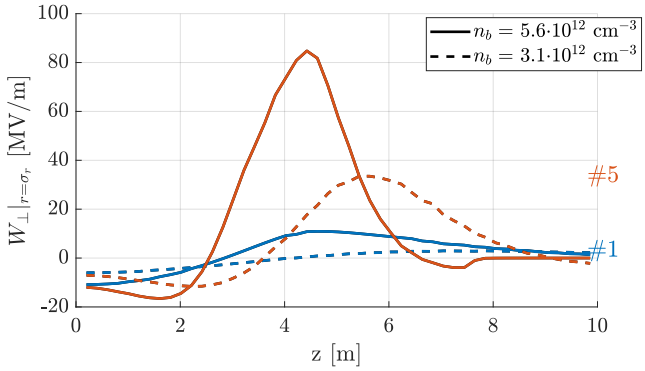

Figure 6.9: Transverse wakefield $W_\perp$ evaluated at the rms width of the proton distributions of the first (blue lines) and fifth (red lines) period as a function of distance in plasma z with $n_b = 5.6 \cdot 10^{12}\,\mathrm{cm}^{-3}$ (solid lines) and $n_b = 3.1 \cdot 10^{12}\,\mathrm{cm}^{-3}$ (dashed lines). Here, $n_{pe} = 0.92 \cdot 10^{14}\,\mathrm{cm}^{-3}$ and $\Delta n_{pe} = 0$.

Since defocused protons diverge in the shape of rings (see e.g. Figures 6.3 or 6.5), the transverse wakefield is evaluated at the radial position of the rms width of the defocused proton distributions in Figure 6.9. This represents the force experienced by the charge density distribution. It shows the increasing transverse wakefield from the first (blue lines) to the fifth (red lines) period, i.e. along the bunch, for both the initially focusing and subsequently defocusing field. Further, protons experience higher transverse wakefield amplitudes for higher (solid lines) than for lower (dashed lines) initial bunch density.
Diverging protons are defocused (i.e. cross from negative to positive $W_\perp$ on Figure 6.9) slightly earlier (approximately $\sim 2.5 - 2.8\,\mathrm{m}$) for the high, than for the low initial bunch density ($\sim 3.6 - 4.2\,\mathrm{m}$). They also reach the peak defocusing values earlier for high ($\sim 4.4 - 4.6\,\mathrm{m}$), than for low initial bunch density ($\sim 5.5 - 7.0\,\mathrm{m}$) and both earlier along the plasma for later along the bunch. This shows that SM evolves faster with higher initial bunch density due to the higher transverse wakefield amplitudes.
The total transverse momentum acquired by protons, and thus the radius of the distributions at the screen, is expected to increase together with the integral below the curves of Figure 6.9. It is therefore clear that later regions (#5 rather than #1) reach larger radii and that the radii are larger for higher initial bunch density, as it is observed in the time-resolved images from experiment and simulations.
While protons in the fifth period (red lines) experience a defocusing wakefield up to $\sim 85\,\mathrm{MV/m}$ for high, they only experience a defocusing wakefield $< 35\,\mathrm{MV/m}$ for low initial bunch density. Once more, this shows the significantly larger defocusing fields diverging protons experience for the higher initial bunch density, leading to the larger

distributions rms values observed in Figure 6.8.
With further propagation along the plasma, defocused proton distributions diverge further. Therefore, the transverse wakefield amplitudes, experienced by the protons, decrease faster than the transverse wakefields evaluated at a fixed radius (Figure 6.7), because protons leave the limited radial extent of the transverse wakefield. The decrease for low initial bunch density is slower, as protons reach large rms widths later along the plasma.

6.2 Effect of Plasma Density

According to linear theory, an increasing plasma density lowers the amplitude of the transverse seed wakefield, when keeping the bunch radius and charge constant. This is due to the fact that the charge in one skin depth decreases. At the same time, the growth rate at a given plasma period is independent of the plasma density, see Section 1.4.6. In the following, I analyze the defocusing of protons with different plasma densities (parameters described in Section 4.5.2) in order to determine whether a lower proton defocusing is measured for higher plasma density as a result of the lower seed wakefield amplitudes with a constant growth rate.
Figure 6.10 shows the normalized time-resolved images with low ($n_{pe} = 0.9 \cdot 10^{14}\,\mathrm{cm}^{-3}$, i.e. $\tau_{pe} = 11.1\,\mathrm{ps}$, Figures a-c) and with high plasma density ($n_{pe} = 2.9 \cdot 10^{14}\,\mathrm{cm}^{-3}$, i.e. $\tau_{pe} = 6.4\,\mathrm{ps}$, Figures d-f). The images with higher density have a shorter time axis than the images with lower density, but cover a similar number of modulation periods.
When convoluting the images from simulations (a, d) with the $\sigma_{res,t} = 1.5\,\mathrm{ps}$ Gaussian temporal resolution (b, e), the fixed temporal resolution affects especially the result with higher plasma density, due to the shorter plasma period and thus a plasma period even closer to the temporal resolution. For the high plasma density, the streak camera resolution corresponds to approximately one quarter of the plasma period, while approximately half of the plasma period is expected to be defocusing. Therefore, defocused proton distributions are not temporally resolved well with the higher plasma density and on-axis charge of surrounding micro-bunches is measured also in the defocused proton regions.
Also in the experimental time-resolved images (c, f) the defocused regions are better resolved for the low plasma density, i.e. their distributions reach approximately zero on-axis density for later periods. Similar to the convoluted image from simulation (e), the streak camera image with high plasma density (f) shows on-axis charge density also at defocused proton regions, whereas original images from simulations (a, d) do not.
Images from both simulations (a, b, d, e) and experiment (c, f) show slightly wider

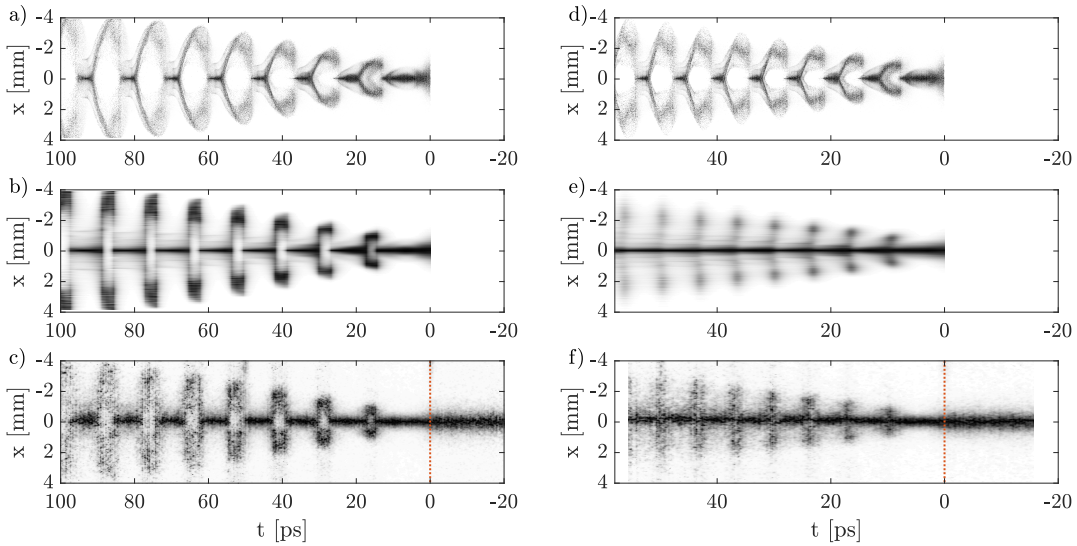

Figure 6.10: Normalized time-resolved images of the modulated bunch with plasma density $n_{pe} = 0.92 \cdot 10^{14}\,\mathrm{cm}^{-3}$ (a-c) and $n_{pe} = 2.9 \cdot 10^{14}\,\mathrm{cm}^{-3}$ (d-f). Images (a, b) show the simulations without, (b, e) with Gaussian temporal resolution convolution with $\sigma_{res,t} = 1.5\,\mathrm{ps}$ and (c, f) the streak camera images. Here, $n_b = 5.6 \cdot 10^{12}\,\mathrm{cm}^{-3}$ and $\Delta n_{pe} = 0$.

defocused proton distributions for the low (a-c) than for the high (d-f) plasma density. While for the low plasma density defocused protons exceed the experimental field of view ($x = \pm 4\,\mathrm{mm}$) from the seventh period on, for the high density defocused protons have not reached the field of view limit over the eighth periods shown here.

6.2.1 Transverse Profiles of Defocused Proton Distributions

Figure 6.11 shows the change in profiles of defocused proton distributions for different plasma densities. At lower density ($n_{pe} = 0.9 \cdot 10^{14}\,\mathrm{cm}^{-3}$) the first (a) and the fifth (b) period show the previously discussed ring distribution of defocused protons with lower on-axis charge density (Section 6.1.1). At higher density ($n_{pe} = 2.9 \cdot 10^{14}\,\mathrm{cm}^{-3}$) the distributions show an on-axis charge density peak for both periods for the experiment (red lines) and convoluted simulation results (dark blue lines).
The difference between the convoluted and non convoluted (bright blue lines) profiles is, as expected, larger for the higher plasma density, corresponding to a shorter wakefield period, thus shorter modulation period. In all cases, the convolution leads to better agreement between simulations and experimental results. The narrow central peak from the convoluted simulation results is expected to be smeared out in the experiment due

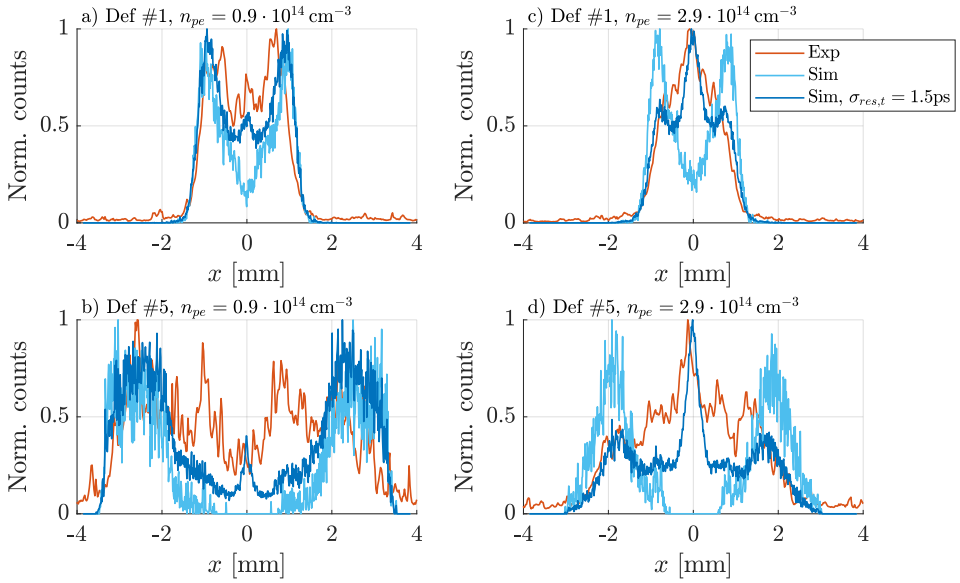

Figure 6.11: Transverse profiles of defocused proton distributions from experiment (red lines) and simulations without (bright blue lines) and with (dark blue lines) $\sigma_{res,t} = 1.5\,\mathrm{ps}$ Gaussian temporal resolution convolution; with plasma density $n_{pe} = 0.9 \cdot 10^{14}\,\mathrm{cm}^{-3}$ (a, b) and $n_{pe} = 2.9 \cdot 10^{14}\,\mathrm{cm}^{-3}$ (c, d), of the first period (a, c) and fifth period (b, d). Here, $n_b = 5.6 \cdot 10^{12}\,\mathrm{cm}^{-3}$ and $\Delta n_{pe} = 0$.

to the limited spatial resolution, the finite slit width of the streak camera and possibly with small spatial misalignment of the light onto the camera slit, if present (see appendix, Section A.5).

At larger radius, the distributions are not affected strongly by the temporal resolution due to the smaller transverse width of surrounding micro-bunches (Section 5.4). The profiles of the fifth period (Figure 6.11 b, d) show that the maximum radius of defocused proton distributions is indeed larger with lower plasma density ($\sim 3.5\,\mathrm{mm}$) than with higher density ($\sim 3.0\,\mathrm{mm}$) in experiment and simulations. In general, for both experiment and simulations the increase in plasma density results in a decrease in width of defocused proton distributions. This is in agreement with a lower defocusing wakefield for higher plasma density, due to lower transverse seed wakefield, whereas the growth rate is not affected when comparing a given plasma period behind the seed position (see Section 1.4.6). The difference is not significant for the first period (Figure 6.11 a, c).

The profiles of both plasma densities and both defocusing periods show good agreement in terms of maximum radius of defocused protons and transverse shape. This underlines again the reliability of the simulations in this regime. They allow to study the self-modulation and wakefield evolution along the plasma and to decouple the effect of the

transverse wakefield and the temporal resolution on the results.
Due to the limited temporal resolution, the rms width of the defocused proton distributions decreases by the overlap with charge density from surrounding micro-bunches, as shown in the following. This effect is the stronger, the shorter the plasma period, i.e. the higher the plasma density.

Width of Defocused Proton Distributions

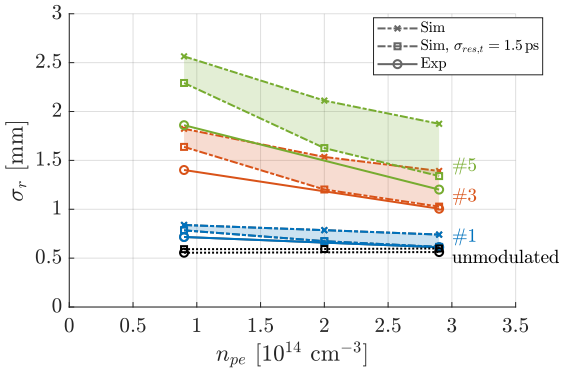

Figure 6.12: The rms width of defocused proton distributions from experiment (circles) and simulations without (crosses) and with (squares) $\sigma_{res,t} = 1.5\,\mathrm{ps}$ resolution convolution as a function of plasma density n_{pe} of the first (blue symbols), third (red symbols) and fifth (green symbols) period and rms width of unmodulated bunch (black symbols). Here, $n_b = 5.6 \cdot 10^{12}\,\mathrm{cm}^{-3}$ and $\Delta n_{pe} = 0$.

Figure 6.12 compares the rms width of defocused proton distributions of the first (blue symbols), third (red symbols) and fifth (green symbols) period to the width of the unmodulated bunch (black symbols) from experiment and simulations. It shows that while the resolution convolution reduces the rms width of the defocused proton distributions due to charge density overlap with surrounding micro-bunches, the width from simulations after convolution (squares) generally remain $< 25\,\%$ wider than experimental (circles) ones.
Overall, the widths of the distributions decrease for increasing plasma density, in experiment and simulations. This is in agreement with expectations of stronger defocusing due to higher transverse seed wakefield amplitudes and similar growth rate for lower plasma density (Section 1.4.6).
The increase in plasma density from $0.9 \cdot 10^{14}\,\mathrm{cm}^{-3}$ to $2.9 \cdot 10^{14}\,\mathrm{cm}^{-3}$, for the given experimental parameters (Section 4.5.2), leads to a decrease of the transverse seed wakefield from $-6.5\,\mathrm{MV/m}$ to $-5.5\,\mathrm{MV/m}$, i.e. by $\sim$ 15%. In the experiment, the defocused width of the fifth period decreases from 1.9 mm to 1.2 mm, i.e. by $\sim$ 37%. However, the larger decrease in rms width for the higher plasma density is expected

to be a combination of the lower transverse wakefield and the lower relative temporal resolution.
Original simulation results without convolution (crosses) confirm that the decrease in defocused width for increasing plasma density is not only an effect of temporal resolution but indeed the result of lower transverse wakefield amplitudes. Their width of the fifth period decrease from 2.6 mm to 1.9 mm, i.e. by $\approx 27\%$.

6.2.2 Transverse Wakefield and Divergence in Simulations

After having established a good agreement between defocused proton distributions from experiment and simulations, the wakefield and SM evolution along the plasma is studied from simulations.

Transverse Wakefield Evolution along the Plasma

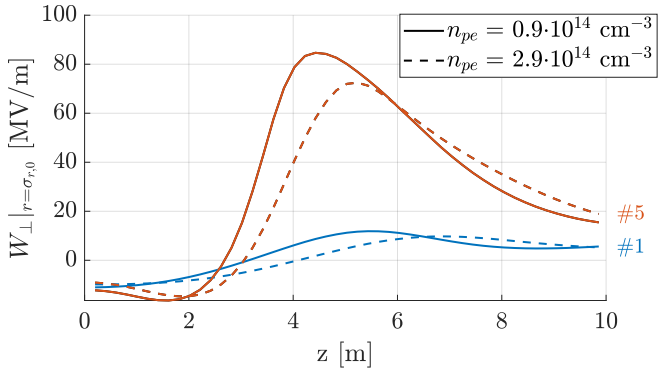

Figure 6.13: Transverse wakefield $W_\perp$ at $r = \sigma_{r,0}$ of defocused proton distributions of the first (blue lines) and fifth (red lines) period as a function of distance in plasma z with plasma density $n_{pe} = 0.9 \cdot 10^{14}\,\mathrm{cm}^{-3}$ (solid lines) and $n_{pe} = 2.9{\cdot}10^{14}\,\mathrm{cm}^{-3}$ (dashed lines). Here, $n_b = 5.6{\cdot}10^{12}\,\mathrm{cm}^{-3}$ and $\Delta n_{pe} = 0$.

The amplitudes of the transverse wakefields of defocused proton distributions of the first (blue lines) and fifth (red lines) period are fairly similar for lower ($n_{pe} = 0.9 \cdot 10^{14}\,\mathrm{cm}^{-3}$, solid lines) and higher ($n_{pe} = 2.9 \cdot 10^{14}\,\mathrm{cm}^{-3}$, dashed lines) plasma density, see Figure 6.13. Wakefield amplitudes evolve from initially focusing to defocusing similarly for the different plasma densities, as expected from the similar phase slippage for different plasma densities, described in the appendix (Section A.7).
The fifth defocusing peak amplitude is slightly higher (85 MV/m) and reached slightly earlier (4.4 m) for lower plasma density than for higher plasma density (72 MV/m at

5.2 m). Again this shows a slightly faster SM evolution due to the higher amplitude of the transverse seed wakefield at lower density. After the peak ($z > 6$ m), the wakefield amplitudes decrease and converge to similar values with the two plasma densities for both periods.
As explained in Section 1.4.6, a lower amplitude of the transverse seed wakefield is expected for higher plasma density, while the growth rate of a given plasma period is similar. This is consistent with the small decrease in wakefield amplitudes as seen in the simulation results when increasing the plasma density.

Defocusing Evolution

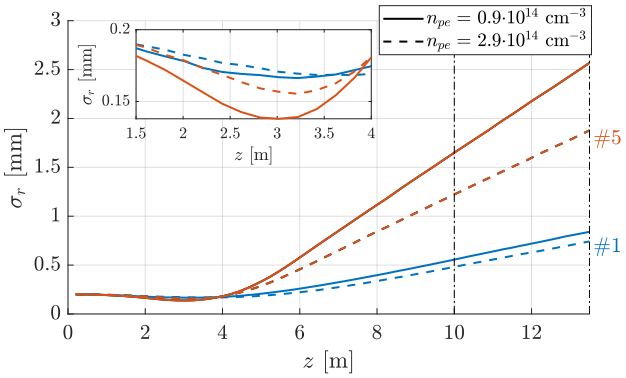

Figure 6.14: The rms width of defocused proton distributions σ_r as a function of propagation distance z (plasma $z = 1 - 10$ m, vacuum $z = 10 - 13.5$ m) with plasma density $n_{pe} = 0.9 \cdot 10^{14}\,\mathrm{cm}^{-3}$ (solid lines) and $n_{pe} = 2.9 \cdot 10^{14}\,\mathrm{cm}^{-3}$ (dashed lines) at a fixed ξ of the first (blue lines) and fifth (red lines) period. Inset zooms in at $z = 1.5 - 4$ m. Here, $n_b = 5.6 \cdot 10^{12}\,\mathrm{cm}^{-3}$ and $\Delta n_{pe} = 0$.

Figure 6.14 shows that, once diverging ($z > 5$ m), the rms width of defocused proton distributions of the first (blue lines) and fifth (red lines) period are consistently wider with lower (solid lines) than with higher (dashed lines) plasma density.
The minima of the transverse distributions are reached at similar distances in plasma ($\sim 3.0 - 3.4$ m) for the different periods and for different plasma densities. The minimum transverse width for lower plasma density (~ 0.14 mm, see inset) is only slightly smaller than for higher plasma density (~ 0.16 mm). This is consistent with the slightly larger transverse seed wakefield amplitude with lower density, leading to a stronger focusing in the first few meters before the wakefield turns defocusing due to the phase slippage between the wakefield and protons. As previously observed for various initial bunch densities, also for the different plasma densities, the similar minimum width at a similar

position along the plasma implies that the slightly stronger divergence for $z > 5\,\mathrm{m}$, at lower plasma density, originates from slightly larger defocusing wakefield amplitudes. This is consistent with what was shown in Figure 6.13.

Transverse Wakefield Experienced by Defocused Proton Distributions

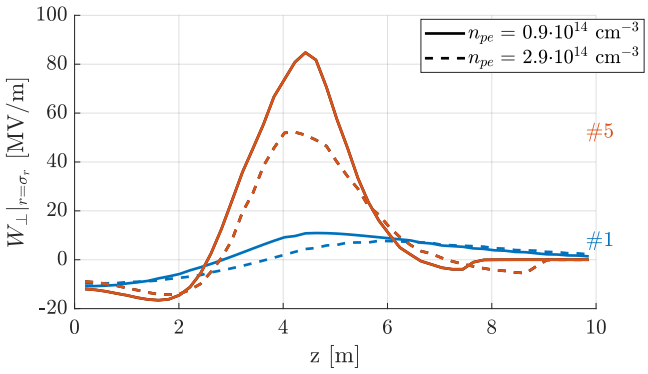

Figure 6.15: Transverse wakefield $W_\perp$ evaluated at the rms width of the proton distributions of the first (blue lines) and fifth (red lines) period as a function of distance in plasma z with plasma density $n_{pe} = 0.9 \cdot 10^{14}\,\mathrm{cm}^{-3}$ (solid lines) and $n_{pe} = 2.9 \cdot 10^{14}\,\mathrm{cm}^{-3}$ (dashed lines). Here, $n_b = 5.6 \cdot 10^{12}\,\mathrm{cm}^{-3}$ and $\Delta n_{pe} = 0$.

As in the analysis for different initial bunch densities, in Figure 6.15, the transverse wakefield is evaluated at the radial position of the rms width of the defocused proton distributions along the plasma for the different plasma densities. Both low (solid lines) and high (dashed lines) densities and both first (blue lines) and fifth (red lines) periods show that due to the phase slippage of the wakefield with respect to the proton bunch during SM, protons are initially focused and start to experience a defocusing field from $\sim 3\,\mathrm{m}$ on.

The wakefield reaches maximum defocusing amplitudes at $\sim 4-5\,\mathrm{m}$ before protons transversely leave the wakefield and thus experience rapidly decreasing wakefield amplitudes. Defocusing wakefield amplitudes, experienced by the protons, are consistently larger for the lower plasma density. Defocused proton distributions of the fifth period reach maximum amplitudes of $\sim 85\,\mathrm{MV/m}$ with low and $\sim 50\,\mathrm{MV/m}$ with high plasma density. The consistently slightly larger defocusing field, as also expected from linear wakefield theory, leads to a larger divergence of protons at lower plasma density, as observed in the time-resolved images from experiment and simulations (Figures 6.10 and 6.11).

6.3 Effect of Plasma Density Gradients

In all cases discussed so far in this chapter, the plasma density is constant over the 10 m long plasma. However, imposing a density gradient can influence the SM development, since during SM growth the wakefield's phase velocity is smaller than that of the protons (Section 1.4.5 and [22]). Therefore, increasing the phase velocity by imposing a positive gradient, or decreasing it with a negative one, is predicted to influence the SM growth rate [27].
The time-resolved images of the self-modulated proton bunch with different plasma density gradients (Figure 4.11) also show a change in divergence of defocused proton distributions in both experiment and simulations. Defocused proton distributions are significantly wider for negative than for positive density gradients. As the plasma density at the entrance remains constant during the study and only the downstream density is varied, the amplitudes of the seed wakefield in the different gradient measurements are identical. This implies, by measuring a change in proton divergence, an effect of the plasma density gradient on the wakefield evolution (e.g. wakefield growth or phase slippage) is measured. The experimental parameters of this study are summarized in Section 4.5.3.

The normalized time-resolved images obtained after the plasma from simulations (a, d), their results convoluted with the streak camera temporal resolution (b, e) and from experiment (c, f) are shown in Figure 6.16, for the most negative density gradient ($\Delta n_{pe} = -1.9\,\%/\mathrm{m}$, Figures a-c) and for the most positive density gradient ($\Delta n_{pe} = 2.0\,\%/\mathrm{m}$, Figures d-f). One can see in all images that defocused proton distributions are wider for $\Delta n_{pe} < 0$ than for $\Delta n_{pe} > 0$, with widths increasing along the bunch. They increase faster for $\Delta n_{pe} < 0$ than for $\Delta n_{pe} > 0$ both in experiment and simulations.
As established also in Section 5.5, the on-axis charge density with positive density gradient is significantly larger than with negative density gradient. This is expected from the counteracting of the phase slippage between the wakefield and protons with a positive density gradient, see Figure 5.21.
Comparing the convolution of the negative (b) and positive (e) density gradient with the original images (a) and (d), one can see the significantly larger change with the positive density gradient. Thus, simulations confirm that the higher on-axis charge density of micro-bunches, surrounding defocused proton regions, with a positive density gradient increases the effect of the limited temporal resolution on defocused proton distributions.

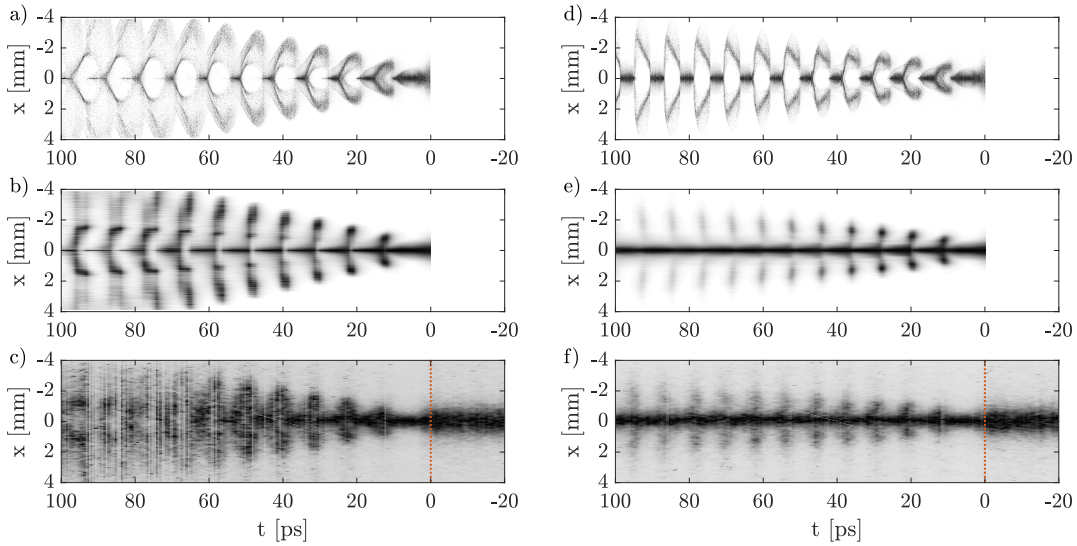

Figure 6.16: Normalized time-resolved images of the modulated bunch with plasma density gradient $\Delta n_{pe} = -1.9\,\%/\mathrm{m}$ (a-c) and $\Delta n_{pe} = 2.0\,\%/\mathrm{m}$ (d-f). Images (a, b) show the simulations without, (b, e) with Gaussian temporal resolution convolution with $\sigma_{res,t} = 1.5\,\mathrm{ps}$ and (c, f) the streak camera images. Here, the plasma entrance density is fixed to $n_{pe,Entr.} = 1.8 \cdot 10^{14}\,\mathrm{cm}^{-3}$ and $n_b = 5.6 \cdot 10^{12}\,\mathrm{cm}^{-3}$.

6.3.1 Transverse Profiles of Defocused Proton Distributions

As also established in the other measurements, Figure 6.17 shows a good agreement of the maximum radius of defocused proton distributions in experiment and simulations for the first (a, c) and fifth (b, d) period. Figure 6.17 confirms that defocused proton distributions are significantly wider with negative (a, b) than with positive (c, d) plasma density gradient in experiment and simulations. This is especially clear for the profiles of period #5, with a maximum radius of the distribution of $\sim 3.5\,\mathrm{mm}$ for $\Delta n_{pe} < 0$ and of $\sim 2\,\mathrm{mm}$ for $\Delta n_{pe} > 0$.

None of the defocused proton distributions from experiment (red lines), analyzed here, show the clear ring structure (double peak in one dimensional profiles), as discussed for the measurements with various initial bunch densities (Section 6.1.1). However, due to the higher plasma density ($n_{pe,Entr.} = 1.8 \cdot 10^{14}\,\mathrm{cm}^{-3}$, i.e. $\tau_{pe,Entr.} = 8.3\,\mathrm{ps}$) here, the relative temporal resolution of the streak camera ($\sigma_{res,t} \approx 1.5\,\mathrm{ps}$) is lower, which leads to more on-axis charge density in defocused regions from surrounding micro-bunches. Further, as mentioned earlier, during the gradient scan the 211 ps streak camera time window was used, as opposed to the 73 ps window for the initial bunch or plasma density scan, which potentially decreased the temporal resolution of the measurement (see Section 3.2.1).

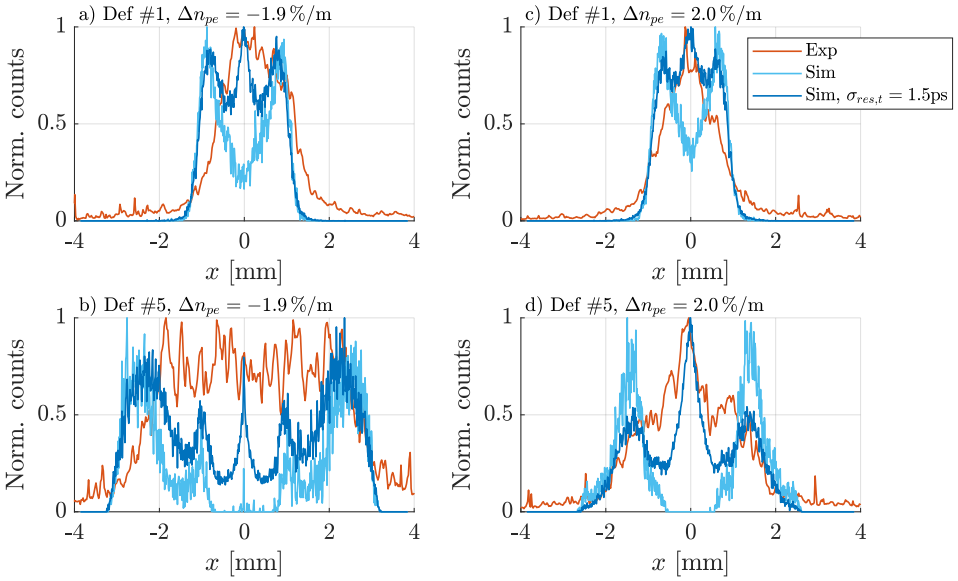

Figure 6.17: Transverse profiles of defocused proton distributions from experiment (red lines) and simulations without (bright blue lines) and with (dark blue lines) $\sigma_{res,t} = 1.5\,\mathrm{ps}$ Gaussian temporal resolution convolution; with plasma density gradient $\Delta n_{pe} = -1.9\,\%/\mathrm{m}$ (a, b) and $\Delta n_{pe} = 2.0\,\%/\mathrm{m}$ (c, d), of the first period (a, c) and fifth period (b, d). Here, $n_{pe,Entr.} = 1.8 \cdot 10^{14}\,\mathrm{cm}^{-3}$ and $n_b = 5.6 \cdot 10^{12}\,\mathrm{cm}^{-3}$.

Due to the significantly higher on-axis charge density of micro-bunches with a positive gradient, as determined in Section 5.5, the effect of the temporal resolution is stronger with positive density gradient, as clearly visible on Figure d). Therefore, the defocused proton distributions from experiment show a relatively flat top profile for negative density gradient (Figures a, b) while they show a central charge density peak (Figures c, d) for positive density gradient. The profiles of the fifth defocusing period with positive gradient (Figure d) shows especially clearly an overlap of two profiles, the defocused protons (wide double peak) with the on-axis peak from surrounding micro-bunches.

This is confirmed by simulations. The defocused proton distributions from simulations (bright blue lines) show significantly lower on-axis charge density for the first periods and even full depletion for the fifth periods. When convoluting the time-resolved images from simulations with the streak camera temporal resolution (dark blue lines) the central dip is less dominant (negative gradient) or even turns into a peak (positive gradient), similarly to the experiment.

After resolution convolution the shape of the defocused proton distributions from simulations agree well with the experimental ones. The convolution of the simulation results from the fifth period with negative density gradient does not recover the charge-density

measured in the experiment. As established earlier, the evolution of the micro-bunches is an intricate process. Here, also the observed defocused proton distributions are significantly influenced by the shape of surrounding micro-bunches, which is assumed to lead to the larger differences between experiment and simulations.
The rms widths of the distributions are analyzed in the following. However, the effect of the temporal resolution decreases the rms width more with positive than with negative density gradient due to higher on-axis charge density remaining in micro-bunches.

Width of Defocused Proton Distributions

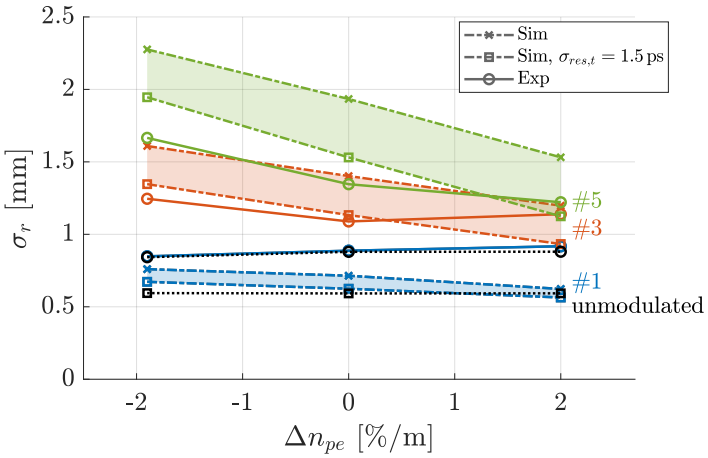

Figure 6.18: The rms width of defocused proton distributions from experiment (circles) and simulations without (crosses) and with (squares) $\sigma_{res,t} = 1.5$ ps resolution convolution as a function of plasma density gradient Δn_{pe} of the first (blue symbols), third (red symbols) and fifth (green symbols) period and rms width of unmodulated bunch (black lines). Here, $n_{pe,Entr.} = 1.8 \cdot 10^{14}\,\mathrm{cm}^{-3}$ and $n_b = 5.6 \cdot 10^{12}\,\mathrm{cm}^{-3}$.

The rms width of the defocused proton distributions for different plasma density gradients (Figure 6.18) leads to the same conclusions as those drawn from the profiles (Figure 6.17). There is a good agreement in terms of trend, but differences in values, with much smaller difference between convoluted simulation (squares) and experimental (circles) results.
Since the profiles (Figure 6.17) change from period #1 to #5, one should compare the rms widths with different gradients for the individual periods only. However, one can see the general trend of increasing defocused width for a negative density gradient and decreasing defocused width for a positive gradient, both in experiment and simulations. The results from simulations without convolution (crosses) confirm that the increase (decrease) in defocused proton distribution width with more negative (positive) gradient

is not only an effect of limited temporal resolution of the diagnostic.

6.3.2 Transverse Wakefield and Divergence in Simulations

A good general agreement between experiment and simulations is obtained for defocused proton distributions with varying plasma density gradients, as measured after the plasma. Thus, again simulations are used to study the evolution of the wakefield and SM along the plasma, here with density gradient.

Transverse Wakefield Evolution along the Plasma

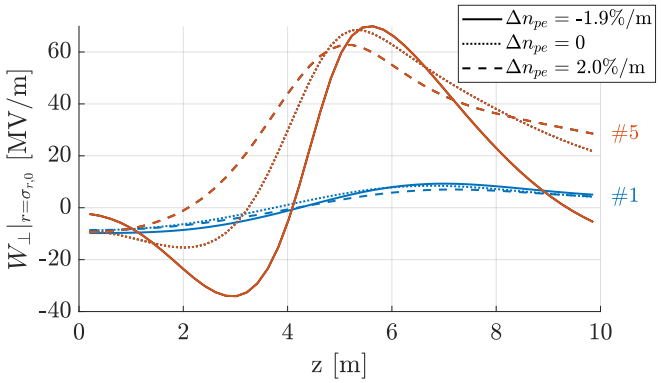

Figure 6.19: Transverse wakefield $W_\perp$ at $r = \sigma_{r,0}$ of defocused proton distributions of the first (blue lines) and fifth (red lines) period as a function of distance in plasma z with plasma density gradient $\Delta n_{pe} = -1.9\,\%/\mathrm{m}$ (solid lines) $\Delta n_{pe} = 0$ (dotted lines) and $\Delta n_{pe} = 2.0\,\%/\mathrm{m}$ (dashed lines). Here, $n_{pe,Entr.} = 1.8 \cdot 10^{14}\,\mathrm{cm}^{-3}$ and $n_b = 5.6 \cdot 10^{12}\,\mathrm{cm}^{-3}$.

The transverse wakefield amplitudes of the defocused proton distributions at a fixed radial position $r = \sigma_{r,0}$ are plotted in Figure 6.19. As here the position along the bunch ξ is fixed, these curves correspond to vertical lines in Figures 5.21 a) and c). Due to the counteracting of the phase slippage between the wakefield and protons with a positive density gradient (dashed lines), the transverse wakefield of the fifth period (red lines) becomes less focusing (due to the adiabatic response) from the start of the plasma $z = 0$, turns defocusing after a few meters ($\sim 2\,\mathrm{m}$) and stays defocusing until the end of the plasma. With negative density gradient (solid lines), the phase slippage is enhanced, as shown clearly by the strong initial focusing of the fifth defocused proton distribution, stronger than with constant density ($\Delta n_{pe} = 0$, dotted lines). The transverse wakefields of defocused protons of the first period (blue lines) are very similar for the different

gradient cases.
The defocusing wakefield reaches slightly higher peak amplitudes with negative (70 MV/m for period #5) than with positive (63 MV/m for period #5) density gradient for both periods. The wakefield amplitudes of the fifth period reach their peak at ~ 5 m before decreasing. Overall, the difference in defocusing amplitudes between $\Delta n_{pe} < 0$, $\Delta n_{pe} = 0$ and $\Delta n_{pe} > 0$ is relatively small in both cases (period #1 and #5). The maximum defocusing amplitude with positive gradient is 90% of the one with negative gradient. The small difference in defocusing wakefield amplitudes shown here is not expected to lead to a difference in proton defocusing as large as it is observed in experiment and simulations with the time-resolved images (see Figures 6.16 and 6.17).

Defocusing Evolution

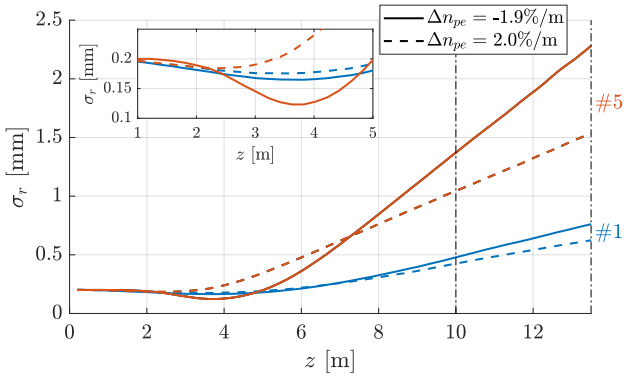

Figure 6.20: The rms width of defocused proton distributions σ_r as a function of propagation distance z (plasma $z = 1-10$ m, vacuum $z = 10-13.5$ m) with plasma density gradient $\Delta n_{pe} = -1.9\,\%/\text{m}$ (solid lines) and $\Delta n_{pe} = 2.0\,\%/\text{m}$ (dashed lines) at a fixed ξ of the first (blue lines) and fifth (red lines) period. Inset zooms in at $z = 1-5$ m. Here, $n_{pe,Entr.} = 1.8 \cdot 10^{14}\,\text{cm}^{-3}$ and $n_b = 5.6 \cdot 10^{12}\,\text{cm}^{-3}$.

Figure 6.20 shows the evolution along the plasma of the rms width of the transverse defocused proton distributions, chosen at a fixed ξ (determined from the defocused proton regions after the plasma). One can see after the plasma ($z > 10$ m) defocused proton distributions diverge faster with negative (solid lines) than with positive (dashed lines) density gradient, for both the first (blue line) and fifth (red lines) periods.
The inset (zoom at $z = 1-5$ m) shows that with positive density gradient, protons are only slightly converging because the initially focusing fields (Figure 6.19) are small and they have to counteract the natural beam divergence. The minimum transverse size of $\sigma_r \approx 180\,\mu$m here is close to the initial transverse size $\sigma_{r,0} = 200\,\mu$m. The positive density

gradient compensates the phase slippage of the wakefield with respect to the protons' velocity. Thus, defocused proton distributions experience defocusing fields early in z and start diverging at $\sim 3\,\mathrm{m}$. However, transverse wakefield amplitudes are larger close to the beam axis ($\lesssim \sigma_{r,0}$, see Section A.7 in the appendix) and have not reached their peak value at this distance in plasma yet. Both these effects lead to defocused proton distributions experiencing smaller defocusing wakefield amplitudes without the initial convergence with the positive density gradient.
The negative density gradient increases the phase slippage of the wakefield with respect to the protons. Therefore, protons that diverge after the plasma, experienced initially increasing focusing fields, as established from Figure 6.19. With a negative gradient, protons are converging significantly stronger (inset of Figure 6.20). The minimum transverse size of the fifth period reaches significantly smaller values ($\sigma_r \approx 120\,\mu\mathrm{m}$), almost a factor of 2 smaller than the initial transverse size $\sigma_{r,0}$. Due to the smaller radial position they experience larger wakefield amplitudes. They start diverging and thus experience defocusing fields later in z, where the wakefield has grown to larger amplitudes, see Figure 6.19. Both the effects described here lead to a stronger divergence of defocused proton distributions with negative density gradient.
Therefore, the increase in defocused width for a more negative density gradient is mainly assigned to the increase in phase slippage between the wakefield and protons and thus the experience of the initially increasing focusing field, as opposed to higher transverse wakefield amplitudes.

Transverse Wakefield Experienced by Defocused Proton Distributions

The transverse wakefield at the ξ position of the defocused protons for the first (blue lines) and fifth (red lines) period are shown in Figure 6.21. Here, the wakefield is evaluated at the radial position equal to the rms width of the transverse profiles of defocused proton distributions (see Figure 6.20), determined at each z, as opposed to evaluated at $r = \sigma_{r,0}$ as on Figure 6.19.
As shown before, due to the wakefield's phase slippage during the SM, the protons that end up as defocused protons after the plasma are initially focused. This can be very clearly seen for period #5. Also, in the negative gradient case (solid line), the experienced wakefield remains focusing over a much longer distance ($\sim 4\,\mathrm{m}$) and is much stronger (focusing field $-W_\perp \approx 36\,\mathrm{MV/m}$) than in the positive density gradient case (dashed lines, $z < 2\,\mathrm{m}$, focusing field $-W_\perp < 10\,\mathrm{MV/m}$). With the positive gradient, the initially focusing field does not increase its strength along the plasma.
With positive gradient, protons experience a defocusing field earlier in z and earlier further

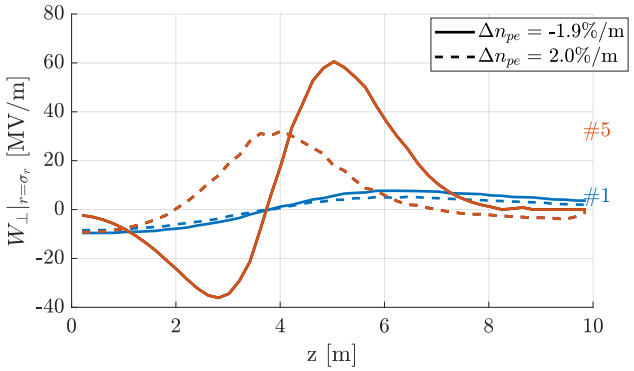

Figure 6.21: Transverse wakefield $W_\perp$ evaluated at the rms width of the proton distributions of the first (blue lines) and fifth (red lines) period as a function of distance in plasma z with plasma density gradient $\Delta n_{pe} = -1.9\,\%/\mathrm{m}$ (solid lines) and $\Delta n_{pe} = 2.0\,\%/\mathrm{m}$ (dashed lines). Here, $n_{pe,Entr.} = 1.8 \cdot 10^{14}\,\mathrm{cm}^{-3}$ and $n_b = 5.6 \cdot 10^{12}\,\mathrm{cm}^{-3}$.

along the bunch. Maximum defocusing amplitudes with positive gradient ($\sim 30\,\mathrm{MV/m}$) are a factor of 2 lower than with negative gradient ($\sim 60\,\mathrm{MV/m}$). This is explained by the lack of initial convergence of finally defocused protons with positive gradient: They reach their maximum experienced defocusing field earlier in z (lower wakefield amplitudes before saturation) and further away from the beam axis (where wakefield amplitudes are large) due to a larger transverse size, see Figure 6.20.
After the protons reach the maximum of experienced defocusing field, the transverse wakefield decreases for both gradients. This is a combination of decreasing wakefield amplitudes along the plasma (Figure 6.19) and larger radial position of the diverging protons, where wakefield amplitudes are also lower.
Once the bunch is fully self-modulated, the presence of a gradient itself is the cause of phase slippage, as indicated by the evolution of re-focusing fields for defocused protons at later z. The earlier the saturation, the more severe the effect of the gradient due to the longer propagation distance with a plasma off-resonance.

This analysis shows that with a negative density gradient, protons that diverge after the plasma experience stronger focusing over the first few meters in plasma. The focusing field keeps protons close to the bunch axis until later distances z. Thus, the protons experience a stronger defocusing wakefield, as wakefield amplitudes grow over the first ($\sim 4\,\mathrm{m}$) in plasma, during SM. Thus, the significantly wider (narrower) defocused proton distributions with more negative (positive) density gradient, visible in time-resolved images after the plasma (Figure 6.16 and 6.17), are not assigned to strongly increasing (decreasing) transverse wakefield amplitudes but to the increasing (decreasing) phase

slippage between the wakefield and protons.

6.4 Conclusion

All measurements reveal an increasing width of defocused proton distributions along the bunch. Simulations show that for each measurement the defocusing field starts at similar distances in plasma for the first five periods. Therefore, this gives evidence for the growth of transverse (defocusing) wakefield amplitudes along the bunch.
It was shown that the on-axis charge density of defocused proton distributions is affected by surrounding micro-bunches in experiment due to the limited temporal resolution. The effect is stronger for higher plasma density, due to the shorter plasma period, and for positive density gradient, due to the higher on-axis charge density of micro-bunches. Therefore, when changing the plasma density (gradient), the defocused proton distributions are more legible for comparison than a single value, as the rms width.
Defocused proton distributions are wider for higher initial bunch densities, both in experiment and simulations. This is in agreement with linear theory predicting higher transverse seed wakefield amplitudes and larger wakefield growth with higher initial bunch density. The measurable phase slippage of the wakefield with respect to the proton bunch is similar for the different initial bunch densities used here (Figure A.25). Therefore, the stronger defocusing of protons with increasing initial bunch density is assigned to the experience of higher transverse wakefield amplitudes. This is confirmed by the transverse wakefield amplitudes, obtained from simulations.
The defocused width is slightly decreasing for increasing plasma density in both experiments and simulations. Also this is in agreement with linear theory, predicting lower transverse seed wakefield amplitudes for higher plasma density, while the wakefield growth is independent of the plasma density for a distance to the seed position, proportional to the plasma period. Also here the phase slippage is essentially independent of the different plasma densities measured (Figure A.25). Thus, the slightly narrower defocused proton distributions with higher plasma density are assigned to the slightly smaller transverse seed wakefields, as confirmed by wakefield amplitudes from simulations.
Time-resolved images from experiment and simulations show significantly wider defocused proton distributions for negative than for positive plasma density gradient. With the constant plasma entrance and the varying exit density during the gradient measurements, the seed wakefield amplitudes remain unchanged. The growth of the wakefield with density gradient is studied in simulations. They reveal that transverse wakefield amplitudes are only slightly larger for negative than for positive density gradient over the first five peri-

ods. The small increase in wakefield amplitudes is not expected to explain the much wider defocused proton distributions, as measured with negative density gradient in experiment and simulations. Instead, simulations suggest that with a density gradient the change in defocused proton distribution is determined by the change in phase slippage between the wakefield and protons. The negative density gradient reinforces the phase slippage, which leads to strong focusing over the first few meters in plasma for the protons that are diverging after the plasma. This initial focusing causes protons to experience the defocusing wakefield close to the beam axis, where transverse wakefield amplitudes are large, after a longer distance in plasma, where wakefield amplitudes are higher due to growth. Thus, the wider defocused proton distributions with negative density gradient are mainly assigned to the increasing phase slippage between the wakefield and protons and only slightly to larger transverse wakefield amplitudes.

7 First Study of Seeding the Self-Modulation of a Proton Bunch with a Preceding Electron Bunch

In previous experiments in AWAKE, proton bunch SM and acceleration of witness electrons were both accomplished in a single plasma. In future experiments in AWAKE, the acceleration process should be separated from the SM process in a second plasma (Section 2.6 and [44]). This would be advantageous as in this case, electron acceleration is not affected by the wakefield's phase slippage during SM evolution (Section 1.4.5 and Section A.7 in the appendix).

As explained in detail in Section 1.4.1, the wakefield driven by a charged bunch in plasma has accelerating and decelerating as well as focusing and defocusing phases. Therefore, only a fraction of the plasma period (one quarter for linear wakefields) is accelerating and focusing for a given charged particle as, e.g. an electron witness bunch to be accelerated in the plasma wakefield. As explained multiple times throughout the thesis, in order to predict where to temporally inject the electrons in the wakefield, phase reproducibility of the proton bunch modulation (and thus phase reproducibility of the wakefield) from event to event is required. As schematically drawn in Figure 7.1 a), we showed in [16] phase reproducible modulation by seeding the SM with the laser pulse (red line), i.e. the RIF, co-propagating with the proton bunch (blue curve). The proton bunch density at the start of the beam-plasma interaction must be high enough to ensure SM to start at the RIF, instead of SM growing from noise. In [16], it was shown that, for the given experimental parameters, SM is phase reproducible with the RIF up to $\sim 1.8\,\sigma_{\xi,p^+}$ ahead of the bunch center and non-reproducible with the RIF further than that. Therefore, RIF seeding was established as a reliable and controllable seeding method and it is used for all measurements presented in this thesis so far. However, using RIF seeding in Run 2, the proton bunch would be sent with the unmodulated head (e.g. Figure 4.1) into the second plasma. We have seen [16, 38] that the head of the bunch could drive a wakefield with non-reproducible phase from event to event. This wakefield (and the modulation of the bunch head) could interfere with the bunch, modulated from the first plasma.

Therefore, a different seeding technique for Run 2 is investigated in this chapter. An

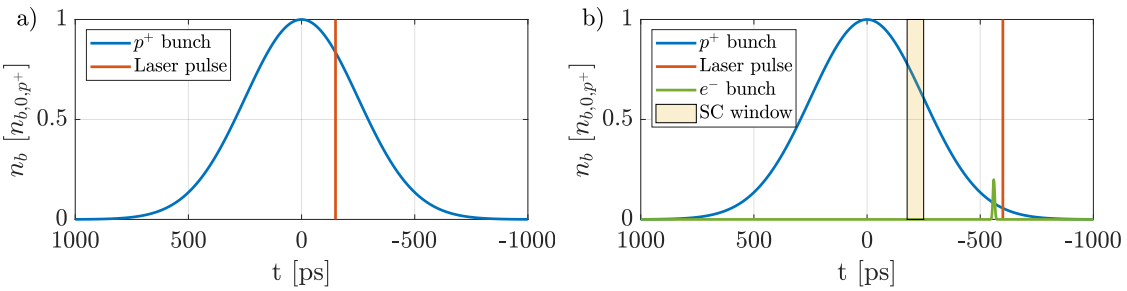

Figure 7.1: Schematic of seeding SM with a) a RIF (red line) close to bunch center or b) a relativistic electron bunch (green curve) ahead of the proton bunch (blue curve) in a pre-performed plasma.

alternative seeding method is a short relativistic electron bunch (green curve) ahead of the proton bunch in a preformed plasma, see schematic in Figure 7.1 b). The unmodulated head of the bunch as it is the case for the RIF seeding (at $t \approx -200\,\mathrm{ps}$ in Figure a), can be avoided with the electron bunch seeding. This has two advantages. One, the wakefield is driven by the entire proton bunch, two, the unmodulated head does not modulate uncontrollably when entering a second plasma (staging). A fully modulated proton bunch, as it is the case when seeding with a preceding short relativistic electron bunch, would be favorable for witness bunch injection into the wakefield of the self-modulated bunch with controllable and reproducible phase. Electron bunch seeding is also studied in [61] using linear wakefield theory.

7.1 Experimental Results

We attempted to demonstrate electron bunch seeding and phase reproducibility in a short experimental time. In the following, I first characterize the electron bunch experimentally, determine the energy distribution of the electron bunch after plasma propagation, without the presence of the proton bunch, and then study the effect of the preceding electron bunch onto the proton bunch SM from time-resolved streak camera images.

Experimental Setup

In the experiment, the plasma density is $n_{pe} \approx 2 \cdot 10^{14}\,\mathrm{cm}^{-3}$, i.e. the wakefield period is $\tau_{pe} \approx 7.9\,\mathrm{ps}$, here with smaller accuracy than typically, as it is determined from the oil temperature, since the vapor density measurement was interrupted. The proton bunch population is measured with the beam current transformer as $N_{p^+} = (2.9 \pm 0.1) \cdot 10^{11}$,

its length is determined with the 1 ns streak camera window as $\sigma_{t,p^+} = 250\,\text{ps}$ and the nominal transverse size of $\sigma_{r,p^+} \approx 200\,\mu\text{m}$ is assumed. During the seeding experiment, the electron bunch is focused at the entrance of the plasma. For measuring the transverse size, we focus the bunch onto a screen 80 cm before the plasma entrance and determine a bunch size of $\sigma_{x,e^-} = 0.56\,\text{mm}$, $\sigma_{y,e^-} = 0.37\,\text{mm}$. For simplicity, a radially symmetric Gaussian bunch with $\sigma_{r,e^-} \approx 0.48\,\text{mm}$ is assumed in the following. Its normalized emittance was determined with a quadrupole scan in each plane to $\epsilon^*_{x,e^-} = 1.5\,\mu\text{m}$ and $\epsilon^*_{y,e^-} = 1.7\,\mu\text{m}$, in the following assumed as $\epsilon^*_{e^-} \approx 1.6\,\mu\text{m}$. The electron bunch charge was measured with a Faraday cup [62] as $Q_{e^-} = (450 \pm 25)\,\text{pC}$.

We acquire time-resolved images of the modulated proton bunch with the streak camera (imaging the OTR screen 3.5 m after the 10 m plasma, setup explained in detail in Section 3.1). Phase reproducibility of the SM implies that micro-bunches always appear at the same time with respect to the seed [16]. Section 3.2.3 introduces the reference laser pulse, a fraction of the ionizing laser pulse, to align single events with a modulation period $\tau_{pe} < 12\,\text{ps}$, despite the streak camera trigger timing jitter of $\sim 5\,\text{ps}$. It was established that the timing jitter between the reference laser pulse and the ionizing laser pulse is $< 1\,\text{ps}$ [47].

We use the reference laser pulse also during the electron bunch seeding experiment in order

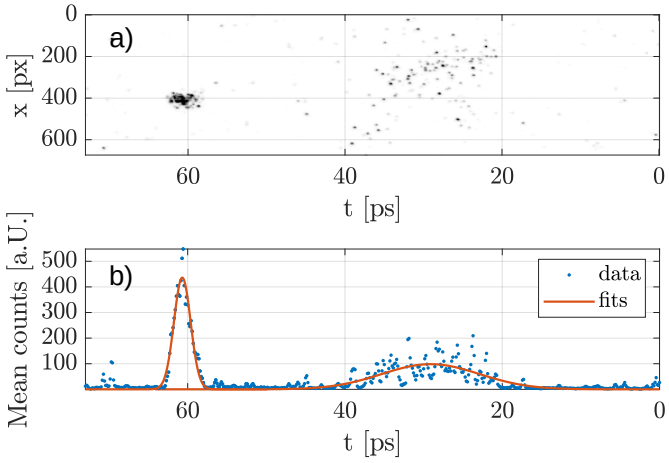

Figure 7.2: a) Streak camera image with electron bunch (at $t \approx 30\,\text{ps}$) and low energy laser pulse (at $t \approx 60\,\text{ps}$); b) Image projection (blue points), fitting a Gaussian function to each signal (red line).

to align single events. If SM is seeded, the phase reproducibility is with respect to the seed, i.e. in this case the preceding electron bunch. We determine the timing jitter between the electron bunch and a low energy ($\sim 1\,\text{mJ}$) version of the laser pulse for ionization. We introduce a small time difference between the laser pulse and the electron bunch with

a translation stage for the UV light producing the electron bunch [63]. We send both onto an OTR screen close to the plasma entrance and acquire the signal of the laser pulse (at $t \approx 60\,\mathrm{ps}$) and electron bunch (at $t \approx 30\,\mathrm{ps}$) with a streak camera to determine their timing jitter, see Figure 7.2. Figure a) shows a single streak camera image, Figure b) the image projection (blue points) to determine the temporal center of each signal with a Gaussian fit (red line) each. Here, the signal of the electron bunch is in the speckle regime, as recommended for conventional use of the streak camera, when only interested in temporal, not spatial (transverse) information, to obtain maximum temporal resolution (Section 3.2.1). As explained in Section 3.2, the image and time axis are linearized and a background image, here the average of 100 single images without electron bunch or laser pulse, was subtracted from the image.
The peak position of the fits to the electron bunch and laser pulse are used as their timing

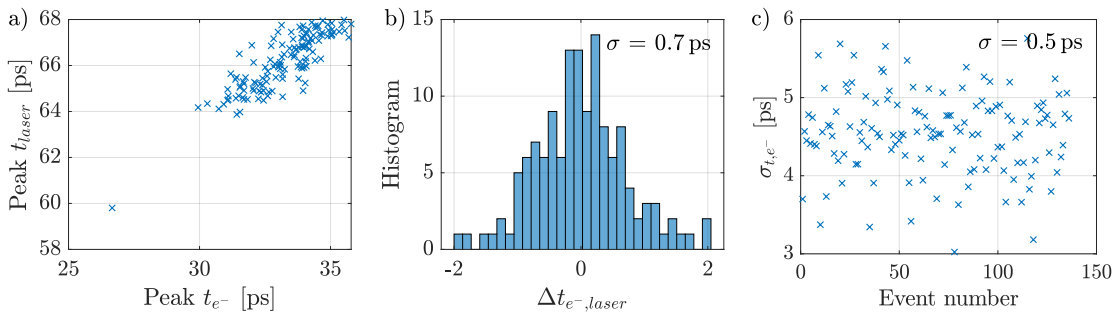

Figure 7.3: Determination of temporal jitter between laser pulse and electron bunch from 136 events. a) Gaussian fit peak position of the laser pulse versus fit peak position of the electron bunch; b) histogram of difference between laser pulse and electron bunch timing, mean value $\overline{\Delta t} = 32.9\,\mathrm{ps}$ subtracted; c) Gaussian fit width of electron bunch.

to determine the relative timing difference between the two. The analysis includes 136 events out of 500 events, where both signal peaks were identified by the Gaussian fits, i.e. not too close to the edge of the image and a peak value significantly above noise. The results show that the signal of the laser pulse and electron bunch move together on the image (Figure 7.3 a). Their relative difference, deviating from its mean value (in this case $\overline{\Delta t} = 23.9\,\mathrm{ps}$), determines the timing jitter between the two (Figure 7.3 b). The standard deviation of the relative difference is 0.7 ps.
This analysis demonstrates that as long as we set the time difference between ionizing laser pulse and electron bunch larger than 0.7 ps or a few times that, the electron bunch is always behind the RIF. It also means that the contribution of the jitter between the two laser pulses (reference and ionizing laser pulse) and between the laser pulses and electron

bunch are both much smaller than the plasma period. Therefore, phase reproducibility is measurable if occurring and we can use the reference laser pulse for both, as a reference with a fixed distance to the RIF or to the preceding electron bunch, i.e. for both seeding methods.
Figure 7.3 c) shows the std width from the Gaussian fits to the signal of the electron bunch. Its width, i.e. the electron bunch length, is $\sigma_{t,e^-} = (4.5 \pm 0.5)\,\mathrm{ps}$.
The experimental parameters are summarized in Table 7.1. The relative timing between proton bunch, electron bunch, ionizing laser pulse and image acquisition is plotted in the schematic of Figure 7.1 b). Streak camera images of the modulated proton bunch shown in this chapter are acquired $\sim 250\,\mathrm{ps}$ ahead of the proton bunch center. The ionizing laser pulse is 600 ps ahead of the bunch center and the electron bunch $\sim 20-40\,\mathrm{ps}$ after the laser pulse. We note here that this time difference is equivalent to $\sim 3-5\,\tau_{pe}$, which means that SMI could develop between the laser pulse and the electron bunch. However, the proton bunch charge between the two is relatively small and SMI development is unlikely. This (long) delay was chosen because precise relative timing between laser pulse and electron bunch was not well known at the time of the measurement.

Parameter	Symbol	Value	Units
Plasma density	n_{pe}	$\sim 2 \cdot 10^{14}$	cm^{-3}
Proton bunch population	N_{p^+}	$(2.9 \pm 0.1) \cdot 10^{11}$	
Proton bunch size	σ_{r,p^+}	~ 200	µm
Proton bunch length	σ_{t,p^+}	250	ps
Proton bunch energy	E_{p^+}	400	GeV
Electron bunch charge	Q_{e^-}	450 ± 25	pC
Electron bunch size	σ_{r,e^-}	~ 480	µm
Electron bunch length	σ_{t,e^-}	4.5 ± 0.5	ps
Electron bunch normalized emittance	$\epsilon^*_{e^-}$	~ 1.6	µm
Electron bunch incoming energy	$E_{e^-,0}$	18	MeV

Table 7.1: Experimental parameters of electron bunch seeding experiment.

Wakefield Driven by the Electron Bunch Observed with the Electron Spectrometer

The electron bunch energy distribution is acquired with the electron spectrometer after the 10 m long plasma (setup in Figure 2.3). The results here are obtained with the spectrometer dipole set to its minimum current 18 A and with quadrupoles turned off. Figure 7.4 shows single spectrometer images after propagation through vapor (a) and

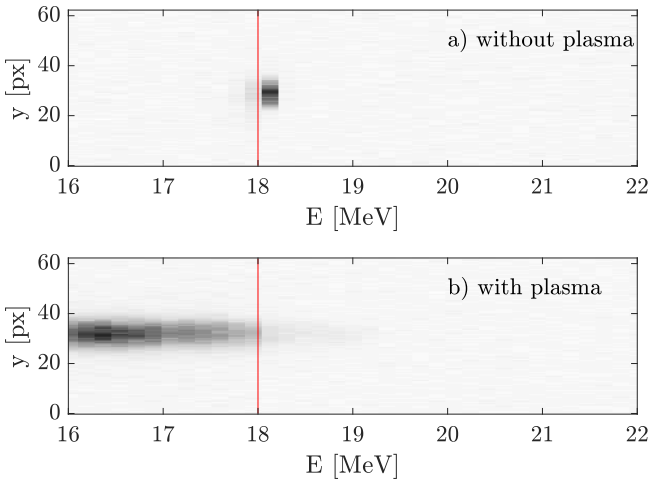

Figure 7.4: Comparison of the energy spectrum of the electron bunch on electron spectrometer a) without, b) with plasma.

through plasma (b). Image a) shows that the electron energy distribution is narrow (incoming energy after the booster 18 MeV) when propagating through vapor. Image b) shows that the distribution is significantly broader when propagating through plasma. The energy spectrum is cut at low energies (16 MeV), because of the limited field of view of the spectrometer, together with the lower threshold for the magnet current, where the electron energy corresponds to a fixed position on the screen proportional to the current magnet. The image indicates that the energy distribution is shifted to lower energies, i.e. electrons are decelerating, because the bunch drives a wakefield in the plasma.
Figure 7.5 shows the waterfall plot of 189 events after propagation through vapor (Figure a) or through plasma (Figure b). It shows that also after plasma propagation the energy distribution is reproducible in the experiment. In Figure c) the mean spectra of the single events are plotted without plasma (blue dashed line, projection of Figure a) and with plasma (red solid line, projection of Figure b). It demonstrates that when the bunch propagates through plasma, most of the electrons lose energy to the wakefield in the plasma.
However, Figures 7.5 b) and c) indicate that while the majority of detected electrons have lost energy, some have gained energy (up to ~ 20 MeV). There are two possible reasons for that. First, the electron bunch is more than half a plasma period (thus wakefield period) long, which means that some electrons may reside in the (weak) accelerating phase of the wakefield. Second, the incoming energy is 18 MeV, i.e. with a $\gamma = 35$ one expects a dephasing of $\Delta t = 13.6\,\mathrm{ps} = 1.7\,\tau_{pe}$ over the 10 m plasma due to the velocity below speed of light. Additionally, Figure b) and c) show energy loss larger than 2 MeV (limited by the field of view) which increases dephasing further (16 MeV $\widehat{=}\ \gamma = 31 \widehat{=}\ \Delta t = 2.2\,\tau_{pe}$) due to the decrease in velocity. Thus, we expect significant dephasing of ~ 2 wakefield periods

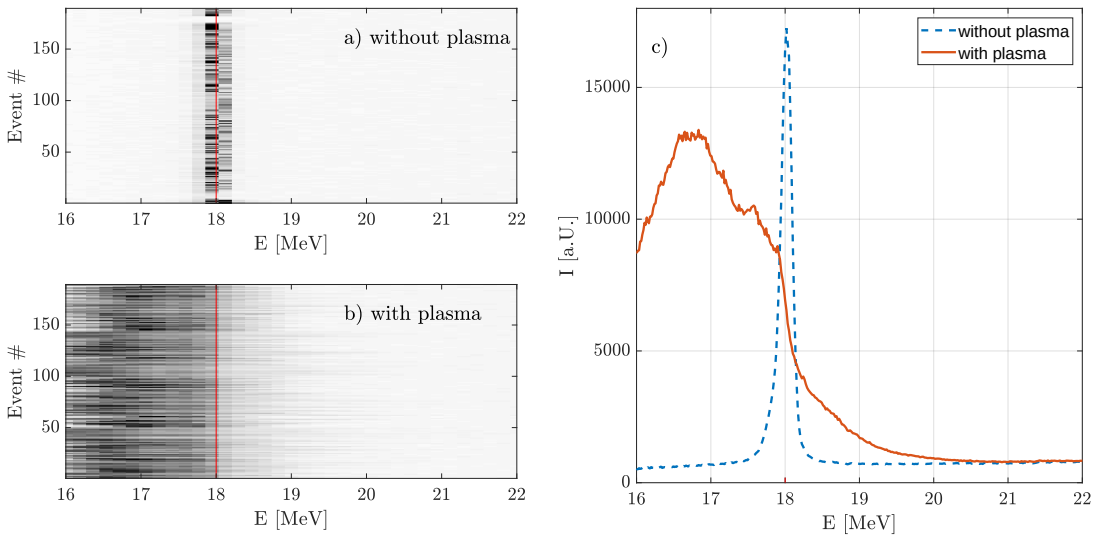

Figure 7.5: Waterfall plot of the integrated electron bunch energy distribution spectrum a) without and b) with plasma; c) mean of the integrated energy distribution spectrum without (blue dashed line) and with (red solid line) plasma.

over the plasma length as a result of the low incoming energy. Therefore, electrons are expected to cross accelerating and decelerating fields along the plasma. The dephasing of the bunch and its effect on the wakefield driven by the bunch are analyzed from simulations later.

This measurement shows that the electron bunch drives wakefields when propagating through plasma. In the following, I study whether the wakefield of the preceding electron bunch leads to phase reproducible proton bunch SM from time-resolved streak camera images.

Analysis of the Phase-Reproducibility of the Proton Bunch Self-Modulation

Figure 7.6 shows the central bunch density modulation ($-0.8\,\mathrm{mm} < x < 1.9\,\mathrm{mm}$ of the streak camera images, see e.g. Figure 3.10 a) for an unrelated measurement) of 12 consecutive events without electron bunch (Figure a) and 26 consecutive events with electron bunch (Figure b). All images are temporally aligned with the reference laser pulse, as explained in Section 3.2.3. We conclude from comparing the intensities from Figure a) and b) that the modulation depth is essentially not influenced by the presence of the electron bunch.

SM is phase reproducible if micro-bunches for all events appear at the same time with respect to the seed, which is at the same time within the observation window, once images

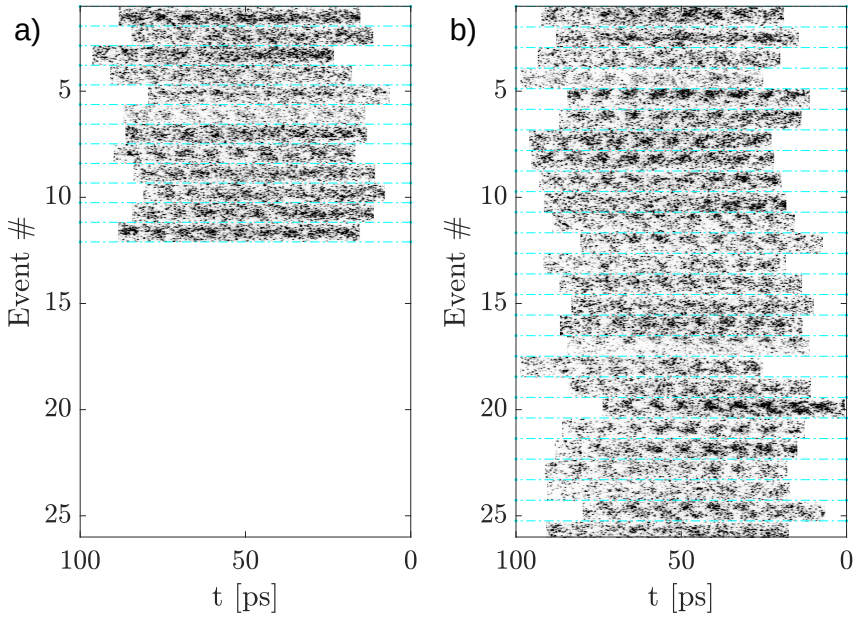

Figure 7.6: Waterfall plots of the central bunch density modulation using the region $-0.8\,\text{mm} < x < 1.9\,\text{mm}$ from time-resolved images; a) without and b) with preceding electron bunch.

have been aligned in time with respect to the reference laser pulse. The waterfall plot without preceding electron bunch (Figure 7.6 a) shows that without the electron bunch, SM is not phase reproducible. Due to the low initial proton bunch density at the RIF, thus low seed wakefield amplitudes, SM grows from noise, as expected [16]. Looking at the waterfall plots with electron bunch (Figure 7.6 b) the position of the micro-bunches is not clearly reproducible either. As a comparison, the reproducibility of micro-bunch positions with seeding by the RIF close to the proton bunch center can be found in Figure 3.9. In the following analysis, it is determined whether the preceding electron bunch increases the SM phase reproducibility in these measurements.

Figure 7.7 shows the average of streak camera images, each normalized to 1 and temporally aligned, i.e. all images on Figure 7.6 a) and b) respectively. The normalized average central bunch density modulation is plotted below.

When SM is not phase reproducible, averaging multiple events smears out the modulation and one would expect not to see any micro-bunch features when using a large number of images. In Figure 7.7 a), the average of events without electron bunch still shows remaining density modulation. This can be explained with the following calculations. The sum of cosine functions with amplitude 1 with random phase is a cosine function with amplitude < 1. The amplitude is the smaller, the larger the phase variations and

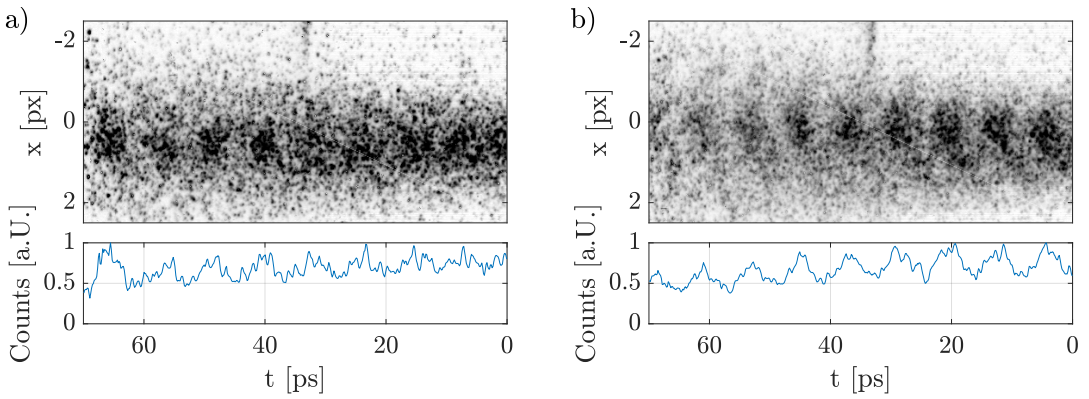

Figure 7.7: Top: average of normalized time-resolved images of a) 12 images without and b) 26 images with preceding electron bunch; bottom: projection over $-0.5\,\mathrm{mm} < x < 1\,\mathrm{mm}$, normalized to 1.

the larger the number of averaged functions, as demonstrated in Figure 7.8. The figure shows that with only 12 events (blue crosses), the modulation depth is expected to be 0.26 ± 0.26 for a random phase over 2π. According to this calculation, the modulation amplitude in Figure 7.7 a) of ~ 0.5 is within the error of the calculation for a phase variation of 2π.

The average of events with a preceding electron bunch (Figure 7.7 b) shows by eye a slightly deeper density modulation than without electron bunch, even though it has about two times as many events as in the Figure a) case. Due to the larger number of events than without electron bunch, if the phase was not reproducible either, the modulation would be with lower amplitude than in the case of Figure a). As this is not the case, this suggests that with electron bunch, the phase is more reproducible. The 26 events with electron bunch lead to a similar modulation depth after averaging of ~ 0.5. Figure 7.8 predicts for 26 events (red circles) a phase range of $\sim 1.2\pi$, from the mean value, but the result would also be within the error bars for a random phase of 2π. This emphasizes that for the analysis described here a larger sample should be taken.

The phase reproducibility is quantified in the following. A similar DFT procedure is used as the one used in [16] to analyze phase reproducibility. First, for each single event the modulation frequency of the bunch is determined by identifying the frequency of the highest peak in the power spectrum (within $50\,\mathrm{GHz} < f_{Mod} < 500\,\mathrm{GHz}$) of the image time profile (central bunch density projection of $-0.8\,\mathrm{mm} < x < 1.9\,\mathrm{mm}$). Zero-padding (768 pixels on both ends) is applied and the profile is multiplied with a Gaussian function with width $\sigma_t = 14.4\,\mathrm{ps}$ centered around the image before calculating the DFT. The average of the frequencies obtained from all events with this procedure is $f_{Mod} = 119.6\,\mathrm{GHz}$, which is close to the expected frequency from the density measurement ($n_{pe} \approx 2 \cdot 10^{14}\,\mathrm{cm}^{-3}$,

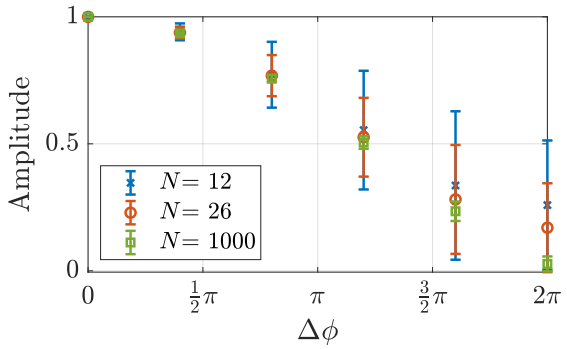

Figure 7.8: Amplitude (difference between maximum and minimum value) of the sum of 12 (blue crosses), 26 (red circles) or 1000 (green squares) cosine functions with amplitude 1 as a function of the range of their phase variations. The error bars correspond to the standard deviation of the amplitude when repeating the calculation with random phase, within their phase range, 1000 times.

i.e. $f_{pe} \approx 127.0\,\text{GHz}$). Subsequently, the corresponding phase value of this fixed frequency of each image within the window and the relative time to the reference laser pulse is determined. From the frequency, phase and reference laser pulse information the relative phase between micro-bunches and the supposedly seed (electron bunch) is obtained.
The results of the relative phase determination with DFT for the events without

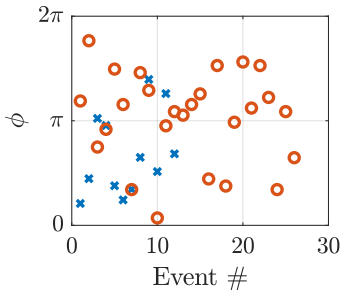

Figure 7.9: Modulation phase for the frequency $f_{Mod} = 119.6\,\text{GHz}$ from the DFT of images without (blue crosses) and with (red crosses) preceding electron bunch.

(blue crosses) and with (red circles) preceding electron bunch are shown in Figure 7.9. This phase difference can take any arbitrary value. In case of phase reproducibility phases of individual events should cluster around one value, whereas in the case of non-reproducibility they should cover a range of $2\,\pi$ (for a large number of events). The relevant quantity to assert phase reproducibility is therefore either the range of phases covered by individual events or the standard deviation of the variations observed around the mean value. In the case of Figure 7.9, the standard deviation of the two cases are comparable ($0.40\,\pi$ without, $0.44\,\pi$ with electron bunch) and essentially equal to half the possible phase range. This means that this phase analysis does not show phase reproducibility with the electron seed of these experiments.

In the following, I study whether the amplitudes of the wakefield of the preceding electron bunch are expected to be high enough for phase reproducible SM from linear wakefield theory considerations and from previous seeding experiments, described in [16].

Wakefield Considerations using Linear Wakefield Theory

Seeding the proton bunch SM with a preceding relativistic electron bunch, requires wakefield amplitudes driven by the electron bunch larger than those driven by the proton bunch, growing from noise. The equations for seed wakefield amplitudes are given in Section 1.4. In the following, the transverse wakefields are compared at the radial position of the incoming proton bunch radius $r = \sigma_{r,p^+,0} = 200\,\mu\text{m}$. The wakefield amplitude is determined behind the bunch. Hence the value corresponds to half the difference between maximum focusing and maximum defocusing (or minimum focusing). Thus, we assume that a strong focusing and weak focusing (due to the adiabatic response) influences SM similarly as a weak focusing and weak defocusing. This enables the comparison of the wakefield from the long Gaussian proton bunch with the adiabatic response, with the one driven by the short preceding electron bunch.
In [16], the minimum wakefield amplitude required for phase reproducible SM is determined as $W_{\perp,\,\text{Seed}} \approx 2\,\text{MV/m}$ (value evaluated behind the bunch) for $n_{pe} = 0.94{\cdot}10^{14}\,\text{cm}^{-3}$. The transverse seed wakefield amplitude, driven by the proton bunch with the RIF $600\,\text{ps} = 2.4\,\sigma_\xi$ ahead of the bunch center, as in the here discussed experiments and with bunch/plasma parameters from Table 7.1, is $W_\perp(p^+) \approx 0.4\,\text{MV/m}$. This shows that, as expected from the low initial bunch density at the RIF, indeed $W_\perp(p^+) < W_{\perp,\,\text{Seed}}$. Thus, the phase non-reproducibility we see in the experiment without the electron bunch is in agreement with the measurements in [16].
The electron bunch (Table 7.1) drives a transverse wakefield of amplitude $W_\perp(e^-) \approx 0.006\,\text{MV/m}$. This value is below the amplitude driven by the proton bunch and thus also below the phase reproducibility threshold, i.e. $W_\perp(e^-) < W_{\perp,\,\text{Seed}}$. According to these considerations we therefore do not expect to seed SM with the incoming electron bunch of the experiment.
However, the size and emittance of the electron bunch is not matched to the ion column. We can calculate the radial focusing force $F_\perp$ using Gauss's law [64] for an infinite cylinder as approximation for the plasma (assuming blowout [65, 66], i.e. all plasma electrons expelled) as

$$F_\perp = e \cdot E_\perp = \frac{1}{2}\frac{e^2\, n_{pe,0}}{\epsilon_0}\, r. \tag{7.1}$$

and use the beam envelope equation

$$\sigma_r^{''} + K^2\,\sigma_r = \frac{{\epsilon_{geo}}^2}{\sigma_r^3}, \tag{7.2}$$

with the linear focusing force $K = \frac{1}{\gamma\, m_e\, c^2}\frac{F_\perp}{r}$ and the geometrical emittance $\epsilon_{geo} = \epsilon^*/\gamma$. For the parameters of the experiment $\sigma_r^{''} \approx -10^5 < 0$, thus the bunch is strongly focused. For a normalized emittance $\epsilon^* = 1.50\,\mu\text{m}$ of a $\gamma = 35$ electron bunch and a plasma density $n_{pe} = 2 \cdot 10^{14}\,\text{cm}^{-3}$, the matched transverse size σ_r is $\sim 12\,\mu\text{m}$ (for $\sigma_r^{''} = 0$), significantly smaller than the size in the experiment ($480\,\mu\text{m}$).
In order to take bunch focusing and dephasing into account, I study the evolution of the electron bunch with parameters of the experiment and the wakefield it is driving along the plasma in simulations in Section 7.2. I show that due to the strong bunch focusing of the mismatched electron bunch simple linear wakefield theory calculations are not sufficient, when comparing the wakefield driven by the incoming electron bunch with the wakefield amplitude threshold for phase reproducibility $W_{\perp,\,\text{Seed}}$.

Outlook

This seeding method has the advantage of decoupling the seed wakefield (driven by the electron bunch) from the wakefield they are supposed to seed (driven by the proton bunch). We note here that for this exploratory experiment little care was given to the relative spatial and angular alignment between the two beams at the plasma entrance. Systematic misalignment, or alignment that varies from event to event from position and pointing jitter of the electron bunch (the proton bunch position and pointing jitter are much smaller) could strongly influence the seeding process. In addition, a better set-up with the laser pulse and electron bunch much ahead ($\sim 1-2\,\text{ns}$) of the proton bunch would avoid possible SM instability between the two. However, the studies presented here motivated that both electron seeding and possible SM instability between the laser pulse and electron bunch will be core measurements during the next experimental run of AWAKE in 2021-2022.

7.2 Simulation Results of the Electron Bunch in Plasma

In this section, I study, using numerical simulations, the wakefield driven by the electron bunch of the experiment in plasma. I use the two-dimensional PIC-Code OSIRIS [51]. With the electron bunch not matched to the plasma, we expect evolution of the electron bunch along the plasma in shape and density and thus of the wakefield it drives. With the low incoming electron bunch energy (18 MeV) we expect dephasing between the electron

bunch and the wakefield. Therefore, I also study the wakefield driven by a similar electron bunch but higher incoming energy as this is also an option for the experiment if required.

In the following I show simulation results of an electron bunch with incoming energy 18 MeV, transverse Gaussian profile with $\sigma_{r,0} = 480\,\mu\text{m}$, longitudinal cosine profile with a FWHM length corresponding to the FWHM of a Gaussian with $\sigma_{\xi,0} = 1.2\,\text{mm}$ (i.e. $\sigma_{t,0} = 4\,\text{ps}$), initialized with its center at $\xi = 3\,\text{mm}$, bunch population $N_{e^-} = 2.5 \cdot 10^9$ (i.e. charge $Q_{e^-} = 400\text{pC}$) and normalized emittance $\epsilon^* = 1.6\,\mu\text{m}$. The bunch propagates through 10 m of plasma with a density of $n_{pe} = 2 \cdot 10^{14}\,\text{cm}^{-3}$ and a radius of $r_{pe} = 1.5\,\text{mm}$. These parameters are similar to the experimental ones (Table 7.1). The simulation window height H is 1.66 mm with $N_r = 1100$ cells radially and the length L is 22.6 mm = 75 ps with $N_\parallel = 3000$ cells longitudinally (baseline simulation).

Validity Tests

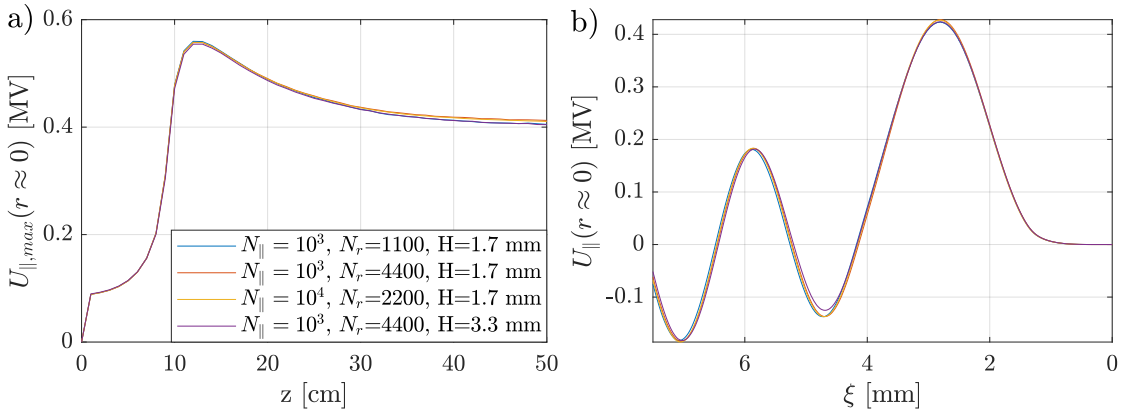

Figure 7.10: Validity tests of OSIRIS simulations increasing the resolution (transverse by a factor of 4, red lines, longitudinal by a factor of 10, yellow lines) or transverse box size (by a factor of 2, violet lines) of the baseline simulation (blue lines); a) maximum longitudinal wakefield potential along the first $z = 50\,\text{cm}$ of plasma; b) longitudinal wakefield potential along the bunch after $z = 30\,\text{cm}$ of plasma.

Figure 7.10 demonstrates that the chosen numerical parameters (N_r, $N_\parallel$, H) are sufficient for physical parameters to be independent of them. The simulations are performed in a short window ($\sim 20\,c/\omega_{pe}$) and over 0.5 m to save time, with 4 times the transverse resolution (red lines) and 10 times the longitudinal resolution (yellow lines). I also increased the simulation window height by a factor of 2 (violet lines) to exclude plasma

boundary effects. The results show that both the maximum wakefield potential in the simulation box (Figure a) and the on-axis potential along the simulation window (Figure b) have the same values with the lower as with the higher resolution ones and for smaller and larger window. It shows that the chosen resolution and simulation window size are sufficient.

Simulation Results of 18 MeV Electron Bunch Driver

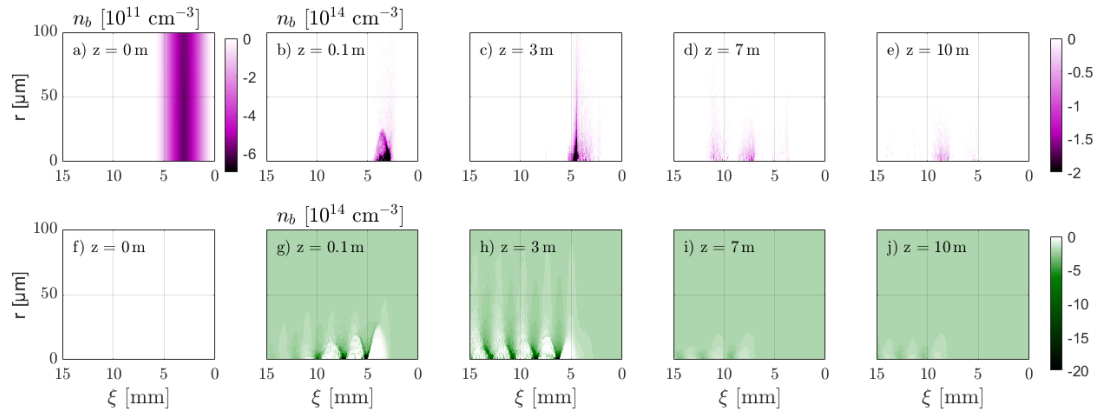

Figure 7.11: Bunch density n_b (a-e) and plasma density n_{pe} (f-j) evolution along the plasma z. Images correspond to a distance in plasma of 0 m (a, f), 0.1 m (b, g), 3 m (c, h), 7 m (d, i) and 10 m (e, j).

Figure 7.11 shows the electron bunch density at initialization (Figure a) and its evolution along plasma (Figures b-e) after $0.1, 3, 7, 10$ m from left to right. The initial bunch ($\sigma_{r,0} = 480$ µm, Figure a) strongly self-focuses at the plasma entrance, since its transverse size and emittance is not matched to the plasma (Section 7.1). Over the first 0.1 m (Figure b), the bunch density increases from its initial $-5.7 \cdot 10^{11}$ cm^{-3} to $-7.5 \cdot 10^{14}$ cm^{-3}, i.e. by a factor of > 1000. Therefore, the bunch density here exceeds the neutral plasma density of $n_{pe} = 2 \cdot 10^{14}$ cm^{-3} by a factor of ~ 4, i.e. the focused bunch is expected to drive a non-linear wakefield. Since the bunch length is on the order of the wakefield period ($\sigma_{t,0} = 4.0$ ps and $\tau_{pe} = 7.9$ ps), the back of the bunch is lost through the defocusing wakefield and the bunch becomes shorter (Figure c) and eventually becomes divided into two (Figure d). Due to the low incoming bunch energy (18 MeV) and energy depletion when driving wakefields, the center of the bunch slows down and moves backwards in the simulation window (dephases), that moves with the speed of light. The bunch dephasing increases the charge loss due to crossing of the defocusing phase of the transverse wakefield. Only a small fraction of the bunch reaches the plasma exit (Figure e).

The corresponding plasma density plots (plasma initiated after $z = 0$, Figure f) show a blow out, i.e. regions without plasma electrons, over the first meters of plasma (Figures g, h), as a result of the non-linear wakefield of the bunch. With bunch depletion, due to dephasing and energy loss, also the plasma density perturbation depth decreases later along the plasma (Figures i, j).

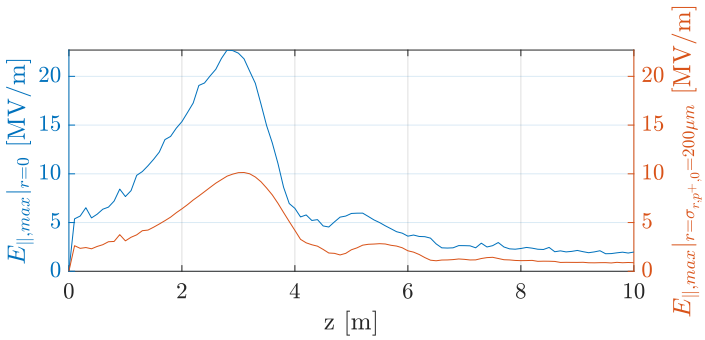

Figure 7.12: Maximum longitudinal wakefield along the bunch $E_{\parallel,max}$ versus distance in plasma z, at radial position $r \approx 0$ (blue curve) and $r = \sigma_{r,0,p^+} = 200\,\mu\text{m}$ (red curve).

The maximum of the longitudinal wakefield $E_\parallel$ along the bunch as a function of distance in plasma is plotted in Figure 7.12. It shows an increase of the wakefield amplitudes over the first few meters due to the strong focusing and increasing bunch density. A bunch shortened by the defocusing wakefield could potentially drive the wakefield more effectively, as electrons in the bunch tail can generally be accelerated by the wakefield driven by the head, if the bunch is long enough.

Figure 7.12 shows that indeed the wakefield of the electron bunch after focusing exceeds the threshold for phase reproducible SM, $E_{\parallel,\,\text{Seed}} \approx 2\,\text{MV/m}$ (for $n_{pe} = 0.94 \cdot 10^{14}\,\text{cm}^{-3}$, calculated from parameters from [16]). Initially, the wakefield is $E_\parallel(e^-) \approx 0.02\,\text{MV/m} < E_{\parallel,\,\text{Seed}}$, as calculated from linear theory (equations in Section 1.4). However, with the bunch focusing over the first 10 cm, amplitudes increase to $E_\parallel(e^-)|_{r=\sigma_{r,p^+,0}} > 2.5\,\text{MV/m}$ (at the incoming proton bunch radius $\sigma_{r,p^+,0}$, red curve) and $E_\parallel(e^-)|_{r=0} > 5\,\text{MV/m}$ (on-axis, blue curve), i.e. indeed $E_\parallel(e^-) > E_{\parallel,\,\text{Seed}}$.

Therefore, simulations predict that the electron bunch of the experiment can drive a wakefield that can seed the wakefield of the proton bunch for phase reproducible SM. Electron bunch parameters should be optimized in order to study whether they can exceed the threshold further.

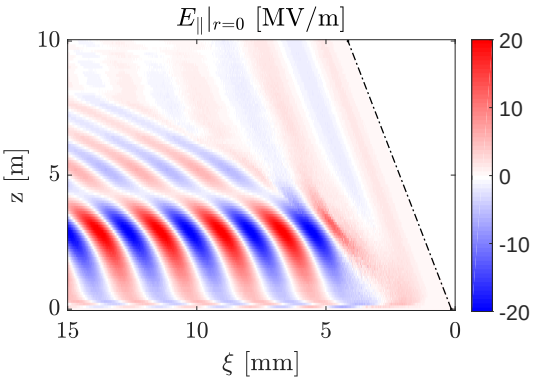

Figure 7.13: Longitudinal wakefield amplitude along the bunch ξ-axis and along the plasma z at $r \approx 0$ driven by 18 MeV electron bunch. Bunch dephases ($\gamma_0 = 35$, black dash-dotted line) with respect to the speed of light (velocity of the simulation window).

However, not only the wakefield amplitude but also its phase is important when trying to seed the SM with a preceding electron bunch. Figure 7.13 shows that the low energy electron bunch moves slower than the speed of light ($\gamma_0 = 35$, see black dash-dotted line). This leads to strong dephasing of the bunch and wakefield, here shown with the longitudinal wakefield $E_\parallel$. The transverse wakefield that leads to SM follows a similar evolution in the ξ-z-plane. The dephasing is also visible on Figure 7.11.

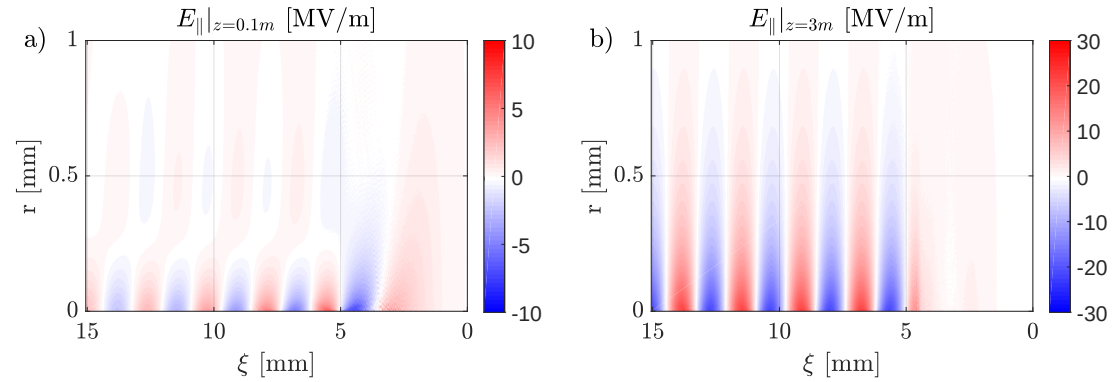

Figure 7.14: Radial extent of the longitudinal wakefield along the bunch ξ after a) 0.1 m and b) 3 m of plasma.

Figures 7.11 g, h) and Figure 7.14 a) show that after self-focusing the electron bunch and wakefield extent become comparable to the transverse size of the proton bunch ($\sigma_{r,0,p^+} = 200\,\mu$m at plasma entrance). Ideally, the wakefield driven by the seed electron bunch should exceed the transverse size of the proton bunch that is to be self-modulated. However, Figure 7.14 b) shows that with electron bunch evolution (and its defocusing) the longitudinal wakefield extends with high amplitude over several hundreds of µm after 3 m.

It is expected that the wakefield amplitudes driven by the electron bunch over the first few meters determine whether SM is seeded. Afterwards, SM is assumed to reinforce itself. A separate study will determine how the wakefield driven by the modulated proton bunch interferes with the one of the electron bunch.

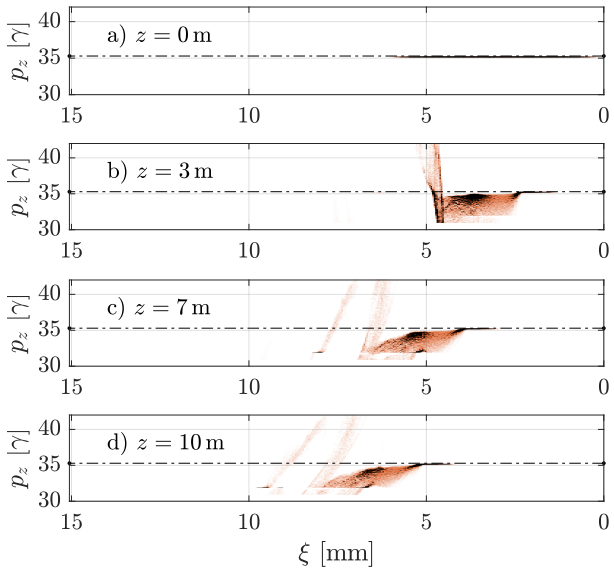

Figure 7.15: Longitudinal momentum p_z of electrons versus bunch position ξ after $z = 0, 3, 7, 10\,\mathrm{m}$ (from a to d) of plasma.

The following determines the effectiveness in driving wakefields of the electron bunch with a length ($\sigma_t = 4\,\mathrm{ps}$) close to the plasma period ($\tau_{pe} = 7.9\,\mathrm{ps}$). The longitudinal momentum evolution of the electron bunch is shown in Figure 7.15. All particles are initialized with a normalized momentum of $p_z = 35\,\gamma$ (Figure a). The evolution (Figures b-d) shows how a large number of electrons in the front of the bunch ($2.5\,\mathrm{ps} < t < 5\,\mathrm{ps}$, Figure b) looses energy ($p_z < 35\,\gamma$), while only a small number of electrons in the back of the bunch ($4.5\,\mathrm{ps} < t < 5\,\mathrm{ps}$, Figure b) gains energy ($p_z > 35\,\gamma$). As energy gain and energy loss do not compensate each other here, the electron bunch is driving a wakefield behind the bunch (Figures 7.12-7.14).

Simulation Results of 165 MeV Electron Bunch Driver

Figure 7.15 also shows the strong dephasing of the electrons (backwards displacement) due to their initially relatively small energy (18 MeV, $\gamma = 35$) and their energy loss along the plasma (Figures 7.15 b-d). The electron bunch velocity below the speed of light leads to dephasing of the electron bunch with respect to the wakefield, that should seed the wakefield of the proton bunch, moving at the speed of light. Dephasing can be avoided

with higher incoming electron bunch energy.
The longitudinal wakefield along the bunch axis and along the plasma, driven by a similar

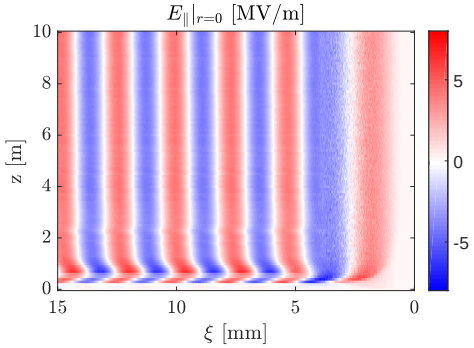

Figure 7.16: Longitudinal wakefield amplitudes along the bunch axis ξ and along the plasma z at $r \approx 0$ driven by 165 MeV electron bunch.

electron bunch as above, but with higher incoming energy (165 MeV instead of 18 MeV) are shown in Figure 7.16. The velocity of the high energy bunch is close to the speed of light ($\gamma_0 > 320$) and essentially does not decrease with propagation in plasma ($\gamma > 200$ after 10 m according to the energy loss, when driving a wakefield as from Figure 7.17), therefore dephasing is successfully avoided. Figure 7.16 shows that the phase of the wakefield is constant along the plasma for $z > 1.5$ m.
The maximum longitudinal wakefield along the bunch with incoming 165 MeV energy

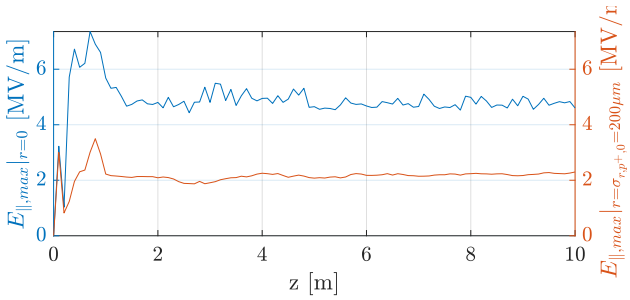

Figure 7.17: Maximum longitudinal wakefield along the bunch $E_{\parallel,max}$ versus distance in plasma z, at radial position $r \approx 0$ (blue curve) and $r = 200$ µm (red curve), driven by the 165 MeV electron bunch.

versus distance in plasma is shown in Figure 7.17 on axis ($r = 0$, blue line) and at the incoming proton bunch radius ($r = \sigma_{r,p^+,0} = 200$ µm, red line). The high energy bunch drives lower maximum wakefield amplitudes (at $r = 0$, ~ 6 MV/m instead of > 20 MV/m for low energy driver, see Figure 7.13) but still above the seed threshold $E_{\parallel,\mathrm{Seed}} \approx 2$ MV/m and with essentially constant amplitude from ~ 1.5 m until the end of the plasma. Using a higher energy electron bunch (165 MeV, i.e. $\gamma > 320$ instead of 18 MeV, i.e. $\gamma \approx 35$) limits its longitudinal evolution (energy loss, dephasing). Thus, the

higher peak wakefield amplitude ($z < 3\,\mathrm{m}$) with the low energy bunch can be explained by its short length, due to defocusing as a result of dephasing. The seed wakefield provided by the high energy bunch is essentially constant along the 10 m plasma as a result of the small evolution. However, the seed wakefield is necessary only over the first few meters of plasma for seeding the wakefield of the proton bunch. The influence of the electron bunch energy on SM of the proton bunch are studied separately from this thesis.

7.3 Conclusion

The analysis of the experimental data shown here does not conclusively prove the seeding of the SM of a proton bunch with a preceding electron bunch. Averaging the streak camera images of multiple events shows a slightly deeper modulation with the electron bunch, but a quantitative analysis of the phase of the SM does not show an increase in phase reproducibility with the electron bunch.
Simulations predict that, due to the strong evolution, the electron bunch of the experiment drives wakefield amplitudes $\sim 2.5 - 10\,\mathrm{MeV}$ at the incoming proton bunch radius over the first 3 m of plasma. This value is larger than the one, determined to be sufficient in order to seed phase reproducible SM with a RIF $\sim 2\,\mathrm{MV/m}$ [16].
However, I only analysed a small sample of experimental data, taken under not ideal conditions. The studies presented here, gave rise to repeat this experiment with a more controlled and monitored electron bunch trajectory and with an electron bunch with smaller transverse size, emittance and length in AWAKE Run 2a (∼2021-2022). We will vary parameters as electron bunch charge and timing between laser pulse and electron bunch within the proton bunch.

8 Conclusions and Outlook

In AWAKE, a proton bunch drives a wakefield in a 10 m long plasma to accelerate externally injected electrons. The proton bunch radially self-modulates in the plasma, transforming the long bunch into a train of micro-bunches that resonantly drive the wakefield. The self-modulation (SM) is seeded with the relativistic ionization front co-propagating within the proton bunch and placed close to its center. In this work, I have analyzed the first approximately ten modulation periods behind the RIF, the start of the self-modulated bunch. I have studied in experiment and numerical simulations micro-bunches and defocused proton distributions, as observed after the plasma. Further, from the simulations, I have analyzed the evolution of the transverse wakefield and of the SM along the plasma and along the bunch.

In the experiment, we only observe the proton distributions after ten meters of plasma, i.e. after growth and saturation of the SM process. However, I have shown in this thesis that some of the characteristics expected from linear PWFA theory can be observed; in particular dependence on initial bunch and plasma densities. Further, I have shown numerical simulation results of the process with parameters similar to those of the experiment to confirm experimental results and gain insight into the processes that lead to the observations. This is possible because there is in general a very good agreement between experimental and simulation results.

In this thesis, I have shown that the modulation frequency of the self-modulated bunch is equal to the plasma frequency from the third micro-bunch on. This implies that for the experimental parameters discussed, the restoring force on displaced plasma electrons during plasma oscillation is dominated by the lack of plasma electrons on the beam axis and that the effect of the positive drive bunch charge on the displaced plasma electrons is smaller than the precision of the modulation frequency analysis presented.
Further, I have shown for the first time that the first modulation period at the start of SM is consistently significantly longer than the plasma period. This is a direct observation of the phase slippage between the wakefield and the relativistic drive bunch train. Simulation results show that the length of the first modulation period increases

during SM along the plasma, which demonstrates the growth of the wakefield along the plasma. I have shown that the length of the first modulation period, measured in the experiment, corresponds to the saturated length, and thus that the wakefield saturates over the 10 m of plasma in the experiment.
I have demonstrated that micro-bunches have a constant length along the bunch and are short compared to the period of the wakefield. Thus, the modulated bunch is suitable for driving wakefields effectively.
From simulation results I have shown that micro-bunches, formed by the focusing wakefield, observed after the plasma, are slightly narrower for a higher wakefield amplitude. However, I have established that the change in width is small and below the spatial resolution of the streak camera images and as a result not measured in the experiment. With a plasma density gradient, not only the wakefield amplitude, but also the phase slippage of the wakefield with respect to the proton bunch changes. I have shown that with a negative gradient micro-bunches are wider, not well confined close to the beam axis, as the transverse wakefield acting on the protons switches between focusing and defocusing multiple times along the plasma. This effect is observed in experiment and simulations.
Interestingly, characteristics of the defocused proton regions yield more information about the evolution of the SM process than the focused regions. This is because the effect of defocusing fields is more cumulative along the plasma and stops once protons transversely leave the wakefield. Defocused protons have in general experienced the wakefield only over the growth of the SM process and reflect its characteristics, the main topic of this thesis.
For the first time, I have shown that defocused proton distributions become wider along the bunch, as a result of transverse wakefields growing along the bunch and that this increase in width depends on the evolution of the transverse wakefield in terms of amplitude and phase. I have demonstrated that a larger amplitude of the transverse wakefield can be measured with the increase in width of the defocused proton distribution, as established by increasing the amplitude of the seed wakefield and/or the wakefield growth by increasing the bunch density or decreasing the plasma density. Moreover, I have demonstrated that a change in the phase slippage of the wakefield, as induced by a plasma density gradient, can be determined from defocused proton distributions. Therefore, these proton distributions prove to be a suitable diagnostic for the amplitude or phase slippage of the transverse wakefield.
The detailed understanding of the SM process and the agreement between experimental and simulation results, shown in this thesis, are essential for further development and

applications of the AWAKE acceleration scheme.

In future AWAKE experiments (Run 2 $\sim$ 2027), we plan to divide the plasma into two stages, one for the proton bunch SM development, one for the electron acceleration by the wakefield driven by the pre-modulated proton bunch. That way, electron acceleration is not affected by the phase slippage of the wakefield during SM development. In previous experiments, we seeded the self-modulation with the RIF close to the proton bunch center. With this method, the unmodulated head of the bunch could self-modulate (phase non-reproducible, SMI), when entering the second plasma. The phase non-reproducible wakefield of the bunch head could interfere with the phase-reproducible, pre-modulated part of the bunch. Thus, I have investigated a different seeding method, seeding SM with a preceding electron bunch in a preformed plasma. With this technique, the entire proton bunch is modulated in the first plasma stage. First experimental results with only < 30 events hint at, but show no clear evidence of phase-reproducibility of proton bunch SM with the preceding electron bunch. These measurements will be continued in 2021, with a better control and monitoring of bunch parameters and spatial and temporal alignment of the beams. Further, I have performed numerical simulations of the process with parameters similar to the experiment. Results show that as the electron bunch is not matched to the wakefield it drives, it strongly self-focuses when entering the plasma. Simulations predict that as a result of the high bunch densities after self-focusing, the bunch drives wakefield amplitudes high enough to seed the self-modulation of the proton bunch.

This thesis summarizes the main achievements of AWAKE Run 1 experiments. We successfully demonstrated the controllable self-modulation of the proton bunch in plasma and the acceleration of electrons in the wakefield driven by the modulated bunch. In upcoming measurements, the goal is to maintain the quality and charge of the injected witness electron bunch during acceleration. The work presented in this thesis contributed significantly to the understanding of the wakefield driven by the modulated bunch and introduces the path towards seeding SM with an electron bunch which may be required for future experiments that separate the self-modulation and acceleration stages. AWAKE Run 2 aims to accelerate electron bunches to the multi-GeV level while maintaining the bunch quality (energy spread on the percent level while controlling the emittance growth), demonstrating the application of the acceleration scheme to high-energy physics experiments.

Glossary

a.U.	arbitrary units	
AWAKE	Advanced Wakefield Experiment	
B_Θ	azimuthal magnetic field	
BPM	Beam Position Monitor	
BTV	Beam Imaging Station	
c	speed of light in vacuum	$c = 2.998 \cdot 10^8\,\mathrm{m/s}$
CERN	European Centre of Nuclear Research	
COG	center of gravity	
CTR	coherent transition radiation	
D	plasma column diameter	
DFT	Discrete Fourier Transform	
ϵ_0	vacuum permittivity	$\epsilon_0 = 8.85 \cdot 10^{-12}\,\frac{\mathrm{As}}{\mathrm{Vm}}$
ϵ^*	normalized bunch emittance	
ϵ_{geo}	geometrical bunch emittance	
e	elementary charge	$e = 1.602 \cdot 10^{-19}\,\mathrm{C}$
e^-	electron	
E	electric field	
E_{Las}	laser pulse energy	
E_{WB}	non-relativistic cold wave-braking field	
exp	experiment	
f	frequency	
f_1	focal length of Schlieren imaging lens	
f_2	focal length of Schlieren imaging lens	
f_{ij}	oscillator strength of transition between atomic state i and j	
f_{Mod}	frequency of the bunch density modulation	

f_{pe}	cold plasma electron frequency	
F	force	
FWHM	full width half maximum	
γ	Lorentz factor	
GUI	graphical user interface	
I_0	zeroth order modified Bessel function of the first kind	
IS	Imaging Station	
k_β	beam betatron wave number	
k_{pe}	plasma electron wave number	
K_0	zeroth order modified Bessel function of the second kind	
K	linear focusing force	
λ_{pe}	plasma electron wavelength	
L_{bunch}	square bunch length	
LINAC	Linear Accelerator	
LHC	Large Hadron Collider	
LWFA	Laser Wakefield Acceleration	
μ_E	highest peak energy of accelerated electrons	
m_e	electron rest mass	$m_e = 9.109 \cdot 10^{-31}\,\mathrm{kg}$
MPP	Max Planck Institute for Physics, Munich, Germany	
η_{plasma}	refractive index of plasma	
η_{vapor}	refractive index of vapor	
N_b	bunch population	
N_i	atom density in atomic state i	
n_b	initial bunch density	
$n_{b,0}$	bunch peak density	
n_{pe}	plasma electron density	
n_{Rb}	Rubidium vapor density	
ω	angular frequency	
ω_β	beam betatron angular frequency	
ω_{ij}	atomic transition frequency between state i and j	

ω_L	laser frequency
ω_{pe}	plasma electron angular frequency
OTR	optical transition radiation
p^+	proton
PIC	Particle-in-cell
PS	Proton Synchrotron
PWFA	Plasma Wakefield Acceleration
Q	bunch charge
r_{pe}	plasma radius
R&D	research and development
Rb	Rubidium
RF	radio-frequency
RIF	relativistic ionization front
rms	root mean square
$\sigma_{r,x,y}$	bunch width in r, x, y
$\sigma_{\xi,t}$	bunch length in ξ, t
$\sigma_{res,r}$	spatial resolution
$\sigma_{res,t}$	temporal resolution
$\sigma_{t,MB}$	micro-bunch bunch length in t
sim	simulation
SM	Self-Modulation
SMI	Self-Modulation Instability
SPS	Super Proton Synchrotron
SSM	Seeded Self-Modulation
std	standard deviation
Θ	Heaviside function
τ_i	i-th modulation period
τ_{ij}	lifetime of atomic state j
τ_{pe}	plasma electron period
t	time in the lab frame
T	temperature

VLC	virtual line camera	
$W_\perp$	transverse wakefield	
$W_\parallel$	longitudinal wakefield	
χ^2	weighted distance squared function	
ξ	spatial coordinate in the co-moving bunch frame	$\xi = ct - z$
ξ_{Seed}	seed position along ξ	

Acknowledgements

I would like to thank everyone from the AWAKE family who has made this work possible and made my years at CERN so special.
I thank my daily supervisor Patric Muggli for being my scientific role model during all these years, for his support and his guidance whenever it was needed. All conclusions of my work arose from the endless discussions with him.
I thank my university professor Allen Caldwell for the support and supervision and my CERN supervisor Valentin Fedosseev for his support onside.
Thanks to Mikhail Martyanov for being batman and sidekick for all my measurements and during my PhD roller coaster. I appreciate that I could always rely on your help, independent of day and time and am very thankful for everything I have learned from you.
Thanks to Joshua Moody for the joint supervision of students and the great teamwork in the tunnel for all these years and my PhD colleagues Mathias Hüther and Fabian Batsch for always being there for each other.
I thank John Farmer for his valuable support with the QV3D simulations, always being responsive to my numerous questions and Mariana Moreira for her help with the OSIRIS simulations.
Special thanks go to the unforgettable Kindergarten Livio Verra, Felipe Peña Asmus and James Chappell for being the best office mates but also my best friends at CERN.
Danke an meine Mama, meinen Papa und meinen Bruder für eure Unterstützung. Gracias al mejor novio, por hacerme la estudiante de doctorado más feliz durante una pandemia.

This work is sponsored by the Wolfgang Gentner Program of the German Federal Ministry of Education and Research (05E15CHA).

List of Figures

List of Tables

Bibliography

[1] C. Grupen and I. Buvat. *Handbook of Particle Detection and Imaging*. Springer-Verlag, 2012.

[2] P. Muggli. Lecture at CERN Accelerator School. 2014.

[3] P. Chen et al. Acceleration of Electrons by the Interaction of a Bunched Electron Beam with a Plasma. *Phys. Rev. Lett.*, 54, 1985.

[4] J. Rosenzweig et al. Experimental Observation of Plasma Wake-Field Acceleration. *Phys. Rev. Lett.*, 61, 1988.

[5] T. Tajima and J. M. Dawson. Laser Electron Accelerator. *Phys. Rev. Lett.*, 43, 1979.

[6] C. E. Clayton et al. Ultrahigh-gradient acceleration of injected electrons by laser-excited relativistic electron plasma waves. *Phys. Rev. Lett.*, 70, 1993.

[7] I. Blumenfeld et al. Energy doubling of 42GeV electrons in a metre-scale plasma wakefield accelerator. *Nature*, 445, 2007.

[8] J. Dawson. Nonlinear Electron Oscillations in a Cold Plasma. *Phys. Rev.*, 113, 1959.

[9] F. F. Chen. *Introduction to Plasma Physics*. Springer US, 1974.

[10] AWAKE Collaboration. Proton-driven Plasma Wakefield Acceleration: a Path to the Future of High-Energy Particle Physics. *Plasma Phys. Control. Fusion*, 56, 2014.

[11] N. Kumar et al. Self-Modulation Instability of a Long Proton Bunch in Plasmas. *Phys. Rev. Lett.*, 104, 2010.

[12] Y. Fang et al. Seeding of Self-Modulation Instability of a Long Electron Bunch in a Plasma. *Phys. Rev. Lett.*, 112, 2014.

[13] E. Adli et al. (AWAKE Collaboration). Experimental Observation of Proton Bunch Modulation in a Plasma at Varying Plasma Densities. *Phys. Rev. Lett.*, 122, 2019.

[14] M. Turner et al. (AWAKE Collaboration). Experimental Observation of Plasma Wakefield Growth Driven by the Seeded Self-Modulation of a Proton Bunch. *Phys. Rev. Lett.*, 122, 2019.

[15] A. Caldwell et al. (AWAKE Collaboration). Path to AWAKE: Evolution of the concept. *Nucl. Instr. Meth. A*, 829, 2016.

[16] F. Batsch et al. (AWAKE Collaboration). Transition between Instability and Seeded Self-Modulation of a Relativistic Particle Bunch in Plasma. submitted to Phys. Rev. Lett., arXiv:2012.09676 [physics.plasm-ph], 2020.

[17] P. Chen et al. Plasma Focusing for High-Energy Beams. *IEEE Transactions on Plasma Science*, 15, 1987.

[18] Y. Fang. Resonant excitation of plasma wakefield. *PhD Thesis, University of Southern California*, 2014.

[19] J. J. Su et al. Stability of the Driving Bunch in the Plasma Wakefield Accelerator. *IEEE Transactions on Plasma Science*, 15, 1987.

[20] V. Hafych et al. (AWAKE Collaboration). In preparation.

[21] K. v. Lotov. Effect of beam emittance on self-modulation of long beams in plasma wakefield accelerators. *Physics of Plasmas*, 22, 2015.

[22] A. Pukhov et al. Phase Velocity and Particle Injection in a Self-Modulated Proton-Driven Plasma Wakefield Accelerator. *Phys. Rev. Lett.*, 107, 2011.

[23] C. B. Schroeder et al. Growth and Phase Velocity of Self-Modulated Beam-Driven Plasma Waves. *Phys. Rev. Lett.*, 107, 2011.

[24] F. Braunmüller et al. (AWAKE Collaboration). Proton Bunch Self-Modulation in Plasma with Density Gradient. *Phys. Rev. Lett.*, 125, 2020.

[25] K. V. Lotov. Controlled self-modulation of high energy beams in a plasma. *Physics of Plasmas*, 18, 2011.

[26] A. Caldwell and K. V. Lotov. Plasma wakefield acceleration with a modulated proton bunch. *Physics of Plasmas*, 18, 2011.

[27] C. B. Schroeder et al. Particle beam self-modulation instability in tapered and inhomogeneous plasma. *Physics of Plasmas*, 19, 2012.

[28] A. Pukhov and I. Kostyukov. Control of laser-wakefield acceleration by the plasma-density profile. *Phys. Rev. E*, 77, 2008.

[29] T. Katsouleas. Physical mechanisms in the plasma wake-field accelerator. *Phys. Rev. A*, 33, 1986.

[30] E. Mobs. The CERN accelerator complex - 2019. 2019.

[31] A. Caldwell et al. Proton-driven plasma-wakefield acceleration. *Nature Physics*, 5, 2009.

[32] C. Bracco et al. Beam studies and experimental facility for the AWAKE experiment at CERN. *Nucl. Instr. Meth. A*, 740, 2014.

[33] E. Öz and P. Muggli. A novel Rb vapor plasma source for plasma wakefield accelerators. *Nucl. Instr. Meth. A*, 740, 2014.

[34] V. Fedosseev et al. Integration of a Terawatt Laser at the CERN SPS Beam for the AWAKE Experiment on Proton-Driven Pasma Wake Acceleration. JACoW, Proceedings of IPAC, 2016.

[35] E. Öz et al. An accurate Rb density measurement method for a plasma wakefield accelerator experiment using a novel Rb reservoir. *Nucl. Instr. Meth. A*, 829, 2016.

[36] W. Demtroeder. Laserspektroskopie. *Springer*, 2007.

[37] B. Rapp. Analysis of Experimental Schlieren Imaging Results of a Plasma Column at the AWAKE Experiment. *Bachelor Thesis, Technical University of Munich*, 2019.

[38] S. Gessner et al. (AWAKE Collaboration). Evolution of a plasma column measured through modulation of a high-energy proton beam. submitted to Phys. Rev. E, arXiv:2006.09991 [physics.acc-ph], 2020.

[39] F. Braunmüller. Conference talk at Advanced Accelerator Concepts Workshop. 2018.

[40] F. Braunmüller et al. Novel diagnostic for precise measurement of the modulation frequency of Seeded Self-Modulation via Coherent Transition Radiation in AWAKE. *Nucl. Instr. Meth. A*, 909, 2018.

[41] J. Chappell et al. (AWAKE Collaboration). Experimental study of extended timescale dynamics of a plasma wakefield driven by a self-modulated proton bunch. *Phys. Rev. Accel. Beams*, 24, 2021.

[42] E. Adli et al. (AWAKE Collaboration). Acceleration of electrons in the plasma wakefield of a proton bunch. *Nature*, 561, 2018.

[43] A.-M. Bachmann and P. Muggli (AWAKE Collaboration). Beam Diagnostics in the Advanced Plasma Wakefield Experiment AWAKE. JACoW, Proceedings of IBIC, arXiv:2012.10097 [physics.acc-ph], 2020.

[44] P. Muggli et al. (AWAKE Collaboration). Physics to plan AWAKE Run 2. *J. Phys.: Conf. Ser. 1596 012008*, 2019.

[45] K. Rieger et al. GHz modulation detection using a streak camera: Suitability of streak cameras in the AWAKE experiment. *Review of Scientific Instruments*, 88, 2017.

[46] M. Martyanov. Characterization Streak Camera. Personal communication.

[47] F. Batsch. Setup and Characteristics of a Timing Reference Signal with sub-ps Accuracy for AWAKE. *J. Phys.: Conf. Ser. 1596 012006*, 2019.

[48] G. Demeter. Propagation of ultrashort resonant ionizing laser pulses in rubidium vapor. *Phys. Rev. A*, 99, 2019.

[49] M. Moreira et al. Influence of proton bunch parameters on a proton-driven plasma wakefield acceleration experiment. *Phys. Rev. Accel. Beams*, 22(3), 2019.

[50] P. Muggli et al. (AWAKE Collaboration). AWAKE readiness for the study of the seeded self-modulation of a 400 GeV proton bunch. *Plasma Phys. Control. Fusion*, 60, 2017.

[51] R. Fonseca et al. OSIRIS: A three-dimensional, fully relativistic particle in cell code for modeling plasma based accelerators. Springer, 2002.

[52] A. Pukhov. Three-dimensional electromagnetic relativistic particle-in-cell code VLPL (Virtual Laser Plasma Lab). *Journal of Plasma Physics*, 61, 1999.

[53] A. Pukhov. Particle-in-cell codes for plasma-based particle acceleration. *CERN Yellow Reports*, 181, 2016.

[54] B. Williamson et al. Betatron radiation diagnostics for AWAKE Run 2. *Nucl. Instr. Meth. A*, 971, 2020.

[55] A. Pukhov and J. P. Farmer. Stable Particle Acceleration in Coaxial Plasma Channels. *Phys. Rev. Lett.*, 121, 2018.

[56] J. P. Farmer and A. Pukhov. TeV acceleration in a Matryoshka plasma channel. *J. Phys.: Conf. Ser. 1596 012065*, 2019.

[57] M. Turner et al. (AWAKE Collaboration). Experimental study of wakefields driven by a self-modulating proton bunch in plasma. *Phys. Rev. Accel. Beams*, 23, 2020.

[58] A. Gorn et al. (AWAKE Collaboration). Proton beam defocusing in AWAKE: comparison of simulations and measurements. *Plasma Phys. Control. Fusion*, 2020.

[59] F. Batsch et al. Interferometer-based high-accuracy white light measurement of neutral rubidium density and gradient at AWAKE. *Nucl. Instr. Meth. A*, 909, 2018.

[60] A.-M. Bachmann and P. Muggli. Determination of the Charge per Micro-Bunch of a Self-Modulated Proton Bunch using a Streak Camera. *J. Phys.: Conf. Ser. 1596 012005*, 2019.

[61] M. Hüther and P. Muggli. Seeding of the self-modulation in a long proton bunch by charge cancellation with a short electron bunch. *Nucl. Instr. Meth. A*, 909, 2018.

[62] I. Gorgisyan et al. Commissioning of beam instrumentation at the CERN AWAKE facility after integration of the electron beam line. *J. Phys.: Conf. Ser. 1067 072015*, 1067, 2018.

[63] V. Fedosseev et al. Generation and Delivery of an Ultraviolet Laser Beam for the RF-Photoinjector of the Awake Electron Beam. JACoW, Proceedings of IPAC, 2019.

[64] H. Wiedemann. *Particle Accelerator Physics*. Springer-Verlag, 1994.

[65] J. B. Rosenzweig et al. Acceleration and focusing of electrons in two-dimensional nonlinear plasma wake fields. *Phys. Rev. A*, 44, 1991.

[66] J. B. Rosenzweig. Nonlinear plasma dynamics in the plasma wake-field accelerator. *Phys. Rev. Lett.*, 58, 1987.

[67] A.-M. Bachmann et al. Schlieren imaging for the determination of the radius of an excited rubidium column. *Nucl. Instr. Meth. A*, 909, 2018.

[68] Nist Strong Lines of Rubidium. URL `https://physics.nist.gov/PhysRefData/Handbook/Tables/rubidiumtable2.htm`. Accessed: 2021-01-25.

[69] M. Turner. First Observation of the Seeded Proton Bunch Self-Modulation in Plasma. *PhD Thesis, Graz University of Technology*, 2017.

Appendix

Appendix A: Supplementary Material

This appendix contains additional information about the topics studied throughout the thesis. First, it describes in more detail the graphical user interface of the laser alignment software, that was introduced in Section 2.3. I explain the functions and how to operate the software. Then, it provides more details on the experimental setup for the plasma radius measurements using Schlieren imaging. Further, I analyze experimentally the plasma light spectrum, emitted when the proton bunch propagates through plasma. Here, excitation of Rb ions is detected, which is assigned to collisions of oscillating plasma electrons with the ions. It is assumed that the plasma light is proportional to the wakefield amplitudes, as for larger amplitudes more collisions are expected due to a larger amount of energy deposited in the plasma. Therefore, I investigate whether the plasma light can serve as a measurement of the amplitude of the wakefield. Subsequently, the results of the location determination of micro-bunches and defocused proton regions, introduced in Section 3.2.4, are shown for all data sets described throughout the thesis from simulations and experiments. Next, I investigate the effect of slight misalignment of the OTR light onto the streak camera slit from simulation results. Then, the radial extent of the transverse wakefield and the phase slippage from different initial or plasma density is obtained from simulations. Further, I study the effect of different incoming bunch emittance on the SM in simulations and show the results of defocused proton distribution analysis from experiment for different proton bunch population. In this context, also the slice emittance growth along the modulated bunch is analyzed from simulations. From simulations, I show that the plasma radius that is assumed in simulations throughout the thesis is sensible and that SM characteristics are robust for larger radii. Lastly, I study the effect of the incoming bunch density slope on SM, when changing the seed position in the experiment and simulations.

A.1 Laser Alignment Software Development

Laser Alignment GUI

The laser alignment GUI, developed for the laser alignment onto the proton bunch trajectory, is shown in Figure A.1. The devices for the acquisition of the proton bunch trajectory (BTVs and BPMs) and of the laser pulse trajectory (BTVs and VLCs) can be selected individually in the top left section. The BPMs read and publish single values to the data acquisition directly. The VLCs and BTVs acquire images, as shown in the figures on the bottom (left for devices before, right for devices after the plasma). From the image, the center of gravity (COG) is determined and used as the value for the position (blue stars plotted on top of the figures). This assumes radial symmetry for both the laser pulse and

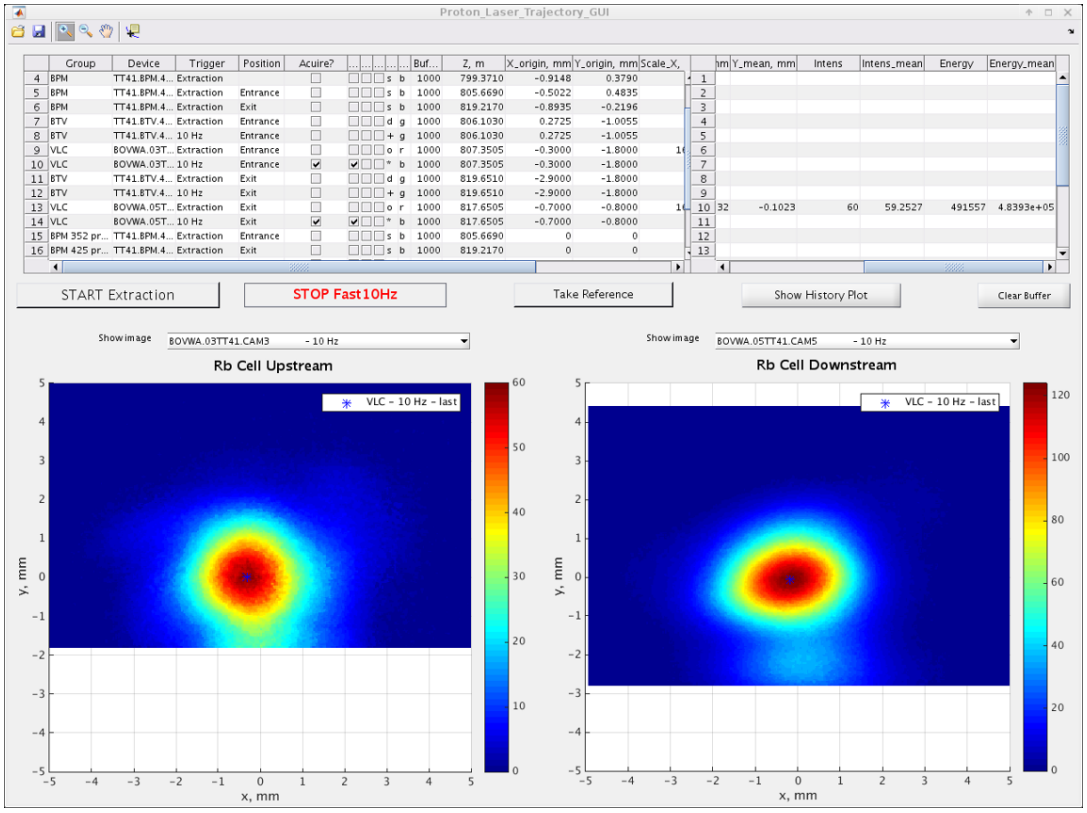

Figure A.1: MATLAB Laser Alignment GUI. Choice of diagnostics (BPMs, BTVs, VLCs) for acquisition and plotting (upper left section), diagnostic value of the previous acquisition from buffer (upper right section), trigger selection for acquisition (central left, 10 Hz trigger from the laser or extraction trigger from SPS). Bottom images show the acquisition for selected devices before (left image) or after (right image) the plasma. Acquisition of selected devices, determination of their mean value, and shifting them to the origin of the plots on the bottom with the function "Take Reference" (center).

the proton bunch.

Two triggers for the acquisition can be selected, the 10 Hz trigger, coming from the laser (GUI acquisition with $\sim$ 1 Hz), or the extraction trigger, coming from the CERN SPS machine, typically every $\sim 7 - 30$ s. Before SM experiments, the 10 Hz trigger is used to acquire the correlation of the laser pulse on BTVs and VLCs and the extraction trigger to acquire the correlation of the proton bunch on BTVs and BPMs. During SM experiments, the extraction trigger is used, acquiring the trajectory of the laser pulse on VLCs and of the proton bunch on BPMs (see Section 2.3).

The top right section of Figure A.1 shows the value of the selected devices of the previous event. The figures on the bottom show the acquisition of selected devices before (left) and

after (right) the plasma. One can choose above the figures (field "Show image") which image (BTV or VLC) to display and in the top left section (check boxes) which acquisition value to plot on top (current BTV/VLC COG and/or COG buffer and/or COG mean value, current BPM value and/or buffer and/or mean value).
The function "Take Reference" acquires the selected devices and continuously determines their mean value. When clicking a second time (stopping the reference acquisition) it shifts the coordinate systems of these devices onto their mean value. This function is used to take the reference trajectory of the proton bunch after its daily alignment before the SM experiment. After taking the reference proton bunch trajectory, the laser pulse trajectory simply needs to be aligned onto the origin of the coordinate system.

Online Laser Alignment Tracking GUI

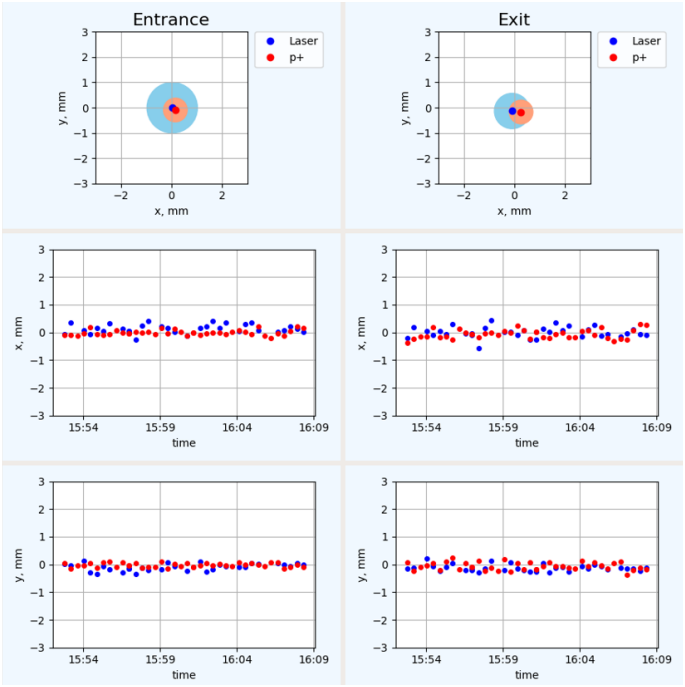

Figure A.2: Python GUI for online monitoring of the COG position of the laser pulse (blue points) and proton bunch (red points), before (left figures) and after (right figures) the plasma. Positions of the previous event (top figures), and history of x (central figures) and y (bottom figures) coordinates.

When the extraction trigger is selected, the laser alignment GUI, described previously, publishes the COG position of the laser pulse and proton bunch into the AWAKE data acquisition system for each event. The variables are then read and displayed by the Python GUI, shown in Figure A.2, developed for online monitoring of the laser beam alignment. The left images display the values from the devices before, the right images from the devices after the plasma. The top figures show the position of the laser pulse (blue) and proton bunch (red) of the previous event. The figures below plot the history of the laser

pulse (blue) and proton bunch (red) position values of previous events for the x (central figures) and y (bottom figures) coordinate. The GUI allows monitoring the alignment of the previous event and observation of (slow) drifts of the laser pulse or the proton bunch trajectory during experiments. In this case (Figure A.2), both beams remained aligned over the $\sim 15\,\text{min}$ of the measurement.

A.2 Experimental Setup for Plasma Radius Determination using Schlieren Imaging

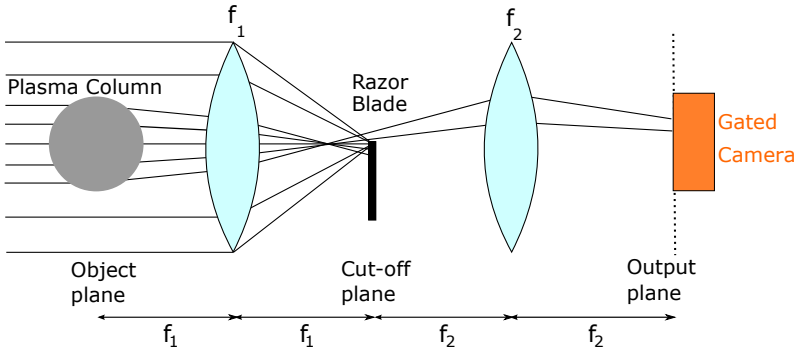

Figure A.3: Schematic of the setup for plasma radius determination with Schlieren imaging: A collimated beam propagates through the plasma column (coming out of the page), is focused and re-collimated by the lenses f_1 and f_2 and sent to a gated camera that images the plasma column. The razor blade in the focus of lens f_1 blocks rays that were not propagating through the plasma to increase the contrast of the image.

The plasma radius is measured using Schlieren imaging. Here, the plasma, created by the ionizing laser pulse, is transversely probed by a collimated imaging laser beam (TOPTICA DLC DL) as schematically shown in Figure A.3. In order to determine the plasma radius, the imaging laser beam must cover the entire radial extent of the plasma column. The initially collimated light is focused by a lens f_1, re-collimated by a second lens f_2 and acquired with a gated camera (ANDOR iStar 334T). The two lenses are arranged to image the plane of the plasma column onto the camera.

A razor blade, placed at the focus of the first lens, blocks part of the laser beam in the absence of plasma. The imaging laser has an approximately Gaussian transverse intensity profile. In the focus of lens f_1, the light distribution is also Gaussian, and here the spatial distribution is determined by the frequency distribution of the light. Therefore, with the razor blade in the focus of lens f_1, blocking part of the beam, the beam remains Gaussian

also after the razor blade, but with lower intensity. With the razor blade in the focus and a height equal to the beam axis, the light intensity decreases by a factor of 2.
Also the transverse intensity profile of the ionizing laser pulse is approximately Gaussian. Therefore, at the boundary between plasma and vapor atoms in the ground state, there is a layer where the laser intensity is high enough to excite the Rb atoms, but not high enough to subsequently ionize them. According to simulations [48], this layer is thin and thus not further considered in the following.
The imaging laser wavelength is tunable between 763 nm and 814 nm (line width < 1 MHz) and thus covers the Rb D2 transition line at 780 nm. The laser wavelength is determined by acquiring a Rb absorption spectrum in the vicinity of the D2 line, covering its hyperfine structure [67]. The imaging laser with scanning wavelength is sent through a reference cell and the light transmission is measured.
Light that propagates through the plasma column is bent at the transition between vapor and plasma. The light that is bent upwards is less blocked by the razor blade in the focus of lens f_1, see Figure A.3. Thus, more of that light, that propagated through the the lower half of the plasma column, reaches the camera, which allows the determination of the plasma radius with significantly higher contrast, when blocking most of the unbent light, than when not.
An example image of the plasma column acquired with the gated camera is shown in Fig-

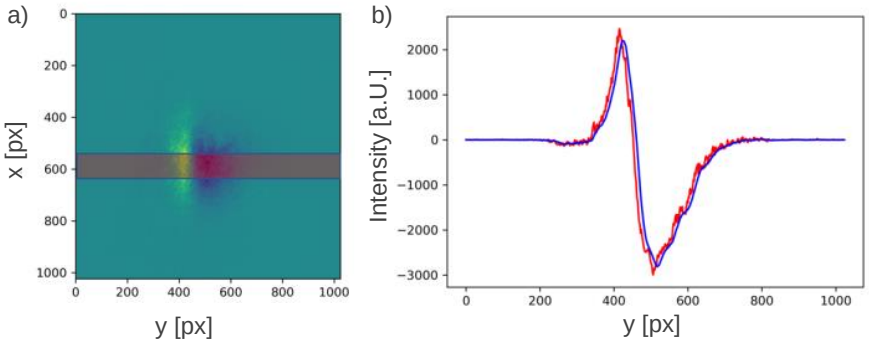

Figure A.4: Figure a) Schlieren image of the plasma column after subtraction of the image without plasma. Figure b) projection of the red bar in Figure a), raw signal (red line) and smoothed signal (blue line), from [37].

ure A.4 a). The ionizing laser pulse propagates from bottom to top. The image, obtained without the plasma, is subtracted. The razor blade (see Figure A.3) blocks most of the undeflected and the light deflected downwards by the plasma, thus the column appears as light with more (top half of the column, $y < 450$ px) and light with less (bottom half of the column, $y > 450$ px) intensity than without the plasma. The projection of the imaging

laser beam of the region, marked with the red bar in Figure A.4 a), is used for the radius determination. The projection (raw signal in red, smoothed signal in blue) is plotted in Figure A.4 b). The projection is asymmetric around the zero crossing point, because the relative amplitudes of the bright and dark peak depend on the razor blade position with respect to the optical axis. With a razor blade blocking more light (higher position in Figure A.3), the dark peak amplitude increases and the bright peak amplitude decreases. The width of the peaks, however, is expected to be independent of the razor blade position and instead only depending on the plasma radius.
In Section 2.4, the plasma radius is measured with the Schlieren imaging technique. Here, results are shown for different plasma radii by varying the energy of the ionizing laser pulse or the acquisition time after plasma creation [37].

A.3 Plasma Light Spectroscopy for Relative Wakefield Amplitudes

In the following chapter, I study whether the plasma light can serve as a novel diagnostic for wakefield amplitudes.
The energy gain by the plasma electrons from the wakefield has to dissipate and the electrons have to return to an atomic bound state. Energy can be dissipated by heating the atoms, continuous bremsstrahlung radiation and emission of light at atomic (and ionic) transition lines. Here, I record the emission of atomic transitions (in the visible) and check whether the amount of light collected is somewhat proportional to the energy dissipated, that is to the amplitude of the wakefield.
I use the plasma light as a diagnostic for the relative amplitude of wakefields. I record the spectrum at the plasma entrance and exit and compare the peak intensities of the transition lines to measure the change in wakefield amplitude along the plasma at the two locations. It has been demonstrated experimentally that the wakefield grows along the plasma from the seed amplitude value of a few tens of MeV to a few hundreds of MeV, see Figure 2.12. One can thus expect the amount of energy, deposited by the bunch into the plasma and perhaps also the emitted atomic light, to scale accordingly. However, a precise light collection efficiency from each point of measurements remains to be determined.
In the following, the plasma density gradient is varied, since with this measurement the amplitude of the wakefield at the plasma entrance remains unchanged, while the one at the exit is expected to vary. Further, the plasma light is measured when varying the proton bunch population. With higher proton bunch population a higher wakefield was determined in [14], due to higher seed wakefield amplitudes and larger wakefield growth

(Section 1.4.6). I will show that also the plasma light intensity increases with higher bunch population, i.e. higher wakefield amplitudes.

A.3.1 Experimental Setup

The plasma light is recorded with an imaging spectrograph (ANDOR Shamrock SR-750) and the gated camera (ANDOR iStar 334T), both installed in a radiation shielded room. Multi mode 300 µm core fibers are used to transport the light from the vapor source view ports to the spectrograph. The light is acquired simultaneously at the plasma entrance and exit view port. A fiber bundle (ANDOR SR-OPT-8009) positions the input of five fibers alongside the spectrograph entrance slit. The five input signals are arranged vertically along the slit, with the horizontal axis corresponding to the wavelength of the dispersed light after the grating. The light of each fiber is summed along the vertical axis to obtain the total light in each input fiber for a certain wavelength.
Each fiber of the bundle has three cores with a diameter of 100 µm. Due to the small fiber diameter, the slit of the spectrograph can be removed. The spatial resolution with the fiber bundle was determined without light dispersion (grating in zeroth order). The numerical aperture of the fiber is 0.22, corresponding to an f-number of ~ 2.3. The spectrograph f-number is 9.7, thus the light overfills the parabolic mirrors inside the spectrograph and some of the light is not collected. Due to the non-matched f-numbers the signal width (FWHM) of the fiber in the image plane is $\sim 120\,\mu m$ (7 pixels), which determines the spatial resolution of the following measurements.
In order to compare the spectral line amplitudes from the plasma entrance and exit, the coupling efficiency, due to the alignment of optics on each end, needs to be calibrated precisely. Thus, the comparison of the light intensity from the plasma entrance and exit is avoided in the following and I only study the change with beam and plasma parameters at each location.
In the following experiments, a spectrograph grating groove density of 150 lines/mm is used. With this grating the dispersion is $\sim 8.8\,nm/mm$ in the object plane. Therefore, the spatial resolution of 120 µm corresponds to a spectral resolution of $\sim 1.1\,nm$, much larger than the expected width of the atomic lines. With a higher spectral resolution, one could potentially study stark broadening from the emitted plasma light. A strong external electric field leads to shifting and splitting of the energy levels and thus to a shifting and splitting of the spectral lines. The time scales are determined by the duration of the electric field (wakefield). In the measurements presented here, the line width is dominated by spectral resolution, thus a change in line width with time could not be analyzed.
The spectrum is measured around the most dominant Rb ion line at 424.4 nm (and close

by Rb ion lines, as e.g. at 429.4 nm and 477.6 nm) [68], i.e. light from ions when decaying from one of their excited states. There is no light detected at these wavelengths, if there is only plasma (without protons) or if the proton bunch propagates through vapor (without laser pulse). Thus, background light from excitation of Rb ions by the laser pulse or proton bunch only is excluded. Only plasma electrons, having gained sufficient oscillating energy from the wakefield, can excite these transitions.

A.3.2 Experimental Results

I determine the intensity of ion lines in the plasma light spectrum from the plasma entrance and exit. I note here that ratios between different spectral lines in general depend on plasma temperature, plasma density and detailed evolution of the various states' population. I therefore compare the intensity of the two persistent lines 424.4 nm, 429.4 nm and 477.6 nm of singly ionized Rb for various beam/plasma parameters. For all measurements, the gated camera gain is 4000 and the gate time of the camera is 1 µs, starting 3 ns before the proton bunch passage and thus represent a time integrated measurement.

Line Intensity versus Plasma Density Gradient

The light is measured during a plasma density gradient scan, keeping the entrance density constant at $n_{pe} = 1.8 \cdot 10^{14}\,\mathrm{cm}^{-3}$. The density gradient is varied between $-1.9\,\%/\mathrm{m}$ and $+2.0\,\%/\mathrm{m}$, which means the density variations are $\sim \pm 20\,\%$ at the exit with respect to that at the entrance. The proton bunch population is $N_{p^+} = (3.0 \pm 0.2) \cdot 10^{11}$ and SM is seeded with the RIF $0.6\,\sigma_\xi$ ahead of the bunch center (parameters in Section 4.5.3).
The light emitted around $\lambda = 424.4\,\mathrm{nm}$ for 28 subsequent events is shown in Figure A.5. The same spectral lines appear at both plasma locations with relatively good intensity consistency for each location from event to event. However, the ratios of the lines between the two locations are different, e.g. the line at 477.6 nm is almost as bright as the one at 424.4 nm at the exit (Figure b), but much less bright at the entrance (Figure a).
The spectra (sum of 28 images, similar to those of Figure A.5) obtained with various density gradients are plotted in Figure A.6. Dashed vertical lines show the wavelengths expected for strong Rb ion atomic lines from [68]. Intensity peaks of the measured spectra coincide well with these lines. The spectra show a change in amplitude of the lines for the $\Delta n_{pe} = -1.9, 0, 2.0\,\%/\mathrm{m}$ (blue, red, green lines) cases. At both measurement locations, at the plasma entrance (Figure a) and exit (Figure b), intensities are largest for the no density gradient ($\Delta n_{pe} = 0$) case.
In Figure A.7, the peak intensities of the $\lambda = 424.4\,\mathrm{nm}$ (Figure a) and $\lambda = 477.6\,\mathrm{nm}$

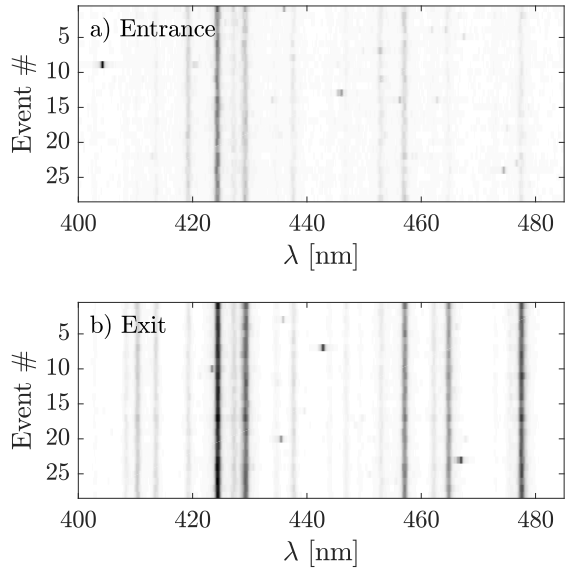

Figure A.5: Plasma light spectrum around $\lambda = 424.4\,\text{nm}$ for 28 subsequent events without plasma density gradient ($\Delta n_{pe} = 0$) at the plasma entrance (a) and exit (b).

(Figure b) Rb ion transitions are plotted for the different plasma density gradients at the plasma entrance (blue circles) and exit (red squares) from the spectra shown in Figure A.6 and the ones obtained with the other gradient values. The intensities are normalized to the mean value without gradient ($\Delta n_{pe} = 0$) and error bars give the standard deviation of the 28 events. The analysis reveals a clear trend of the emitted light intensity as a function of the density gradient. While it has been established earlier that the relative intensity between the plasma entrance and exit varies for the different transitions lines, comparing Figure a) with Figure b) shows that a density gradient changes the intensity of different transitions essentially equally and at the two locations. With our hypothesis, this figure suggests that in general, both at the plasma entrance and exit, the deposited energy and wakefield amplitude decreases with increasing gradient, perhaps with slight increase for $\Delta n_{pe} = 0.4\,\%/\text{m}$ with respect to $\Delta n_{pe} = 0$.

The light collection geometry (not described) was not changed during the measurements. Light is collected from a fixed volume. For Figure A.7, the number of emitters (ions) changed from minimum to maximum for Δn_{pe} from $-1.9\,\%/\text{m}$ to $2.0\,\%/\text{m}$. Yet the signal decreased for a positive gradient $\Delta n_{pe} > 0$. The fact that the signal decreases (or is equal) for $\Delta n_{pe} > 0$, even though the numbers of electrons n_{pe} and emitters n_i increase, shows that indeed the wakefield energy, deposited in the observation volume, is lower (i.e. more electrons with less energy per electron leads to less total energy).

It is expected that the decrease with $\Delta n_{pe} < 0$ on Figure A.7 originates from the smaller number of micro-bunches and charge observed with these negative gradient values [24]. The decrease for $\Delta n_{pe} > 0$ is expected to originate from less modulation and thus also a

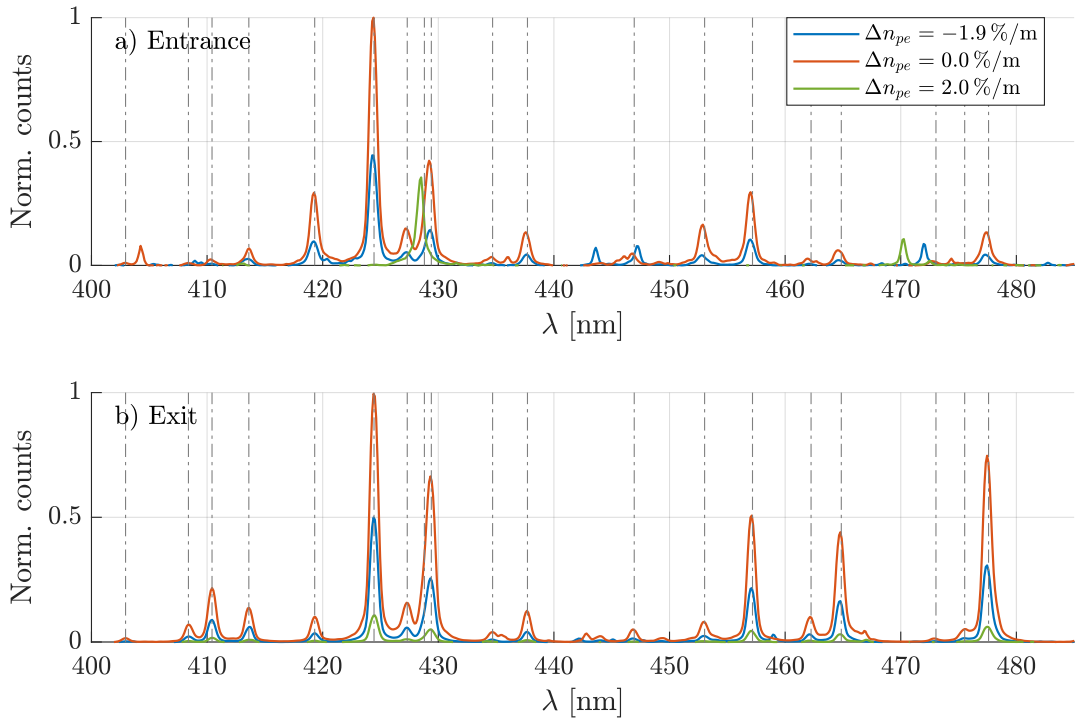

Figure A.6: Average of the plasma light spectra at $\lambda = 400 - 480\,\text{nm}$ with most negative ($\Delta n_{pe} = -1.9\,\%/\text{m}$, blue line), without ($\Delta n_{pe} = 0$, red line) and most positive ($\Delta n_{pe} = 2.0\,\%/\text{m}$, green line) density gradient at the plasma entrance (a) and exit (b).

lower wakefield amplitude driven.

The measurement at the plasma exit is consistent with theoretical [27] and simulation [58] results. The maximum proton bunch radius after the plasma is also measured with the imaging stations (set up in Figure 2.10) during the density gradient scan and it is compared to the result with simulations [58]. As explained in Section 2.5.1 and in [14], the maximum radius of proton distributions increases with increasing amplitude of the transverse wakefield. The dependency of the maximum distribution radius r_{max} on the plasma density gradient, shown in Figure A.8, is very similar to that of the intensity of ion transition lines at the plasma exit, shown in Figure A.7. However and unexpectedly, the signal at the plasma entrance follows the same trend, when expected to remain unchanged. This could indicate that the measurement is not local over the 1 µs integration time and for example that plasma light collected at the entrance is dominated by light coming from further along the plasma.

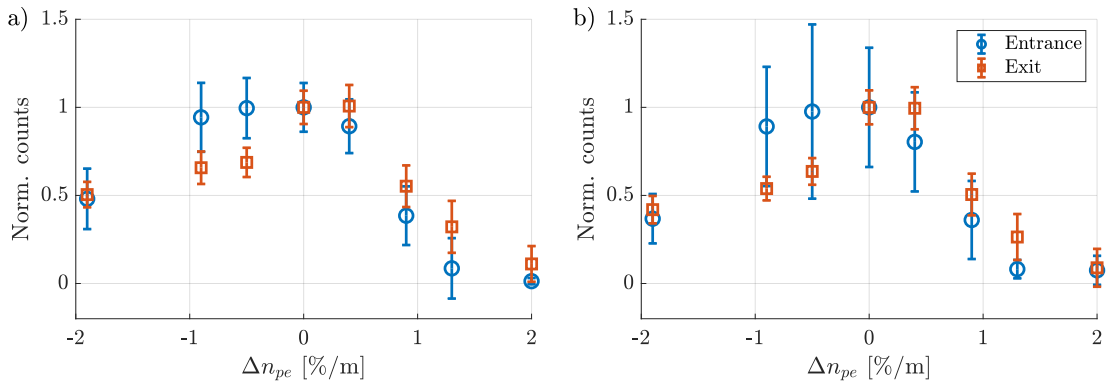

Figure A.7: Peak intensity of the a) $\lambda = 424.4\,\text{nm}$ and b) $\lambda = 477.6\,\text{nm}$ Rb ion transition lines with varying plasma density gradient Δn_{pe}, measured at the plasma entrance (blue circles) and exit (red squares), both background subtracted and normalized to the value with $\Delta n_{pe} = 0$. The error bars give the standard deviation of the variation of the 28 spectra.

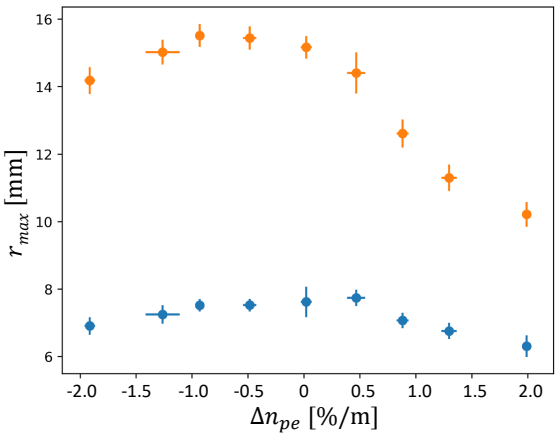

Figure A.8: Maximum radius of time-integrated proton bunch distribution r_{max} as a function of plasma density gradient Δn_{pe}, measured 2 m (blue symbols) and 10 m (yellow symbols) after the plasma [58].

Line Intensity versus Proton Bunch Population

Unlike in the case of plasma density gradient, the amplitude of the wakefield can be increased over the entire 10 m of plasma by increasing the proton bunch population, increasing seed wakefield amplitudes and growth rate, see Section 1.4.6. Thus, in the following, I measure the plasma light for different proton bunch population. The change in intensity of transition lines at the plasma entrance during the density gradient scan with fixed plasma entrance density indicates that the plasma light measurement is not local. Therefore, only the measurement at one location, the plasma exit, is analyzed in the following. The plasma density is constant along the plasma ($\Delta n_{pe} \approx 0$) and $n_{pe} = 1.8 \cdot 10^{14}\,\text{cm}^{-3}$.

As the reproducibility of the measurement was demonstrated previously (Figure A.5), the average of the spectra using ≥ 30 subsequent events is analyzed for different proton bunch population in Figure A.9. As mentioned earlier, without the proton bunch

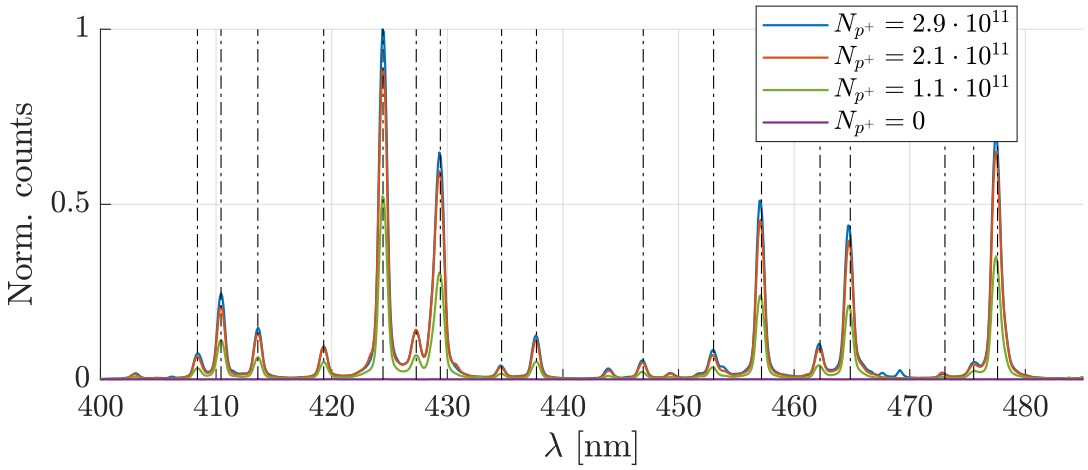

Figure A.9: Average of $\sim$ 30 plasma light spectra with various Rb ion transition lines (black dash-dotted lines) for different proton bunch populations $N_{p^+} = [0, 1.1, 2.1, 2.9] \cdot 10^{11}$ (violet, green, red, blue curve).

(i.e. only laser pulse), none of the Rb ion transition lines ($N_{p^+} = 0$, violet curve) are observed. The bunch population is increased from $N_{p^+} = (1.10 \pm 0.03) \cdot 10^{11}$ (green curve) over $N_{p^+} = (2.1 \pm 0.1) \cdot 10^{11}$ (red curve) to $N_{p^+} = (2.9 \pm 0.2) \cdot 10^{11}$ (blue curve). One can see a systematic increase in the intensity of each transition line with increasing bunch population. With our hypothesis, this corresponds to an increasing wakefield amplitude with increasing proton bunch population.

From the spectra the peak intensity of the $\lambda = 424.4\,\text{nm}$ (blue circles), $\lambda = 429.4\,\text{nm}$ (red squares) and $\lambda = 477.6\,\text{nm}$ (green crosses) transition lines are plotted in Figure A.10 as a function of bunch population, all normalized to their peak value. The figure shows a significant and similar increase of the light emission for all three transition lines when increasing the bunch population. The number of emitters remains constant for the N_{p^+}

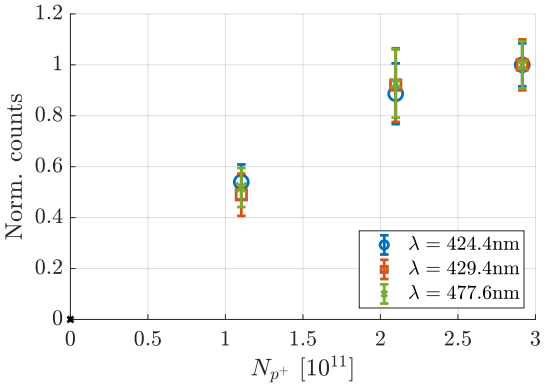

Figure A.10: Peak intensity of the Rb ion transition lines at 424.4 nm (blue circles), 429.4 nm (red squares) and 477.6 nm (green crosses) as a function of proton bunch population, background subtracted and normalized to the maximum mean value. The error bars give the std of the measurements.

variation. In a thermodynamic equilibrium one can expect the amount of light to be proportional to n_i and T_e, since $n_e \approx n_i$. The product $n_i \cdot T_e$ corresponds to the energy deposited by the wakefield. Therefore, this result is also consistent with the expectation of an increasing amplitude of the wakefield for increasing bunch population.

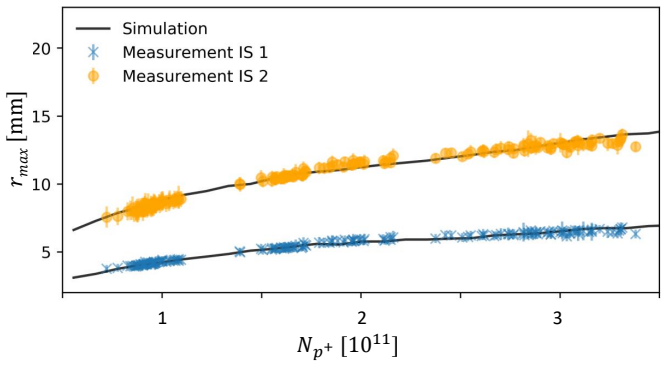

Figure A.11: Maximum radius of time-integrated proton bunch distribution r_{max} as a function of proton bunch population N_{p^+}, measured 2 m (blue crosses) and 10 m (yellow circles) after the plasma, from [69].

As shown before for the gradient scan, the intensity of the transition lines is also consistent with the measurements of the maximum radius of the time-integrated proton bunch during the bunch population scan. Figure A.11 from [69] shows that the maximum radius of defocused proton distributions r_{max} at both imaging stations (after 2 m, blue crosses and 10 m, yellow circles) increases with increasing proton bunch population N_{p^+}. Note that r_{max} has a constant (assuming that the incoming radius is independent of bunch population) contribution from the bunch radius without plasma, i.e. without defocusing fields. The transverse profile of the incoming bunch is Gaussian, i.e. a value for r_{max} is not defined without plasma. However, one can see from the figure that the maximum radius scales with the bunch population very similar as the intensity of Rb ion transition lines, shown in Figure A.10.
As noted earlier, changing the bunch population also affects other bunch parameters (e.g. emittance, radius, waist position) by some small amount [20]. However, it is expected that the population change dominates the observed effect, as also shown in [14].

Conclusion

The plasma light measurements rely on the hypothesis that the amount of light, emitted by excited ions, depends on the energy gained by the plasma electrons from the wakefield. With this hypothesis, measurements at the plasma exit are consistent with other measurements and with some theoretical ($\propto N_{p^+}$) expectations. However, to be consistent, it also has to be assumed that the collected light is not emitted locally, but to some extent

averaged over the plasma length (entrance to exit). This assumption was not verified experimentally.

A.4 Locations of Focused and Defocused Proton Regions

Time-resolved images are obtained 3.5 m after 10 m of plasma from experiments and simulations. The temporal positions of focused (micro-bunches) and defocused proton regions are determined with the weighted distance squared function χ^2 using a parabola as fit function, as explained in detail in Section 3.2.4.
In experimental images, the on-axis charge density profiles of individual micro-bunches overlap, potentially an effect of the limited temporal resolution. The method's uncertainty of temporal location of (de)focused regions increases, if the profiles of subsequent micro-bunches overlap, while they have a different peak value and/or if the profiles of the individual micro-bunches are longitudinally not symmetric.
In simulations, the on-axis charge density profiles of individual micro-bunches do not overlap for the experimental parameters of this thesis. However, the depletion between micro-bunches increases the uncertainty of the temporal location of defocused proton regions. Further, non-symmetric micro-bunch profiles and high frequency structure of micro-bunches increase the uncertainty of micro-bunch central locations.
In this section, I summarize the location of micro-bunches and defocused proton regions for the various scans from experiment and simulations, as obtained from the χ^2-fit method. The locations are used throughout the analysis of this thesis.

The location of micro-bunches (a, c) and defocused proton regions (b, d) for the initial bunch densities $n_b = 5.6 \cdot 10^{12}\,\mathrm{cm}^{-3}$ (a, b) and $n_b = 3.1 \cdot 10^{12}\,\mathrm{cm}^{-3}$ (c, d) on the time-resolved images are shown for the experiment (Figure A.12) and the simulations (Figure A.13). The determination for the lowest ($n_{pe} = 0.9 \cdot 10^{14}\,\mathrm{cm}^{-3}$, Figures a, b) and highest ($n_{pe} = 2.9 \cdot 10^{14}\,\mathrm{cm}^{-3}$, Figures c, d) plasma density in the framework of this thesis are plotted for the experimental (Figure A.14) and the simulation results (Figure A.15). The results with a plasma density gradient of $\Delta n = -1.9\,\%/\mathrm{m}$ (a, b) and $\Delta n = 2.0\,\%/\mathrm{m}$ (c, d) with plasma entrance density $n_{pe,Entr.} = 1.8 \cdot 10^{14}\,\mathrm{cm}^{-3}$ can be found for the experiment (Figure A.16) and simulation (Figure A.17). Figure A.18 shows the locations for the normalized bunch emittance $\epsilon^* = 3.6\,\mu\mathrm{m}$ (a, b) and $\epsilon^* = 1.0\,\mu\mathrm{m}$ (c, d) from simulations. Finally, the results for the seed position $\xi_{Seed} = -0.7\,\sigma_\xi$ behind (a, b) and $\xi_{Seed} = 0.6\,\sigma_\xi$ ahead (c, d) of the bunch center are plotted from experiment (Figure A.19) and simulations (Figure A.20) and for the seed position $\xi_{Seed} = -0.6\,\sigma_\xi$ from simulations in Figure A.21.

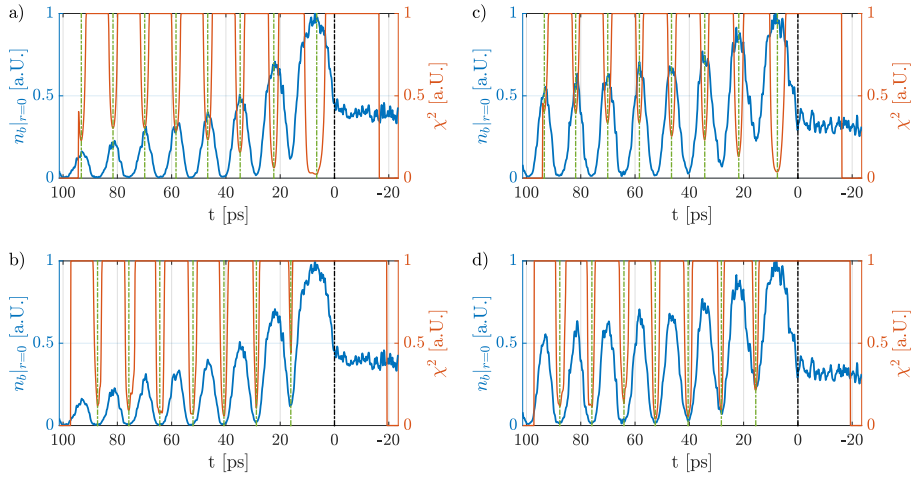

Figure A.12: Central bunch density $n_b|_{r=0}$ modulation (projection of $|x| \leq 0.1\,\mathrm{mm}$ from time-resolved images, blue lines), weighted distance squared function χ^2 (cut for high values, red lines) using a parabola as polynomial fit to the data and its minima (green dashed-dotted lines), location of micro-bunches (a, c) and defocused proton regions (b, d) with initial bunch density $n_b = 5.6 \cdot 10^{12}\,\mathrm{cm}^{-3}$ (a, b) and $n_b = 3.1 \cdot 10^{12}\,\mathrm{cm}^{-3}$ (c, d) from experiment. Here, $n_{pe} = 0.92 \cdot 10^{14}\,\mathrm{cm}^{-3}$ and $\Delta n_{pe} = 0$.

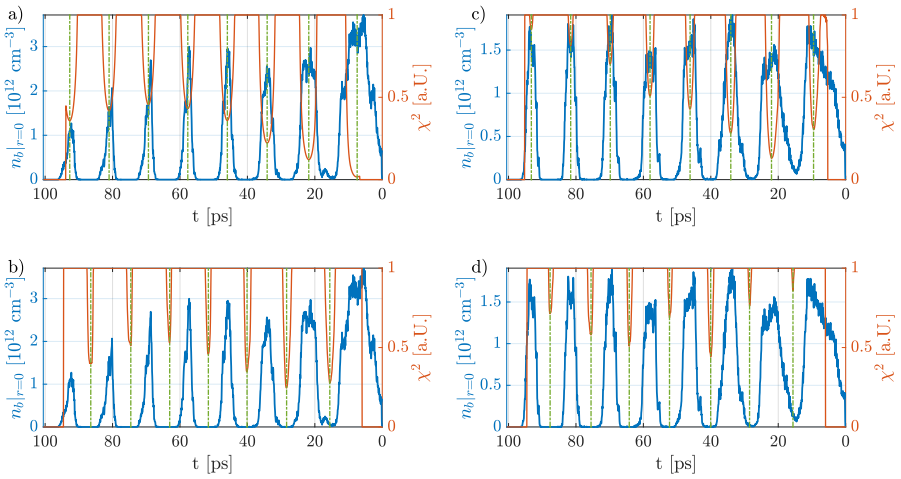

Figure A.13: Central bunch density $n_b|_{r=0}$ modulation (projection of $|x| \leq 0.1\,\mathrm{mm}$ from time-resolved images, blue lines), weighted distance squared function χ^2 (cut for high values, red lines) using a parabola as polynomial fit to the data and its minima (green dashed-dotted lines), location of micro-bunches (a, c) and defocused proton regions (b, d) with initial bunch density $n_b = 5.6 \cdot 10^{12}\,\mathrm{cm}^{-3}$ (a, b) and $n_b = 3.1 \cdot 10^{12}\,\mathrm{cm}^{-3}$ (c, d) from simulations. Here, $n_{pe} = 0.92 \cdot 10^{14}\,\mathrm{cm}^{-3}$ and $\Delta n_{pe} = 0$.

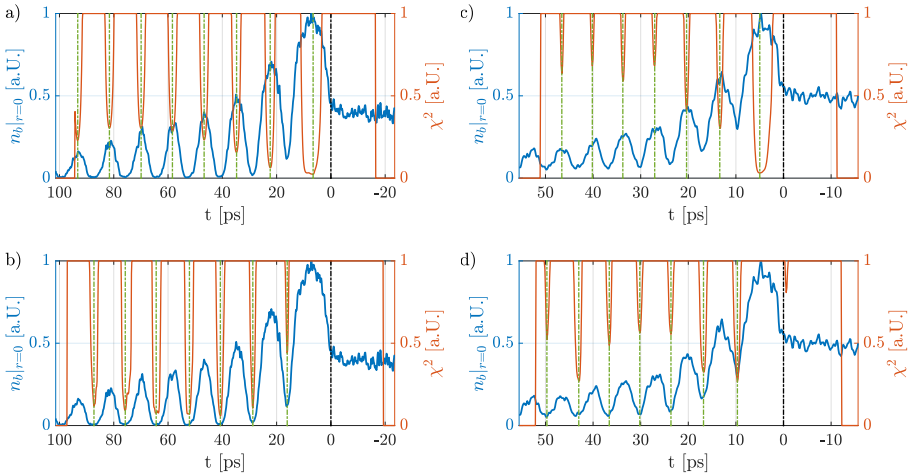

Figure A.14: Central bunch density $n_b|_{r=0}$ modulation (projection of $|x| \leq 0.1\,\mathrm{mm}$ from time-resolved images, blue lines), weighted distance squared function χ^2 (cut for high values, red lines) using a parabola as polynomial fit to the data and its minima (green dashed-dotted lines), location of micro-bunches (a, c) and defocused proton regions (b, d) with plasma density $n_{pe} = 0.92 \cdot 10^{14}\,\mathrm{cm}^{-3}$ (a, b) and $n_{pe} = 2.9 \cdot 10^{14}\,\mathrm{cm}^{-3}$ (c, d) from experiment. Here, $n_b = 5.6 \cdot 10^{12}\,\mathrm{cm}^{-3}$ and $\Delta n_{pe} = 0$.

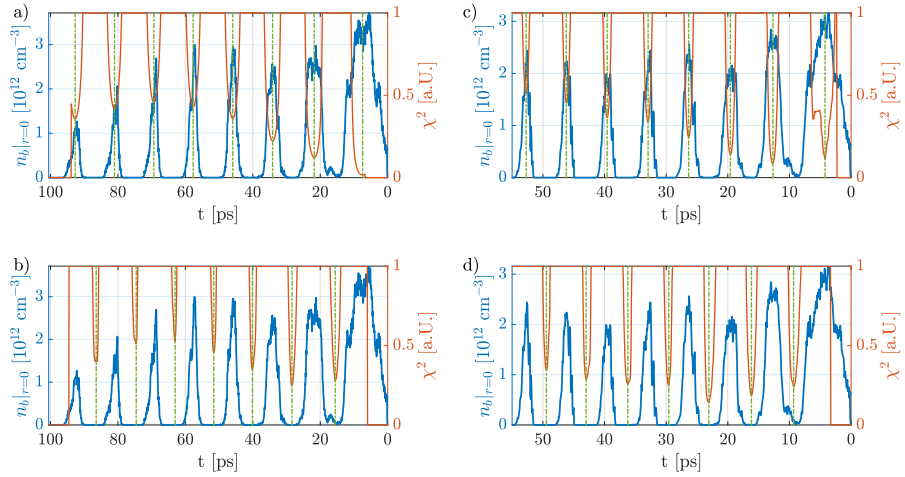

Figure A.15: Central bunch density $n_b|_{r=0}$ modulation (projection of $|x| \leq 0.1\,\mathrm{mm}$ from time-resolved images, blue lines), weighted distance squared function χ^2 (cut for high values, red lines) using a parabola as polynomial fit to the data and its minima (green dashed-dotted lines), location of micro-bunches (a, c) and defocused proton regions (b, d) with plasma density $n_{pe} = 0.92 \cdot 10^{14}\,\mathrm{cm}^{-3}$ (a, b) and $n_{pe} = 2.9 \cdot 10^{14}\,\mathrm{cm}^{-3}$ (c, d) from simulations. Here, $n_b = 5.6 \cdot 10^{12}\,\mathrm{cm}^{-3}$ and $\Delta n_{pe} = 0$.

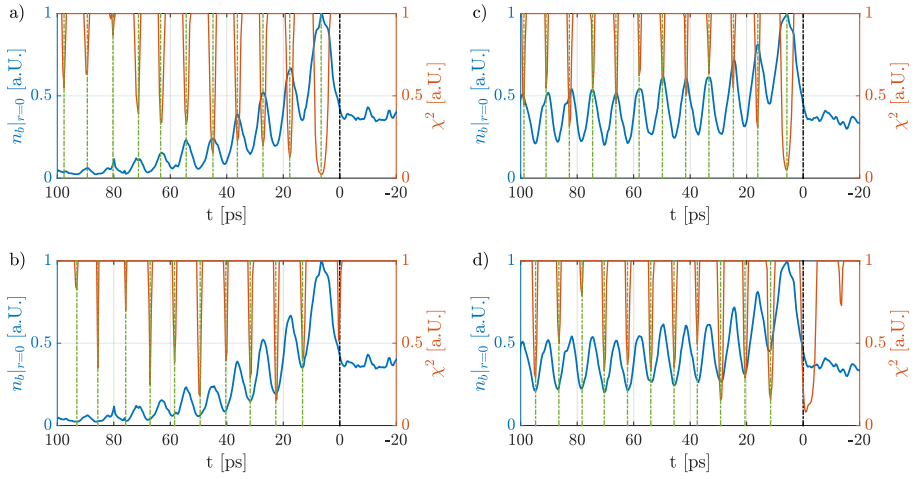

Figure A.16: Central bunch density $n_b|_{r=0}$ modulation (projection of $|x| \leq 0.1\,\mathrm{mm}$ from time-resolved images, blue lines), weighted distance squared function χ^2 (cut for high values, red lines) using a parabola as polynomial fit to the data and its minima (green dashed-dotted lines), location of micro-bunches (a, c) and defocused proton regions (b, d) with plasma density gradient $\Delta n = -1.9\,\%/\mathrm{m}$ (a, b) and $\Delta n = 2.0\,\%/\mathrm{m}$ (c, d) from experiment. Here, $n_{pe,Entr.} = 1.8 \cdot 10^{14}\,\mathrm{cm}^{-3}$ and $n_b = 5.8 \cdot 10^{12}\,\mathrm{cm}^{-3}$.

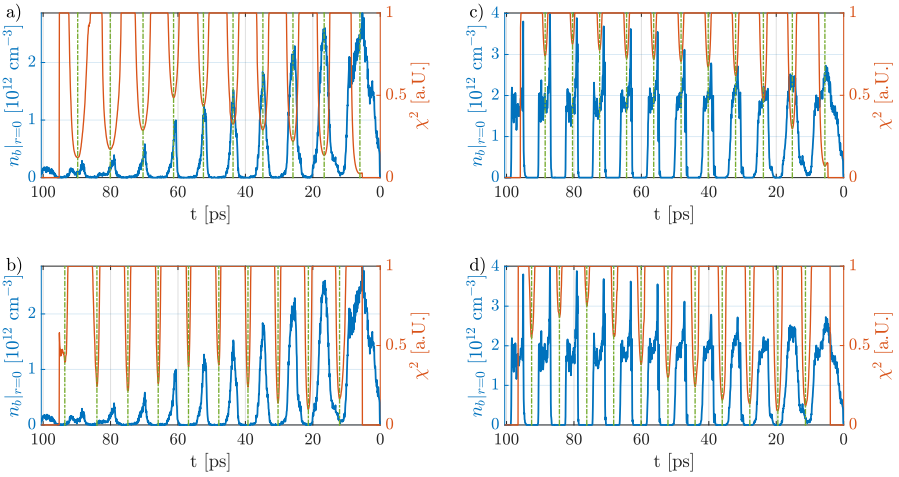

Figure A.17: Central bunch density $n_b|_{r=0}$ modulation (projection of $|x| \leq 0.1\,\mathrm{mm}$ from time-resolved images, blue lines), weighted distance squared function χ^2 (cut for high values, red lines) using a parabola as polynomial fit to the data and its minima (green dashed-dotted lines), location of micro-bunches (a, c) and defocused proton regions (b, d) with plasma density gradient $\Delta n = -1.9\,\%/\mathrm{m}$ (a, b) and $\Delta n = 2.0\,\%/\mathrm{m}$ (c, d) from simulations. Here, $n_{pe,Entr.} = 1.8 \cdot 10^{14}\,\mathrm{cm}^{-3}$ and $n_b = 5.4 \cdot 10^{12}\,\mathrm{cm}^{-3}$.

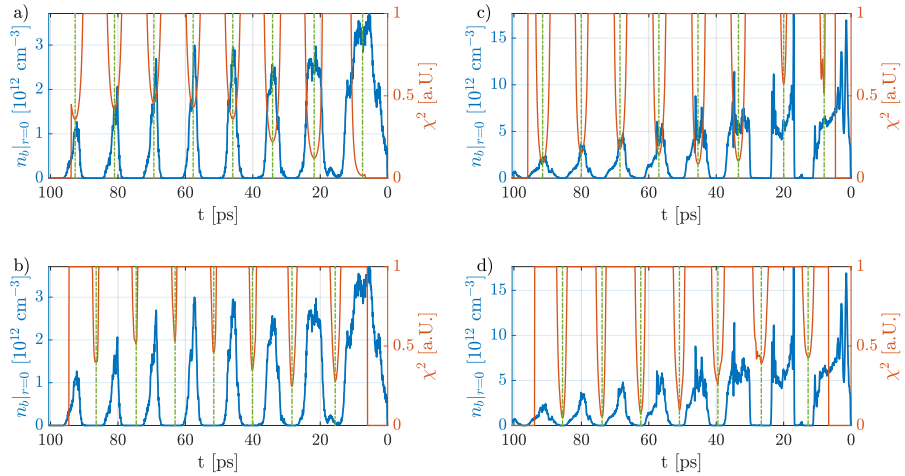

Figure A.18: Central bunch density $n_b|_{r=0}$ modulation (projection of $|x| \leq 0.1\,\mathrm{mm}$ from time-resolved images, blue lines), weighted distance squared function χ^2 (cut for high values, red lines) using a parabola as polynomial fit to the data and its minima (green dashed-dotted lines), location of micro-bunches (a, c) and defocused proton regions (b, d) with normalized incoming bunch emittance $\epsilon^* = 3.6\,\mu\mathrm{m}$ (a, b) and $\epsilon^* = 1.0\,\mu\mathrm{m}$ (c, d) from simulations. Here, $n_{pe} = 0.92 \cdot 10^{14}\,\mathrm{cm}^{-3}$, $n_b = 5.6 \cdot 10^{12}\,\mathrm{cm}^{-3}$ and $\Delta n_{pe} = 0$.

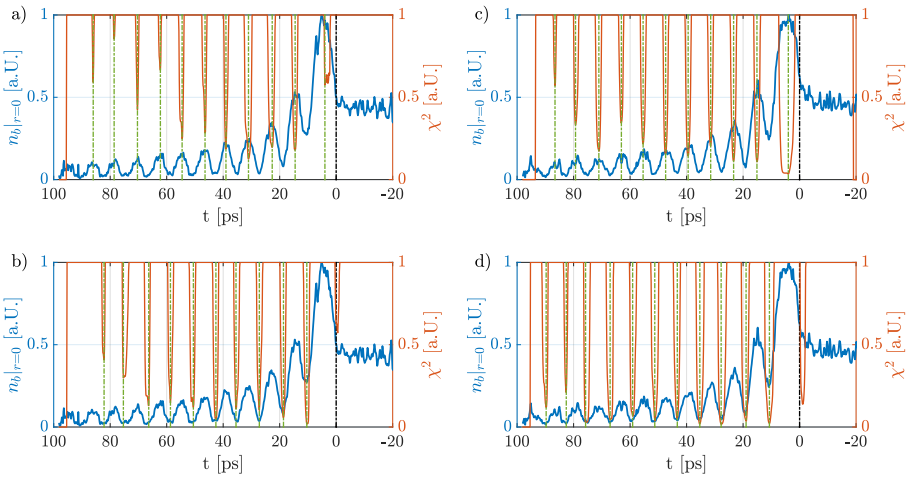

Figure A.19: Central bunch density $n_b|_{r=0}$ modulation (projection of $|x| \leq 0.1\,\mathrm{mm}$ from time-resolved images, blue lines), weighted distance squared function χ^2 (cut for high values, red lines) using a parabola as polynomial fit to the data and its minima (green dashed-dotted lines), location of micro-bunches (a, c) and defocused proton regions (b, d) with seed position $\xi_{Seed} = -0.7\,\sigma_\xi$ ($n_b = 3.9 \cdot 10^{12}\,\mathrm{cm}^{-3}$, Figures a, b) and $\xi_{Seed} = 0.6\,\sigma_\xi$ ($n_b = 4.1 \cdot 10^{12}\,\mathrm{cm}^{-3}$, Figures c, d) from experiment. Here, $n_{pe} = 2.0 \cdot 10^{14}\,\mathrm{cm}^{-3}$ and $\Delta n_{pe} = 0$.

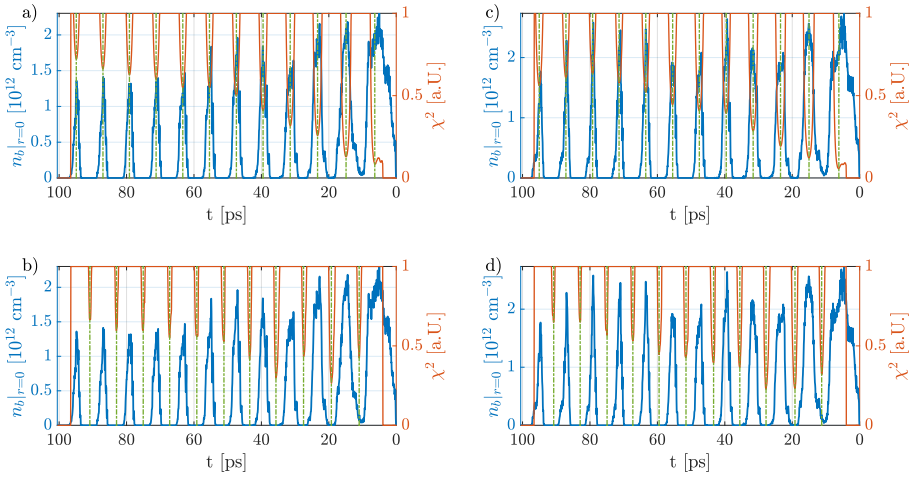

Figure A.20: Central bunch density $n_b|_{r=0}$ modulation (projection of $|x| \leq 0.1\,\mathrm{mm}$ from time-resolved images, blue lines), weighted distance squared function χ^2 (cut for high values, red lines) using a parabola as polynomial fit to the data and its minima (green dashed-dotted lines), location of micro-bunches (a, c) and defocused proton regions (b, d) with seed position $\xi_{Seed} = -0.7\,\sigma_\xi$ ($n_b = 3.9 \cdot 10^{12}\,\mathrm{cm}^{-3}$, Figures a, b) and $\xi_{Seed} = 0.6\,\sigma_\xi$ ($n_b = 4.1 \cdot 10^{12}\,\mathrm{cm}^{-3}$, Figures c, d) from simulations. Here, $n_{pe} = 2.0 \cdot 10^{14}\,\mathrm{cm}^{-3}$ and $\Delta n_{pe} = 0$.

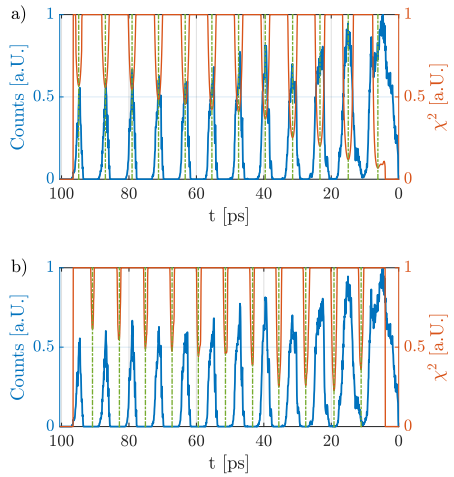

Figure A.21: Central bunch density $n_b|_{r=0}$ modulation (projection of $|x| \leq 0.1\,\mathrm{mm}$ from time-resolved images, blue lines), weighted distance squared function χ^2 (cut for high values, red lines) using a parabola as polynomial fit to the data and its minima (green dashed-dotted lines), location of micro-bunches (a) and defocused proton regions (b) with seed position $\xi_{Seed} = -0.6\,\sigma_\xi$ ($n_b = 4.1 \cdot 10^{12}\,\mathrm{cm}^{-3}$) from simulations. Here, $n_{pe} = 2.0 \cdot 10^{14}\,\mathrm{cm}^{-3}$ and $\Delta n_{pe} = 0$.

A.5 OTR Light Misalignment onto the Streak Camera Slit

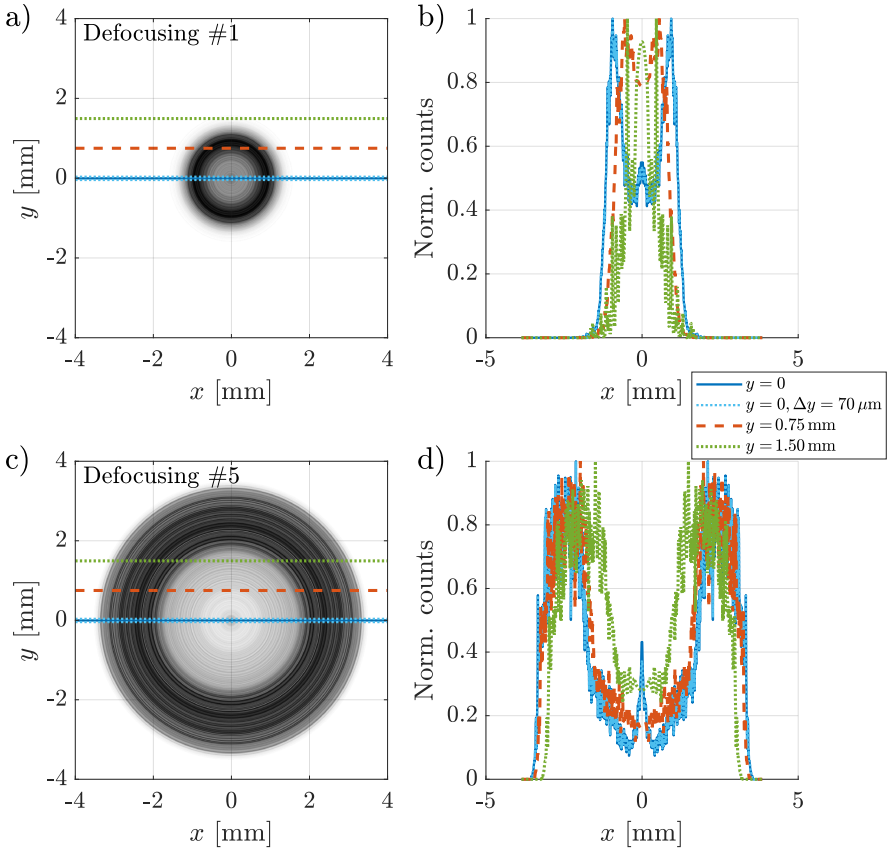

Figure A.22: Transverse charge density distributions of defocused proton regions (a, c) and line outs (b, d) from images (a, c) along x at $y = 0$ (dark blue solid line), $y = 0.75$mm (red dashed line), $y = 1.5$mm (green dotted line) and average over the slit width of $\Delta y = 70\,\mu$m at $y = 0$ (bright blue dotted line). Images correspond to the first (a, b) and fifth (c, d) period. Charge density distributions from the simulation with parameters of Table 4.4 at the position of the OTR screen after $\sigma_{res,t} = 1.5$ ps Gaussian temporal resolution convolution.

In the following, the effect of spatial misalignment of the OTR light from the proton bunch onto the streak camera slit is investigated from time-resolved images obtained from simulations. It was established in Section 3.1 that the signal of the streak camera is acquired through a slit (74 µm width at the OTR screen), much smaller than the transverse extent of the radial symmetric light signal (unmodulated head $\sigma_r \approx 570\,\mu$m at the OTR screen, defocused proton distributions generally wider than this), and thus that the light intensity on the images corresponds to the bunch charge density. Throughout the thesis, similar time-resolved images are obtained from simulations by plotting the bunch

density, transversely central through the bunch, with a slice width equal to the grid size ($\delta x, \delta y = 10\,\mu\text{m}$). As the bunch signal is much wider than the slit width, the profiles for a single pixel (dark blue solid lines) or averaging over the slit width (bright blue dotted lines) lead to similar profiles, see Figure A.22.

Generally, the OTR light of the proton bunch signal could be slightly misaligned with respect to the streak camera slit in the experiment. As the proton bunch charge density in simulations is obtained from a slice, central of the bunch, Figure A.22 studies how spatial misalignment of the light with respect to the slit affects the profiles of defocused proton distributions. Here, the result is shown for the first (a, b) and fifth (c, d) defocused proton region from the time-resolved images 3.5 m after the plasma and after convolution with the $\sigma_{res,t} = 1.5\,\text{ps}$ streak camera temporal resolution. The parameters of the simulation can be found in Table 4.4. In images (a, c), the radially symmetric charge density profile of the defocused protons, obtained from the simulations 2D-output is rotated over 180°.[3] Images (b, d) show the transverse profile along x for a central slice ($y = 0$, blue lines), and a misalignment of $y = 0.75$mm (red dashed lines) and $y = 1.5$mm (green dotted lines). Figure A.22 d) shows that, as expected, a spatial misalignment of the OTR light onto the slit, generally leads to charge densities of the profiles at smaller radius. Therefore, a ring of defocused protons appears with a radius the smaller, the larger the misalignment. Thus, spatial misalignment could be a reason for a slightly smaller maximum radius of defocused proton distributions, as well as higher charge density close to the bunch axis, that are measured in the experiment, when compared to the simulations (Figure 6.3 b). It would also explain why the on-axis peak at $x = 0$ is not measured experimentally, as it is predicted by simulations as a result of the convolution with temporal resolution of the experiment from surrounding micro-bunches, with high on-axis charge density. However, as the first defocused proton distributions from experiment and simulations agree well (Figure 6.3 a), and a large misalignment would lead to a significantly different shape, as observed in Figure A.22 b), the spatial misalignment of the light in experiment is expected to be small ($< 1\,\text{mm}$). Therefore the experimental results are compared with the on-axis profile from simulations throughout this thesis.

Similarly to the analysis of defocused proton distributions including spatial misalignment of the light with respect to the streak camera slit, the effect onto transverse profiles of micro-bunches is studied in Figure A.23. The simulation here corresponds to the measurement with the most negative plasma density gradient ($\Delta n_{pe} = -1.9\,\%/\text{m}$, parameters in Table 4.7), as here the effect of misalignment is expected to have a larger impact and profiles from experiment and simulations deviate. It was established in Section 5.4 (see Figure 5.19) that transverse micro-bunch profiles from simulations with the negative gra-

[3] Alternatively the 3D output of the simulation that contains the particle positions can be used.

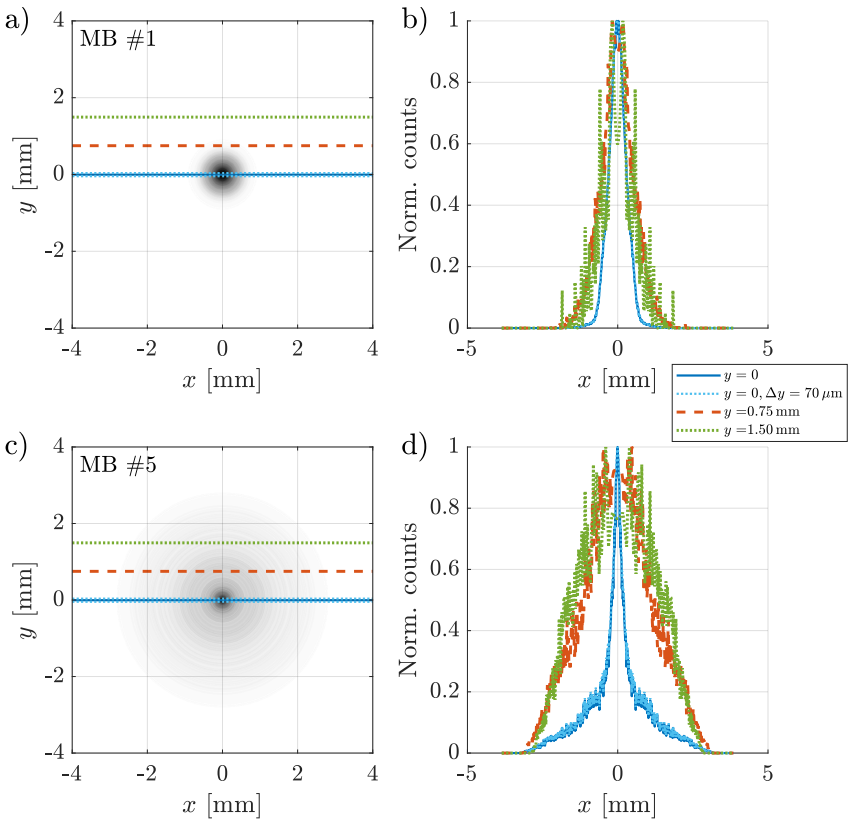

Figure A.23: Transverse charge density distributions of micro-bunches (a, c) and line outs (b, d) from images (a, c) along x at $y = 0$ (dark blue solid line), $y = 0.75$mm (red dashed line), $y = 1.5$mm (green dotted line) and average over the slit width of $\Delta y = 70\,\mu$m at $y = 0$ (bright blue dotted line). Images correspond to the first (a, b) and fifth (c, d) period. Charge density distributions from the simulation with parameters of Table 4.7 with plasma density gradient $\Delta n_{pe} = -1.9\,\%/\text{m}$ at the position of the OTR screen after $\sigma_{res,t} = 1.5\,$ps Gaussian temporal resolution convolution.

dient consist of a broad profile (from defocused protons due to the phase slippage of the transverse wakefield) and a narrow on-axis peak (tightly focused protons). The transverse profile of the fifth micro-bunch (Figure A.23 c, d) show that with spatial misalignment the on-axis peak (blue lines) would disappear and instead only the broad wing of protons would be measured (green dotted and orange dashed lines). This figure thus provides a possible explanation for the difference between the transverse micro-bunch profiles from experiment and simulations in Figure 5.19.

Misalignment of the OTR light on the streak camera slit was not measured experimentally. It is recommended to align the slit onto the maximum signal of the unmodulated proton

bunch after each proton bunch alignment in future measurements.

A.6 Radial Extent of the Transverse Wakefield

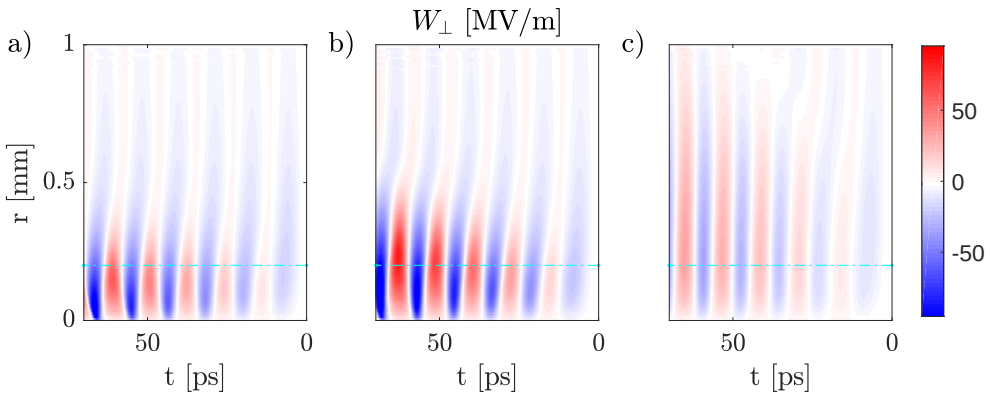

Figure A.24: Transverse wakefield along the bunch t and along the radius component r for the simulation with parameters of Table 4.4 after a) 3 m, b) 5 m and c) 10 m of plasma. Proton bunch incoming radius $\sigma_{r,0} = 200\,\mu\text{m}$ (cyan dash-dotted line).

Figure A.24 shows the transverse wakefield $W_\perp$ after 3 m (a), 5 m (b) and 10 m (c) of plasma from the simulation with input parameters of Table 4.4. The figures show the radial extent of the transverse wakefield. It shows a stronger dependency of the transverse wakefield amplitude on the radial position for shorter (a, b), than for longer distances (c) in plasma. Throughout this thesis, typically the wakefield is evaluated at $r = \sigma_{r,0}$ (cyan dash-dotted line), the proton bunch radius at the plasma entrance, i.e. at the waist.

A.7 Phase Slippage between the Wakefield and Protons

Figure A.25 shows the transverse wakefield at the fixed radial position of the initial bunch radius $W_\perp|_{r=\sigma_{r,0}}$ along the bunch ξ and along the plasma. One can see the phase slippage of the wakefield with respect to the protons with propagation distance in plasma, especially evident during SM development ($z < 6\,\text{m}$). The highly relativistic protons do not move longitudinally, i.e. have a fixed ξ-position along the bunch over the entire distance in plasma z. Thus, the transverse wakefields, experienced by the protons, correspond to vertical lines in the two dimensional plots of Figure A.25. The change in sign implies a change in direction of the transverse wakefield. Therefore, generally (with constant plasma

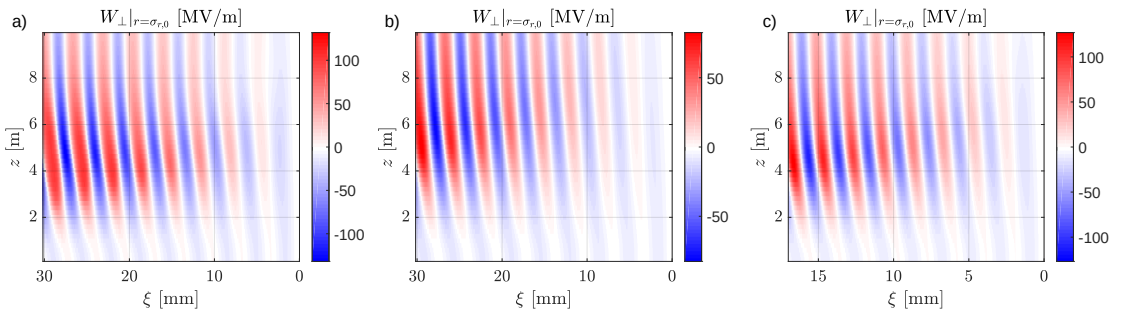

Figure A.25: Transverse wakefield at $r = \sigma_{r,0} = 200\,\mu\text{m}$ along the bunch ξ and along the plasma z for a) $n_{pe} = 0.92 \cdot 10^{14}\,\text{cm}^{-3}$, $n_b = 5.6 \cdot 10^{12}\,\text{cm}^{-3}$, b) $n_{pe} = 0.92 \cdot 10^{14}\,\text{cm}^{-3}$, $n_b = 3.1 \cdot 10^{12}\,\text{cm}^{-3}$, c) $n_{pe} = 2.9 \cdot 10^{14}\,\text{cm}^{-3}$, $n_b = 5.6 \cdot 10^{12}\,\text{cm}^{-3}$. Here, $\Delta n_{pe} = 0$ in all cases.

density, as in all cases presented here) protons experience both focusing and defocusing fields along the plasma propagation. The phase slippage decreases towards larger plasma distances, once the bunch is fully modulated ($z > 6\,\text{m}$). The phase slippage leads to a lengthening of the first modulation period, see Section 5.1. Figure A.25 shows that the phase slippage of the transverse wakefield with respect to the protons is essentially similar for the highest (a) and lowest (b) initial bunch density, as well as for the lowest (a, b) and highest (c) plasma density (with the plasma period the characteristic length scale in ξ) analyzed in this thesis.

A.8 Effect of Incoming Bunch Emittance on Self-Modulation

Reference [21] suggests that for a long bunch in plasma, a lower bunch emittance leads to larger amplitudes of the (transverse) wakefield. According to the calculations and simulations, for higher emittance the excited wave is not able to confine particles radially during the SM process. Therefore, in the following, I study from simulations the effect of the incoming bunch emittance on the evolution of transverse wakefield amplitudes and diverging protons along the plasma.

The incoming proton bunch emittance is not measured in the experiment on an event to event basis. However, during a dedicated experiment, the proton bunch divergence (without plasma) is measured with four screens, located close to and up to $\sim 20\,\text{m}$ behind the waist. Monte-Carlo calculations applied to the divergence suggest that the bunch emittance is significantly lower for lower bunch population [20]. In the experiment, a change in bunch population is expected to further influence the transverse size and the waist location of the bunch, as confirmed by the Monte-Carlo simulation studies in [20]. This makes a study of the effect of changing bunch emittance on the SM in the experiment nontrivial.

Outside this section, I thus keep a constant normalized emittance of 3.6 µm, the nominal value, for all simulations presented in this thesis.
When comparing the evolution of defocused proton distributions along plasma propagation, one has to distinguish between the effect of increasing natural divergence with increasing bunch emittance and the effect of possibly increasing transverse wakefield amplitudes with decreasing bunch emittance as predicted from [21]. In the following, I study the SM evolution with two simulations using the parameters from Table 4.4 and a normalized emittance of either 1.0 µm or 3.6 µm.
The time-resolved images of the self-modulated proton bunch 3.5 m after 10 m of plasma

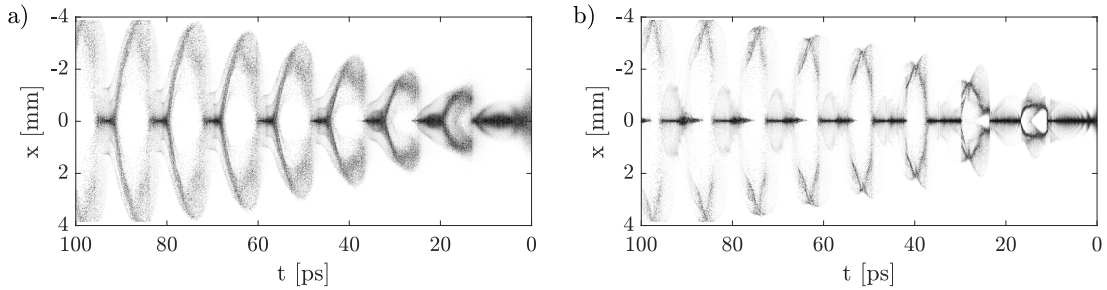

Figure A.26: Normalized time-resolved images from simulations with a normalized bunch emittance of a) $\epsilon^* = 3.6\,\mu m$ and b) $\epsilon^* = 1.0\,\mu m$. Here, $n_b = 5.6 \cdot 10^{12}\,cm^{-3}$, $n_{pe} = 0.9 \cdot 10^{14}\,cm^{-3}$ and $\Delta n_{pe} = 0$.

are shown in Figure A.26. One can see significantly more high frequency structure of the modulation with the lower ($\epsilon^* = 1.0\,\mu m$, Figure b) than with the higher ($\epsilon^* = 3.6\,\mu m$, Figure a) incoming bunch emittance. The time-resolved images for the two emittance values do not show a clear difference in transverse width of defocused proton distributions. I analyze the evolution of the divergence of defocused proton distributions, together with transverse wakefield amplitudes, along the plasma in the following. The ξ-locations of defocused proton regions along the bunch, determined from images after the plasma are fixed, as explained in Section 3.2.4, and can be found in Figure A.18.

A.8.1 Defocusing along the Plasma (Simulations)

I study the effect of the incoming bunch emittance on the amplitude of the transverse wakefield and on the divergence of defocused proton distributions.

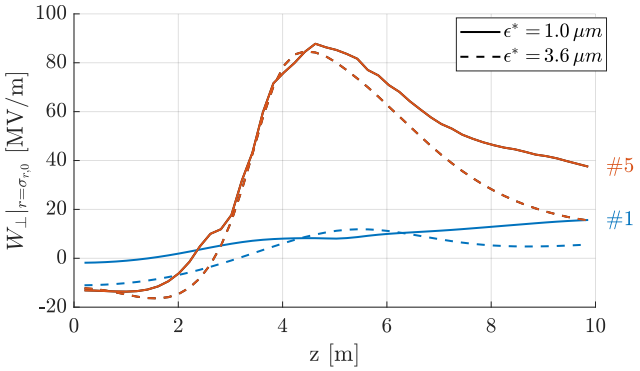

Figure A.27: Transverse wakefield at $r = \sigma_{r,0}$ of defocused proton regions of the first (blue lines) and fifth (red lines) period as a function of distance in plasma z with normalized incoming bunch emittance $\epsilon^* = 1.0\,\mu\text{m}$ (solid lines) and $\epsilon^* = 3.6\,\mu\text{m}$ (dashed lines). Here, $n_b = 5.6 \cdot 10^{12}\,\text{cm}^{-3}$, $n_{pe} = 0.9 \cdot 10^{14}\,\text{cm}^{-3}$ and $\Delta n_{pe} = 0$.

Transverse Wakefield along the Plasma

The transverse wakefield amplitudes at the location of defocused proton regions of the first (blue lines) and fifth (red lines) periods for different incoming bunch emittance are shown in Figure A.27. For both periods and emittance values, wakefield amplitudes are initially ($z = 0$) focusing and turn defocusing after $\sim 3\,\text{m}$, due to the phase slippage between the wakefield and protons during SM, for constant plasma density. Except for the first period with low emittance (blue solid line), the amplitudes of the defocusing wakefields reach a maximum value at $\sim 4 - 5\,\text{m}$ and then decrease with further propagation in plasma. The transverse wakefield for the low emittance does not reach a maximum amplitude over the first period over the 10 m of plasma. After $\sim 6\,\text{m}$, the amplitudes of the transverse wakefields are generally larger with lower (solid lines) than with higher (dashed lines) incoming emittance, which is in agreement with what is predicted in [21].
Next, I study the effect of the transverse wakefield on the divergence of defocused proton distributions for the two emittance cases.

Defocused Proton Distributions along the Plasma

The change in rms width of defocused proton distributions along the plasma is plotted in Figure A.28. As expected, the bunch propagating in vacuum (black lines) expands faster for higher (dashed lines) than for lower (solid lines) emittance due to the larger natural divergence. As shown in all studies in Section 6, with a constant plasma density over the 10 m, defocused protons are initially focused (i.e. protons converge) before the transverse

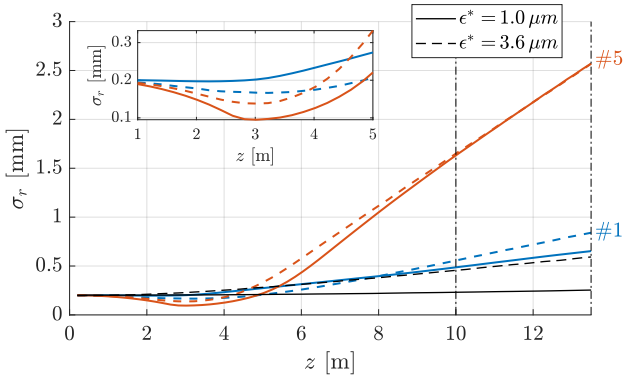

Figure A.28: The rms width of defocused proton distributions σ_r as a function of propagation distance z (plasma $z = 1 - 10\,\text{m}$, vacuum $z = 10 - 13.5\,\text{m}$) with normalized incoming bunch emittance $\epsilon^* = 1.0\,\mu\text{m}$ (solid lines) and $\epsilon^* = 3.6\,\mu\text{m}$ (dashed lines) at a fixed ξ of the first (blue lines) and fifth (red lines) period and without plasma (black lines). Inset zooms in at $z = 1 - 5\,\text{m}$. Here, $n_b = 5.6 \cdot 10^{12}\,\text{cm}^{-3}$, $n_{pe} = 0.9 \cdot 10^{14}\,\text{cm}^{-3}$ and $\Delta n_{pe} = 0$.

wakefield turns defocusing after a few meters in plasma (see Figure A.27). One can see that the start of the divergence does not vary significantly between the first (blue lines) and fifth (red lines) period, for either of the two emittance cases (see inset of Figure A.28). In the fifth period, protons are stronger converging over the first meters of plasma with lower (solid lines) than with higher (dashed lines) incoming bunch emittance, even though focusing fields are lower (Figure A.27), due to the smaller natural divergence that focusing fields have to counteract.

Protons start to diverge at $\sim 3 - 4\,\text{m}$. The higher transverse (defocusing) wakefield after $\sim 5\,\text{m}$ with lower emittance leads to stronger divergence. However, with low emittance the natural divergence is smaller. With transverse wakefield amplitudes growing along the bunch, one can observe at what position along the bunch the effect of the transverse wakefield dominates over the effect of natural divergence: The width of the proton distribution after the plasma ($> 10\,\text{m}$) of the first period is larger for higher emittance, i.e. here, the higher natural divergence dominates over the lower wakefield amplitude for higher emittance. The width of the distribution of the fifth period at the position of the OTR screen ($z = 13.5\,\text{m}$) is essentially equal for the two emittance cases. This shows that the increase in transverse (defocusing) wakefield with lower bunch emittance compensates for the lower natural divergence in the fifth period, as transverse wakefield amplitudes are growing along the bunch (Section 1.4.3).

This analysis shows that concluding on a change in the transverse wakefield for changing incoming bunch emittance in the experiment is very challenging. The analysis is limited to defocused proton distributions that have diverged to radial positions $\leq 4\,\text{mm}$, the

aperture limit of the OTR light transport. With the experimental parameters used here, protons reach this radial position over the first six periods behind the seed (see e.g. Figure A.26). The analysis of the divergence of defocused proton distributions from above shows that over the first five periods the distributions in the different emittance cases are largely effect by both the transverse wakefield but also the natural divergence. Decoupling the two effects in experiment is intricate.

Reference [20] shows that the emittance changes when changing the incoming bunch population. Additionally, as mentioned earlier, a change in bunch population is expected to affect the transverse size and waist position of the bunch in the experiment. Therefore, when the incoming bunch population is changed in the experiment, a change in the amplitude of wakefields is expected due to both the change in initial bunch density and the change in emittance. To avoid the superposition of multiple effects, studies with different incoming bunch populations are generally excluded from this thesis. Nevertheless, experimentally determined widths of defocused proton distributions for different bunch populations are shown in the next section.

A.8.2 Effect of Bunch Population (Experiment)

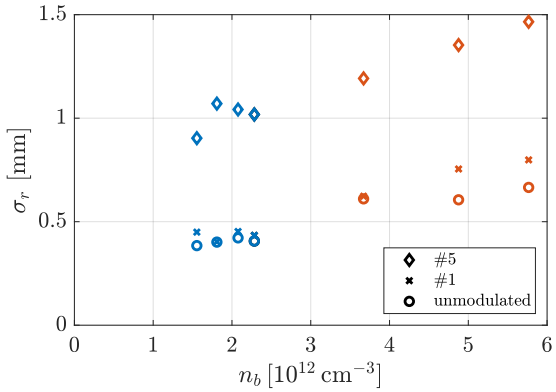

Figure A.29: The rms width σ_r of defocused proton distributions of the first (crosses) and fifth (diamonds) period and the unmodulated bunch head (circles) as a function of initial bunch density. Measurements with a bunch population of $N_{p^+} = (0.9 \pm 0.1) \cdot 10^{11}$, $\sigma_\xi = 250\,\mathrm{ps}$ and $\xi_{Seed} = [-0.1, 0.4, 0.7, 0.9]\,\sigma_\xi$ (blue symbols) and with a bunch population of $N_{p^+} = (2.8 \pm 0.2) \cdot 10^{11}$, $\sigma_\xi = 300\,\mathrm{ps}$ and $\xi_{Seed} = [0.1, 0.6, 1.0]\,\sigma_\xi$ (red symbols). Here, $n_{pe} = 2.0 \cdot 10^{14}\,\mathrm{cm}^{-3}$ and $\Delta n_{pe} = 0$.

The rms widths determined from time-resolved streak camera images, using the procedure of Section 3.2.8, for the two bunch population cases are shown in Figure A.29. The beam

density is increased by increasing the total bunch population from $N_{p^+} \approx 0.9 \cdot 10^{11}$ (blue symbols) to $N_{p^+} \approx 2.8 \cdot 10^{11}$ (red symbols) and additionally varying the seed position for a given bunch population. From [20], an increase in emittance is expected when increasing the bunch population. Therefore, from the study above, the increase in divergence σ_r with beam density n_b is expected to be a superposition of the increase in transverse wakefield amplitudes due to increasing beam density, the decrease in transverse wakefield amplitudes due to increasing emittance and the increase in natural divergence due to increasing emittance.

The transverse width of the unmodulated head of the bunch (circles) is indeed larger for higher bunch population, which can be assigned to the larger natural divergence. Potentially defocused proton distributions of the fifth period (diamonds) are slightly wider with low bunch population than when extrapolating the rms widths of measurements with high bunch population. This is more dominant when comparing them to the unmodulated width (circles). This could be explained with the larger transverse (defocusing) wakefield with lower incoming bunch emittance with the lower bunch population. However, the results are not conclusive.

A.9 Emittance Growth along the Modulated Bunch

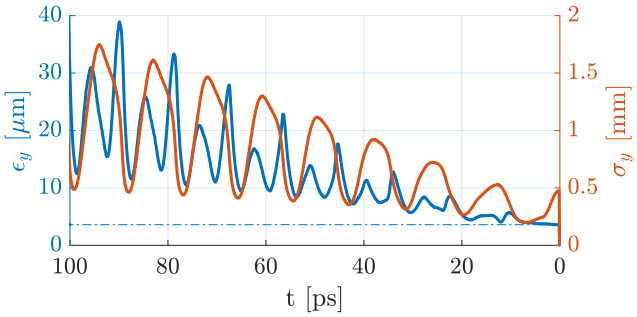

Figure A.30: The rms width σ_y (red solid line) and normalized slice emittance ϵ_y (blue solid line) along the bunch axis t from the simulation (parameters Table 4.4, except $n_{pe} = 1.0 \cdot 10^{14}\,\mathrm{cm}^{-3}$) after 10 m of plasma with an incoming normalized bunch emittance 3.6 µm (blue dash-dotted line).

A change in slice emittance along the modulated bunch is expect to influence the transverse bunch evolution during plasma and vacuum propagation. The statistical emittance along the modulated bunch after 10 m of plasma from the simulation with parameters of Table 4.4 (except $n_{pe} = 1.0 \cdot 10^{14}\,\mathrm{cm}^{-3}$) is studied in Figure A.30. It shows the rms width

σ_y of the transverse y distribution of particles (red solid line), where x and y are equal as the studies here are radial symmetric. The minima in size σ_y correspond to the location of micro-bunches. One can see a small increase in width of micro-bunches along the bunch. Also the corresponding slice emittance ϵ_y in y (or x) (blue solid line) increases along the bunch from the incoming normalized bunch emittance of 3.6 µm (blue dash-dotted line). At the start of SM ($t = 0$), where the wakefield is zero, the emittance essentially does not increase with the plasma propagation. One can see that the emittance reaches local minima at the position of the micro-bunches and the value increases along the bunch. The ninth micro-bunch here has a minimum emittance of 12 µm, i.e. an increase by a factor > 3 of the incoming emittance.
In the experiment, micro-bunch widths are measured 3.5 m after the plasma. As the slice emittance is not known in the experiment, in order to conclude on widths at the plasma exit, we rely on simulations, comparing the modulated bunch before and after the 3.5 m vacuum propagation. Due to the increase of emittance along the bunch, micro-bunches further behind in the bunch are expected to diverge faster during the subsequent vacuum propagation than early micro-bunches. The increasing width is counteracting as later micro-bunches are wider and therefore diverge slower. This must be considered when analyzing the widths of micro-bunches at the OTR screen. However, simulations (e.g. Figure 5.18 for micro-bunches, Figures 6.8, 6.14, 6.20 for defocused proton distribution) demonstrate that the comparison of SM characteristics, measured at the OTR screen, lead to similar conclusions as to ones measured at the plasma exit.

A.10 Effect of Plasma Radius on Self-Modulation in Simulations

I showed in Section 2.4 using Schlieren imaging that the plasma radius in the experiment is expected to be $r_{pe} > 1$ mm. The simulations used for the SM characterization throughout this thesis are obtained with a fixed plasma radius of $r_{pe} = 1$ mm, see Table 4.4. In the following, I study whether simulation results differ for a plasma radius twice that value.

Longitudinal Bunch Profile

In Chapter 5, I analyze characteristics of the micro-bunches of the self-modulated proton bunch from the on-axis charge density from time-resolved images, obtained at the position of the OTR screen, i.e. 3.5 m after the plasma. Figure A.31 shows that the on-axis charge density profile is essentially similar for the narrower ($r_{pe} = 1$ mm, blue solid line) and the wider $r_{pe} = 2$ mm, red dotted line) plasma radius. Therefore, simulation results obtained

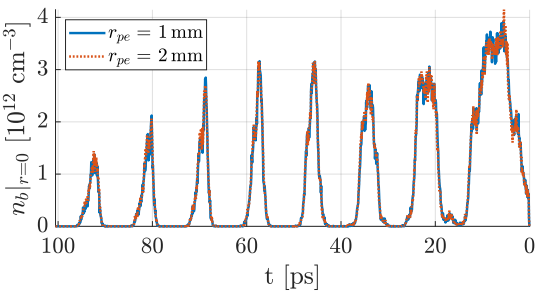

Figure A.31: Longitudinal on-axis charge density profile of the self-modulated proton bunch profile at the position of the OTR screen with plasma radius $r_{pe} = 1\,\text{mm}$ (blue solid line) and $r_{pe} = 2\,\text{mm}$ (red dotted line) from simulations with parameters of Table 4.4.

from the longitudinal profile of the self-modulated bunch in Chapter 5 can be assumed as independent of the input for the plasma radius within this range.

Defocusing along the Plasma

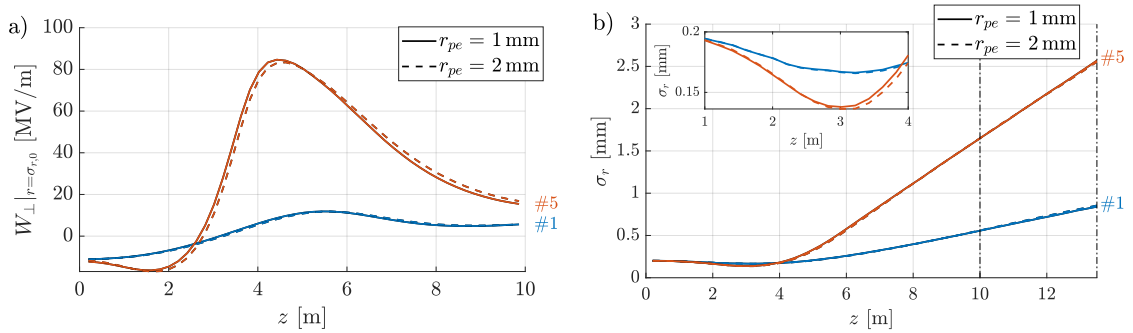

Figure A.32: a) Transverse wakefields at $r = \sigma_{r,0}$ and b) rms width; both of defocused proton regions at a fixed ξ of the first (blue lines) and fifth (red lines) period as a function of propagation distance z (plasma $z = 1 - 10\,\text{m}$, vacuum $z = 10 - 13.5\,\text{m}$) with plasma radius $r_{pe} = 1\,\text{mm}$ (solid lines) and $r_{pe} = 2\,\text{mm}$ (dashed lines) from simulations with parameters of Table 4.4. Inset in b) zooms in at $z = 1 - 4\,\text{m}$.

In Chapter 6, transverse wakefields and divergence of defocused proton distributions are analyzed. Figure A.32 shows that, according to simulations, also the results on defocused protons are not expected to change on a measurable scale if the plasma radius was twice as wide. The transverse wakefield (Figure a) and the divergence of defocused protons (Figure b) follow similar values along the plasma z for a plasma radius of 1 mm (solid lines) and 2 mm (dashed lines) for both periods. Deviations for the fifth period (red lines) are $< 7\,\%$ (maximum at $z = 3.5\,\text{m}$) for the transverse wakefield $W_\perp|_{r=\sigma_r}$ and $< 5\,\%$ (maximum at

$z = 5\,\mathrm{m}$) for the rms width σ_r. Note that potentially differences might increase along the bunch, but they remain small for distances close to the seed point, as analyzed throughout this work.

A.11 Effect of Initial Bunch Density Slope

Throughout the thesis the initial bunch density is varied by moving the seed position (RIF in experiment or cut in simulations) along the longitudinal Gaussian bunch. In the following I study if this is a sensitive approach or if the change in initial bunch density slope, when moving the seed position, is expected to influence the SM characteristics, studied in this thesis.

I determine defocused proton distributions with different seed positions with a bunch population $N_{p^+} = (2.8 \pm 0.1) \cdot 10^{11}$, bunch length $\sigma_\xi = 9\,\mathrm{cm}$ and a plasma density of $n_{pe} = 2 \cdot 10^{14}\,\mathrm{cm}^{-3}$. From this measurement, I compare the results of a seed point behind the bunch center ($\xi_{Seed} = -0.7\,\sigma_\xi$) that corresponds to a similar initial bunch density ($n_b = 3.9 \cdot 10^{12}\,\mathrm{cm}^{-3}$) as a seed point ahead of the bunch center ($\xi_{Seed} = 0.6\,\sigma_\xi$, i.e. $n_b = 4.1 \cdot 10^{12}\,\mathrm{cm}^{-3}$).

As the initial bunch densities are similar, also the seed wakefield amplitudes are. The longitudinal slope of the initial bunch density has two consequences. First, the wakefield with seed position in the front is increasingly focusing along the bunch between seed position and a given period, while it is increasingly defocusing (already at $z = 0$) for the seed position behind the center (Section 1.4). Second, with increasing bunch density (frontal seed position), there is a larger number of protons between the seed position and the modulation period studied (here #1 and #5) that can contribute to the wakefield than with seeding behind. If the defocusing wakefield is larger (i.e. also wider defocused proton distributions) for the frontal seed position, the latter is expected to dominate.

I show from experiments and simulations that the difference in defocusing (wakefield) is small when seeding with a fixed distance ahead or behind the bunch center. Therefore, the change in slope of the bunch density profile (for studies over the first five defocusing periods behind the seed position) can be neglected when changing the initial bunch density by changing the seed position in all studies presented in this thesis.

Figure A.33 shows the normalized time-resolved images 3.5 m after the 10 m long plasma for the seed position $\xi_{Seed} = -0.7\,\sigma_\xi$ (a-c) and $\xi_{Seed} = 0.6\,\sigma_\xi$ (d-f) from simulations (a, b, d, e) and experiment (c, f). The streak camera images here resolve the defocused proton distributions slightly better than the simulation images (a, d) after the temporal resolution convolution (b, e). This suggests a slightly higher resolution than $\sigma_{res,t} = 1.5\,\mathrm{ps}$ in the

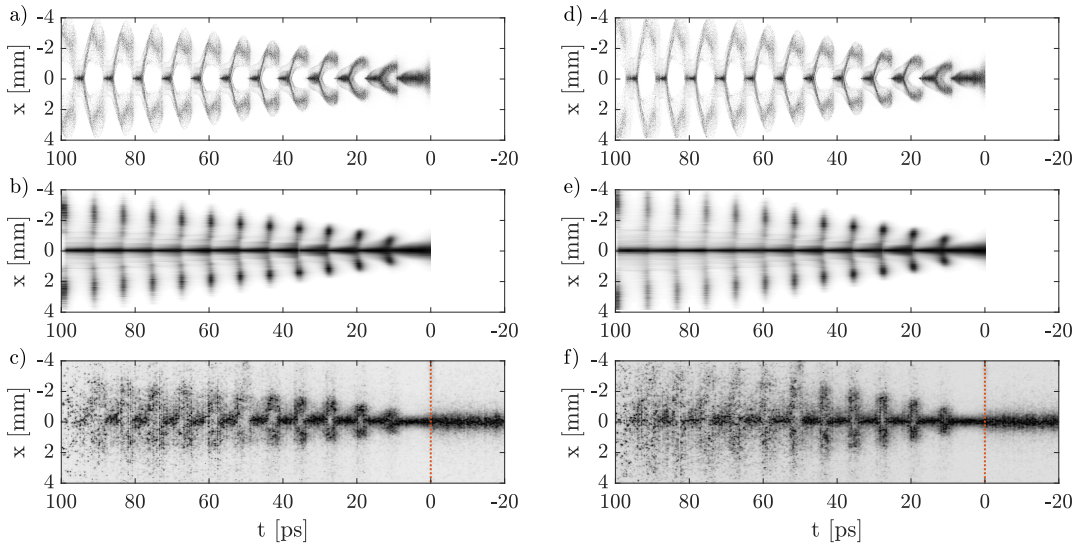

Figure A.33: Normalized time-resolved images of the modulated bunch with seed position $\xi_{Seed} = -0.7\,\sigma_\xi$ ($n_b = 3.9 \cdot 10^{12}\,\mathrm{cm}^{-3}$, a-c) and $\xi_{Seed} = 0.6\,\sigma_\xi$ ($n_b = 4.1 \cdot 10^{12}\,\mathrm{cm}^{-3}$, d-f). Images (a, b) show the simulation results without, (b, e) with $\sigma_{res,t} = 1.5\,\mathrm{ps}$ Gaussian temporal resolution convolution and (c, f) the streak camera images. Here, $n_{pe} = 2.0 \cdot 10^{14}\,\mathrm{cm}^{-3}$ and $\Delta n_{pe} = 0$.

experiment during this measurement.
All images, from simulations (a, b, d, e) and from experiment (c, f) show slightly narrower defocused proton distributions with a seed position behind the bunch center. However, differences appear to be small. I study quantitatively the difference in the profiles of the defocused proton distributions in the following.
The determination of the location of focused and defocused proton regions can be found in Section A.4.

A.11.1 Transverse Profiles of Defocused Proton Distributions

Figure A.34 shows the transverse profiles of defocused proton distributions for a seed position $-0.7\,\sigma_\xi$ behind (a, b) and $0.6\,\sigma_\xi$ ahead of (c, d) the bunch center. The profiles of the first period (a, c) show very good agreement between the experimental ones (red lines) and the ones from simulations after convoluting with the streak camera temporal resolution (dark blue lines). Also in the fifth period (b, d) the maximum radius of the distributions agree well from experiment and simulations. For the seed position behind the center (b), the maximum radius is slightly larger from the simulation. As in previous

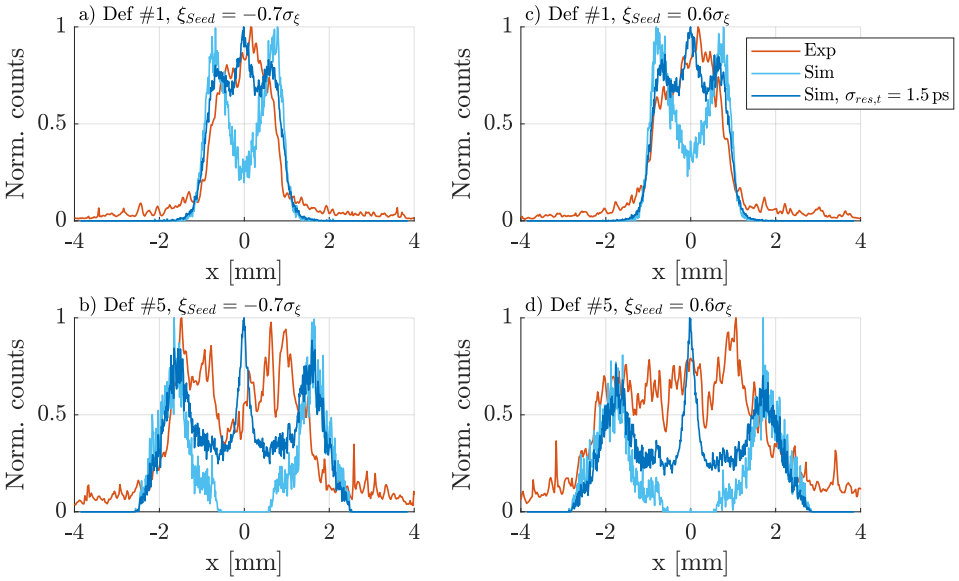

Figure A.34: Transverse profiles of defocused proton distributions from experiment (red lines) and simulations without (bright blue lines) and with (dark blue lines) $\sigma_{res,t} = 1.5\,\mathrm{ps}$ Gaussian temporal resolution convolution; (a, b) with seed position $\xi_{Seed} = -0.7\,\sigma_\xi$, $n_b = 3.9{\cdot}10^{12}\,\mathrm{cm}^{-3}$ and (c, d) with $\xi_{Seed} = 0.6\,\sigma_\xi$, $n_b = 4.1{\cdot}10^{12}\,\mathrm{cm}^{-3}$ (a, c) of the first period, (b, d) of the fifth period. Here, $n_{pe} = 2.0 \cdot 10^{14}\,\mathrm{cm}^{-3}$ and $\Delta n_{pe} = 0$.

studies, the charge density around to the bunch axis is higher in the experiment for the fifth period. Both these differences between the profiles from experiment and simulations can be explained with a small spatial misalignment of the OTR light onto the streak camera slit, as studied in Section A.5.

As also concluded from the time-resolved images, the profiles of the defocused proton distributions when seeding ahead or behind the bunch center are similar. The profiles seeding $-0.7\,\sigma_\xi$ behind the bunch center are slightly narrower than the ones with $0.6\,\sigma_\xi$. This can be either the result of the change in the initial bunch density slope and/or due to the slightly higher initial bunch density with the frontal seed point, that is slightly closer to the bunch center ($n_b = 4.1 \cdot 10^{12}\,\mathrm{cm}^{-3}$ as opposed to $n_b = 3.9 \cdot 10^{12}\,\mathrm{cm}^{-3}$). To decouple the effect from the difference in initial bunch density and the initial bunch density slope, the rms width is plotted as a function of the initial bunch density in the following. As even the combination of the two has only a small effect on the defocused proton distributions (Figure A.34), I conclude that the initial bunch density slope has only a small effect on the defocused proton distributions.

Figure A.35 shows the rms width of the defocused proton distributions as a function of initial bunch density. As seen in all measurements discussed in this thesis, the widths

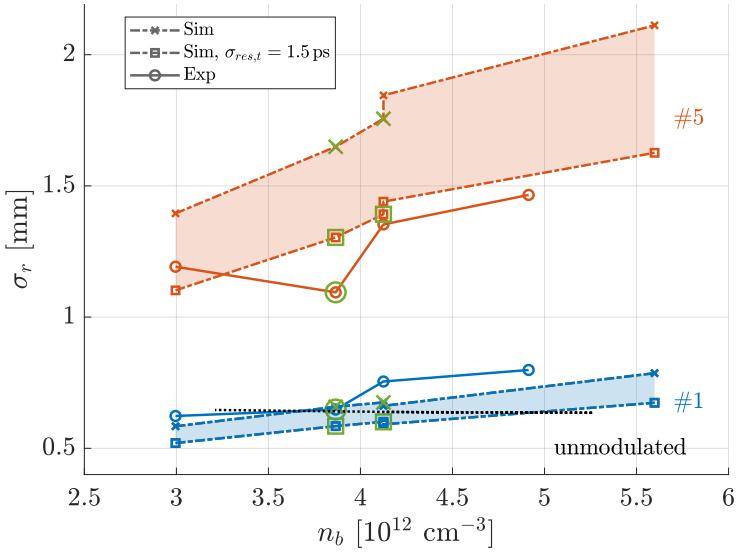

Figure A.35: The rms width of defocused proton distributions from experiment (circles) and simulations without (crosses) and with (squares) $\sigma_{res,t} = 1.5$ ps resolution convolution) as a function of initial bunch density n_b for the first (blue lines) and fifth (red lines) period and rms width of unmodulated bunch (black lines). Seed positions behind the bunch center ($\xi_{Seed} = -0.7\,\sigma_\xi$, i.e. $n_b = 3.9 \cdot 10^{14}\,\mathrm{cm}^{-3}$ in experiment and simulation and $\xi_{Seed} = -0.6\,\sigma_\xi$, i.e. $n_b = 4.1 \cdot 10^{14}\,\mathrm{cm}^{-3}$ in simulation) marked in green. Here, $n_{pe} = 2.0 \cdot 10^{14}\,\mathrm{cm}^{-3}$ and $\Delta n_{pe} = 0$.

from simulations after convoluting the images with the streak camera resolution (squares) agree relatively well with the ones from experiment (circles). Widths of the fifth period (red lines) are generally slightly wider from simulations, due to the higher charge density around the bunch axis measured in the experiment (see Figure A.34).

Results from a seed position behind the bunch center are marked in green. The rms width of the fifth defocused proton distribution is slightly smaller with the seed position $-0.6\,\sigma_\xi$ behind than with $0.6\,\sigma_\xi$ ahead of the bunch center (both at $n_b = 4.1 \cdot 10^{14}\,\mathrm{cm}^{-3}$) in the simulation. However, the difference is very small. Also in the experiment, the distributions with a seed position $-0.7\,\sigma_\xi$ behind the bunch center (i.e. $n_b = 3.9 \cdot 10^{14}\,\mathrm{cm}^{-3}$, symbols marked green) are smaller than the interpolation from the beam densities with seed positions ahead of the bunch center. The experiment shows a slightly stronger dependence of the defocused proton distributions on the initial bunch density slope than the simulations. This analysis shows that the effect of the initial bunch density slope on the transverse width of defocused proton distributions is significantly smaller than the effect of the change in initial bunch density, over the range analyzed in this thesis.

A.11.2 Defocusing along the Plasma (Simulations)

I study the evolution of the transverse wakefield amplitudes and defocused proton distributions with the seed positions from the experiment ($-0.7\,\sigma_\xi$ and $0.6\,\sigma_\xi$). As earlier, the experimental results are compared with a simulation with exactly the same distance to the bunch center behind and ahead of the bunch ($\pm 0.6\,\sigma_\xi$) to distinguish between the effect of the change in initial bunch density and the effect of the initial bunch density slope.

Transverse Wakefield along the Plasma

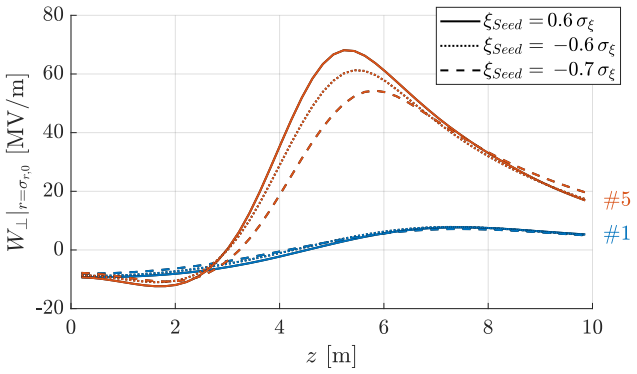

Figure A.36: Transverse wakefield at $r = \sigma_{r,0}$ of defocused protons of the first (blue lines) and fifth (red lines) period as a function of distance in plasma z with seed position $\xi_{Seed} = 0.6\,\sigma_\xi$ (solid lines), $\xi_{Seed} = -0.6\,\sigma_\xi$ (dotted lines), $\xi_{Seed} = -0.7\,\sigma_\xi$ (dashed lines). Here, $n_{pe} = 2.0 \cdot 10^{14}\,\mathrm{cm}^{-3}$ and $\Delta n_{pe} = 0$.

Figure A.36 shows that the transverse wakefield amplitudes of defocused proton distributions of the fifth period (red lines) are slightly larger with the seed position $0.6\,\sigma_\xi$ ahead (solid line) than with the seed position $-0.7\,\sigma_\xi$ behind (dashed line) along the 10 m of plasma. The amplitudes with a seed position $-0.6\,\sigma_\xi$ behind (dotted line) are consistently between the two. This shows that the increase in the defocusing wakefield when changing the seed position from $-0.7\,\sigma_\xi$ to $0.6\,\sigma_\xi$ is a combination of both the increasing initial bunch density and the change in slope of the initial bunch density profile.
However, the change in wakefield amplitude is small. The maximum defocusing decreases from $\sim 68\,\mathrm{MV/m}$ ($0.6\,\sigma_\xi$) over $61\,\mathrm{MV/m}$ ($-0.6\,\sigma_\xi$) to $54\,\mathrm{MV/m}$ ($-0.7\,\sigma_\xi$). Thus, the decrease in maximum amplitude of the wakefield is $\sim 10\,\%$ due to the change in slope from $\pm 0.6\,\sigma_\xi$.
The maximum amplitude of the defocusing wakefield of the first period (blue lines) is very similar for the three seed positions. It is essentially equal for the seed positions $\pm 0.6\,\sigma_\xi$ ($8.3\,\mathrm{MV/m}$) and decreases slightly for the seed position $-0.7\,\sigma_\xi$ ($7.3\,\mathrm{MV/m}$).

Figure A.36 shows that generally, as a result of the similar initial bunch density, the difference in amplitude of transverse wakefields is small for the three seed positions discussed here.

Defocused Proton Distributions along the Plasma

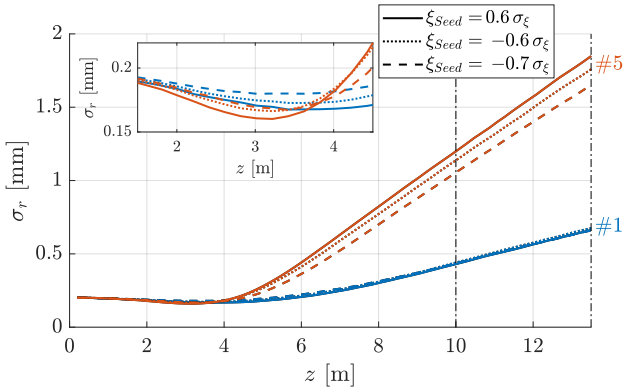

Figure A.37: The rms width of defocused proton distributions σ_r as a function of distance in plasma z with seed position $\xi = 0.6\,\sigma_\xi$ (solid lines), $\xi = -0.6\,\sigma_\xi$ (dotted lines) and $\xi = -0.7\,\sigma_\xi$ (dashed lines) at a fixed ξ of the first (blue lines) and fifth (red lines) period and without plasma (black lines). Inset zooms in at $z = 1 - 5\,\mathrm{m}$. Here, $n_{pe} = 2.0 \cdot 10^{14}\,\mathrm{cm}^{-3}$ and $\Delta n_{pe} = 0$.

The same conclusion can be drawn from the evolution of defocused proton distributions along the plasma, as plotted in Figure A.37. The similar defocusing fields over the first period (Figure A.36) result in a similar evolution of the diverging protons (Figure A.37, blue lines). In agreement with the small increase in defocusing fields over the fifth period from $-0.7\,\sigma_\xi$ over $-0.6\,\sigma_\xi$ to $0.6\,\sigma_\xi$ (Figure A.36), also the defocused proton distributions are slightly increasing (red lines). The slightly larger transverse wakefield is not only shown by the wider distributions during defocusing ($z > 5\,\mathrm{m}$) but also by the narrower distributions during initial focusing ($2\,\mathrm{m} < z < 4\,\mathrm{m}$, see inset), so results are consistent.
The width of the defocused proton distribution of the fifth period at the position of the OTR screen ($z = 13.5\,\mathrm{m}$) is 1.9 mm for the seed position ahead and 1.8 mm behind the bunch center with $\xi_{Seed} = \pm 0.6\,\sigma_\xi$. The difference of 0.1 mm is below the spatial resolution of $\sim 0.2\,\mathrm{mm}$ (FWHM) of the experiment, see Section 3.2.1.
This analysis shows that, according to simulations, the increase in defocusing wakefield for longitudinally increasing initial bunch density (frontal seed position), due to a larger number of protons driving the wakefield between the seed position and the modulation period analyzed dominates over the lack of initial defocusing at $z = 0$ as for seeding behind

the bunch center and leads to slightly wider defocused proton distributions. However, the difference is smaller than the experimental resolution. Therefore, I assume throughout the analysis of this thesis that the effect of changing initial bunch density, when moving the seed position from the bunch center ahead of the bunch, dominates over the change in initial bunch density slope.

Appendix B: Publications

BEAM DIAGNOSTICS IN THE ADVANCED PLASMA WAKEFIELD EXPERIMENT AWAKE

A.-M. Bachmann[1,2*], Max Planck Institute for Physics, Munich, Germany
P. Muggli, Max Planck Institute for Physics, Munich, Germany
[1]also at TU Munich, Munich, Germany
[2]also at CERN, Geneva, Switzerland
on behalf of the AWAKE Collaboration

Abstract

In AWAKE a self-modulated proton bunch drives wakefields in a plasma. Recent experiments successfully demonstrated many aspects of the self-modulation of the drive bunch as well as acceleration of test electrons. Next experiments will focus on producing a multi-GeV accelerated electron bunch with low emittance and low energy spread. The experiment requires a variety of advanced beam diagnostics to characterize the self-modulated proton bunch at the picosecond time scale. These include optical transition radiation and a streak camera for short and long time scale detailed imaging of self-modulation and hosing, coherent transition radiation for modulation frequency measurements in the 100–300 GHz frequency range and multiple fluorescent screens for core and halo measurements. An overview of these diagnostics will be given.

INTRODUCTION

AWAKE operates at one of the lowest plasma densities of all currently available plasma-based accelerator experiments. The plasma electron density n_{e0} determines the fastest time-scale τ of characteristics of the bunch modulation with the plasma electron angular frequency, $\omega_{pe} = \left(n_{e0}e^2/\epsilon_0 m_e\right)^{1/2}$, with $\tau = 2\pi/\omega_{pe}$, where constants have usual meaning: e, charge of the electron: ϵ_0, vacuum permittivity; m_e, mass of the electron; c, the speed of light in vacuum. For $n_{e0} = 10^{14}$–$10^{15}\,\mathrm{cm}^{-3}$ this corresponds to $\tau = 3.5$–$11.1\,\mathrm{ps}$. The time resolution needed to directly observe the modulation is thus at the limit of currently commercially available streak cameras ($\approx 200\,\mathrm{fs}$). The density also determines the smallest spatial scale through the cold plasma collisionless skin depth c/ω_{pe}. The main phenomena to resolve are the structure of the proton bunch that drives plasma wakefields and of the wakefields themselves. The incoming proton bunch is much longer than the wakefields' period τ. Thus it experiences self-modulation (SM) as it travels through the plasma [1]. The SM process acts on the bunch through the periodic focusing and defocusing transverse wakefields along the bunch, generating a train of micro-bunches with periodicity $\sim \tau$ and shorter than τ.

To study this fundamental beam-plasma interaction process in detail, we acquire time-resolved transverse images of the modulated bunch density distribution measuring the optical transition radiation with a streak camera [2, 3]. With multiple fluorescent screens along the beam path, we acquire time integrated images of the modulated bunch to complement the time-resolved images [4]. Additionally, with heterodyne receivers the frequency of the modulation can be measured independently [5]. We measure energy, energy spread and charge capture of an electron bunch, externally injected and accelerated in the plasma with an electron spectrometer [6, 7].

We describe the diagnostics that were used in the first round of experiments (2016–2018). We also briefly outline the diagnostic challenges for the upcoming experiments (starting 2021) that will focus on the accelerated bunch quality. As with all plasma-based accelerators beam diagnostics must measure small spatial and temporal scales, typically µm and 100 fs, respectively. In addition, diagnostic measurements must be integrated into compact spaces and measure simultaneously properties of very different beams, the high population, long duration and long β-function proton bunch and the low population, short duration and small spatial size electron bunch. Moreover, in these experiments, they must overlap in space and time with $\ll \tau$ and c/ω_{pe} accuracy at the plasma entrance, an overlap that also complicates diagnostics at the plasma exit.

THE AWAKE EXPERIMENT

In the AWAKE experiment the transverse central 2 mm diameter of a 10 m long rubidium (Rb) vapor source is ionized by a 4 TW (peak power) Ti:Sapphire laser pulse. An $\approx 12\,\mathrm{cm}$-long CERN SPS proton bunch propagates through the plasma. The long proton bunch drives wakefields in the plasma. Focusing and defocusing transverse fields alternate along the bunch with the wakefields' period $\sim \tau$. The wake-

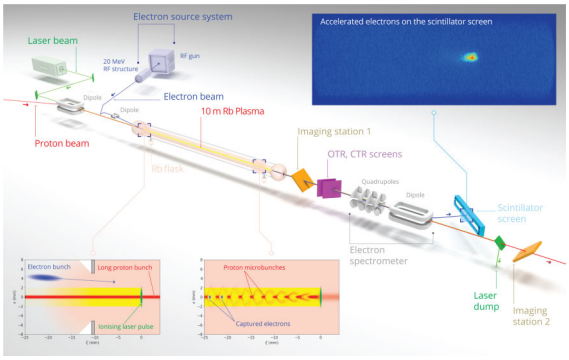

Figure 1: Layout of the AWAKE experiment [6].

* bachmann@mpp.mpg.de

fields act back on the long proton bunch, leading to radial modulation. The modulation is seeded with the ionizing laser-pulse co-propagating within the proton bunch (Seeded Self-Modulation) [8]. In the focusing phase of the wakefields protons remain on axis, while in between in the defocusing phase protons diverge, resulting in micro-bunching. The modulated proton bunch resonantly drives wakefields. The longitudinal wakefields accelerate a short electron bunch, generated on a photo-cathode and externally injected [9]. Beam diagnostics are placed downstream of the plasma to characterize the modulated proton bunch and the accelerated electrons. The fluorescent screens to measure the time integrated transverse distribution of the proton bunch are shown in Fig. 1, referred to as imaging station 1 and 2. The radial extent of defocused proton distribution depends on the transverse wakefields' amplitude they have experienced [4]. Two thin metal screens (OTR, CTR screen in Fig. 1) allow for the measurement of the optical transition radiation (OTR) and coherent transition radiation (CTR) emitted by the protons and micro-bunches, respectively, when entering the screens. The OTR is sent to a streak camera, acquiring a time-resolved image of the transverse distribution of a slice of the modulated proton bunch. The CTR is detected by heterodyne receivers to determine the modulation frequency of the bunch train. The charge and energy of the electron bunch after acceleration in the plasma are measured with the electron spectrometer.

PROTON BUNCH DIAGNOSTICS

In the following we describe the diagnostics used to characterize the modulated proton bunch driving the plasma wakefields and we show some example results.

Optical Transition Radiation and Streak Camera for Time-Resolved Transverse Distribution Measurements

The modulated bunch propagates through a foil (280 µm silicon wafer coated with 1 µm mirror-finished aluminium) where OTR, carrying the spatio-temporal pattern of the proton bunch distribution, is emitted [2]. The screen is placed 3.5 m after the plasma exit (see Fig. 1). The light is relay imaged onto the slit (20 µm) of a streak camera (Hamamatsu C10910-05) acquiring the time-resolved transverse bunch density distribution. These images can display the long time evolution of the self-modulated train and defocused protons. The evolution of the protons leaving the bunch is captured only over a few wakefields' periods due to aperture limitations of the imaging system (field of view $x \approx \pm 4$ mm in Fig. 2).

To reach the best time resolution, the camera must be operated in a speckle regime. The time resolution then reaches ≈ 0.8 ps. However, we image the transverse bunch density distribution and operate with larger intensity images in order to obtain single images of the bunch structure. The OTR signal (equal in duration to that of the proton bunch) lasts for ≈ 1 ns, much longer than the shortest time window (73 ps) with maximum time resolution, potentially further decreasing the time resolution. This typically decreased the time resolution to ≈ 2 ps for the short time window.

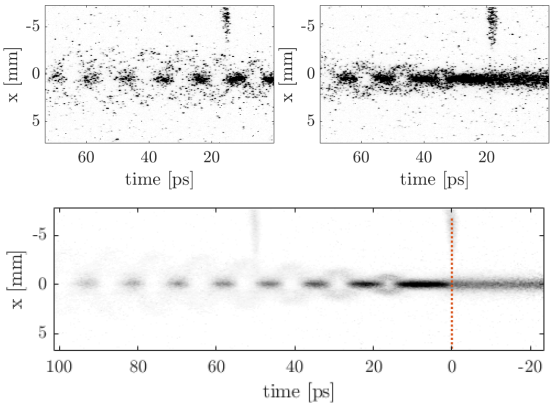

Figure 2: Single streak camera image of the start of the SM (top right), single streak camera image with a 50 ps time delay to the start of the SM (top left) and sets of the two time delays of 20 streak camera images each, stitched together using the timing reference signal (bottom).

To decrease the noise of the images, we average several acquisitions of the same position along the bunch from successive events. This requires a repetitive signal (reproducibility of the modulation) and a very stable trigger for the diagnostic ($< \tau$) or an independent signal tied in time to the modulation itself. The electronic trigger jitters on the tens of picoseconds scale. We therefore send a mirror bleed replica of the laser pulse that ionizes the Rb vapor, and thus starts the self-modulation of the bunch, to the streak camera together with the OTR. We offset it from the OTR signal along the camera slit (see signal at $x \leq -4$ mm in Fig. 2). This time reference signal has an accuracy of 0.6 ps with respect to the ionizing laser pulse and thus with the start of the self-modulation. This replica combined with a tunable delay, serves as a time reference that can be used to average and stitch multiple events [10]. The averaging of multiple events allows for images of the modulated bunch with a much higher signal to noise ratio than with single images. By stitching the images of the shortest time window, i.e. combining a number of image sets taken with various reference signal delays with respect to the start of the self-modulation, we can measure fast time scale details along the bunch, as well as examine modulation structures with greater time resolution over a long time scale (see Fig. 2).

At the location of the OTR screen, the RMS transverse size of the proton bunch is ≈ 580 µm and the transverse size of the micro-bunches is similar [3]. Measurements show that the spatial resolution is on the order of 180 µm.

Figure 2 shows an example of a single image of the proton bunch near the start of the SM (top right), a single image with camera trigger and reference laser pulse shifted by 50 ps (top left) and of two sets of images (20 events each), acquired with a 50 ps trigger delay in between and "stitched"

together (bottom). Here the first reference signal timing is without delay with respect to the ionizing laser pulse, marked with the red dashed vertical line in the stitched image. This corresponds to the start of the plasma, here at time $t = 0$. In this case the plasma electron density is $n_{e0} = 0.9{\times}10^{14}$ cm^{-3} and thus $\tau = 11.7$ ps.

We use the space and time-resolved transverse slice of the modulated proton bunch density mapped from the streak camera images for qualitative and quantitative characterization of the self-modulated bunch. The position, shape and length of the proton micro-bunches is crucial for plasma wakefield acceleration experiments. The driver charge (here protons) should ideally be in the decelerating and focusing phase of the wakefields (one fourth of the plasma period in linear wakefield theory [11]). This would lead to large plasma wakefields' amplitudes and thus large acceleration and focusing of injected particles when placed at the right longitudinal position within the wakefields' period.

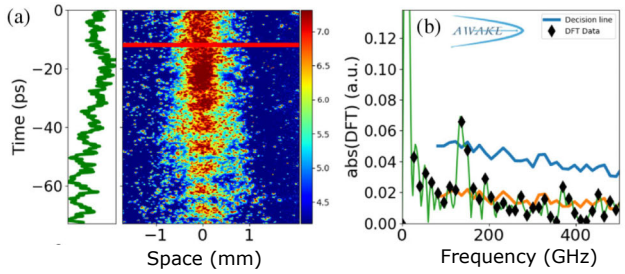

Figure 3: Image a) shows a streak camera image of the self-modulated proton bunch (moving from the bottom to the top) with the plasma starting at the red horizontal line and the projection of the central density distribution with the green curve on the left, b) shows the DFT of the projection, with determined peaks marked with black diamonds and the dominant frequency above the noise threshold determined as 137 GHz with $n_{e0} = 2.5 \times 10^{14}$ cm^{-3} (from [3]).

With the time-resolved bunch density maps the modulation frequency can be determined using the discrete Fourier transform (DFT) of the modulated bunch train [3]. This is shown in Fig. 3, with the streak camera image of a single event and the projection of the central bunch density in green on the left and the DFT and peak determination on the right. With a plasma period of $\tau < 11$ ps and a resolution of ≈ 2 ps, an upper bound of the micro-bunch length can be determined. The relative charge per micro-bunch can be measured, taking into account the effect of the streak camera slit on the transverse distribution [12]. This is particularly important for example when studying the effect of plasma density gradients on the SM process and validate theory and simulation predictions [13]. Competing instabilities of a particle bunch in the plasma, as the hosing instability, can be analyzed by studying the non-axi-symmetric behaviour of the modulated bunch with the time-resolved images [14]. In all studies the 3.5 m of vacuum propagation between the plasma exit and the OTR screen, and thus additional divergence of protons, needs to be taken into account.

Fluorescent Screens for Time Integrated Transverse Distribution Measurements

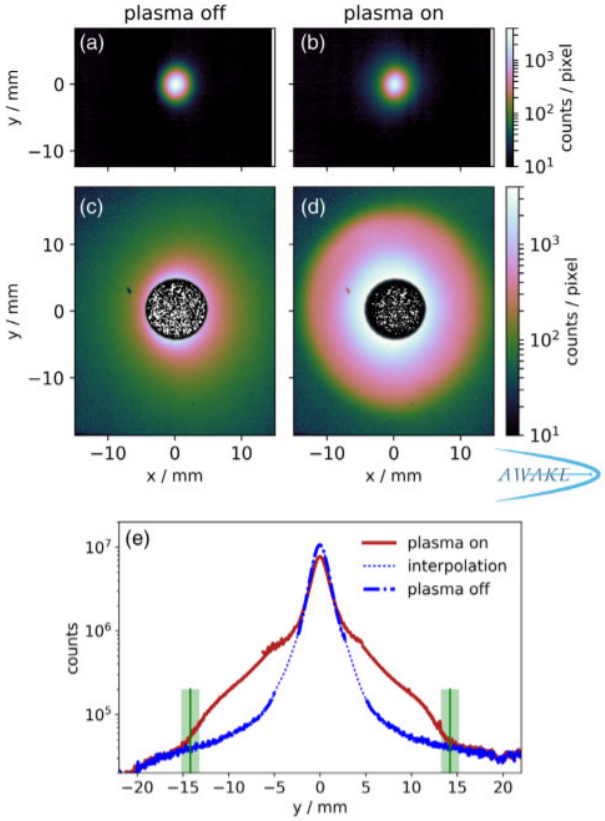

Figure 4: Time integrated transverse proton bunch density distribution acquired with fluorescent screens for the measurement of defocused protons and transverse wakefields' amplitude determination (from [4]). Images a), b) show core images, c), d) halo images for the same events with a), c) plasma OFF and b), d), plasma ON. Image e) shows the reconstructions of the bunch profile from the two cameras, as well as the value determined for the halo radius (green lines) and its uncertainty (green shaded regions). These images were obtained at imaging station 2 ($\approx$ 10 m from the plasma exit). Similar images were obtained at imaging station 1.

Fluorescent screens are placed along the beam line before and after the plasma, measuring the time integrated transverse proton bunch distribution, see Fig. 4. The radial modulation of the bunch in plasma leads to divergence of protons in defocusing regions between the focused regions of the micro-bunches. These protons appear as a halo around the bunch core on the imaging stations $\approx$ 2 m and $\approx$ 10 m after the plasma. The halo's radial extent is a measure of the integrated defocusing wakefields the protons have experienced [4]. At each of the two imaging stations, the light is divided into two light paths with a camera each. One camera measures the entire bunch distribution with parameters adjusted to the high density core of the bunch. This image also gives information about the beam alignment and eventual kicks of the beam by the plasma when beam and plasma are

misaligned. For the second camera the light passes through a mask, blocking the high intensity light from the dense core. Parameters are adjusted to measure the low light level halo. The combination of the two images enables a larger dynamic range measurement of the entire radial bunch distribution, detecting for the same event the significantly lower intensity of the signal from defocused protons (halo) around the core without saturation. The halo measurements have successfully shown that wakefields grow along the proton bunch [4], as predicted by theory and simulation results. SM, an axi-symmetric bunch-plasma mode of interaction produces a circular core and halo, when the finite radius plasma and the proton beam are well aligned. On the contrary, the hosing instability [15] is a non-axi-symmetric mode of interaction that may produce correspondingly asymmetric core and halo. Some of the self-modulation and hosing characteristics can thus be studied from time-integrated and time-resolved images of the proton bunch.

Heterodyne Detectors for Modulation Frequency Measurements Using Coherent Transition Radiation

We obtain an independent frequency measurement of the proton bunch modulation by analysing the CTR emitted when the bunch train enters a foil (Al-coated silicon oxide screen) placed after the plasma (see Fig. 1). The CTR signal is in the $f_{CTR} \approx 100 - 300$ GHz frequency range for plasma electron densities in the $n_{e0} \approx 10^{14}$–10^{15} cm^{-3} range. This microwave signal is transported with waveguides to heterodyne detectors. They consist of a frequency-tunable, local oscillator synthesizer, an amplifier/frequency multiplier chain, a sub-harmonic mixer and an oscilloscope [5]. The signal at f_{CTR} is mixed with a reference signal at approximately the same frequency $f_{ref} \cong f_{CTR}$, guessed from the rubidium, thus plasma density $f_{CTR} \cong f_{pe} \sim n_{e0}^{1/2}$. The difference frequency signal at $f_{IF} = |f_{CTR} - f_{ref}|$ is acquired with a fast, multi-GHz bandwidth oscilloscope. The reference signal is generated by the frequency multiplication of a tunable local low frequency oscillator (f_{LO}) as $f_{ref} = n_{harm} f_{LO}$, with harmonic number n_{harm}. One can then determine $f_{CTR} = n_{harm} f_{LO} \pm f_{IF}$ from measurements of f_{IF} with multiple f_{LO} with small frequency increments, for a fixed f_{CTR}.

In the experiment, the CTR signal is split in three and analyzed with three heterodyne systems covering the entire 100–300 GHz frequency range. For low plasma densities, this diagnostic provides simultaneous information about two or three of the modulation harmonics. Detection of harmonics of the modulation signal indicates deep modulation of the bunch radius and thus formation of a micro-bunch train with $\tau = 1/f_{CTR}$ period. The heterodyne systems provide short (~duration of the proton bunch), low frequency (5–20 GHz) signals on the oscilloscope, consisting of only a few periods. We use DFT to determine f_{IF}.

The modulation frequency of the proton bunch has been measured with this technique and compared to the results obtained from DFT analysis of streak camera images and the plasma frequency expected from the plasma density (when measuring the vapor density and assuming full ionization of the Rb valence electron) [3]. It was also used to measure the modulation frequency as a function of plasma density gradients [13]. There is very good agreement between the modulation frequencies obtained from DFT of streak camera images time profiles and from CTR signals. Moreover, CTR signals at the second harmonic of the modulation frequency were also detected, confirming the deep modulation of the bunch density.

ELECTRON BUNCH DIAGNOSTICS

The electron bunch is externally injected into the wakefields, driven by the proton bunch. We characterize the accelerated electron bunch after the plasma with the spectrometer.

Spectrometer for Charge, Energy and Energy Spread Measurements

For electron injection, temporal synchronization between the self-modulation of the driver and the short electron bunch is ensured by emitting the electrons from a photo-cathode with a frequency-tripled fraction of the ionizing laser pulse. They are accelerated from the RF-cathode through a booster structure and injected into the plasma (oblique or on axis injection) with initially $\approx$ 18 MeV and accelerated up to multiple GeV [6]. At injection, the bunch charge is $\lessapprox$ 1 nC and the RMS length estimated to be $\gtrapprox$ 5 ps [16], thus on the order of the wakefields' period. This injection scheme thus corresponds to injecting electrons at many phases of the wakefields (2π) and letting the wakefields capture and accelerate a fraction of the incoming bunch population. The electrons may dephase through energy gain and loss.

In the current setup, after the plasma exit the electrons are focused with two quadrupoles and bent with a dipole onto a scintillator screen (see Fig. 1), imaged onto a camera in a dark room [17].

The dipole introduces a correlation between the horizontal position and energy of the electrons on the screen. Thus the peak energy and the energy spread of the accelerated electron distribution can be measured [6, 16].

The relation between light and charge was acquired exposing the screen directly with a beam with known charge [18]. Using the light-charge calibration one can determine the charge after the plasma, and thus capture rate of the injected electrons [6].

DIAGNOSTICS FOR FUTURE EXPERIMENTS

In previous experiments, the goal was to demonstrate and study the self-modulation of the proton bunch in plasma and to show that electrons can be accelerated in wakefields driven by the resulting bunch train. The electron bunch length was comparable to the wakefields' period to ensure covering all phases of the wakefields, ensuring that electrons would

be captured for all events, regardless of the relative timing of electrons with respect to the wakefields. In addition, electrons were injected at an angle with respect to the proton bunch propagation axis.

In upcoming measurements [19], the focus will be on preserving the quality of the accelerated electron bunch, such as high charge, low emittance and low energy spread. Those can only be achieved with a short electron bunch ($\ll \tau$) injected at the right phase of the wakefield, focusing and accelerating. The electron bunch parameters must be tailored such that plasma electron blow-out can be reached with a transverse size matched to the ion column focusing force to preserve slice emittance. Beam loading needs to be reached, to obtain a narrow energy spread and preserve the projected emittance [20].

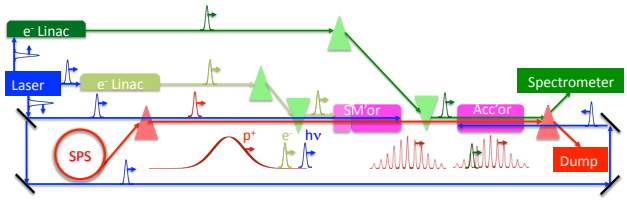

Figure 5: AWAKE setup planned for future measurements.

During the SM growth the phase of the wakefields evolves [21, 22], i.e. their phase velocity is slower than the proton bunch velocity [23]. Electrons will thus be injected after the proton bunch is fully modulated. Therefore two plasma stages, separated by a short gap for electron injection will be used, as shown in Fig. 5. The first plasma stage is for the SM of the long proton bunch, the second plasma stage for the acceleration of the electron bunch in the wakefields driven by the fully modulated proton bunch. The first plasma stage will include a plasma density step for wakefields to maintain amplitudes comparable to that at their saturation value, over long distance [13]. We want to monitor the effect of the density step on the plasma electron density perturbation sustaining wakefields at the end of the plasma with a new THz shadowgraphy diagnostic.

These experiments will bring new diagnostics challenges, both on the entrance and exit side of the plasma. The matched β-function of the $\approx$ 150 MeV electron beam to an ion column of density 10^{14}–10^{15} cm^{-3} is $\beta_{0m} \approx$ 4–13 mm. With a normalized emittance of 2 mm·mrad this corresponds to a waist transverse size of $\sigma_r \approx$ 5–10 µm, very challenging to produce and measure, especially in the Rb vapor environment. The bunch length σ_ξ on the order of 60–100 µm can be measured by electro-optic sampling or CTR interferometry. It can be monitored on a single-event-basis by measuring the CTR energy E_{CTR} and the bunch population N, and using the dependence $E_{CTR} \sim N^2/\sigma_\xi$. The spatial alignment between the two beams will be measured and monitored in the presence of the two bunches with very different parameters (population, β-function, size and length) using conventional (protons) and new Cherenkov diffraction (electrons) beam position monitors [24].

At the plasma exit, the bunch energy spectrum will be measured using a standard imaging magnetic spectrometer (quadrupoles, dipole). The accelerated electron and the modulated proton bunch overlap in space and time. Thus measuring the electron bunch emittance requires a diagnostic that separates the two bunches or the two signals. In the first category, measuring the transverse size in the non-dispersive plane of the magnetic spectrometer, the equivalent of a quadrupole scan in a single or multiple events, can in principle yield emittance [25]. In the second category, measuring the betatron radiation by the accelerated electron bunch can yield an emittance measurement [26]. Also diffraction radiation measurements, taking advantage of the difference in relativistic factor between the accelerated electrons and the protons, may provide an emittance and other bunch measurements [27, 28].

CONCLUSION

AWAKE is the first proton-beam-driven wakefield accelerator [8]. It proved the concept of seeded self-modulation and the acceleration of externally injected electrons up to 2 GeV over 10 m of plasma.

The experiment operates with a low plasma density, putting the typical time scale of observation in the few picoseconds regime. We use OTR and a streak camera with a reference laser signal to obtain detailed images of the proton bunch self-modulation over hundreds of picoseconds while preserving picosecond resolution. Stitching many events together greatly suppresses the noise of the streak camera images. We also use heterodyne detection of CTR emitted by the bunch train to directly measure the modulation frequency, including its harmonics.

Together with more standard beam diagnostics, including screens and energy spectrometer, these diagnostics have allowed for a detailed understanding of the SM process [3, 4, 13, 16] and for the demonstration of acceleration of externally injected electrons to GeV energies [6].

Future experiments will focus on producing an accelerated electron bunch with significant charge, low relative energy spread, while essentially preserving its incoming emittance. These experiments present a number of new challenges for diagnostics, which include: size and alignment measurements at the micron scale; synchronization at the sub-picosecond scale; single-event measurements of all incoming and outgoing parameters, including the emittance of the accelerated bunch.

Because of its typical operating frequency range (100–300 GHz), this accelerator pushes diagnostics typical of RF accelerators, operating in the GHz frequency range, towards those, typical of other plasma-based accelerators, operating at higher plasma densities and thus in the THz frequency range.

REFERENCES

[1] N. Kumar *et al.*, "Self-Modulation Instability of a Long Proton Bunch in Plasmas", *Phys. Rev. Lett.*, vol. 104, p. 255003, 2010. doi:10.1103/physrevlett.104.255003

[2] K. Rieger *et al.*, "GHz modulation detection using a streak camera: Suitability of streak cameras in the AWAKE experiment", *Rev. of Scientific Instruments*, vol. 88, p. 025110, 2017. doi:10.1063/1.4975380

[3] E. Adli *et al.* (AWAKE Collaboration), "Experimental Observation of Proton Bunch Modulation in a Plasma at Varying Plasma Densities", *Phys. Rev. Lett.*, vol. 122, p. 054802, 2019. doi:10.1103/PhysRevLett.122.054802

[4] M. Turner *et al.* (AWAKE Collaboration), "Experimental Observation of Plasma Wakefield Growth Driven by the Seeded Self-Modulation of a Proton Bunch", *Phys. Rev. Lett.*, vol. 122, p. 054801, 2019. doi:10.1103/PhysRevLett.122.054801

[5] F. Braunmueller *et al.*, "Novel diagnostic for precise measurement of the modulation frequency of Seeded Self-Modulation via Coherent Transition Radiation in AWAKE", *Nucl. Instr. and Meth. in Phys. Res. A*, vol. 909, p. 76, 2018. doi:10.1016/j.nima.2018.02.080

[6] E. Adli *et al.* (AWAKE Collaboration), "Acceleration of electrons in the plasma wakefield of a proton bunch", *Nature*, vol. 561, p. 363, 2018. doi:10.1038/s41586-018-0485-4

[7] E. Gschwendtner, M. Turner *et al.* (AWAKE Collaboration), "Proton-driven plasma wakefield acceleration in AWAKE", *Phil. Trans. R. Soc. A.*, vol. 377, p. 20180418, 2019. doi:10.1098/rsta.2018.0418

[8] P. Muggli *et al.* (AWAKE Collaboration), "AWAKE readiness for the study of the seeded self-modulation of a 400 GeV proton bunch", *Plasma Physics and Controlled Fusion*, vol. 60, no. 1, p. 014046, 2017. doi:10.1088/1361-6587/aa941c

[9] K. Pepitone *et al.*, "The electron accelerators for the AWAKE experiment at CERN — baseline and future developments", *Nucl. Instr. and Meth. in Phys. Res. A*, vol. 909, p. 102, 2018. doi:10.1016/j.nima.2018.02.044

[10] F. Batsch *et al.*, "Setup and Characteristics of a Timing Reference Signal with sub-ps Accuracy for AWAKE", *Journal of Physics: Conference Series (JPCS)*, to be published. arXiv:1911.12201

[11] P. Chen *et al.*, "Plasma Focusing for High-Energy Beams", *IEEE Transactions on Plasma Science*, vol. 15, no. 2, pp. 218–225, 1987. doi:10.1109/TPS.1987.4316688

[12] A.-M. Bachmann and P. Muggli, "Determination of the Charge per Micro-Bunch of a Self-Modulated Proton Bunch using a Streak Camera", in *Proc. 4th European Advanced Accelerator Concepts Workshop (EAAC2019)*, La Biodola, Isola d'Elba, Italy, Sep. 2019. arXiv:1912.02162

[13] F. Braunmueller, T. Nechaeva *et al.* (AWAKE Collaboration), "Proton Bunch Self-Modulation in Plasma with Density Gradient", submitted for publication. arXiv:2007.14894

[14] M. Moreira *et al.*, "Signatures of the self-modulation instability of relativistic proton bunches in the AWAKE experiment", *Nucl. Instrum. Meth. A*, vol. 909, p. 343, 2018. doi:10.1016/j.nima.2018.03.014

[15] D. H. Whittum *et al.*, "Electron-hose instability in the ion-focused regime", *Phys. Rev. Lett.*, vol. 67, p. 991, 1991. doi:10.1103/PhysRevLett.67.991

[16] M. Turner *et al.* (AWAKE Collaboration), "Experimental study of wakefields driven by a self-modulating proton bunch in plasma", emphPhys. Rev. Accel. Beams, vol. 23, p. 081302, 2020. doi:10.1103/PhysRevAccelBeams.23.081302

[17] J. Bauche *et al.*, "A magnetic spectrometer to measure electron bunches accelerated at AWAKE", *Nucl. Instrum. Meth. A*, vol. 940, p. 103, 2019. doi:10.1016/j.nima.2019.05.067

[18] F. R. Keeble, "Measurement of the electron energy distribution at AWAKE", Ph.D. Thesis, University College London, London, United Kingdom, 2019.

[19] P. Muggli (AWAKE Collaboration), "Physics to plan AWAKE Run 2", *Journal of Physics: Conference Series 224 (JPCS)*, to be published. arXiv:1911.07534v2

[20] V. K. Berglyd Olsen *et al.*, "Emittance preservation of an electron beam in a loaded quasilinear plasma wakefield", *Phys. Rev. Accel. Beams*, vol. 21, p. 011301, 2018. doi:10.1103/PhysRevAccelBeams.21.011301

[21] A. Pukhov *et al.*, "Phase velocity and particle injection in a self-modulated proton-driven plasma wakefield accelerator", *Phys. Rev. Lett.*, vol. 107, p. 145003, 2011. doi:10.1103/PhysRevLett.107.145003

[22] C. B. Schroeder *et al.*, "Growth and Phase Velocity of Self-Modulated Beam-Driven Plasma Waves", *Phys. Rev. Lett.*, vol. 107, p. 145002, 2011. doi:10.1103/PhysRevLett.107.145002

[23] A. Caldwell and K. Lotov, "Plasma wakefield acceleration with a modulated proton bunch", *Phys. Plasmas*, vol. 18, p. 103101, 2011. doi:10.1063/1.3641973

[24] T. Lefèvre *et al.*, "Cherenkov Diffraction Radiation as a tool for beam diagnostics", presented at the IBIC'19, Malmö, Sweden, Sep. 2019, paper THAO01.

[25] J. Chappell *et al.*, "Progress Towards a Single-Shot Emittance Measurement Technique at AWAKE", in *Proc. IPAC'19*, Melbourne, Australia, May 2019, pp. 3742–3745. doi:10.18429/JACoW-IPAC2019-THPGW067

[26] B. Williamson *et al.*, "Betatron radiation diagnostics for AWAKE Run 2", *Nucl. Instrum. Meth. A*, vol. 971, p. 164076, 2020. doi:10.1016/j.nima.2020.164076

[27] M. Bergamaschi *et al.*, "Noninvasive Micrometer-Scale Particle-Beam Size Measurement Using Optical Diffraction Radiation in the Ultraviolet Wavelength Range", *Phys. Rev. Applied*, vol. 13, p. 014041, 2020. doi:10.1103/PhysRevApplied.13.014041

[28] R. B. Fiorito, C. P. Welsch, H. D. Zhang, and A. G. Shkvarunets, "Novel Single Shot Bunch Length Diagnostic using Coherent Diffraction Radiation", in *Proc. IPAC'15*, Richmond, VA, USA, May 2015, pp. 1150–1152. doi:10.18429/JACoW-IPAC2015-MOPWI004

Journal of Physics: Conference Series **1596** (2020) 012005 doi:10.1088/1742-6596/1596/1/012005

Determination of the Charge per Micro-Bunch of a Self-Modulated Proton Bunch using a Streak Camera

A.-M. Bachmann[1,2,3], **P. Muggli**[2,1]

[1] CERN, Geneva, Switzerland
[2] Max-Planck Institute for Physics, Munich, Germany
[3] Technical University Munich, Munich, Germany

E-mail: anna-maria.bachmann@cern.ch

Abstract. The Advanced Wakefield Experiment (AWAKE) develops the first plasma wakefield accelerator with a high-energy proton bunch as driver. The 400 GeV bunch from CERN Super Proton Synchrotron (SPS) propagates through a 10 m long rubidium plasma, ionized by a 4 TW laser pulse co-propagating with the proton bunch. The relativistic ionization front seeds a self-modulation process. The seeded self-modulation transforms the bunch into a train of micro-bunches resonantly driving wakefields. We measure the density modulation of the bunch, in time, with a streak camera with picosecond resolution. The observed effect corresponds to alternating focusing and defocusing fields. We present a procedure recovering the charge of the bunch from the experimental streak camera images containing the charge density. These studies are important to determine the charge per micro-bunch along the modulated proton bunch and to understand the wakefields driven by the modulated bunch.

1. Introduction

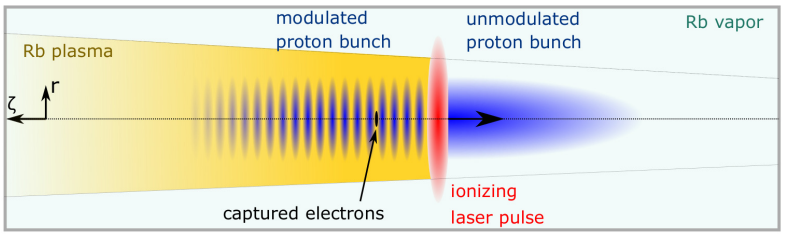

Figure 1. Sketch of the AWAKE principle, using a proton bunch as plasma wakefield driver to accelerate externally injected electrons

AWAKE uses the CERN SPS proton bunch as a plasma wakefield driver. The bunch propagates through 10 m of plasma, created by laser ionization of a rubidium (Rb) vapor. The laser pulse co-propagates with the proton bunch, seeding the self-modulation with the relativistic ionization front, i.e. with the abrupt beam plasma interaction within the bunch [1]. Along the plasma (with a density of $n_{pe} = 2{\cdot}10^{14}\,\mathrm{cm}^{-3}$ for the measurements reported here) the long proton bunch ($\sigma_\zeta \approx 9\,\mathrm{cm}$) divides into micro-bunches, spaced by the plasma wavelength ($\lambda_{pe} \approx 2.4\,\mathrm{mm}$) [2, 3]. The micro-bunches resonantly drive wakefields in the plasma. The wakefields accelerate an injected electron witness bunch [4]. The principle of the experiment is sketched in Figure 1.

In the following we present a method to determine the charge in each micro-bunch from time-resolved images of the proton bunch transverse distribution. The images are produced by a streak camera.

2. Method

In this section we explain the analysis of the streak camera images [5] applied for the determination of the charge per micro-bunch.

2.1. Streak Camera as Diagnostic

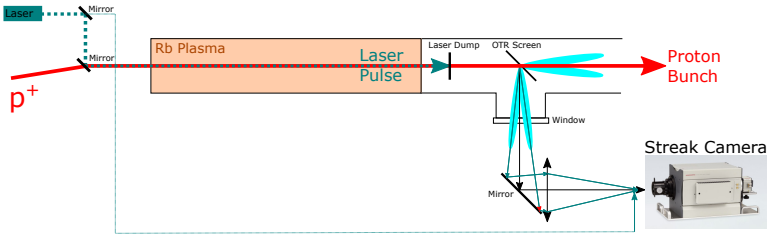

Figure 2. Transport of OTR light of a modulated proton bunch to streak camera at AWAKE (not to scale)

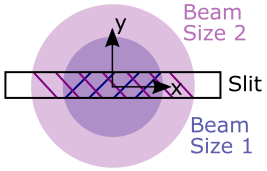

Figure 3. Light collection of a streak camera for different signal widths

After the Rb plasma the modulated proton bunch propagates through an optical transition radiation (OTR) screen (280 µm thick Silicon wafer coated with 1 µm thick mirror-finished aluminium), placed 3.5 m after the plasma exit [3], see Figure 2. We collect the backwards emitted OTR that contains the spatio-temporal information of the proton bunch charge distribution and transport it to a streak camera (Hamamatsu C10910-05 model, 16-bit, 2048 x 2048 pixel ORCA-Flash4.0 CMOS sensor, binned to 512 x 512 pixels for streak operation). The imaging system has a limited aperture (±4 mm in Figure 4 and 5 and later). We operate the camera with a slit width of 20 µm, an MCP gain of 40 and a time window of 73 ps. The time resolution is ≈ 1 ps in this time window. Light is collected by the streak camera through a slit for temporal resolution. Thus, for a cylindrically symmetric light signal, as the transverse image of the proton bunch, with a size larger than the slit width, the larger the size, the smaller the fraction of light that is transmitted through the slit (Figure 3). The streak camera image thus contains information about the bunch charge density and not the charge.

2.2. Streak Camera Images

The streak camera produces a time resolved image of the proton bunch transverse charge distribution [5]. The temporal evolution of the streak voltage leads to a time interval per pixel that varies along the image. Therefore we interpolate the original image to linearize the time axis. We subtract from each image a background image, obtained by averaging seven images without proton bunch. Images are weighted by the measured incoming proton bunch population. We acquire two series of images (each 20 images with plasma, two images without plasma) with ≈ 50 ps delay between series. Together with the proton bunch OTR, we send to the streak camera a replica of the ionizing laser pulse (≈ 120 fs long) that we also delay by 50 ps for each series. This reference laser pulse is sent onto the edge of the image to minimize the overlap with the proton bunch signal (see top edge on Figure 4 and 5). With this laser pulse time reference we can sum images in a series with the same time delay, despite the ≈ 20 ps trigger jitter of the streak camera. We stitch the series together to obtain long time scale images with short time scale resolution. This method is described in reference [6] of these proceedings.
The result without plasma is shown in Figure 4 and with plasma in Figure 5. Here $t = 0$

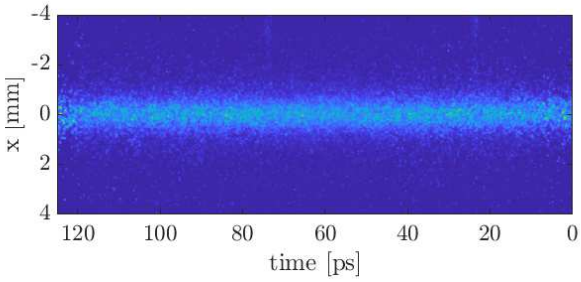

Figure 4. Stitched streak camera image of the proton bunch after propagation without plasma (bunch front at $t = 0$). The marker laser pulses used for stitching are at the top edge of the image. The bunch density is almost uniform along the bunch.

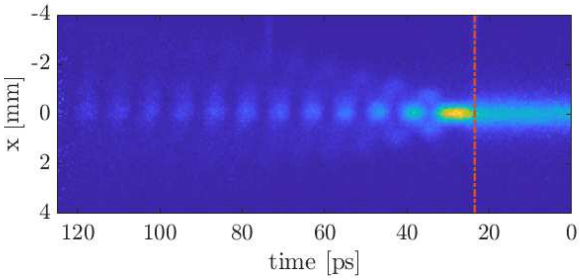

Figure 5. Stitched streak camera image of the proton bunch with plasma. The red line shows the location of the ionizing laser pulse ($t = 24\,\mathrm{ps}$). The head of the bunch ($t < 24\,\mathrm{ps}$) propagated through vapor. The tail ($t > 24\,\mathrm{ps}$) propagated through plasma and is self-modulated.

corresponds to 6 ps behind the proton bunch center, with a bunch length of $\sigma_\zeta = 300\,\mathrm{ps}$ and a total population of $N_{p^+} = (2.8 \pm 0.2) \cdot 10^{11}$. The transverse center of the bunch $x = 0$ was determined as the peak of a Gaussian fit of the unmodulated head of the bunch, before the ionizing laser pulse ($t < 24\,\mathrm{ps}$). After propagation through Rb vapor, the bunch charge distribution is uniform (Figure 4). After propagating through plasma (Figure 5), the proton bunch is self-modulated. One can see the micro-bunches along the propagation axis as well as defocused protons in between. The image shows that the charge density of the micro-bunches decreases along the bunch. In the following we present a method to determine the charge per micro-bunch for a change in width (radius) along the bunch.

2.3. Micro-Bunch Temporal Structure

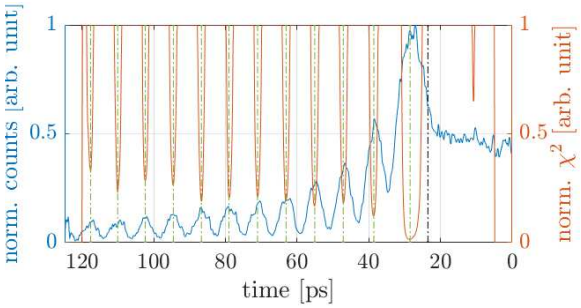

Figure 6. Determination of the longitudinal center of micro-bunches with the central projection of the modulated bunch (blue solid line), the ionizing laser pulse timing (black dashed line), the weighted distance squared function χ^2 (orange solid line) and its minima (green dashed line)

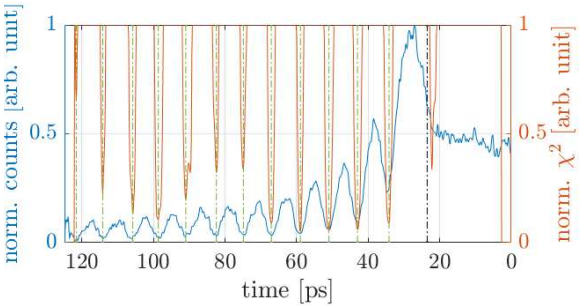

Figure 7. Determination of the beginning and end of micro-bunches with the central projection of the modulated bunch (blue solid line), the ionizing laser pulse timing (black dashed line), the weighted distance squared function χ^2 (orange solid line) and its minima (green dashed line)

For further analysis we first determine the longitudinal (temporal) center of the micro-bunches. The central projection ($-0.1\,\mathrm{mm} \leq x \leq 0.1\,\mathrm{mm}$) of Figure 5 is shown in Figure 6

and 7 with the blue solid line. For determining the center of the micro-bunches (Figure 6), we fit a second order polynomial $f(t_i, \vec{\lambda}) = \lambda_1 + \lambda_2\, t_i + \lambda_3\, {t_i}^2$, with start points $\vec{\lambda} = \{\lambda_1, \lambda_2, \lambda_3\}$, constraining $\lambda_3 < 0$, i.e. a downwards opened parabola to the bunch projection. We let the fit move along the projection centered at time t_i and fit over a range $\{t_i - \Delta t : t_i + \Delta t\}$ and $\Delta t = 2.7\,\mathrm{ps}$, to include most of the data points of a micro-bunch, but avoid covering more than one bunch for the given plasma wakefield period ($T_{pe} = 7.9\,\mathrm{ps}$ at $n_{pe} = 2 \cdot 10^{14}\,\mathrm{cm}^{-3}$). The weighted distance squared function χ^2, giving the difference between the model expectation $f(t_i|\vec{\lambda})$ and the measured projection y_i is given by

$$\chi^2 = \sum_i \frac{(y_i - f(t_i|\vec{\boldsymbol{\lambda}}))^2}{\omega_i^2}. \tag{1}$$

We weight the fit with the curvature of the parabola $\omega_i = \lambda_3$, as we expect the strongest curvature in the center of the micro-bunch. The result of the χ^2 fit is shown with the orange solid line in Figure 6, restricting the plot to the low values of the function for better visualization. The temporal center of the micro-bunches is defined as the minima of the function, indicated with the green vertical dashed lines.
We use a similar analysis but constraining the curvature fit parameter to $\lambda_3 > 0$, i.e. an upwards opened parabola, to find the minimum between two micro-bunches, corresponding to the maximum defocused regions, see Figure 7. Figures 6 and 7 show that this automatic procedure finds the micro-bunch center, as well as their beginning and end.

2.4. Micro-Bunch Size Determination

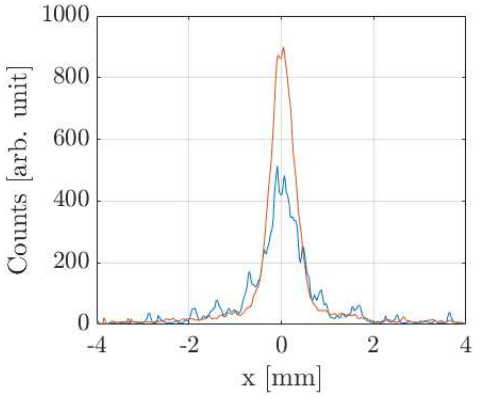

Figure 8. Transverse intensity profile of the first micro-bunch in Figure 5 (red line) and of the unmodulated bunch in Figure 4 (blue line), averaged over $t = 28\,(\pm\,0.4)\,\mathrm{ps}$

We use the temporal center of the micro-bunches and defocused areas to determine the transverse and longitudinal width of the micro-bunches. A transverse profile of the first micro-bunch of Figure 5 (at $t = 28\,\mathrm{ps}$, obtained from Figure 6, averaged over $\pm 0.4\,\mathrm{ps}$) is shown in Figure 8 as an example, demonstrating the typical transverse shape of the micro-bunches. The profiles suggest that there is more charge in the micro-bunch (red line) than in the incoming bunch (blue line) over the same time range. This is not possible, since the proton bunch is strongly relativistic, i.e. protons cannot move longitudinally with respect to each other. This is a good illustration of the slit effect. The micro-bunch width is less that that of the incoming bunch, thus more light is collected through the slit, giving the impression that it contains more charge. Instead, only its charge density is larger (see below).
In order to avoid having to assume a transverse (or longitudinal) profile for the micro-bunches, we plot the running sum of counts over each micro-bunch. For the transverse width we calculate

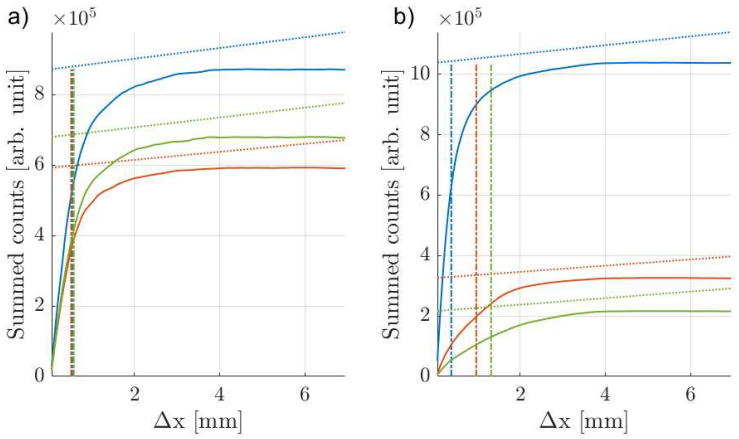

Figure 9. Transverse running sum of counts for the unmodulated (a) and modulated (b) bunch over the time range of micro-bunch number one (blue solid line), four (red solid line) and nine (green solid line). The vertical dashed lines show the micro-bunch width, where the sum reaches 60% of the final value.

the running sum of counts from the bunch center ($x = 0$, Figure 8) to the edge of the image over the time range of each micro-bunch, as determined in Figure 7. We use the time ranges of the micro-bunches of the modulated bunch to calculate the corresponding sums in the unmodulated bunch. Figure 9a) shows the profiles of the unmodulated bunch (Figure 4) for comparison, and Figure 9b) of the modulated bunch (Figure 5). We linearly fit the profiles for $\Delta x > 4\,\mathrm{mm}$, corresponding to summation of background, as the light collection from the proton bunch is limited by the imaging aperture. The subtraction of the linear function (dashed lines in Figure 9) leads to saturation of the profiles. We define the bunch width (radius) as the radial position at which the sum reaches 60% of the final value, indicated with the vertical dash-dotted lines. As expected, the width along the unmodulated bunch remains essentially constant, see 9a). For the modulated bunch, 9b) shows the running sum over the micro-bunch number one, four and nine, also representing the shape over the other micro-bunches. Unlike the unmodulated bunch, the width (vertical lines) of the individual micro-bunches is changing along the bunch.

The transverse width of each micro-bunch along the bunch is plotted in Figure 10 (red circles)

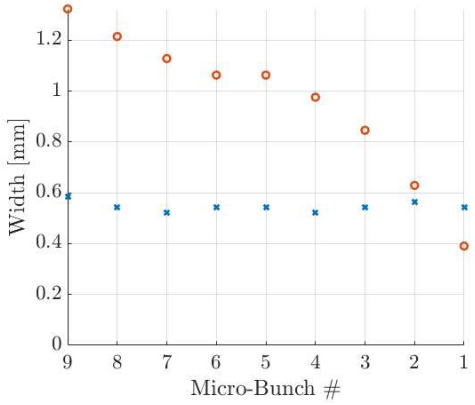

Figure 10. Transverse width of the first nine micro-bunches of the modulated bunch (red circles) and the unmodulated bunch (blue crosses), determined with the procedure shown in Figure 9.

and compared to the width of the incoming bunch (blue crosses) with a mean of 540 ($\pm$ 20 µm). One can see that the width of the signal is increasing along the image.

We use a similar approach to determine the length of the micro-bunches, see Figure 11. The micro-bunch length before and after the micro-bunch center here differ from each other and are thus treated individually. We calculate the running sum of counts from the center of the micro-bunch (Figure 6) to its beginning and end (Figure 7). For the given measurement, the

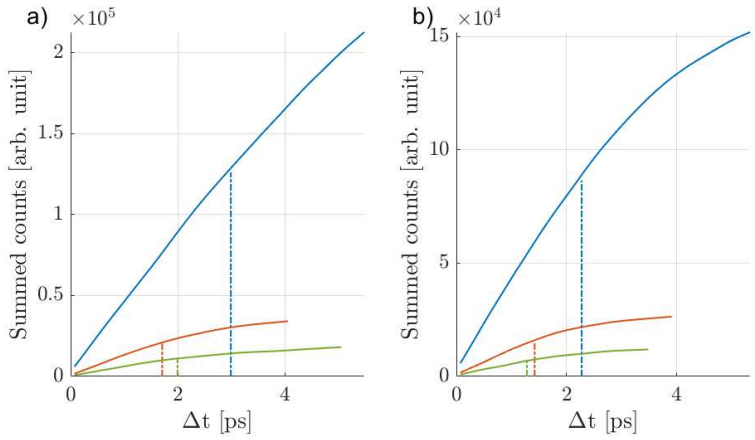

Figure 11. Longitudinal running sum of counts from each micro-bunch center to its beginning (a) or end (b) for micro-bunch number one (blue solid line), four (red solid line) and nine (green solid line). The vertical dashed lines show the micro-bunch length, where the sum reaches 60% of the final value.

bunch is not fully modulated near the ionization front, thus the counts between the micro-bunches do not reach the value 0, i.e. the sums do not saturate. Therefore we limit the range of summation with the beginning (11a) and end (11b) of the micro-bunch and the time of the ionizing laser pulse as the beginning of the first micro-bunch. Here we sum over the transverse range $-70\,\mu\text{m} < x < 70\,\mu\text{m}$ for a less noisy profile. The vertical dash-dotted lines indicate the determined micro-bunch length, where the sum reaches 60% of the final value.

The lengths are summarized in Figure 12 for each micro-bunch along the bunch. The length

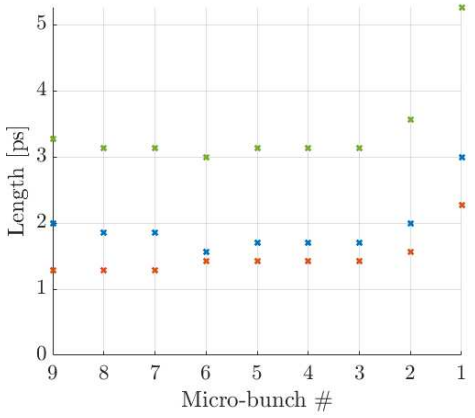

Figure 12. Length of the first nine micro-bunches from the micro-bunch center to its beginning (blue crosses) or end (red crosses), determined with the procedure shown in Figure 11, and their sum (green crosses)

from the center to the beginning as blue, from the center to the end as red, and the sum of the two as green crosses. One can see that the first two micro-bunches are longer and after the third micro-bunch the length saturates to $3.1\,(\pm 0.1)\,\text{ps}$. In the following we use the length of the micro-bunches for the unmodulated bunch for the comparison of charge in a given length along the bunch. Note that temporal resolution might lower the counts per pixel for a signal with time structure, as the modulated bunch, while it should not affect a signal without, as the unmodulated bunch.

3. Results

Since the proton bunch is cylindrically symmetric, its image onto the streak camera slit is also symmetric. With the minimum bunch diameter (780 µm at the OTR screen from Figure 10, corresponding to 220 µm at the streak camera slit due to the de-magnification by the OTR light transport) being larger than the slit width (20 µm), the streak camera image profile at each time

(Figure 8) can be interpreted as a measurement of the bunch charge density as a function of time $n(r,t)$ or $n(x,t)$ on the images. The charge at each time of the image, or in each micro-bunch as determined above, can be calculated multiplying the charge density by $2\pi\, r\, dr$.

3.1. Charge Determination of the Proton Bunch

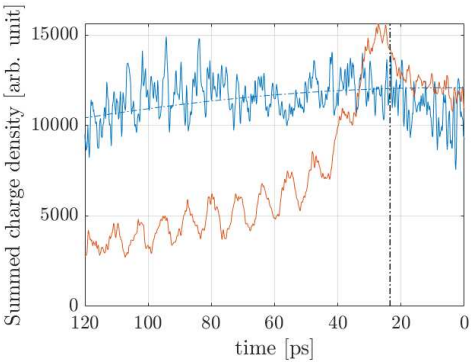

Figure 13. Charge density summed transversely over the unmodulated bunch (blue solid line) and over the modulated bunch (red solid line), theoretical Gaussian profile (blue dashed line) and timing of ionizing laser pulse (black dashed line)

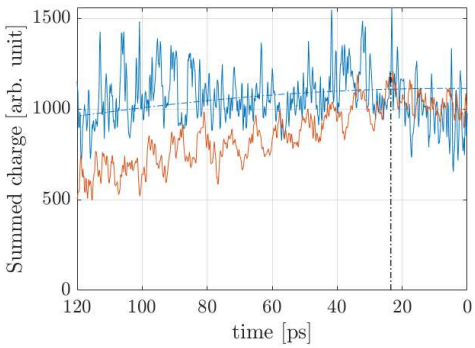

Figure 14. Charge summed transversely over the unmodulated bunch (blue solid line) and over the modulated bunch (red solid line), theoretical Gaussian profile (blue dashed line) and timing of ionizing laser pulse (black dashed line)

We apply this procedure to calculate the charge of the image of the unmodulated (Figure 4) and modulated bunch (Figure 5). To avoid the signal from the timing reference laser pulse we use only half of the image ($x > 0$). We compare the charge density summed transversely over the entire modulated bunch (red curve) with the unmodulated bunch (blue curve) in Figure 13. As expected, the shape for the unmodulated bunch follows the Gaussian bunch distribution (with length $\sigma_\zeta = 300\,\mathrm{ps}$ and $t = 0$ being 6 ps behind the bunch center and amplitude normalized to the measured profile), indicated with the blue dashed line. The summation of the modulated bunch includes focused and defocused protons. Summing the charge density transversely over the bunch before the start of the plasma ($t < 24\,\mathrm{ps}$) leads to similar values for the modulated bunch and the incoming bunch, as expected. Summing the charge density transversely over the bunch within the plasma ($t > 24\,\mathrm{ps}$) shows significantly lower counts of the modulated bunch than the incoming bunch. The sum of the modulated bunch also exhibits the periodic modulation from the self-modulation process.

The decrease in signal along the image in Figure 13 for the modulated bunch (red curve) is caused by the increase in width (see Figure 10, red circles). We can account for the effect of the slit and determine the charge of the image by multiplying the images containing the charge density with $2\pi\, r\, dr$. Figure 14 shows the sum of the charge over the modulated bunch (red curve) compared to the incoming bunch (blue curve). It shows that the charge along the self-modulated bunch is very close to that of the unmodulated bunch, following the Gaussian profile. The procedure recovers the same charge for parts of the bunch before the plasma ($t < 24\,\mathrm{ps}$). However, it retains some of the modulation in the charge density and the recovered charge decreases along the bunch when compared to the incoming bunch charge. These deviations are probably due to light collection and detection limitations of the diagnostic. Protons are more and more defocused along the bunch (see [2]) and images show that they fall out of the imaged field ($-4\,\mathrm{mm} < x < 4\,\mathrm{mm}$) later along the bunch. Also, the bunch charge density decreases

further along the bunch. The streak camera has a limited signal to noise ratio and low level light is not detected, falling below the detection threshold. The effects increase along the bunch. Figure 14 shows how well the charge along the bunch can be determined with this diagnostic and procedure. Now, that we have developed a procedure, to recover the charge in the bunch from the measurement of its charge density, and determined its limitation, we can measure the charge carried by each micro-bunch, i.e. not including the charge of defocused protons, and compare it to the incoming charge.

3.2. Charge Determination of Individual Micro-Bunches

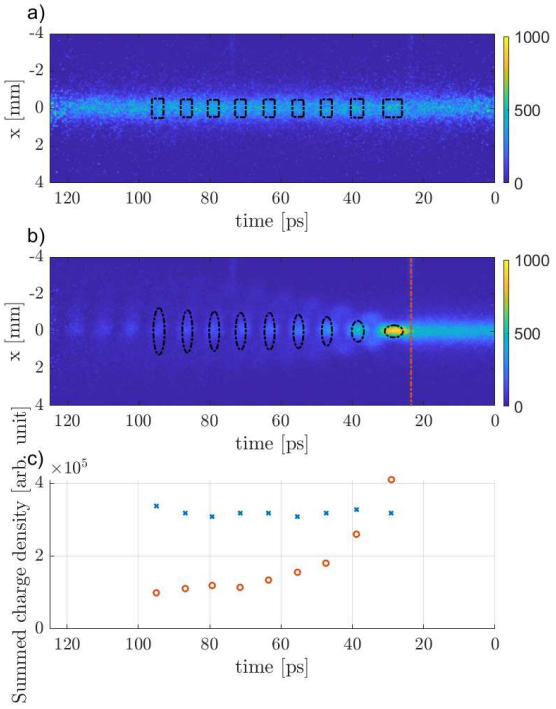

Figure 15. Streak camera images of the unmodulated (a) and modulated (b) bunch. The squares in a) represent the width of the unmodulated bunch and the length of the micro-bunches, the ellipses in b) show the widths and length of the micro-bunches. Summing the counts of the image, representing the charge density $n(r,t)$, over the indicated squares or ellipses leads to c) for the unmodulated (blue crosses) and the modulated (red circles) bunch.

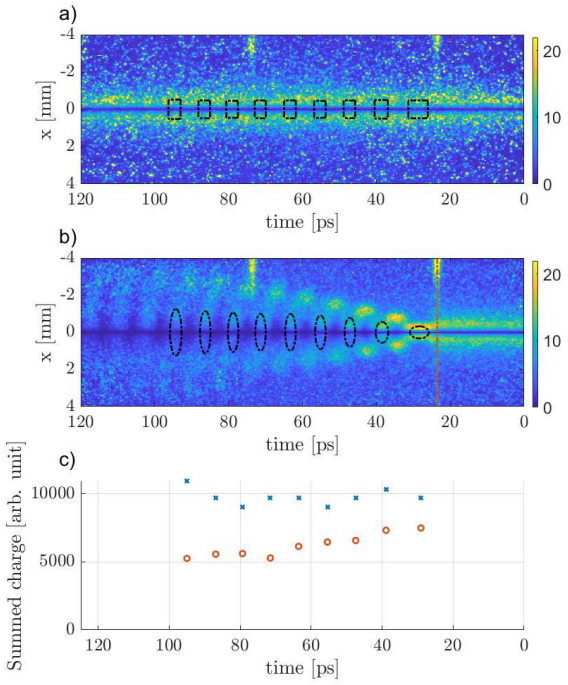

Figure 16. The streak camera images multiplied by $2\pi\, r\, dr$ revealing the charge is shown in a) for the unmodulated and in b) for the modulated bunch. The squares in a) indicate the width of the unmodulated bunch and length of the micro-bunches, the ellipses in b) the width and length of the micro-bunches. Figure c) shows the charge $n(r,t)\, 2\pi\, r\, dr$ summed over the squares (blue crosses) and ellipses (red circles).

We use the transverse width and length of the incoming bunch and the micro-bunches, as obtained using the procedure detailed in section 2 (Figures 10 and 12), to determine the relative charge per micro-bunch. For comparison of the charge in each micro-bunch with the charge in the incoming bunch, we use the same time ranges for the summation on the images of the modulated and unmodulated bunch.

Summation of the charge density, as given by the original streak camera image, over the range of the micro-bunches, is shown in Figure 15. The image of the unmodulated bunch, where the squares indicate the transverse width of the unmodulated bunch and the length of the micro-bunches, is shown in a); the image of the modulated bunch, with the ellipses of the width and length of the micro-bunches in b). In c) the charge density summed over the squared areas in a) (blue crosses) and over the ellipses in b) (red circles) is shown. One can see that the summed charge density for the unmodulated bunch remains essentially constant (considering the limitation of this procedure, the longitudinal bunch position close to the center, and the difference in length for the first micro-bunches and thus summation length being small). In constrast, the summed charge density of the micro-bunches decreases rapidly along the bunch, due to the increasing radial size of the signal (see Figure 10). This is consistent with Figure 13, where the charge density of the unmodulated bunch follows the Gaussian bunch distribution, while the charge density of the modulated bunch decreases along the bunch.
In order to determine the charge per micro-bunch we multiply the streak camera images $n(r,t)$ by $2\pi\, r\, dr$, as shown in Figure 16a) for the unmodulated and b) for the modulated bunch. We sum over the same squares and ellipses as described above, in order to determine the charge per micro-bunch. Figure c) compares the charge per micro-bunch with the charge of the incoming bunch. Again, we expect the charge of the unmodulated bunch to be essentially constant (central position within the long Gaussian bunch and small changes in micro-bunch length), which is confirmed by the measurement in blue. In red it is demonstrated that also the charge per micro-bunch is roughly constant along the bunch. The mean charge per micro-bunch covered in the ellipse is $64\,(\pm 9)\%$ of the charge covered in the squares of the incoming bunch.

4. Summary

We showed that because of the streak camera slit the streak camera images must be interpreted as charge density of the proton bunch after 3.5 m of propagation in vacuum and not in the plasma. We presented a procedure that recovers the charge in the bunch from the streak camera images. Applying the procedure we demonstrated that the charge in each micro-bunch is constant along the bunch for the first nine micro-bunches. The charge in the micro-bunches corresponds to more than 60% of the charge of the incoming bunch, over the same time period, within limitations of the diagnostic. This procedure will be used to characterize the result of the self-modulation process on the proton bunch and potentially for studying the resulting wakefields.

5. Acknowledgments

This work is sponsored by the Wolfgang Gentner Program of the German Federal Ministry of Education and Research.

References

[1] P. Muggli et al. (AWAKE Collaboration), Plasma Physics and Controlled Fusion, 60(1) 014046 (2017).
[2] M. Turner et al. (AWAKE Collaboration), Phys. Rev. Lett. 122, 054801 (2019).
[3] E. Adli et al. (AWAKE Collaboration), Phys. Rev. Lett. 122, 054802 (2019).
[4] E. Adli et al. (AWAKE Collaboration), Nature 561, 363367 (2018).
[5] K. Rieger et al., Rev. of Scientific Instruments 88, 025110 (2017).
[6] F. Batsch et al., submitted for EAAC2019 proceedings, arXiv:1911.12201.

Nuclear Inst. and Methods in Physics Research, A 909 (2018) 387–390

Contents lists available at ScienceDirect

Nuclear Inst. and Methods in Physics Research, A

journal homepage: www.elsevier.com/locate/nima

Schlieren imaging for the determination of the radius of an excited rubidium column

A.-M. Bachmann [a,b,c,*], M. Martyanov [b], J. Moody [b], A. Pukhov [d], P. Muggli [b,a]

[a] CERN, Geneva, Switzerland
[b] Max-Planck Institute for Physics, Munich, Germany
[c] Technical University Munich, Munich, Germany
[d] Heinrich-Heine-Universität Düsseldorf, Düsseldorf, Germany

ARTICLE INFO

Keywords:
AWAKE
Schlieren imaging
Plasma diagnostics
Plasma wakefield acceleration

ABSTRACT

AWAKE develops a new plasma wakefield accelerator using the CERN SPS proton bunch as a driver Muggli et al. (2017). The proton bunch propagates through a 10 m long rubidium plasma, induced by an ionizing laser pulse. The co-propagation of the laser pulse with the proton bunch seeds the self modulation instability of the proton bunch that transforms the bunch to a train with hundreds of bunchlets which drive the wakefields. Therefore the plasma radius must exceed the proton bunch radius. Schlieren imaging is proposed to determine the plasma radius on both ends of the vapor source. We use Schlieren imaging to estimate the radius of a column of excited rubidium atoms. A tunable, narrow bandwidth laser is split into a beam for the excitation of the rubidium vapor and for the visualization using Schlieren imaging. With a laser wavelength very close to the D2 transition line of rubidium ($\lambda \approx 780$ nm), it is possible to excite a column of rubidium atoms in a small vapor source, to record a Schlieren signal of the excitation column and to estimate its radius. We describe the method and show the results of the measurement.

1. Introduction

In AWAKE the CERN SPS proton bunch propagates through a 10 m long rubidium (Rb) vapor source. An ionizing laser is co-propagating with the proton bunch, so that the front half of the bunch travels through Rb vapor and the back half of the bunch interacts with the Rb plasma. The creation of the hard edge plasma seeds the self-modulation of the particle bunch in a plasma, which divides the 12 cm long proton bunch into micro bunches at the plasma period ($\lambda_{pe} \approx 1$ mm). The bunchlets modulate the electron plasma density and drive the wakefield resonantly. It is foreseen to accelerate injected electrons in the wakefield [1]. The principle of the AWAKE project is sketched in Fig. 1.

Since the proton bunch has to propagate inside the plasma channel a diagnostic is necessary to show that the plasma radius is larger than the proton bunch radius ($\sigma_r \approx 200$ μm). We propose Schlieren imaging to determine the plasma radius. In this paper we report on using Schlieren imaging to measure the radius of a column of excited Rb atoms [2]. The experiment serves as a preparation for the plasma radius measurement.

2. Method

The principle of Schlieren imaging is sketched in Fig. 2. The setup consists of two focusing lenses and an opaque object (cut-off) blocking light at the focal point of the first lens. A beam of collimated light propagates through the setup covering the transparent object to be visualized and that is placed in front of the first lens. The two lenses are arranged to form an image of the object onto the camera. The rays propagating through the object (orange and red in Fig. 2) are slightly bent by the transparent medium with a different refractive index than the surrounding medium. While the unbent rays (black) cross each other at the first lens focal point, the bent rays cross each other at a shifted position along the optical axis. Thus unbent rays can be blocked with a cut-off, while rays bent away from the cut-off can pass. The shift of the bent rays depends on the difference in the refractive index between the imaged object and the surrounding medium and on the propagation distance inside the object.

Here we use this method to image a column of excited Rb atoms surrounded by atoms in the ground state. The refractive index of

* Corresponding author at: CERN, Geneva, Switzerland.
E-mail address: anna-maria.bachmann@cern.ch (A.-M. Bachmann).

https://doi.org/10.1016/j.nima.2017.12.062
Received 30 November 2017; Accepted 21 December 2017
Available online 28 December 2017

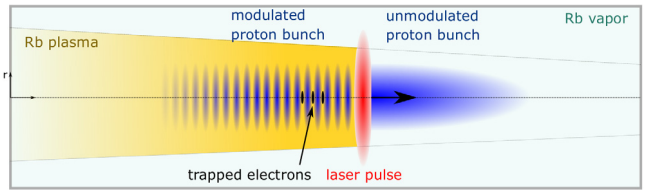

Fig. 1. Sketch of the AWAKE principle.

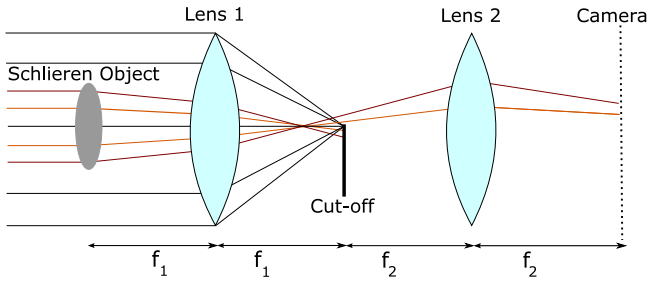

Fig. 2. Sketch of the Schlieren imaging principle with f_1 and f_2 the focal lengths of lens 1 and lens 2 [3]. (For interpretation of the references to color in this figure legend, the reader is referred to the web version of this article.)

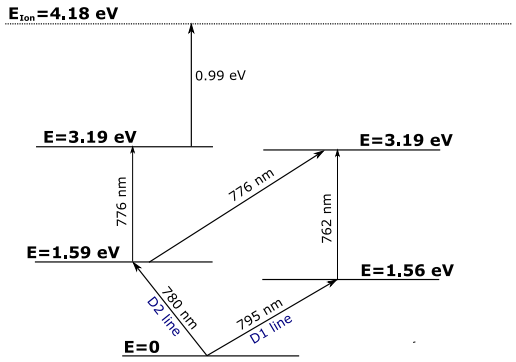

Fig. 3. Simplified atomic level structure of Rb with transitions near the wavelength of interest (D2 line) [5].

vapor for light with a frequency ω_L near the medium optical transition frequency ω_{ij} from the lower state i to the upper state j is [4]

$$n_{vapor} = \sqrt{1 + \frac{N_i\, e^2}{\epsilon_0\, m_e} \sum_{j \neq i} \frac{f_{ij}}{\omega_{ij}^2 - \omega_L^2 + i\gamma_{ij}\omega_L}}, \tag{1}$$

with N_i the density of atoms in the lower state i, f_{ij} the oscillator strength of the transition and $\gamma_{ij} = 1/\tau_{ij}$ with τ_{ij} the lifetime of the upper state j, e the elementary charge, ϵ_0 the vacuum permittivity and m_e the electron mass. Due to the resonant denominator, the index of refraction can be very different from one when $\omega_L^2 \simeq \omega_{ij}^2$, i.e. when the laser frequency is close to the transition frequency (anomalous dispersion). At room temperature the vast majority of the electrons are in the lower state, contributing to an index of refraction very different from one. Rubidium has a single electron on its external O shell, therefore N_i is equal to the Rb vapor density. Excitation of the transition with a near resonant frequency laser beam depopulates the ground state and thus changes the index of refraction of the pumped volume. At low pumping intensity the change in index is proportional to the laser beam intensity. At higher intensity saturation occurs with the maximum depopulation reaching at most 50% of the original population, when using a continuous wave (CW) laser.

Fig. 3 shows a simplified atomic level structure of Rb. Rubidium has a transition line at $\lambda \approx 780$ nm from the ground to the first excited state (D2 line). This transition is easily accessible with commercial lasers. For the radius measurement a CW laser (DLC DL pro from TOPTICA) is used. It is tunable from 763.1 nm to 813.6 nm, has a line width of less than 1 MHz and a maximum power of 138 mW. The laser can be fine tuned over a range of 50 GHz by applying voltage onto a piezo element that changes the laser cavity length.

The laser frequency is determined with absorption spectroscopy before the radius measurement of the excited column. The top of Fig. 4 shows the absorption spectrum near the Rb D2 line obtained by scanning the piezo voltage and recording with a photodiode the laser intensity transmitted through the Rb vapor. Natural Rb is composed of two isotopes, ^{85}Rb with an abundance of 72% and ^{87}Rb with an abundance of 28%. Each of the ground states is split into two hyperfine states. The four lines arising in the absorption spectrum can be used for the laser frequency determination on a very precise level as the frequency distances between the hyperfine states are very well known. They are 6.835 GHz for ^{87}Rb and 3.037 GHz for ^{85}Rb [6].

Fig. 5 shows the experimental setup. The vacuum cube containing the Rb can be heated with electrical tapes to produce Rb vapor. The vapor density can be calculated from the vapor temperature and the vapor pressure expression [7]. For instance a vapor temperature of $T = 150$ °C corresponds to a Rb vapor density of $n_{\mathrm{Rb}} \approx 1 \cdot 10^{14}$ cm^{-3}. To avoid saturation of the absorption lines and to resolve the hyperfine structure of the atoms ground states, the absorption spectrum for the laser frequency determination must be recorded at a lower Rb density ($T = 40$ °C, blue line in Fig. 4) before further heating up the source ($T = 150$ °C, red line in Fig. 4) to reach a sufficiently high Rb vapor density for a detectable Schlieren signal.

As shown in the setup of Fig. 5 the tunable laser is used for excitation (pump beam) and imaging (Schlieren beam): 90% of the beam intensity is focused with a lens (focal length $f_{L_p} = 200$ mm) onto the center of the Rb cube as pump beam. With a 50:50 beam splitter the remaining 10% is divided into the Schlieren beam and a probe beam for the laser frequency determination. The Schlieren beam also excites the medium, but due to its much lower intensity (additional filtering before propagation through the Rb vapor) than that of the pump beam, the index of refraction the Schlieren beam experiences is dominated by the effect of the pump beam. For the laser frequency determination the probe beam propagates through the Rb vapor anti parallel to the pump beam and onto a photodiode for absorption spectroscopy. The signal is normalized with a second photodiode placed at the exit of the laser to take into account intensity fluctuations while changing the laser frequency. The Schlieren beam propagates transversely to the pump beam through the vapor and into the Schlieren setup (see Fig. 2). The Schlieren and the pump beam can be blocked independently in order to obtain four different images with the CCD camera: both beams blocked, only the Schlieren beam blocked, only the pump beam blocked or none of the beams blocked. The probe beam for absorption spectroscopy is blocked during the Schlieren measurement, since the piezo voltage–laser frequency dependency was determined at low Rb vapor density.

3. Results

Fig. 6 shows images obtained with the four beam configurations. Fifteen images are averaged in each case. During the acquisition of the various images no slow laser intensity variation was observed. A horizontal razor blade (cut-off) blocks half of the Schlieren beam from below the focal point of the first lens, see Fig. 2. Fig. 6(a) was recorded blocking both beams, i.e. this image corresponds to the camera background and as expected shows no features. When recording the image in Fig. 6(b) the Schlieren beam was blocked. Thus this image shows the fluorescence of the column of excited Rb atoms. It shows the pump beam propagating horizontally, with the highest intensity reached at the beam waist ($x \simeq 0$) as expected. Note the low intensity of this signal with respect to that of Fig. 6(c) and (d). The Schlieren beam is recorded head-on covering the waist of the pump beam when present.

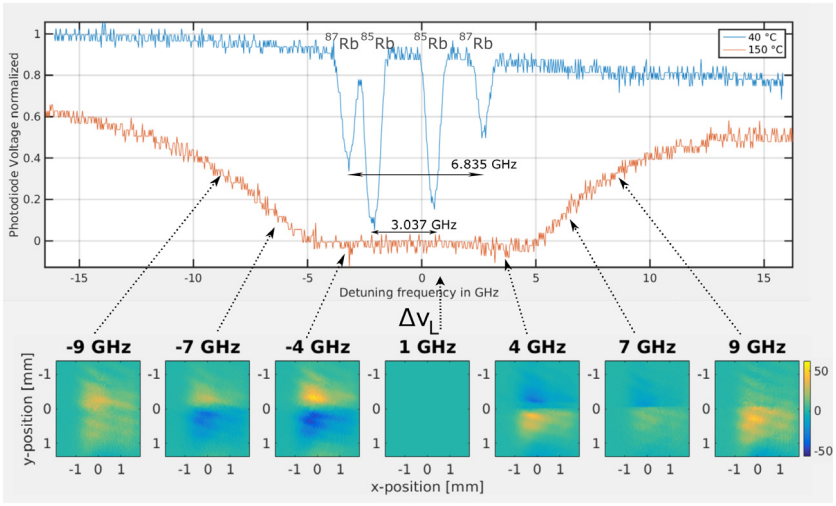

Fig. 4. Absorption spectrum near the Rb D2 line for two different Rb cube temperatures (top) and Schlieren signal of the excited Rb column with a horizontal razor blade as cut-off at high density (T = 150 °C) for different laser detuning frequencies $\Delta\nu_L$ (bottom). (For interpretation of the references to color in this figure legend, the reader is referred to the web version of this article.)

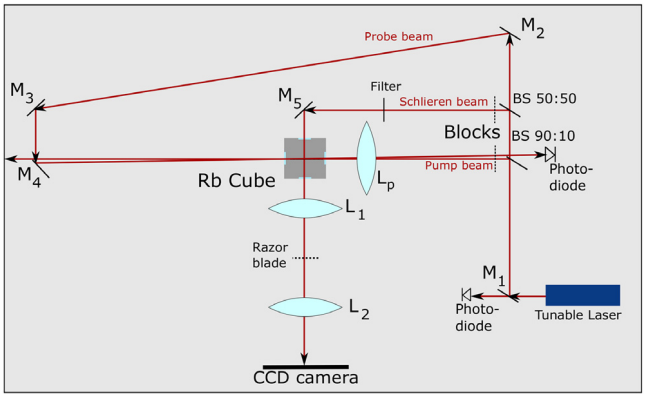

Fig. 5. Sketch of the setup for Schlieren imaging of an excited Rb column with absorption spectroscopy for the laser frequency determination.

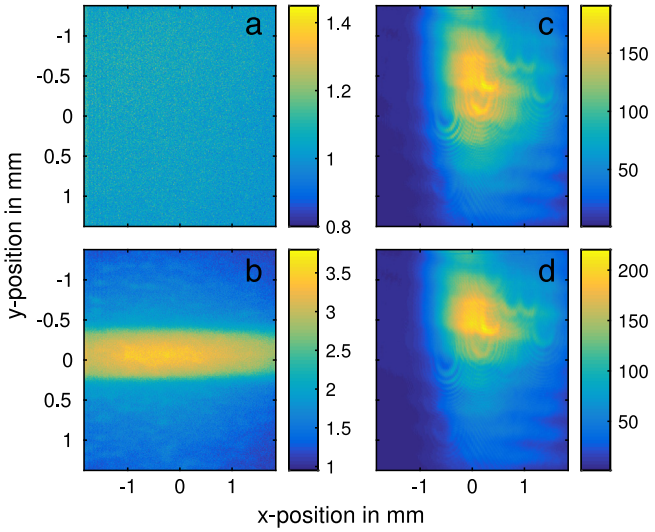

Fig. 6. CCD camera images in the four blocking configurations at high density (T = 150 °C) and a laser detuning frequency $\Delta\nu_L = -8.7$ GHz: (a) Schlieren and pump beam blocked, (b) only Schlieren beam blocked, (c) only pump beam blocked, (d) neither Schlieren nor pump beam blocked.

Fig. 6(c) shows the image of the Schlieren beam when the pump beam is blocked, i.e. without the presence of a transparent object (the excited Rb vapor column). This image shows the light of the Schlieren beam that is not blocked by the razor blade, which is slightly less than half of the unblocked Schlieren beam. Fig. 6(d) is the image with both beams propagating through the Rb vapor, i.e. the Schlieren image.

In order to extract the image of the region that was excited by the pump beam, image a is subtracted from each of the other three images. Then images (b) and (c) are subtracted from image (d). The resulting image is called the "Schlieren signal" in the following.

Fig. 4 shows the Schlieren signal for different laser detuning frequencies $\Delta\nu_L = (\omega_L - \omega_{ij})/2\pi$, $\Delta\nu_L = 0$ corresponds to the center of the four D2 transition lines. With a horizontally oriented razor blade as cut-off, the undeflected and the downwards deflected rays are blocked. This razor blade geometry displays a vertical index gradient in the object and is suitable for imaging the effect of the cylindrical, horizontally propagating laser beam of this experiment. For a negative (positive) detuning frequency $\Delta\nu_L$, the Schlieren beam is defocused (focused) by the excited Rb column, whose refractive index is smaller (larger) than one, as the surrounding medium (see Eq. (1)). Due to the blocking of downwards deflected rays by the razor blade this leads to a decrease (increase) of light on the camera in the lower half of the column and an increase (decrease) of light in the upper half of the column, which is observed in the Schlieren signals of Fig. 4 for different laser detuning frequencies.

For detuning frequencies $\Delta\nu_L \geq \pm 9$ GHz the Schlieren signal starts to fade. Here the pump does not sufficiently excite the vapor (due to the larger difference between the laser and the transition frequency) and the deflection of the Schlieren beam is too small to be detected. Approaching the transition frequency the Schlieren signal becomes stronger, since the excitation by the pump beam increases and the difference in the refractive indices between non-excited and excited vapor also increases. With this setup the laser frequency cannot approach the transition frequency arbitrarily close: If the laser frequency is too close to the transition frequency the attenuation of the Schlieren beam by the Rb vapor becomes too strong and the Schlieren beam undetectable, as depicted in the central image of Fig. 4, obtained with a detuning frequency $\Delta\nu_L = +1$ GHz.

From the four images (see Fig. 6) the radius of the excitation column is estimated. Fig. 7 shows lineouts integrated along the x-coordinate of the images: The blue dotted line of the fluorescence image (as e.g. in Fig. 6(b)) is multiplied by a factor of 15 for a better size comparison with the Schlieren signal, the red dotted line. We see again that the

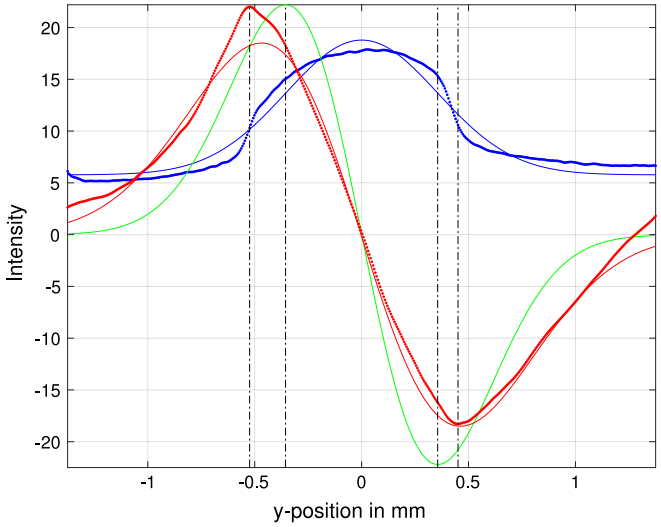

Fig. 7. Lineouts integrated along the x-coordinate of the images as shown in 6, recorded at high density ($T = 150$ °C) and a laser detuning frequency $\Delta\nu_L = -1.9$ GHz: the lineout of the fluorescence image (b), multiplied by a factor 15 (blue dotted line), its Gaussian fit (blue solid line), the fit's derivative (green solid line) and of the Schlieren signal (red dotted line) with a Gaussian derivative fit (red solid line). (For interpretation of the references to color in this figure legend, the reader is referred to the web version of this article.)

intensity of the Schlieren signal is significantly higher than the signal obtained by recording the fluorescence.

The laser beam has a Gaussian transverse profile. Assuming that the pump laser intensity is low enough not to reach saturation of the D2 transition, the depletion of the Rb ground state and thus the fluorescence signal is expected to follow the transverse pump beam profile. Since the Abel transform of a Gaussian is again a Gaussian the fluorescence light is fitted with a Gaussian function (blue solid curve). Using Eq. (1) and a Taylor expansion (since in the saturated case $N_j = N_i$ for a Rb density of $n = 1 \cdot 10^{15}$ cm^{-3} and a detuning frequency of $\Delta\nu_L = -1.9$ GHz the refractive index $n_{vapor} \approx 1.005$) the variation of the index of refraction of the Rb is $n_{vapor}(r) \approx 1 + \alpha/2 \cdot N_i(r)$ with a constant α, thus also a Gaussian function. Schlieren imaging produces a signal that is proportional to the first spatial derivative of the refractive index $\partial n/\partial y$ of the transparent object for a horizontal knife edge [3]. Thus the Schlieren signal (red dotted points) is fitted with the derivative of a Gaussian function (red solid curve). For comparison, additionally the derivative of the Gaussian fit (blue solid line) is plotted (green curve).

The dashed black vertical lines indicate the extremes of the green curve and of the red data points of the Schlieren signal. The similar extreme positions of the two curves support the assumption that the radius of the excited Rb vapor column can be measured with Schlieren imaging. We determine the radius from the distance of the extremes. The results obtained with Schlieren imaging with a laser detuning frequency of $\Delta\nu_L = -1.9$ GHz show an excitation column diameter of $d = 0.97$ mm on the CCD camera. The fluorescence image indicates a diameter of $d = 0.71$ mm. Including the optical magnification of the two lenses of the Schlieren setup ($M = 4/3$) this corresponds to an excitation radius of $r = 0.36$ mm for the Schlieren signal and $r = 0.27$ mm for the fluorescence signal. Thus the excited column radius, determined with Schlieren imaging, is close to the one measured from the fluorescence light.

4. Conclusions

We demonstrate, using Schlieren imaging, that the radius of an excited column of Rb vapor can be determined with an accuracy of approximately 30%. We used split versions of a laser beam tuned to near the D2 Rb line for the measurement. For a laser frequency very close to the D2 Rb transition line a large enough number of Rb atoms were excited and a Schlieren signal of the column was recorded. The radius of the excitation column for a laser detuning frequency of $\Delta\nu_L = -1.9$ GHz was determined with this method as $r = 0.36$ mm.

In the AWAKE experiment a short ($\tau \approx 100$ fs), powerful ($P \approx 4$ TW) laser pulse with a central wavelength of $\lambda \approx 780$ nm pumps and ionizes the Rb vapor. The laser bandwidth is broad enough (FWHM 10 nm) to also pump optical transitions from the upper level of the D2 line as well as the D1 line (see Fig. 3). This will depopulate the population of the upper state of the D2 transition, which will modify the index of refraction at large pump intensities, possibly bringing it to near one, when the ground state population is fully depleted. This may make the transition from a depleted ground state population region ($n_{vapor} \simeq 1$) to an ionized region ($n_{plasma} = \sqrt{1 - \omega_{pe}^2/\omega_L^2}$) difficult to observe using Schlieren imaging, since $\omega_L^2 \gg \omega_{ij}^2$. Further experiments will explore this case.

We want to repeat the measurement tuning the imaging laser to the wavelength of the Rb transition line from the first to the second excited state ($\lambda \approx 776$ nm, see Fig. 3) in order to resolve transitions from a region of Rb in the first excited state, that is expected to surround the plasma column when the column is excited by the short laser pulse.

In contrast to the steady state process of the shown Schlieren experiment of a Rb excitation column created by a CW laser, the Rb excitation and ionization by the short pulsed laser is a dynamic process. We can potentially use a gated camera to time resolve the evolution of the excited/ionized Rb column.

Acknowledgment

This work is sponsored by the Wolfgang Gentner Program of the German Federal Ministry of Education and Research (05E15CHA).

References

[1] P. Muggli, et al., AWAKE readiness for the study of the seeded self-modulation of a 400 GeV proton bunch, Plasma Phys. Control. Fusion (2017) (in press). arXiv:170801087.
[2] A.-M. Bachmann, Measurement of the plasma radius in a vapor cell using Schlieren imaging (Master thesis), 2016.
[3] G.S. Settles, Schlieren and Shadowgraph Techniques, Springer, 2001.
[4] W. Demtroeder, Laserspektroskopie, Springer, 2007.
[5] J.E. Sansonetti, Wavelengths, transition probabilities, and energy levels for the spectra of rubidium (RbI through RbXXXVII), Phys. Chem. Ref. Data 35 (1) (2006).
[6] D.A. Steck, Rubidium 87 D Line Data, 2008.
[7] E. Öz, P. Muggli, A novel Rb vapor plasma source for plasma wakefield accelerators, Nucl. Instrum. Methods Phys. Res. A 740 (2014).

Toward Determination of a Rubidium Plasma Column using Schlieren Imaging

A-M. Bachmann[1,2,3], **J. T. Moody**[2], **M. Martyanov**[2], **V. Fedosseev**[1], **P. Muggli**[2,1]
[1] *CERN, Route de Meyrin, 1211 Geneva, Switzerland*
[2] *Max Planck Institute for Physics, Föhringer Ring 6, 80805 Munich, Germany*
[3] *TUM, Arcisstrasse 21, 80333 Munich, Germany*
E-mail: anna-mara.bachmann@cern.ch

Abstract: Schlieren imaging is investigated as a plasma radius diagnostic at AWAKE. The Schlieren signal from an ionizing laser pulse propagating through rubidium vapor is presented. Hints for laser filamentation were observed under laser pulse depletion conditions.

1. Motivation for Plasma Radius Measurements at AWAKE

AWAKE seeks to develop a new plasma wakefield accelerator using the CERN SPS proton bunch as a driver [1]. A laser pulse propagates through a 10 m long rubidium vapor source, ionizing a column over the length of the source. The proton bunch co-propagates with the laser pulse. The sharp ionization edge seen by the proton bunch seeds the transverse self-modulation that transforms the long bunch into micro-bunches that resonantly drive the wakefields. The plasma radius must exceed the proton bunch radius. We want to use Schlieren imaging to determine the plasma radius. We use a tunable, narrow bandwidth laser to transversely probe the column of ionized and excited rubidium. We operate the imaging laser at a wavelength very close to the D2 transition line of rubidium ($\lambda = 780\,\mathrm{nm}$), in order to achieve a large difference in refractive index between non-excited and excited or ionized rubidium. We are investigating how to distinguish between excited and ionized rubidium in Schlieren images.

2. Principle of Schlieren Imaging as a Plasma Radius Diagnostic

At Schlieren imaging, an initially collimated beam of the imaging laser is focused to a point by a lens and subsequently re-collimated by a second lens, see Fig. 1. When a transparent object with a different refractive index than the surrounding medium is present in front of the first lens, rays are bent by the transparent object and are displaced in the focal plane. By placing a blade in the focal plane covering half the focal point, rays deflected towards the blade are blocked, while those deflected away from it can pass it. These rays can reach a camera placed after the second lens. We arrange the two lenses to image the plane of the transparent object into the plane of the camera. If one blocks the bottom half of the focal spot, a horizontally cylindrical transparent object, such as a column of excited or ionized rubidium surrounded by non-excited rubidium, appears as half a bright zone (upwards deflected rays) and half a dark zone (downwards deflected rays).

The refractive index of vapor for laser light with a frequency ω_L near the medium optical transition frequency ω_{ij} from the lower state i to the upper state j is $n_{vapor} = \sqrt{1 + \frac{N_i e^2}{\varepsilon_0 m_e} \sum_{j \neq i} \frac{f_{ij}}{\omega_{ij}^2 - \omega_L^2 - i\gamma_{ij}\omega_L}}$, with N_i the density of atoms in the lower state i, f_{ij} the oscillator strength of the transition and $\gamma_{ij} = 1/\tau_{ij}$ with τ_{ij} the lifetime of the upper state j, e the elementary charge, ε_0 the vacuum permittivity and m_e the electron mass [2]. The index of refraction can strongly differ from one when $\omega_L^2 \simeq \omega_{ij}^2$, i.e. when the frequency of the imaging laser used for Schlieren imaging is close to the transition frequency (anomalous dispersion). It is expected to be difficult to distinguish between a ground state depleted region ($n_{vapor} \simeq 1$) and an ionized region ($n_{plasma} = \sqrt{1 - \omega_{pe}^2/\omega_L^2}$) using Schlieren imaging, since $\omega_L^2 \gg \omega_{pe}^2$.

3. Setup of Schlieren Imaging for Plasma Radius Measurements at AWAKE

We investigate whether we can use Schlieren imaging to determine the transverse size of an excited or ionized

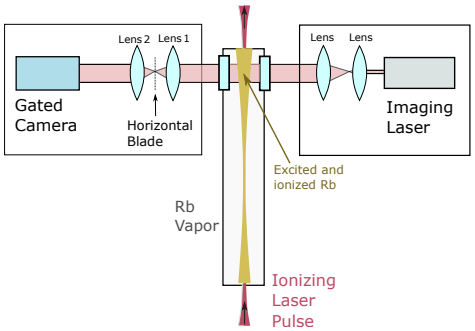

Fig 1. Setup for Schlieren Imaging of a column of excited and ionized rubidium vapor

column of rubidium vapor with a neutral density of $2 \cdot 10^{14}\mathrm{cm}^{-3}$. For this purpose we send an ionizing, 100 fs laser pulse with a central wavelength of 780 nm and a FWHM bandwidth of 15 nm through the rubidium vapor

source. For the results presented here, the energy of the laser pulse is approx 6 mJ in order to investigate the laser filamentation regime. At this low laser pulse energy only a few percent of the pulse energy is transmitted through the whole length of the rubidium vapor source.
The imaging laser beam, a CW laser DLC DL pro from TOPTICA, is directed perpendicularly to the ionizing laser pulse through the viewports at the end of the source, as shown in Fig. 1. The imaging laser is tunable from 763.1 nm to 813.6 nm, has a line width of less than 1 MHz and a maximum power of 138 mW. By applying voltage onto a piezo element, the laser cavity length is changed and the laser frequency can be fine tuned over a range of 50 GHz. We determine the laser frequency with rubidium absorption spectroscopy at the D2 transition line at 780 nm. For the Schlieren measurements we operate it with a laser frequency detuned by approx 5 GHz from the $5P_{3/2}, F = 3$ excited to the $5S_{1/2}$ ground state transition of ^{85}Rb. Images are recorded with an ANDOR iStar 334T gated camera to amplify the signal over short time scales.

4. Preliminary Results of the Schlieren Imaging Measurements

An example for recorded Schlieren images is shown in Fig. 2. The laser light is amplified (camera gain 4000) and

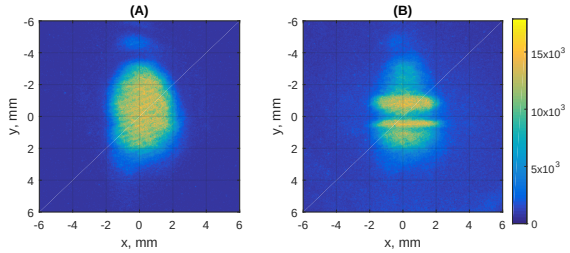

Fig 2. Schlieren images obtained with the ionizing laser beam (A) and without out it (B)

gated over 1µs. The image without the ionizing laser pulse is shown in Fig. 2 (A). This corresponds to an image without transparent object (no excitation or ionization). Fig. 2 (B) shows the image when the ionizing laser pulse is sent through the rubidium, recorded right after the pulse passage. It shows the effect on the imaging laser of an excited or ionized column of rubidium, visualized with Schlieren imaging.
The difference between the Schlieren image with and without the ionizing laser pulse is shown in Fig. 3. The profile obtained by averaging the image along the ionizing laser propagation distance (x) between $-1\,\text{mm} \leq x \leq 1\,\text{mm}$ is shown on the right hand side. For a single excitation or ionization column a single minimum and a single maximum are expected in the intensity profile. For this event multiple minima and maxima are visible in the profile. The multiple bright and dark columns in the Schlieren image suggest filamentation of the ionizing laser pulse, occurring in the low laser energy regime. This will be further investigated by scanning different parameters, such as rubidium density, ionizing laser pulse energy, imaging laser frequency, etc. and comparing the results to head-on images of the ionizing laser pulse transverse profile, obtained as reported by J.T. Moody in these proceedings [3].

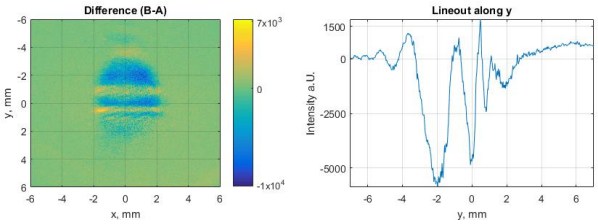

Fig 3. Difference of the two images in Fig. 2 (B)-(A) (left), profile of the image averaged between $-1\,\text{mm} \leq x \leq 1\,\text{mm}$ (right)

5. Conclusion

Schlieren imaging is used to visualize transparent objects with a different refractive index than the surrounding medium. We investigate using it to visualize a column of excited or ionized rubidium. We have measured a Schlieren signal of the changing refractive index of rubidium, created by an ionizing laser pulse propagating through rubidium vapor. Preliminary results show hints for laser filamentation of the laser pulse operating it in the low energy regime, appearing as multiple columns of excited or ionized rubidium vapor in the Schlieren image. We will correlate the results with head-on images of the ionizing laser pulse transverse profile [3].

6. References

[1] A. Caldwell et al., Phys. Plasmas **18**, 103101 (2011)
[2] W. Demtroeder in *Laserspektroskopie*, (Springer Verlag, 2007).
[3] J. T. Moody et al., "Multi Keldysh Regime Resonant Ionizing Laser Pulse Propagation Through a Ten Meter Rubidium Vapor Source at AWAKE", The proceedings of this conference (COFIL2018).